SUBMILLIMETER SPECTROSCOPY OF THE CARINA NEBULA: OBSERVATIONS, OPERATIONS AND UPGRADES OF THE SOUTH POLE IMAGING FABRY-PEROT INTERFEROMETER

A Dissertation

Presented to the Faculty of the Graduate School

of Cornell University

in Partial Fulfillment of the Requirements for the Degree of

Doctor of Philosophy

by

Thomas Edward Oberst

August 2009

SUBMILLIMETER SPECTROSCOPY OF THE CARINA NEBULA: OBSERVATIONS, OPERATIONS AND UPGRADES OF THE SOUTH POLE IMAGING FABRY-PEROT INTERFEROMETER

Thomas Edward Oberst, Ph.D.

Cornell University 2009

We present the results of a $\sim$ 250 arcmin^2 mapping of the 205 μm [NII] fine-structure line emission over the northern Carina Nebula, including the Car I and Car II HII regions. Spectra were obtained using the South Pole Imaging Fabry-Perot Interferometer (SPIFI) at the Antarctic Telescope and Remote Observatory (AST/RO) at South Pole. New upgrades and modifications to the SPIFI instrument are discussed, and full details of SPIFI-AST/RO integration and calibration are provided. At the time of these observations, SPIFI had a spectral resolving power of $\sim$ 4250, a FWHM beam size of $\sim$ 54$''$, and a noise equivalent power (NEP) referred to the front end of the receiver of $\sim 2.5 \times 10^{-15}$ W Hz$^{-1/2}$ ($\sim$ 1.4 times the background limit). These data constitute the first ground-based detection of the 205 μm [NII] line, and only the third detection overall since those of the Cosmic Background Explorer (COBE) Far Infrared Absolute Spectrophotometer (FIRAS) and the Kuiper Airborne Observatory (KAO) in the early 1990s.

We supplement the 205 μm data with new reductions of far-infrared fine-structure spectra from the Infrared Space Observatory (ISO) in 63 μm [OI], 122 μm [NII], 146 μm [OI], and 158 μm [CII]; the 146 μm [OI] data include 90 raster positions which have not been previously published. Morphological comparisons are made with optical, radio continuum and CO maps. The 122/205 [NII] line ratio is used to probe the density of the low-ionization gas, and the 158/205

[CII]/[NII] line ratio is used to probe the fraction of C^+ arising from photodissociation regions (PDRs). The [OI] and [CII] lines are used to construct a PDR model of Carina following Kaufman *et al*. (1999). When the PDR properties are compared with other sources, Carina is found to be more akin to 30 Doradus than galactic star-forming regions such as Orion, M17, or W49. This is consistent with the view of Carina as a more evolved region, where much of the parent molecular cloud has been ionized or swept away.

BIOGRAPHICAL SKETCH

Thomas Edward Oberst was born on July 27, 1979 in Pittsburgh, Pa., and raised in the Troy Hill neighborhood near downtown Pittsburgh. After studying studio arts for a brief time, Oberst earned undergraduate degrees in physics and mathematics from Duquesne University. He pursued graduate studies in physics at Cornell University, where the current work was conducted.

While at Cornell, Oberst served as an NSF Integrative Graduate Education and Research Traineeship (IGERT) Fellow, an NSF Cornell Science Inquiry Partnerships (CSIP) Fellow, and a NASA Graduate Student Research Program (GSRP) Fellow. He received the first Cranson and Edna B. Shelley Teaching Assistant Award from Cornell University's Department of Astronomy. He also served as a science writer intern at the Cornell Chronicle, where one of his stories helped win a silver medal for science journalism from the Council for Advancement and Support of Education (CASE). Oberst lived in Rome, Italy, for six months and has traveled in six continents – including three trips to South Pole to collect the data presented here.

Oberst is currently an Assistant Professor of Physics at Westminster College. He lives with his wife, Emily, and son, Ross, in Wexford, Pa., close to their family and friends in Pittsburgh. In his free time, Oberst is an active environmentalist, artist, weekend warrior, DIYer, and Steelers devotee.

Members of the Cornell Submillimeter Astronomy Group at the Geographic South Pole, January 29, 2004. From left to right: Research Associate Thomas Nikola, the author, and Professor Gordon J. Stacey. (*Credit: Patricia Douglas*)

For my father

Edward James Oberst (1944-1998)

ACKNOWLEDGEMENTS

I thank the following individuals and groups, who have contributed either directly or indirectly to this work:

My mother, Karen D. Snyder, my wife, Emily S. Oberst, and all other family members who have supported me with love and encouragement. Cornell classmates Gabriel G. Shaughnessy, Benjamin M. Hunt and Andrew R. Schmidt, for collaborations on early graduate classwork as well as continued friendship and support.

The Cornell University Submillimeter Group, who pioneered the SPIFI campaign long before I joined the group, who taught me everything I know about submillimeter astronomy, and who shouldered much of the work behind the present results: Gordon J. Stacey, Thomas Nikola, Stephen C. Parshley and Steven Hailey-Dunsheath. All others who designed, built and operated SPIFI before me, including C. Matt Bradford, Alberto D. Bolatto, James M. Jackson, Mark R. Swain, Maureen L. Savage and Jacqueline A. Davidson. Approximately 15 undergraduate student researchers who contributed to SPIFI during my time at Cornell – especially Julia Kamenetzky, who reduced a significant portion of the ISO data presented here. Peter A. R. Ade, Carole E. Tucker and the Cardiff group, for providing SPIFI's filters. Our collaborators at the Harvard-Smithsonian Center for Astrophysics (CFA), who supported SPIFI observations at the AST/RO: Antony A. Stark, Adair P. Lane, Andrea Löhr, Nicholas F. H. Tothill and Jules I. Harnett. Jacob W. Kooi, for operating local oscillators at the AST/RO during SPIFI calibration. K. Sigfrid Yngvesson and the TREND group, for use of the TREND laser at the AST/RO during SPIFI calibration. The RPSC South Pole Science Support Team, for constructing *Spifihaus* and other logistical

support: Paul Sullivan, Al Baker, and their crew. South Pole Station machinist and winterover Allan Day, for troubleshooting SPIFI equipment on several occasions. Our collaborators at the NASA Goddard Space Flight Center (GSFC), for hosting and mentoring me at the GSFC on three occasions, for providing SPIFI's current thermistor-sensed bolometers, and for contributing hardware and support to our next generation of TES bolometers: Dominic J. Benford, Johannes G. Staguhn, Christine A. Allen and S. Harvey Moseley.

My past and present Special Committee members, including Veit Elser and Donald L. Hartill, for your guidance. Cornell University, the Graduate School, the Department of Physics, and the Department of Astronomy, for giving me this opportunity. NASA and the NSF, for funding this work through the following grants: NASA GSRP NNG05GK70H; NSF IGERT DGE-9870631; NSF CSIP DGE-0231913; and NSF OPP-0094605, -0338149, and -0126090.

Finally, I extend extra special gratitude to Stephen C. Parshley for enduring a winter at South Pole to ensure the success of this project.

Thank you.

TABLE OF CONTENTS

LIST OF TABLES

LIST OF FIGURES

CHAPTER 1

THE SPIFI SOUTH POLE CAMPAIGN

The South Pole Imaging Fabry-Perot Interferometer (SPIFI) is a direct-detection spectrometer which operates in the submillimeter (submm; λ = 200 μm – 1 mm) regime, at the frontier between far-infrared (FIR) and radio wavelength astronomy. SPIFI's conception was motivated by the need to study the star-forming regions and galactic nuclei of the Milky Way and nearby galaxies. These sources are enshrouded by optically opaque dust, and emit most of their energy via FIR and submm line and continuum radiation.

Between 1997 and 2003, SPIFI conducted six observing campaigns at the 15 m James Clerk Maxwell Telescope (JCMT) on Mauna Kea, measuring several novel Galactic and extragalactic emission spectra in the 370 μm ^{12}CO(7→6) and [CI] spectral lines. However, as its name implies, SPIFI was specifically designed to take advantage of the exceptional submm transparency of the Earth's atmosphere at the Geographic South Pole, where the 200 μm telluric "window" (which is completely unavailable at most temperate sites) opens for a few months each winter.

Starting in 2003, SPIFI underwent a series of modifications and updates in preparation for deployment to the Antarctic Submillimeter Telescope and Remote Observatory (AST/RO) at South Pole. These previously unpublished changes – along with special South Pole operational considerations – are presented in this chapter. Section 1.1 motivates the choice of South Pole as SPIFI's observing site, providing a brief history of site studies and submm astronomy at the Pole. It also introduces new SPIFI 205 μm skydip data. Section 1.2 describes SPIFI's new High Order Fabry-Perot Interferometer (HOFPI), stepper motors,

filters, and calibration unit. Finally, Section 1.3 discusses SPIFI installation and operation on the AST/RO, including the Nasmyth mount, foreoptics, field of view, remote controls and cryo-maintenance.

With these preparations in place, SPIFI conducted its first successful observations from South Pole in August, 2005, mapping the Carina Nebula in 205 μm [NII] emission. The data enabled the estimation of several physical parameters of the interstellar medium (ISM) in the Carina region, and constituted the first direct detection of the 205 μm [NII] line from a ground-based observatory. These observational results are presented in Chapter 2.

1.1 Submillimeter Astronomy at South Pole

1.1.1 A Brief History

Prehistory

Shortly after Amundsen and Scott first reached the Geographic South Pole in December 1911 and January 1912, speculations about the benefits of conducting astronomical observations from Antarctica arose. The expeditions had noted high altitudes and low humidity on the Antarctic Plateau – favorable conditions for observing. Later in 1912, Admiral Robert E. Peary – who had led the first expedition to the North Pole in 1909 – sent a letter to Edwin B. Frost, director of the venerable Yerkes Observatory in Williams Bay, Wis., suggesting that continuous observations from Antarctica could yield valuable results. Peary even estimated the largest part he could transport to an Antarctic site, as well as special on-site construction considerations. However, Frost was unenthusiastic about the sug-

gestion, responding three weeks later that useful observations from Antarctica would be logistically impossible (Indermuehle *et al*. 2005).

Substantial motivation for Antarctic astronomy did not arise again until mid-century, when the International Council of Scientific Unions (ICSU) proposed the "International Geophysical Year" (IGY) to be held from July, 1957, to December, 1958. The IGY was modeled after the International Polar Years of 1882 - 1883 and 1932 - 1933, and coordinated observations of geophysical phenomena were planned by scientists around the world. The first astrophysical experiment in Antarctica took place during IGY planning, when cosmic ray detectors were installed at Mawson station in 1955 (Parsons 1957a, 1957b).

US scientists had proposed building an IGY station at the South Pole, but no firm plans existed until a USSR delegation to a July 1955 IGY conference in Paris – who had arrived two days late – announced their intent to build one. The French conference chairman immediately announced that the committee members "have [already] accepted the offer of the United States to erect and man a South Pole station." With this political motivation in place, President Dwight D. Eisenhower ordered Operation Deep Freeze, by which the US Navy began constructing a station at the Geographic South Pole on November 20, 1956 (Dufek 1957). The station has been continuously occupied since that date, and was officially named the Amundsen-Scott South Pole Station in 1961. Despite its political origins, the establishment of the South Pole station paved the way for modern astrophysics in Antarctica.

The First Photon-Collecting Instruments

As early as 1957, South Pole station crews began collecting daily meteorological (radiosonde) data (Chamberlin 2001), verifying the stable conditions and low precipitable water vapor (PWV) levels there (§1.1.2). In 1964, in conjunction with another cosmic ray detector project, a 3.5 inch optical telescope was used to make a semi-quantitative analysis of stellar and solar observing conditions at South Pole – a follow-up report in 1970 by Arne A. Wyller of the US National Academy of Science cited excellent "seeing" conditions and recommended the Pole as an observing site (Indermuehle *et al*. 2005). Between 1979 and 1982 a second small telescope was deployed to the Pole to measure solar eigenmodes (*e.g.* Grec *et al*. 1980).

Unfortunately, claims of excellent seeing at the Pole did not hold up: measurements by the Automated Astrophysical Site Testing Observatory (AASTO; Storey 1998) found seeing that averaged FWHM = 1.″8 (Loewenstein *et al*. 1998; Travouillon *et al*. 2003b), as compared to 0.″5 – 1.″0 at the best temperate sites. This has been attributed to atmospheric turbulence driven by katabatic winds at the top of a temperature-inversion layer several hundred meters above ground (Marks *et al*. 1996; Marks *et al*. 1999; Travouillon *et al*. 2003a). Because the polar atmosphere is believed to be very stable above this inversion layer, optical astronomers have shifted focus from the Pole to the higher elevation sites on the Antarctic Plateau. At the French-Italian station at Dome Concordia (Dome C; Figure 1.1; Table 1.1), which sits 462 m higher than the Pole at an elevation of 3233 m, the median seeing was measured to be 0.″27 – two to three times lower than the best mid-latitude sites – and the best seeing there was measured to be 0.″07 – the lowest value reported anywhere (Lawrence *et al*. 2004).

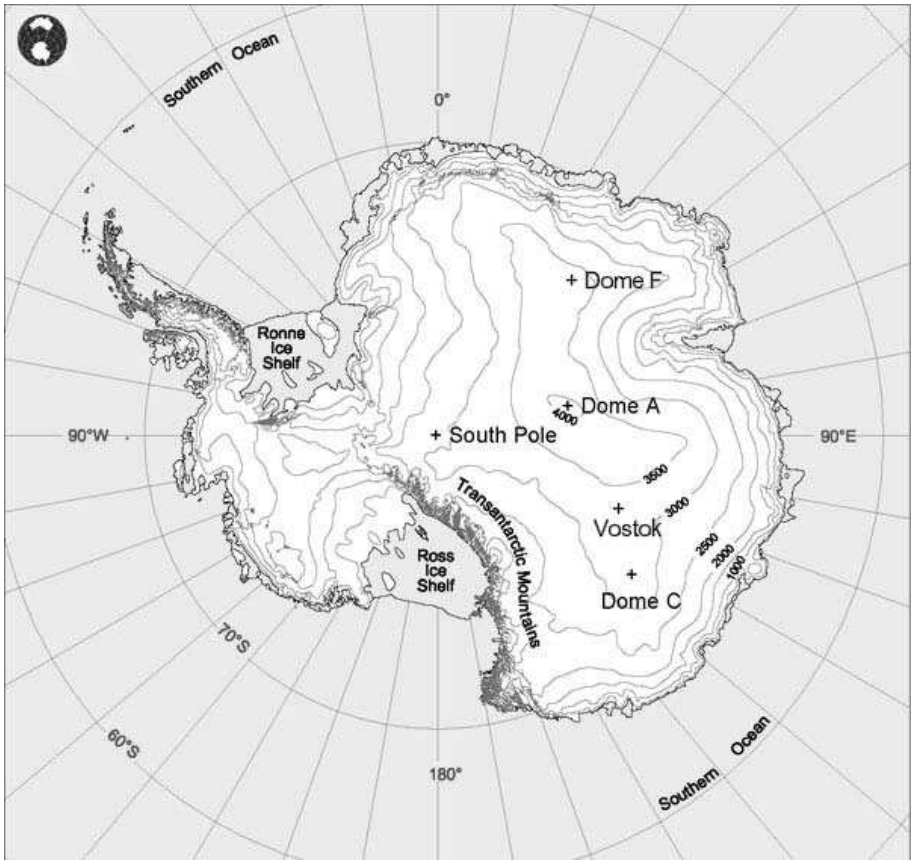

Figure 1.1: Scientific Research Stations on the Antarctic Plateau
Basic map obtained from the Australian Antarctic Data Center (AADC)

Table 1.1: Scientific Research Stations on the Antarctic Plateau

Station	**Location**	**Elevation**
South Pole	90°S, 0°E	2771 m
Vostok	77°S, 104°E	3529 m
Dome Concordia (C)	75°S, 125°E	3233 m
Dome Fuji (F)	77°S, 37°E	3786 m
Dome Argus (A)	81°S, 77°E	4093 m

Station coordinates and elevations obtained from the Antarctic Digital Database (ADD), version 4.1, www.add.scar.org

At longer wavelengths, however, seeing is not the limiting factor. Rather, IR, submm, and millimeter (mm) wavelength observations suffer their most severe degradation due to absorption by telluric water vapor, which can decrease atmospheric transmission to near 0 % at most temperate sites (§1.1.2). By the early 1980s, two decades of twice-daily radiosonde measurements and additional site studies (Smythe & Jackson 1977; Murcray *et al*. 1981) indicated that PWV levels at the Pole were consistently better than Mauna Kea, one of the best developed sites for long-wavelength astronomy.

Submillimeter Instruments in Antarctica

The first submm instrument in Antarctica was the 45 cm Emission Millimetrique (EMILIE) telescope, which measured the diffuse Galactic (dust) emission at ∼ 900 μm from South Pole during the 1984 – 85 summer (Pajot 1989). EMILIE had had previous success at the Canada-France-Hawaii Telescope on Mauna Kea (Pajot *et al*. 1986a, 1986b). It was the most ambitious and logistically challenging scientific project yet attempted in Antarctica, requiring liquid helium (ℓ-^{4}He) to be transported all the way from the US (Indermuehle *et al*. 2005).

Using an upgraded version of EMILIE, a team from the AT&T Bell Laboratories attempted to measure the cosmic microwave background (CMB) anisotropy from the Pole during the austral summer of 1986 - 87 (Wright 1994; Indermuehle *et al*. 2005). Among the team members was Antony A. Stark, who would later become the director of the Antarctic Submillimeter Telescope and Remote Observatory (AST/RO) and a senior scientist of the 10 m South Pole Telescope (SPT). The team returned in the summer of 1988 – 89 and collected CMB measurements at 350, 450 and 600 μm (Dragovan *et al*. 1989). Their receiver con-

Table 1.2: History of Submillimeter Astronomy Projects in Antarctica

Instrument	**Deployment**	**Bands ($\sim \lambda$ or ν)**	**References***
EMILIE	Nov. – Dec. 1984	900 μm	Pajot *et al*. 1986
AT&T 1.2 m	Nov. – Dec. 1988	350, 450 & 600 μm	Dragovan *et al*. 1989
AST/RO	1995 – 2005	200 μm – 1.3 mm	Stark *et al*. 1997b, 2001
230 GHz SIS	1995 – 2005	230 GHz	–
WANDA	1995 – 2005	492 & 810 GHz	Walker *et al*. 1992; Honingh *et al*. 1997
492 GHz SIS quasioptical	1995 – 2005	492 GHz	Zmuidzinas & LeDuc 1992; Engargiola *et al*. 1994
PoleSTAR	2000 – 2005	810 GHz	Groppi *et al*. 2000
TREND	2003 – 2005	1.5 THz	Gerecht *et al*. 2003
SPIFI	2003 – 2005	200 & 350 μm	Swain *et al*. 1998
SPT	2007 –	200 μm – few mm	Ruhl *et al*. 2004

*References are for instrumentation articles only, with the exception of the AT&T 1.2 m, for which Dragovan *et al*. (1989) is the only publication. Scientific results can be found in the following sources: for EMILIE, see Pajot *et al*. (1989); for AST/RO receivers, a full list of (> 100) publications can be found online at http://www.cfa.harvard.edu/~adair/AST_RO/pub.html; for the South Pole 10 m, see Staniszewski *et al*. (2008).

sisted of a 1.2 m primary and 32-pixel bolometer array cooled to ~ 1 K by a ^{3}He fridge, which also required the transport of ℓ-^{4}He to the Pole.

Both EMILIE and the AT&T instrument were summertime projects. Significant effort was required to transport, assemble and disassemble the instruments in an ~ 4 month window with little return in observing time. What observing time they did have was during the warmest, wettest months of the year. For significant progress to take place, a year-round observatory was needed.

That need was finally met in 1995 by the Antarctic Submillimeter Telescope and Remote Observatory (AST/RO), which became the first full-time (and hence winter-over) telescope at the Pole (Stark 1989; Stark *et al*. 1997b, 2001).

The AST/RO had an off-axis Gregorian optical design with a 1.7 m primary optimized for $\lambda \sim 200$ μm - 1.3 mm. The AST/RO hosted six receivers throughout its lifespan (1995 – 2005), which are summarized in Table 1.2. Its most significant scientific contributions include arcminute-resolution CO and [CI] emission mapping projects in the Magellanic Clouds (*e.g.* Stark *et al*. 1997a), the Galactic center (*e.g.* Martin *et al*. 2004), and the Carina Spiral Arm (Zhang *et al*. 2001), and the first direct detection of the 205 μm [NII] emission from a ground-based observatory (Oberst *et al*. 2006) and subsequent 205 μm [NII] mapping of the Carina Nebula (Chapter 2 of the present work).

The great success of the AST/RO motivated the design and construction of the 10 m South Pole Telescope (SPT; Ruhl *et al*. 2004; Padin *et al*. 2008). Like the AST/RO, SPT has a Gregorian optical design and operates from $\lambda \sim 200$ μm – a few mm. However, SPT can achieve a factor of ~ 36 lower noise equivalent flux density (NEFD) per beam at 350 μm than AST/RO (Stark *et al*. 1998) and is equipped with an array of 1000 superconducting transition edge-sensed (TES) bolometers. The SPT is currently conducting a Sunyaev-Zel'dovich effect survey as a means to search for large galaxy clusters at high redshifts, aiming to constrain the dark energy equation of state (Staniszewski *et al*. 2008).

Despite great success at South Pole, submm observing conditions are expected to be even better at higher elevation sites on the Antarctic Plateau. Dome Argus (Dome A; Figure 1.1; Table 1.1), the highest point on the plateau, may be the best submm site on Earth. Site-testing projects are currently being conducted at both Dome C (Calisse *et al*. 2004) and Dome A (Kulesa *et al*. 2008), and an automated submm telescope is planned for Dome A (Walker *et al*. 2004).

1.1.2 Site Studies

The submm is a relatively new regime of observational astronomy at the frontier between FIR- and mm-wavelength studies. Its great scientific potential lies in both the submm brightness of many astrophysical sources and the ability of submm photons to pierce dust-enshrouded regions in galaxies. Unfortunately, observing these photons from ground-based observatories is extremely difficult. Molecules in the Earth's atmosphere absorb strongly in the submm bands, so that much of the astronomical flux ariving at the top of the atmosphere never reaches the ground. For example, during SPIFI observations of the Carina Nebula – discussed in the next chapter – line-of-sight (l.o.s.) transmission was < 5 % at 205 μm.

Furthermore, this atmospheric opacity results in a bright (very emissive) submm sky: for the [NII] observations presented in this thesis, the sky is $\gtrsim$ 10,000 times brighter than the spectral lines we observe. This bright sky results in a photon "background," the statistical arrival rates of which produce a background noise much larger than the shot noise from source photons. For an ideal system, this (approximately shot noise dominated) background is the dominant noise in the system. In space, the background would be much smaller. A second source of noise, generally important only for submm photometers, is fluctuations in transmission due to turbulence in the atmosphere, or "sky noise". We discuss opacity and sky noise here, and background noise in §1.2.2.

Opacity

The submm opacity of the Earth's atmosphere is due to thousands of pressure-broadened absorption lines occurring between 200 μm and 1 mm.[1] Although many molecular species are to blame, water vapor is by far the greatest offender. As a result, opacity studies are often divided into an H_2O component and everything else – the "dry-air" component. We consider first the water.

Precipitable Water Vapor Measurements The most common measure of atmospheric H_2O content is "precipitable water vapor" (PWV): the depth of liquid water that would result from condensing all the water vapor in a vertical column (of cross-sectional unit area) extending from the ground to the top of the atmosphere. Submm observations can usually only occur when PWV $\lesssim 1$ mm. Although rare, select conditions on Earth can produce such a low PWV:

- *Dry sites*: sites that are naturally dry due to weather patterns (deserts)
- *High elevation sites*: as the atmosphere thins with altitude, so does the abundance of water vapor
- *Cold sites*: as the temperature drops, so does the the partial pressure for saturation, lowering the abundance of water vapor

Therefore, the combination of dry, high, and cold (which are typically not mutually exclusive) makes for the best submm observatory sites. The Antarctic Plateau possesses this combination: its Polar location limits solar radiation to

[1]For extensive catalogs of molecular transitions, see the Cologne Database for Molecular Spectroscopy (CDMS) at http://www.astro.uni-koeln.de/cdms/, or the Molecular Spectroscopy catalog of the NASA Jet Propulsion Lab (JPL) at http://spec.jpl.nasa.gov.

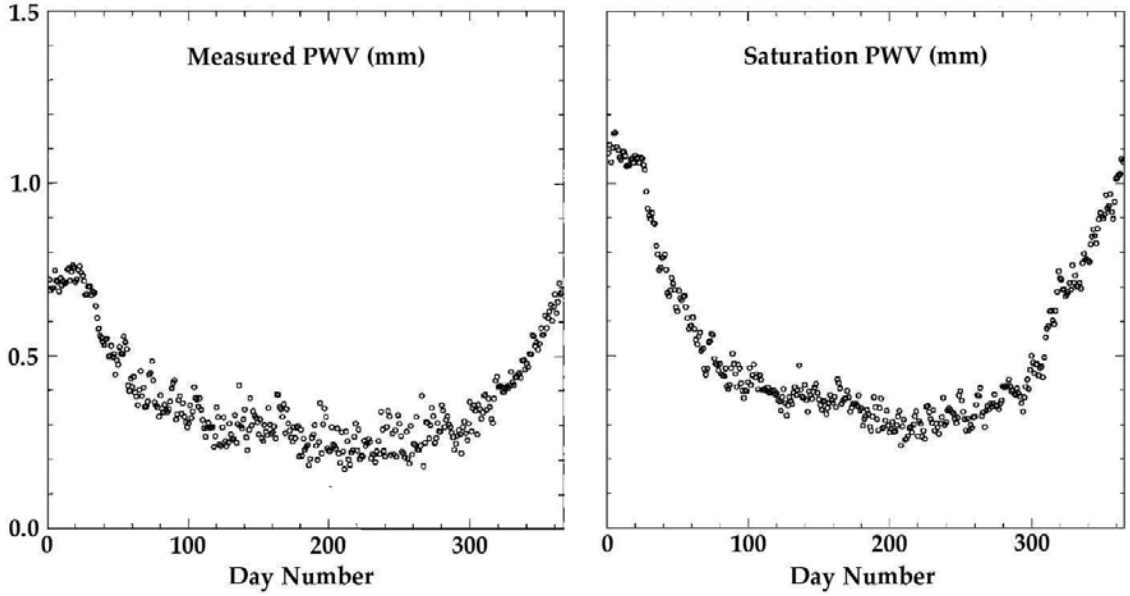

Figure 1.2: Average PWV During the Polar Year (1961 – 1999)
Measured radiosonde (left panel) and calculated saturation (right panel) PWVs at South Pole, binned by day of the year and averaged from 1961 – 1999. The median measured value in the wintertime is 0.27 mm. The PWV is seen to be at or near saturation for much of the Polar winter. (Chamberlin 2001).

incident angles of $\lesssim 23.5^\circ$ and it rests atop an ice sheet with an average thickness of nearly 1.5 miles.[2] In particular, South Pole, the most developed site on the Plateau, has an elevation of 2771 m (Figure 1.1; Table 1.1) and average wintertime temperature of -57 °C.[3]

Meteorological radiosonde measurements of precipitable water vapor (PWV) have been made twice per day by the South Pole station crew since at least 1961. Chamberlin (2001) has plotted the complete data from 1961 – 1999, averaged and binned for each day of the year (Figure 1.2, left panel). The median value in the wintertime is 0.27 mm. For comparison, he has also plotted the theoretical PWV at saturation (Figure 1.2, right panel). At South Pole's av-

[2]Antarctic Digital Database (ADD), version 4.1, www.add.scar.org
[3]NOAA International Station Meteorological Climate Summary Version 4.0, released February, 1997

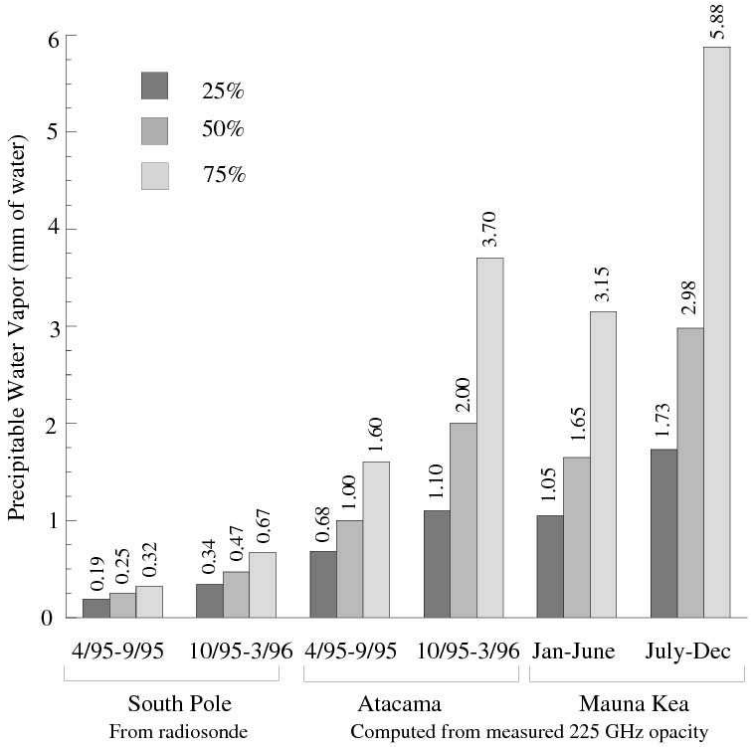

Figure 1.3: PWV Quartiles at South Pole, Atacama, and Mauna Kea
PWV quartiles are shown at the world's three best developed sites for submm astronomy, grouped into the best and worst six months at each site. The wettest quartile at the Pole has less PWV than the driest quartile at the other sites. (Lane 1998).

erage wintertime temperature of -57 °C, the partial pressure of water vapor at saturation is ~ 0.5 % of its value at 0 °C (Goff & Gratch 1946). Thus, the Pole's frigid temperatures have a dessicating effect, causing the air to saturate at very low PWV levels. From Figure 1.2 it is clear that the air is at or near saturation for much of the Polar winter.

Figure 1.3 (Lane 1998) shows quartile PWVs at the three best developed sites for submm astronomy – South Pole, Atacama, and Mauna Kea – divided into the six best months and six worst months of the year. Measured 225 GHz opacity was used to derive the PWV values at Mauna Kea and South Pole, and may overestimate PWV at Mauna Kea by ~ 12 % (Stark *et al*. 2001). Even so, the 75th

percentile during wetter half of the year at Pole is lower than the 25th percentile for the driest half of the year at both Atacama and Mauna Kea. During the best quartile, South Pole's PWV is < 0.19 mm.

Although PWV is a major factor affecting opacity, it is not a direct measure of opacity, so ranking sites by PWV can have caveats. Some of the complicating factors include:

1. At colder sites, a greater abundance of H_2O vapor molecules are in lower rotational energy levels. It is these lower levels which are responsible for most of the absorption in the short submm bands.
2. At lower elevation sites, the H_2O vapor lines are more severely pressure broadened.
3. During the driest weather at submm sites, and at lower elevation sites, absorption due to the dry air opacity component (see Page 13) becomes more significant.

At a given low PWV level, these factors combine to give South Pole worse submm opacities than Atacama. But measured PWVs at the two sites are not the same (Figure 1.3). According to the atmospheric model of Pardo *et al*. (2001; discussed on page 16), for frequencies above 980 GHz, telluric transmission is expected to be similar at the two sites when Atacama has ~ 1.75 times higher PWV than Pole. In Figure 1.3, we see that PWVs at Atacama are typically much greater than 1.75 times the PWVs at South Pole, suggesting that South Pole still has better submm opacity.

Direct Opacity Measurements While PWV is the largest single factor affecting opacity, thousands of other telluric absorption lines also contribute a "dry

air" opacity component. During the driest weather at submm sites, this component can play a significant role. For this reason, and to avoid the complications discussed above, direct opacity measurements at the frequency to be observed are preferred.

Opacity is given by:

$$\eta_{\mathrm{atm},\nu}(z) = \exp\left\{ -\int_{s_1}^{s_2} \alpha_\nu(s')\,\mathrm{d}s' \right\} = \exp\left\{ -\tau_\nu A(z) \right\} \tag{1.1}$$

where $\alpha_\nu(s)$ is the absorption coefficient as a function of elevation (s), $A(z)$ is the "airmass" as a function of zenith angle (z), and τ_ν is the optical depth *at zenith* ($z = 0$). The subscript ν indicates frequency dependence. The term "opacity" is sometimes used to refer to $\alpha(s)$ and other times to τ_ν. Here we adopt the convention of observational astronomers and use "opacity" to describe τ_ν.

The airmass is the ratio of the optical path through the atmosphere along the line of sight to the zenith thickness of the atmosphere:

$$A(z) = \frac{\int_{s_1}^{s_2} \mathrm{d}s'}{\Delta s_{\mathrm{zenith}}} \tag{1.2}$$

In the single-slab (plane-parallel) model of the atmosphere, $A(z) = \csc(z)$. A more precise curved-atmosphere (spherical) model is (Chamberlin & Bally 1994):

$$A(z) \approx -0.0045 + \frac{1.00672}{\cos(z)} - \frac{0.002234}{\cos^2(z)} - \frac{0.0006247}{\cos^3(z)} \tag{1.3}$$

Opacity can be measured using the "skydip" method, whereby the brightness temperature of the sky is measured at several zenith angles and fit by a function of the form:

$$T_{\mathrm{sky},\nu}(z) = T_{\mathrm{ref}} - \left[\eta_{\mathrm{tel},\nu} T_{\mathrm{atm}}\left(1 - e^{-\tau_\nu A(z)}\right) + (1 - \eta_{\mathrm{tel},\nu}) T_{\mathrm{tel}}\right] \tag{1.4}$$

where $T_{\mathrm{sky},\nu}$ is the measured brightness temperature, η_{tel} is the telescope efficiency, and T_{atm}, T_{tel}, and T_{ref} are the temperatures of the atmosphere, telescope, and a reference blackbody, respectively. The terms $(1 - e^{-\tau_\nu A(z)})$ and $(1 - \eta_{\mathrm{tel},\nu})$ represent the emissivities of the sky and telescope, respectively. Note that the precise form of Equation 1.4 can be specific to the experimental setup used (*cf. e.g.* Dragovan *et al.* 1990; Chamberlin & Bally 1994); the form shown here corresponds to the SPIFI-AST/RO skydips of 2005 (Page 18), in which the reference blackbody was located at the spectrometer's entrance window and had a temperature (T_{ref}) higher than the total signal measured from the telescope (the term in square brackets). Since τ_ν is typically the only free parameter, it can easily be determined via χ^2 fitting.

A handful of submm skydip studies have been conducted at South Pole since the late 1980s. These studies, summarized in Table 1.3, have unanimously verified the quality of the submm sky above the Pole. Of particular interest is the work of Peterson *et al.* (2003), who were able to measure and compare $\tau_{860\,\mathrm{GHz}}$ at Mauna Kea, Atacama, and South Pole using identical tipper radiometers developed by Carnegie Mellon University (CMU) and the National Radio Astronomy Observatory (NRAO). Their data suggest that sub-median opacity conditions at South Pole and Atacama are similar, with lower H_2O opacities at Pole (due to lower ambient temperatures) offsetting lower dry-air opacities at Atacama (due to lower surface pressures). However, Peterson *et al.* (2003) also find that Pole has three times lower sky noise than Atacama (Page 21), suggesting that Pole is the superior site.

During 2001, both a Fourier Transform Spectrometer (FTS) and a CMU/NRAO tipper were deployed at the AST/RO (Chamberlin *et al.* 2003).

Table 1.3: Submillimeter Opacity Studies at South Pole

Authors	**Study Dates**	ν **(GHz)**	**Select Results**
Dragovan *et al*. (1990)	Jan. 1987	427	$0.10 < \tau < 0.20$
Chamberlin & Bally (1994, 1995)	day 3 – 180, 1992	225	$\tau < 0.055$ 75% of the time from day 70 – 180
Chamberlin *et al*. (1997)	Feb. – Nov., 1995	492	$\tau < 0.72$ 1/2 of the time
Peterson *et al*. (2003)	1998 – 2002	860	*see text*
Chamberlin *et al*. (2003)	day 180 – 220, 2001	806, 808, 868 & 1492	τ(8XX GHz) ~ 0.5 $\sim$ 25 % of the time

Opacity data were collected at 806 GHz, 808 GHz, 860 GHz and 1452 GHz and used to establish a set of linear scaling laws for converting τ-values between the frequencies. In particular, the 860 $\rightarrow$ 1452 GHz scaling law proved valuable in deriving transmission values for SPIFI 205 μm observations (Chapter 2):

$$\tau_{1452\,\mathrm{GHz}} = 1.714\,\tau_{860\,\mathrm{GHz}} + 0.530 \tag{1.5}$$

Transmission Models Opacity and PWV data, along with detailed knowledge of telluric absorption lines, can be used to produce models of atmospheric transmission. At present, the most evolved model is the Atmospheric Transmission at Microwaves (ATM) model of Pardo *et al*. (2001), which is based partly on data from site studies listed in Table 1.3. Figure 1.4 plots ATM model zenith transmission profiles of the 200 μm telluric window for the best 25th, 50th, and 75th quartiles of opacity during the South Pole winter. The PWV values are taken from Lane (1998) (Figure 1.3). It can be seen that observing is nearly impossible in the 75th quartile, for which transmission is well below 1 %. SPIFI observations (Chapter 2) were conducted in conditions ranging between the 25th

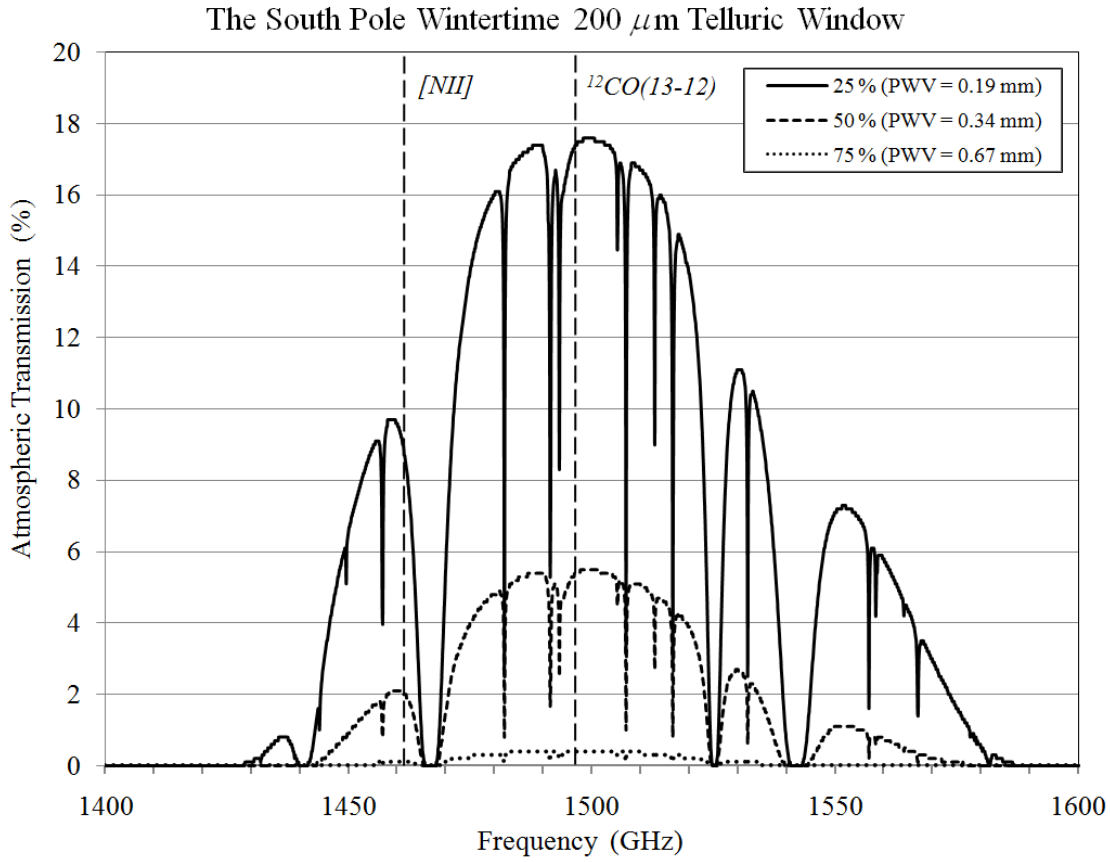

Figure 1.4: The South Pole Wintertime 200 μm Telluric Window

Atmospheric transmission at zenith is plotted versus frequency for the best 25th, 50th, and 75th quartiles of opacity during the South Pole winter. PWV values are taken from Lane (1998). The plot was generated using the Pardo *et al*. (2001) ATM model calculator on the Atacama Pathfinder Experiment (APEX) website (http://www.apex-telescope.org/sites/chajnantor/atmosphere/transpwv/), with PWV values scaled up by a factor of 1.75 to account for the relative dry air opacity contributions at South Pole and Atacama (Pardo *et al*. 2001; Peterson *et al*. 2003). The vertical dashed lines indicate the positions of the [NII] (1461 GHz) and ^{12}CO(13→12) (1497 GHz) spectral transitions.

and 50th opacity quartiles, during which the 1461.132 GHz (205.1782 μm) zenith transmission averaged 4.54 %.

SPIFI 205 μm Skydips In September 2005, the SPIFI receiver was used to perform several skydips from the AST/RO at 200 μm, 205 μm, and 370 μm. These measurements were used to refine the relationship between the opacity obtained by the 860 GHz CMU/NRAO tipper on the AST/RO rooftop – which had been used to provide τ-values during the SPIFI campaign – and the 200 μm, 205 μm, and 370 μm opacities obtained by SPIFI. Measurements of $T_{\rm sky}$ were taken at z = 20°, 30°, 40°, 50°, 60°, and 70° and fit with Equation 1.4 using the spherical atmosphere model of Equation 1.3. Results for 205 μm are shown in Figure 1.5.

Sky brightness measurements at the largest zenith angles ($A(70°)$ = 2.9 airmasses) are lower than expected and were therefore not used to fit $\tau_{205\mu\rm m}$. With all other parameters held fixed, the data points at 2.9 airmasses could be incorporated into the fit by lowering $T_{\rm atm}$ by 1.3 K in skydip 1 and by 3.2 K in skydip 2, while keeping its assumed value of 229 K for $A(z) \leq A(60°)$ = 2.0 airmasses. It is thus possible that the effects of the temperature inversion layer over the Antarctic Plateau (Page 4) may have influenced these high-airmass data points.

To compare the opacities measured by SPIFI with those of the AST/RO CMU/NRAO tipper during the same time period, tipper values of $\tau_{860\,\rm GHz}$ were converted to $\tau_{1452\,\rm GHz}$ using Equation 1.5. However, the SPIFI skydips were done near the frequency of the 205.1782 μm [NII] spectral line, or 1461.132 GHz. This frequency lies on the opposite side of a sub-window of the 200 μm window from 1452 GHz (Figure 1.4), and does not have the same transmission. The relation-

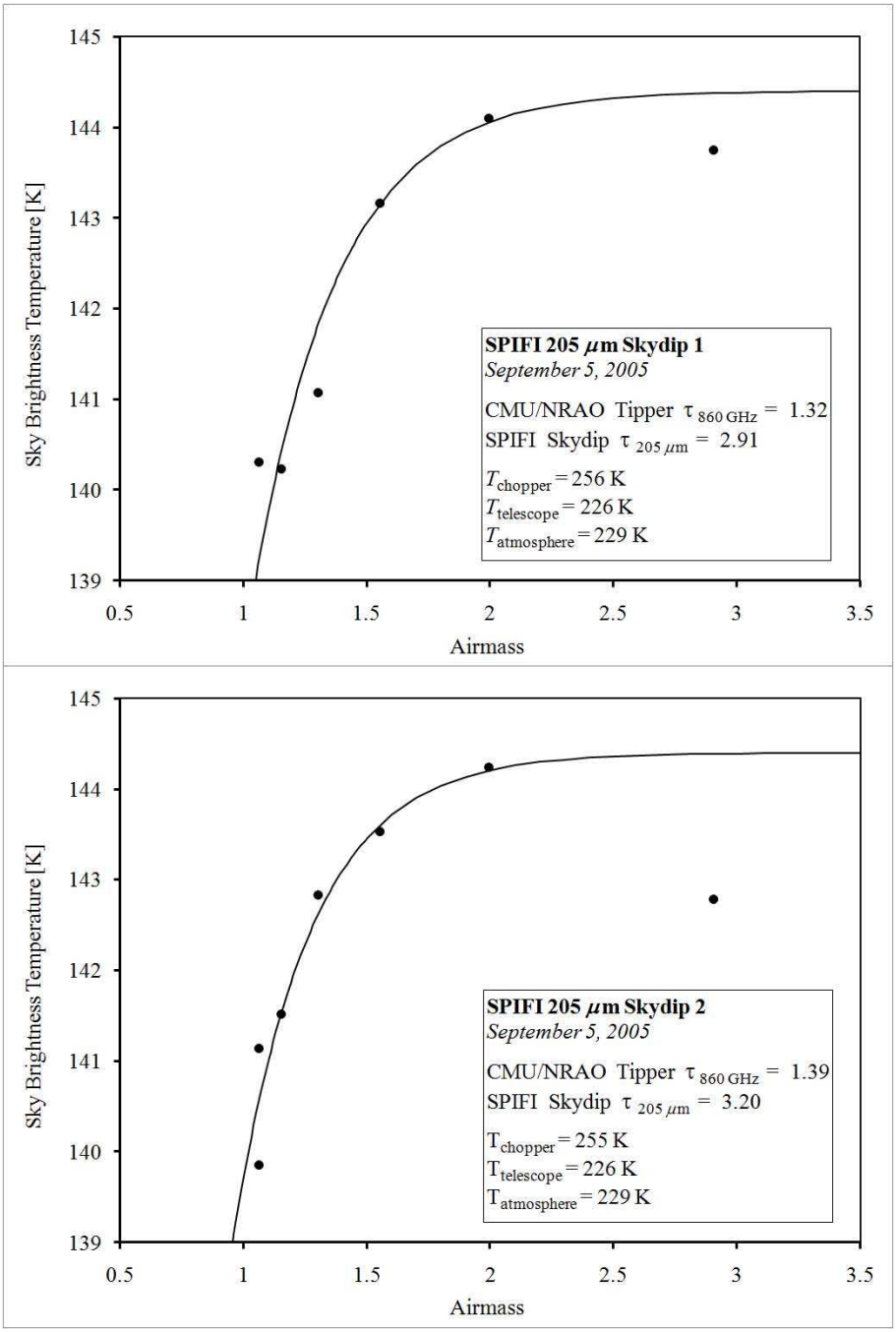

Figure 1.5: SPIFI-AST/RO 205 μm Skydips

On September 5, 2005, two skydips were obtained at 205 μm by SPIFI on the AST/RO. Sky brightness was measured at z = 20°, 30°, 40°, 50°, 60°, and 70°, and χ^2 fitting was used to determine $\tau_{205\mu m}$. Assumed temperature values are shown on each plot. The highest airmass data point on each plot is lower than expected – possibly due to atmospheric temperature inversion – and was not included in the fit.

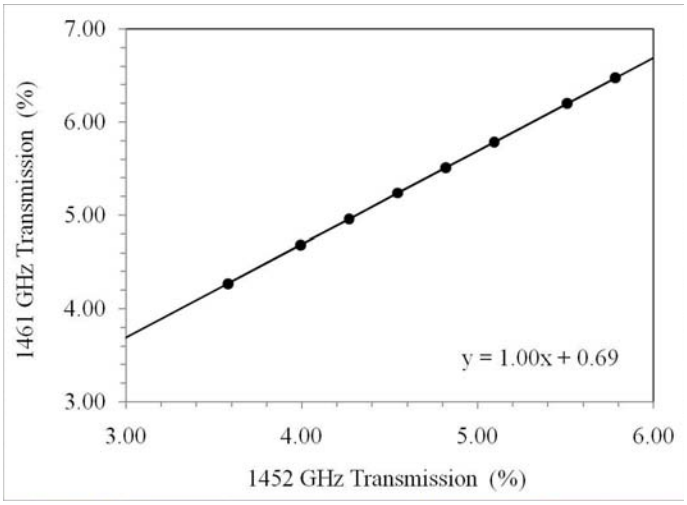

Figure 1.6: 1452 GHz → 1461 GHz Transmission Scaling Relationship
Transmissions at 1452 and 1461 GHz are found to be linear and related by a fixed offset within the range of transmissions encountered during SPIFI South Pole observations (~ 3 % – 6 %). The data are based on outputs from the ATM model of Pardo *et al*. (2001).

ship was determined using the ATM model calculator (Pardo *et al*. 2001) on the Atacama Pathfinder Experiment (APEX) website[4] and was found to be extremely linear within the range of 1461 GHz transmissions encountered during SPIFI observations (Figure 1.6):

$$T_{1461\,\mathrm{GHz}} = T_{1452\,\mathrm{GHz}} + 0.69\ \% \tag{1.6}$$

After scaling, the CMU/NRAO tipper was found to be in excellent agreement with the SPIFI skydips. To reach exact agreement, offsets of -0.08 and 0.01 would need to be added to the tipper $\tau_{860\,\mathrm{GHz}}$ (corresponding to relative errors of 6.0 % and 0.7 %) for skydips 1 and 2, respectively. A slightly larger offset of -0.202 was found during 370 μm SPIFI Moon observations in August, 2005, and was ultimately used to determine $\tau_{1461\,\mathrm{GHz}}$ during SPIFI observations (§2.3.2).

[4]http://www.apex-telescope.org/sites/chajnantor/atmosphere/transpwv/

Sky Noise

The second factor (after opacity) making the South Pole an excellent submm observing site is sky noise: fluctuations in the total power measured by a detector due to variations in atmospheric emissivity and path length on timescales of $\sim$ 1 s. Sky noise is due to the turbulent motion of air cells with different temperatures and pressures in the Earth's atmosphere, and is manifested as a systematic error in flux measurements.

One measure of sky noise is the root-mean-squared (rms) deviation of opacity, $\langle\sigma_\tau\rangle$. Peterson *et al*. (2003) computed $\langle\sigma_\tau\rangle$ values during 2 hr intervals from the data of their extensive 860 GHz opacity study. At the median, sky noise at South Pole was $\sim$ 3 times lower than at Atacama and $\sim$ 4 times lower than at Mauna Kea (Table 1.4). Their results confirm the findings of previous sky noise studies at mm wavelengths (*e.g.* Lay & Halverson 2000): that South Pole has consistently lower sky noise than other developed submm sites.

Sky noise can be largely eliminated through chopping and background subtraction (§1.3.3). During SPIFI observations, the AST/RO tertiary was chopped at 2 Hz, and we find that sky noise does not play a significant role in the noise of our 205 μm observations of the Carina Nebula (Chapter 2). Rather, the SPIFI system is dominated by "photon noise" due the statistical arrival rates of photons from the warm, emissive sky and telescope (see §1.2.2).

Table 1.4: Sky Noise Quartiles at South Pole, Atacama, and Mauna Kea

$\sigma(\tau)$	25%	50%	75%
South Pole	<0.01	0.03	0.07
Chajnantor	0.05	0.10	0.18
Mauna Kea	0.08	0.13	0.24

Root-mean-squared (rms) deviations of 860 GHz opacity over 2 hr intervals for the best 25th, 50th and 75th quartiles at the respective sites (Peterson *et al*. 2003)

1.2 SPIFI Modifications and Upgrades

The South Pole Imaging Fabry-Perot Interferometer (SPIFI) is a direct-detection imaging spectrometer which operates near the background photon noise limit. SPIFI was designed to take advantage of the low submm opacity at South Pole – especially in the 200 μm window, which is unavailable at all other developed sites save for Atacama. SPIFI is well described in the literature (Swain *et al*. 1998; Bradford 2001; Bradford *et al*. 2002) and hence only a brief overview is given here.

SPIFI's defining feature are its tandem Fabry-Perot Interferometers (FPIs) with tunable plate separations. Unlike traditional, long-slit grating spectrometers which require one focal plane dimension for spectral information, FPIs can obtain a two-dimensional image at each spacing of the FPI etalon (at each given resonant wavelength). (*I.e.* long-slit gratings are spectral multiplexers and FPIs are spatial multiplexers.) Stepping the etalon spacing yields a "data-cube" – 2D spatial and 1D spectral. Therefore, the FPI can be significantly faster than a grating for mapping extended objects. The FPI also will have advantages in relative pointing between map positions and in relative flux calibration, given changing sky transmission. There is, however, a trade-off in the required inte-

gration time per spectrum: FPIs must "scan," stopping to integrate individually at several different plate separations, whereas gratings obtain an instantaneous spectrum by integrating just once at a given grating position. Thus, a grating spectrometer will be superior for the detection of weak lines from point sources.

FPIs also have advantages over heterodyne receivers. First, the instantaneous bandwidth of heterodyne receivers is limited to several GHz. This can restrict them from observing velocity-broadened extragalactic lines, for example. FPIs, on the other hand, can, in principle, be scanned over arbitrarily large bandwidths. Furthermore, an FPI like SPIFI has sensitivity limited by photon shot noise, while the heterodyne receiver is fundamentally limited by the so-called quantum noise associated with the detection of phase. This quantum noise ($T_N \approx h\nu/k_B$; *e.g.* Rieke 2003) can be much larger than the photon background, and most heterodyne receivers are several factors away from being quantum noise limited. There is, however, a trade-off in resolving power: the resolving power of an FPI is limited, whereas that of a heterodyne receiver is not. Therefore, the heterodyne receiver is still the instrument of choice to obtain velocity-resolved spectra of narrow astrophysical lines.

SPIFI's detector consists of a 5×5 array of thermistor-sensed silicon bolometers. They are cooled by a nested adiabatic demagnetization refrigerator (ADR) (~60 mK), ^{3}He refrigerator (~300 mK), pumped ℓ–^{4}He tank (~1.5 K) and pumped ℓ–N_2 tank (~56 K). The optics and FPIs are housed in a separate Dewar from the detector, which is only cooled to ~ 3.8 K. Plans to upgrade SPIFI to a few hundred pixel array of transition edge sensed (TES) bolometers are well developed. In addition to providing greater spatial resolution and field-of-view, the new TESs would yield significantly lower noise-equivalent-power

(NEP) and a faster readout speeds. However, early TES arrays were overly fragile, and required a redesign. A more robust generation of TES arrays have since been developed and a prototype for the Cornell Submm Group is currently being prepared at the National Institute of Standards and Technology (NIST) in Boulder, Co. During this period – which includes the 2004 and 2005 South Pole winters – SPIFI continued to observe with its original array.

After previous success at the JCMT (*e.g.* Bradford *et al*. 2003, 2005), SPIFI began preparing for its South Pole campaign in early 2003. A number of critical upgrades and modifications were made involving the FPIs, filtration, and the calibration unit. These changes are described in the following sections. Integration with the AST/RO telescope is discussed in §1.3.

1.2.1 Fabry-Perot Interferometers

Introduction

A Fabry-Perot Interferometer (FPI) consists of two plane-parallel partially reflective surfaces, or "plates," whose separation forms a resonance cavity. The cavity passes only integer multiples of half wavelengths:

$$d = n\lambda_\nu/2 \tag{1.7}$$

where d is the plate separation, n is the order of the interference fringes, and λ_ν is the resonant, or transmitted, wavelength (the subscript ν indicates frequency dependence: $\lambda_\nu = c/\nu$). Light entering the FPI undergoes multiple internal reflections, and is partially transmitted each time it reaches the second plate. This

results in multiple beam interference which can produce highly resolved interference patterns.

An FPI is characterized by its finesse and transmission. The finesse, $\mathcal{F}_\nu$, is approximately equal to the average number of reflections in the resonance cavity. Finesse is conceptually equivalent to the "Q" of a resonator, so that higher $\mathcal{F}_\nu$ results in "sharper," more highly resolved transmission peaks. In terms of the spectral profile of the instrument, $\mathcal{F}_\nu$ can be calculated as the ratio of the free spectral range (FSR), $\Delta\lambda_{\nu,\,\mathrm{FSR}}$, to the full width at half maximum (FWHM; also "resolution element"), $\Delta\lambda_{\nu,\,\mathrm{FWHM}}$. The FSR is the wavelength difference between peaks of adjacent orders ($\Delta n = 1$), and is equal to λ_ν / n. For a perfect FPI, $\mathcal{F}_\nu$ is determined entirely by the reflectance, r_ν, of the plates and for $r_\nu > 0.5$ can be approximated by:

$$\mathcal{F}_\nu = \frac{\pi\sqrt{r_\nu}}{1 - r_\nu} = \frac{\Delta\lambda_{\nu,\,\mathrm{FSR}}}{\Delta\lambda_{\nu,\,\mathrm{FWHM}}} \tag{1.8}$$

In real FPIs, the measured $\mathcal{F}_\nu$ (right-hand-side) is always slightly lower than the theoretical $\mathcal{F}_\nu$ (center) due to deviations of the plates from plane parallelism, absorbance of the plates, plate defects, and aperture effects due to the finite size of the instrumental point spread function (which in the best case is limited by diffraction).

The transmission profile of the FPI cavity is Lorentzian, and is given in terms of $\mathcal{F}_\nu$ as:

$$t(\nu) = \left[1 + \left(\frac{2\mathcal{F}_\nu}{\pi}\sin\left(\frac{2\pi d\nu}{c}\right)\right)^2\right]^{-1} \tag{1.9}$$

Although an FPI is fully characterized by $\mathcal{F}_\nu$ and $t(\nu)$, it is useful to also introduce the resolving power, R_ν, which is a measure of the minimum resolvable

separation of two independent spectral lines. For an FPI, R_ν is the product of the order and finesse. In terms of the instrument's spectral profile, R_ν can also be expressed as the ratio of the resonant wavelength to the FWHM:

$$R_\nu = n\mathcal{F}_\nu = \lambda_\nu/\Delta\lambda_{\nu,\,\mathrm{FWHM}} \tag{1.10}$$

For a given $\mathcal{F}_\nu$, R_ν is fully selectable by choice of n. However, "leakage" (§1.2.2) becomes a greater concern at high n, placing an effective upper limit on R. Thus, for a given n, R_ν is limited by the upper limits on $\mathcal{F}_\nu$ discussed above – the most fundamental of these being diffraction.

To maintain fairly high cavity transmission, it is important to keep the finesse relatively modest ($\mathcal{F}_\nu \lesssim 60$; Equation 1.9). However, higher $\mathcal{F}_\nu$ is desired to increase R_ν (Equation 1.10). For a given application, an FPI designer must therefore weigh the relative importance of transmission and resolving power when choosing the plate reflectance.

On a separate note, for use in future discussion, an FPI's finesse can also be expressed in terms of the mechanical separation of the plates, Δd, as follows: for a given FPI order, n, different plate separations (d_1 and d_2) correspond to different transmission wavelengths ($\lambda_{\nu,1}$ and $\lambda_{\nu,2}$). Using Equation 1.7 twice and taking the difference, we obtain:

$$\Delta d = n\Delta\lambda_\nu/2 \tag{1.11}$$

If we let $\Delta\lambda_\nu$ correspond to an "optical" resolution element ($\Delta\lambda_\nu = \Delta\lambda_{\nu,\,\mathrm{FWHM}}$), then Δd will correspond to a "mechanical" resolution element ($\Delta d = \Delta d_{\mathrm{FWHM}}$).

Combining this result with Equation 1.8, we find:

$$\mathcal{F}_\nu = \frac{\lambda_\nu}{2\Delta d_{\mathrm{FWHM}}} \tag{1.12}$$

SPIFI's Tandem Fabry-Perots

SPIFI employs two tandem FPIs. The first, the High Order Fabry-Perot Interferometer (HOFPI), is operated in high orders and determines the transmission profile and resolving power of SPIFI. The second, the Low Order Fabry-Perot Interferometer (LOFPI), is operated in low orders and selects (*i.e.* transmits) the HOFPI order of interest (n_{HOFPI}) from amongst the many resonant wavelengths transmitted by the HOPFI. A broad bandpass filter (§1.2.2), in turn, selects (*i.e.* transmits) the LOFPI order of interest (n_{LOFPI}) from amongst the many resonant wavelengths transmitted by the LOFPI. In this sense, the LOFPI "filters" the HOFPI and the bandpass "filters" the LOFPI (see Figures 1.11 and 1.12). The bandpass filter can be a third FPI (and for early observing runs it was), so SPIFI has been described as a "triple Fabry-Perot" (*e.g.* Bradford *et al.* 2002).

To produce a spectrum, the HOFPI transmission peak (at a pre-selected order n_{HOFPI}) is "scanned" over the desired wavelength range (with this range usually being centered on one or more astrophysical or calibration lines). In practice, this means that flux is collected at several different fixed HOFPI plate separation increments. For Nyquist sampling, each increment corresponds to one-half of one resolution element ($\Delta d_{\mathrm{FWHM}}/2 = \lambda_\nu/(4\mathcal{F}_\nu)$; Equation 1.12 above). During a HOFPI scan, the LOFPI plate separation is usually held fixed at a low order (n_{LOFPI}) and centered on the desired wavelength range. In certain cases when wide spectral bandwidths are desired, it may be necessary to scan the LOFPI at

the same time as the HOFPI, in order to keep the LOFPI transmission high at each wavelength sampled by the HOFPI (*i.e.* to keep the LOFPI in resonance with the HOFPI).

Varying FPI plate separation is a challenge in a vacuum-sealed cryogenic environment. SPIFI's FPIs are manufactured with nested chassis: one plate is attached to an outer "fixed" chassis and the other to an inner "movable" chassis. To maintain parallelism, the chassis are joined by a spring-loaded "flex-vane" parallelepiped system (Bradford *et al*. 2002). Prior to the South Pole campaign, the inner chassis was scanned by an piezoelectric transducer (PZT) and a capacitor bridge measured the separation. The maximum PZT translation, or throw, was 60 μm for the HOFPI and 20 μm for the LOFPI. The HOFPI had an additional gross ($\leq$ 2.5 cm) translation stage mounted on a roller-bearing and controlled by a coarse hand-crank outside the Dewar. To parallelize the plates, three additional 20 μm throw PZTs were spaced at 120° around each movable plate.

A New HOFPI and Cryogenic Stepper Motors

During early runs at the JCMT, several major disadvantages of SPIFI's Fabry-Perots became apparent:

1. Because the gross translation stage was operated by a coarse hand-crank (via which it was impossible to precisely track changes in plate separation, Δd), wavelength calibration (§2.3.3) had to be repeated after each gross translation. This process normally took a few minutes, but could take up to a half-hour if problems developed.
2. The bandwidth per spectrum was limited by the 60 μm throw of the scanning PZT. For an observation wavelength of$\sim$ 360 μm and a finesse of $\sim$

30, for example, SPIFI was limited to a spectral bandwidth of ~ 10 resolution elements (number of elements = scan length / travel per element $= 60\,\mu\text{m}/(360\,\mu\text{m}/(2 \times 30)) = 10$; Equation 1.12). This was not a problem when an astrophysical line and a calibration line were separated by fewer than 10 resolution elements. If the separation were greater, however, this required use of the hand-crank between measurements of a calibration line and astrophysical line, making it difficult to pursue the latter.

3. The plates did not stay parallel during gross translations, and thus required reparallelization.
4. The translation stage was prone to vibrations whose amplitude could occasionally be significant compared to a resolution element, Δd_{FWHM}. These vibrations were only rarely an issue at 370 μm, but would have been more troublesome at the shorter (200 μm window) wavelengths we observed on AST/RO. The vibrations were likely a result of the removal of the (damping) grease from the roller-bearings – a necessity for the low-pressure cryogenic environment inside SPIFI.

All of these problems were tied to the limited throw of the scanning PZT, which necessitated the roller-bearing gross translation stage. For the South Pole campaign, these issues were addressed by replacing both the scanning PZT and roller-bearing stage in both the HOFPI and the LOFPI with a single precision rotary cryogenic stepper motor (one motor each for the HOFPI and LOFPI). To change plate separation, each stepper motor drives a lead screw anchored to the FPI's movable plate. Unlike the PZT, the stepper motor throw is large: it is limited only by the chosen length for the lead screw. The FPI plate separation, however, is limited by the size of the flex-vane (*i.e.* the flexure allowed between the inner and outer chassis of each FPI). Thus, to allow large translations, a new

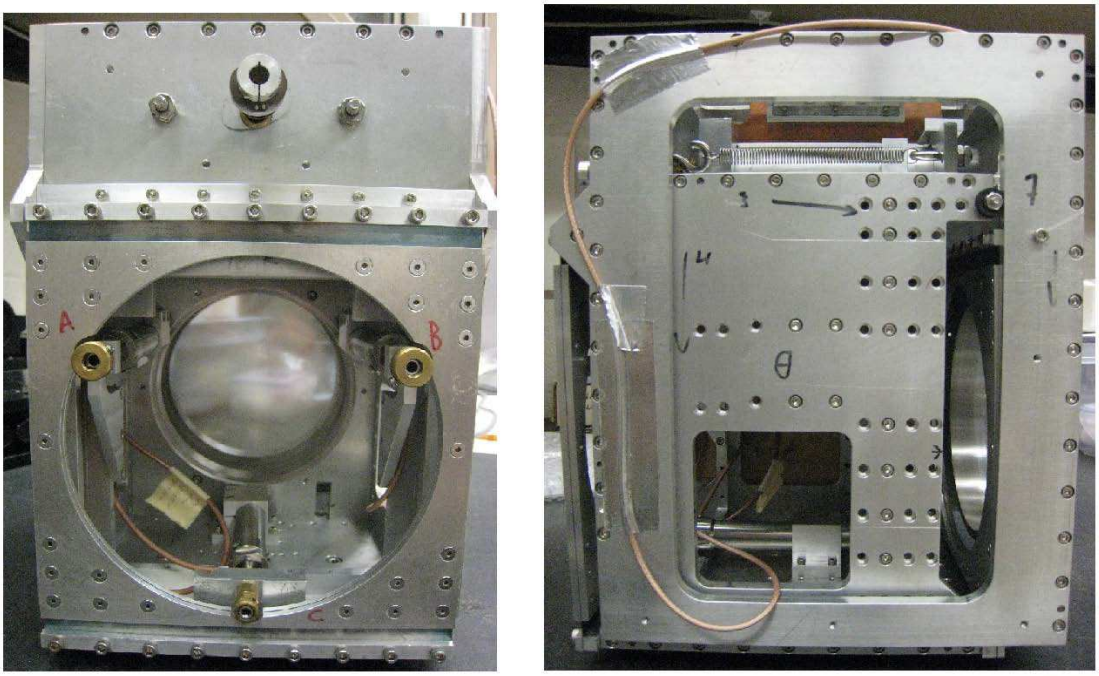

Figure 1.7: The New SPIFI HOFPI

Left Panel: View of the HOFPI along the beam path. The two mesh rings, with 12 cm inner diameters, can be seen near the rear of the circular opening. The three parallelizing PZTs, labeled "A," "B," and "C," are spaced at 120° around the mesh. The stepper motor lead screw coupler is seen at the top center of the HOFPI chassis.
Right Panel: Side view of the HOFPI, perpendicular to the beam path. The outer and inner (flex-vane) chassis are visible, as well as one of the flex-vane springs near the top of the image.

HOFPI was constructed with a flex-vane > 4 times larger than the original. The new HOFPI is shown in Figure 1.7.

The stepper motors chosen for SPIFI are the Phytron Extreme Environment series motors (VSS-UHVC model 42.200.0.6, 4-wire). They are constructed from specially selected materials and lubricants that allow them to operate at temperatures approaching 1 K, although they were mounted on the SPIFI pumped ℓ–N_2 (~56 K) surface. Careful assembly, cleaning, and conditioning results in low outgas rates that allow them to operate at pressures down to 10^{-11} mbar

Table 1.5: SPIFI Cryogenic Stepper Motor Drive Trains

Specification	**HOFPI**	**LOFPI**
Counts per Revolution ($\frac{1}{2}$ step mode)	400	400
Lead Screw (TPI)	80	80
Gear Reduction Ratio	3.75	75.0
Plate Separation per Count (mech. μm)*	0.21165	0.01058

* Calculated by taking the reciprocal of the product of the first three rows and converting to μm, and verified to 0.00001 μm accuracy by PoleSTAR LO measurements. Mechanical ("mech.") microns refers to physical plate separation, d, as opposed to "optical" microns, λ_ν (Equation 1.7).

(well below SPIFI's typical $\gtrsim 5 \times 10^{-7}$ mbar vacuum). The motors are controlled by low-noise Phytron SINCOS linear power stages housed in a room-temperature rack-mounted electronics box which communicates with the main SPIFI control computer.

The greatest advantage of the stepper motors is that, once calibrated, plate separation can be precisely tracked over the entire available range of translation of the HOFPI or LOFPI plates ($\sim$ 2 cm). The stepper motor reports its incremental rotation in step numbers, or "counts," which are managed by the control computer. In addition, with the new stepper motors, the plates are found to maintain parallelism over cm-scale translations. The new design thus eliminated all of the problems of the old FPIs while at the same time improving observing efficiency and ease-of-use. The following list outlines the advantages of the new FPIs:

1. Wavelength calibration only needs to be performed once – at the beginning of an observing session – since plate separation can now be precisely tracked over large translations. This means that each astrophysical line no

longer requires its own nearby calibration line, so that more astrophysical lines are available to SPIFI.

2. Spectral scans can now contain a large number of resolution elements (*i.e.*, SPIFI's spectra can have extremely large bandwidths), since the stepper motor throw is limited only by the size of the flex-vane and lead screw, since the plates stay parallel over large translations, and since plate separation can be precisely tracked over large translations.
3. Performing spectral scans and changing plate separations (to change wavelengths or orders) is fast and easy: just tell the computer how many counts to advance the stepper motors by.
4. Without the need to recalibrate, reparallelize, or manually translate the FPIs, the new design greatly improves SPIFI's observing efficiency.

Table 1.5 lists some of the key specifications of SPIFI's stepper motor drive trains.

Metal Meshes

The "plates" of SPIFI's FPIs are made of thin square-grid metal meshes stretched over stainless steel rings. For these meshes, reflectivity is determined by the ratio of the wire thickness, $2a$ (where a is the wire radius), to the spacing between wires (or "grid constant"), g (Sakai & Genzel 1983). Figure 1.8 plots reflectivity as a function of wavelength for several values of $2a/g$. Because reflectivity influences finesse and transmission (Equations 1.8 and 1.9), the mesh must be carefully chosen for the intended wavelength and application.

As part of the HOFPI and LOFPI redesign, new meshes were installed in both FPIs to strike a balance between finesse and cavity transmission at 205 μm (Equation 1.9), our primary target wavelength for South Pole observations (Chapter 2). We chose modest finesse to assure high transmission. The transmission is limited primarily by plate absorption, which gets worse at shorter wavelengths. Properties of the new meshes – BM 0500-01 electroformed precision screens from Buckbee-Mears/InterNet, Inc. – are listed in Table 1.6.

Table 1.6: Properties of New SPIFI Meshes

Mesh Property	**Value**
Material	Ni
Resistivity, ρ_{Ni} (Ω m)	6.58×10^{-8}
Grid constant, g (μm)	50.8
Wire radius, a (μm)	5.7
Screen thickness, t (μm)	5.08

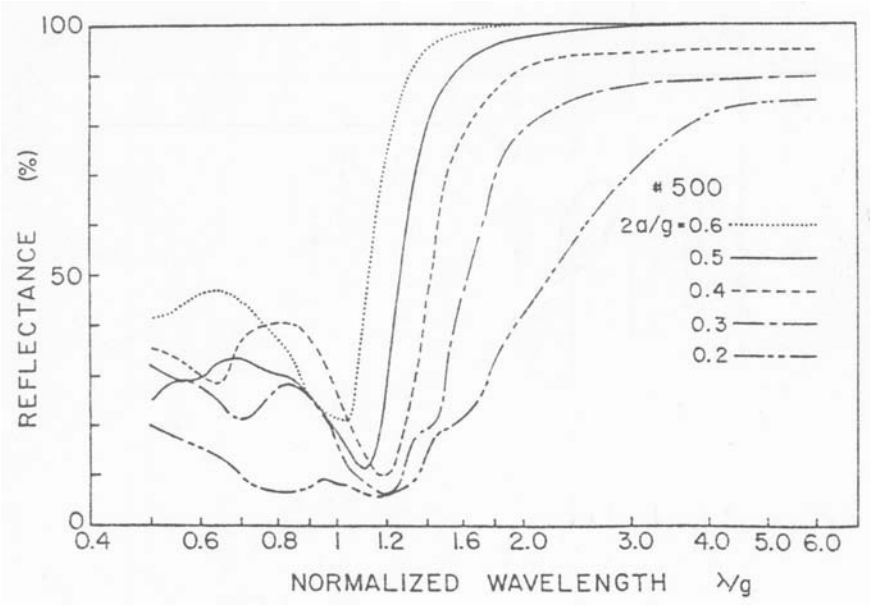

Figure 1.8: Metal Mesh Reflectance

Metal mesh reflectance (r) is plotted as a function of normalized wavelength (λ/g) for several values of $2a/g$, where a is the wire radius and g is the wire spacing (or "grid constant"). (Sakai & Genzel 1983)

HOFPI and LOFPI Characterization

The first step in characterizing and calibrating an FPI is to determine (and adjust, if desired) the order of the FPI, n. Knowledge of n allows one to convert between mechanical (d) and optical (λ) microns (Equation 1.7 or 1.11), which is necessary for the operation of the FPI (to tune the FPI for different spectral lines). The order is also required to determine the resolving power of the FPI, R_ν, either using the center term of Equation 1.10 (if the finesse is readily available) or the right-hand term (if the spectral profile of the FPI is readily available, in which case n is used to convert the FWHM to optical microns). Note that n is *not* required to determine $\mathcal{F}_\nu$, which can be found by dividing the FSR by the FWHM with both still in mechanical microns, if the spectral profile of the FPI is available (by combining Equations 1.7 and 1.8).

To determine the order of an FPI, at least two distinct spectral calibration lines are needed. If the FPI is scanned over both lines, the separation of the line in mechanical microns (Δd) can be measured. If the known separation of the lines ($\Delta\lambda_\nu$) is less than a FSR (which is very rare), Equation 1.11 can be used to solve for n). If the separation of the lines is greater than a FSR, then the lines do not fall at the same order, and Equation 1.11 becomes:

$$\Delta d = (n_2\lambda_{\nu,2} - n_1\lambda_{\nu,1})/2 \tag{1.13}$$

Since the n_1 and n_2 are integers, there will be discrete solutions to this equation. Multiple solutions are possible – usually the correct solution is obvious by *a priori* knowledge about the approximate spacing between the plates (*e.g.* by placing calipers between the FPI plates before closing the Dewar). In the ab-

sence of this knowledge, one can solve for the exact order by measuring a third spectral calibration line.

For SPIFI, spectral calibration (absorption) lines are typically provided by placing a known gas in a small submm-transparent cell and backlighting the cell with a blackbody radiation source. A specialized gas cell of this type was constructed for the SPIFI-AST/RO mount, but, unfortunately, did not perform well (§1.2.3). Fortunately, the AST/RO hosted heterodyne receivers whose local oscillators could produce (emission) lines that could be used for SPIFI wavelength calibration. In particular, the Terahertz REceiver with NbN HEB Device (TREND; Gerecht *et al.* 2003) used a CO_2 laser to pump a CD_3OH laser line at 205.4229 μm (very near the 205.1782 [NII] line), and the 810 GHz PoleSTAR receiver (Groppi *et al.* 2000) had a tunable LO. Together, these laser sources were used to calibrate the HOFPI and LOFPI in the 200 and 350 μm submm windows for which SPIFI was configured for South Pole operations.

The narrow width of these laser lines ($\Delta\lambda_{\rm FWHM} \sim 100$ kHz) traced the spectral profile of the HOFPI, providing a quick means of characterizing the HOFPI finesse and resolving power (once the HOFPI order was known; Equations 1.8 and 1.10). In a similar manner, with the HOFPI fixed on the laser line, LOFPI scans traced the spectral profile of the LOFPI, providing a quick means of characterizing the LOFPI finesse and resolving power (once the LOFPI order was known). In the context of the new HOFPI and LOFPI, we discuss the characterization of FPI properties here; a full discussion of spectral wavelength and brightness calibrations for South Pole observations is reserved for §2.3.

The TREND laser was directed from the Coudé optical bench to the SPIFI entrance window on the Nasmyth platform by two aluminum flat mirrors

Table 1.7: HOFPI and LOFPI Characterization at 205 μm

	HOFPI Predicted[b]	**HOFPI Measured**[c]	**LOFPI Predicted**[b]	**LOFPI Measured**[d]
Finesse, $\mathcal{F}$	26.2	17.6 ± 0.5	26.2	11.0 ± 1.0
Selected order,[a] n	242	242 ± 2	17	17 ± (< 1)
Resolving power, R	6340	4250 ± 120	445	187 ± 17
Mesh reflectance, r (%)	88.7	–	88.7	–
Cavity transmittance, t (%)	78.4	–	78.4	–

[a] The orders are those selected for the SPIFI Carina Nebula observations (Chapter 2). [b] Predicted values are calculated using the model of Sakai & Genzel (1983). [c] HOFPI measurements were conducted using the 205.4229 μm CD_3OH line of the TREND laser. [d] LOFPI measurements were conducted using the PoleSTAR 810 GHz local oscillator. All values have been scaled to 205.1782 μm.

(AST/RO optics are discussed in §1.3). To avoid detector saturation and overheating from this strong (several mW) source, the beam was attenuated (by a factor of $\sim 10^8$) by placing a thin piece of cardboard in the beam path. A total of 115 HOFPI spectral profiles were collected against the laser source: all had high signal-to-noise ratios (average SNR ~ 100) and several covered more than a free spectral range. The spectral profiles obtained were mostly representative of the intrinsic finesse of the etalons, although some of the lines were broadened by laser radiation entering the FPI cavity off-axis. To precisely determine the centroids and FWHMs of the resulting profiles, Lorentzian functions were fit using χ^2 methods (§2.4.1). The results are listed in Table 1.7 while Figures 1.9 and 1.10 show example spectra.

The LOFPI was measured in a similar manner using the 810 GHz (~ 370 μm) local oscillator of the PoleSTAR receiver at the AST/RO. (SPIFI's filter wheel made it possible to easily switch between the 200 and 350 μm windows during observations (§1.2.2)). Results for the LOFPI at 205 μm are also listed in Table 1.7. The low finesse of the LOFPI comes as a surprise – particularly because its

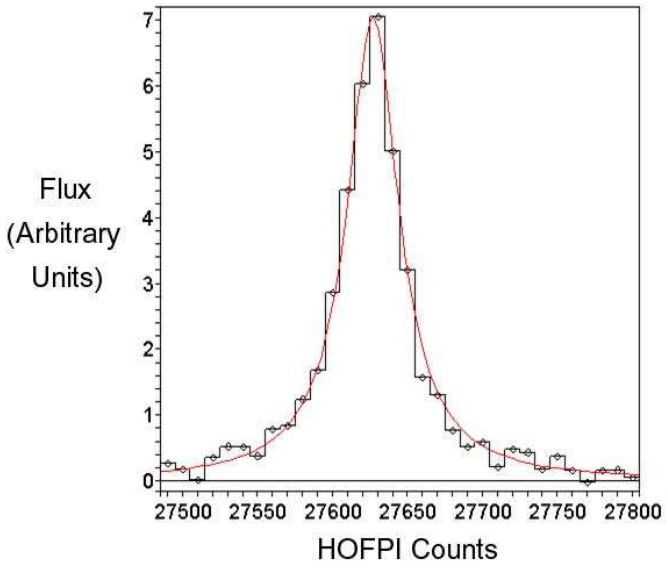

Figure 1.9: Single Pixel HOFPI Scan of the TREND CD_3OH Laser Line

One example of the 115 total calibration spectra collected by scanning the HOFPI over the 205.4229 μm CD_3OH TREND laser line at the AST/RO. The *x*-axis measures HOFPI counts (Table 1.5) ranging from 27490 to 27800 in increments of 10, and the *y*-axis measures specific flux in arbitrary units (prior to wavelength and flux calibrations, §2.3). In terms of wavelength, the x-axis increases (*i.e.* is redder) to the right. Because the laser line is narrower than the HOFPI transmission peaks, this spectrum traces the HOFPI profile. The smooth curve is a Lorentzian χ^2 fit to the data (§2.4.1). The spectrum shown was taken with detector pixel 13.

meshes are identical the HOFPI's. The LOFPI does not determine SPIFI's resolving power, but low LOFPI finesse can permit leakage from out-of-band HOFPI orders. The most likely culprits are non-flat meshes (see the parallelization discussion below) or other mesh imperfections, although poor plate parallelization could also play a role. LOFPI parallelization was repeated at least once after the measurement in Table 1.7, making it possible that the LOFPI finesse during South Pole observations was as high as $\mathcal{F} \sim 14$, which was the highest measured LOFPI finesse during 2004-2005 summer testing. The listed value ($\mathcal{F} \sim 11$) is the average of 15 scans of the PoleSTAR LO. The measured HOFPI finesse, on the

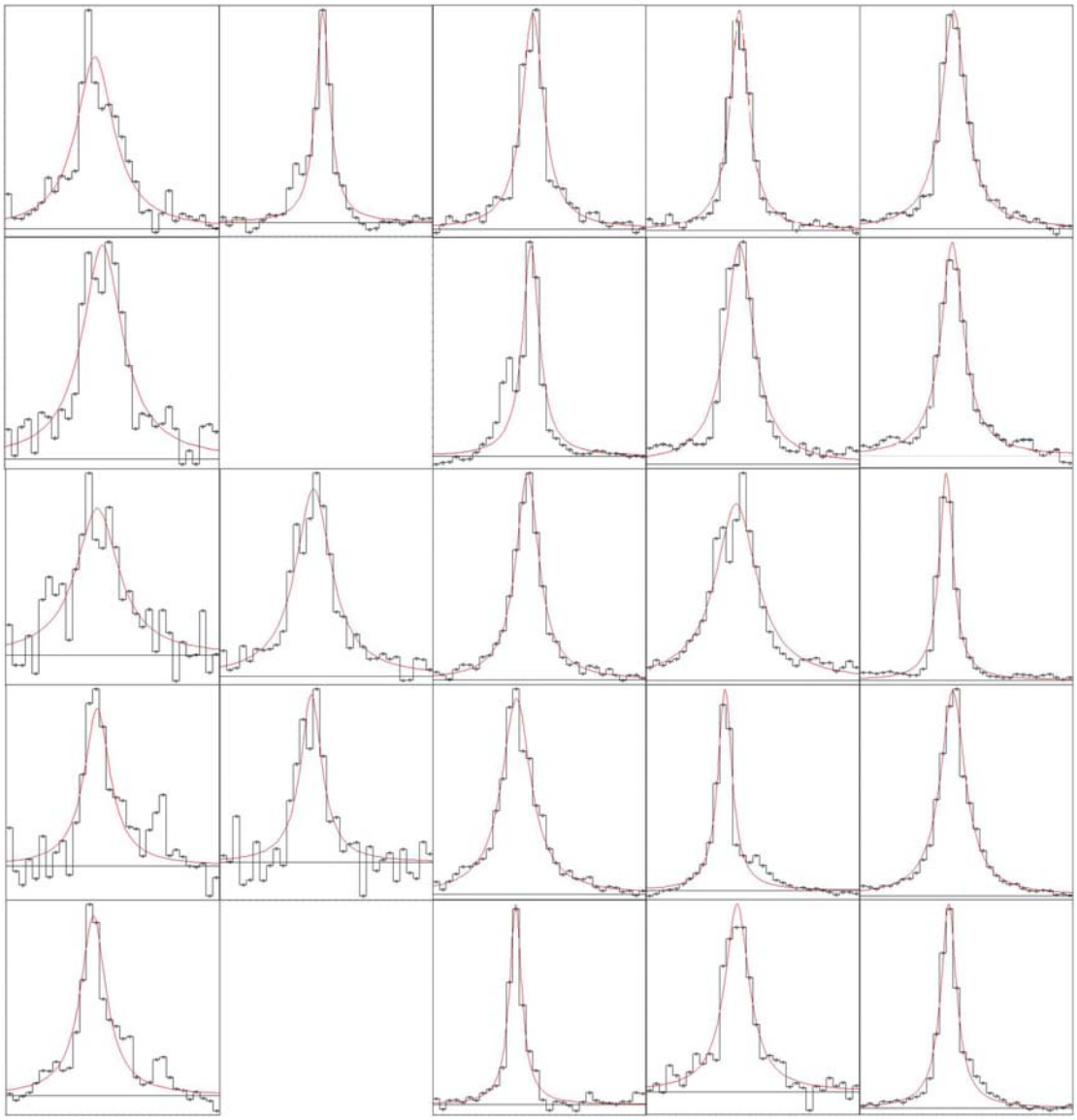

Figure 1.10: Full Array HOFPI Scan of the TREND CD_3OH Laser Line

This plot shows spectra from each pixel of SPIFI's 5×5 detector array for a single HOFPI scan over the 205.4229 μm CD_3OH TREND laser line at the AST/RO. The axes for each pixel match those of Figure 1.9, with HOFPI counts on the *x*-axis from 27490 to 27800 in increments of 10 and specific flux in arbitrary units on the *y*-axis. In terms of wavelength, the x-axis increases (*i.e.* is redder) to the right. Data points and bars represent measured values and the smooth curves are χ^2 Lorentzian fits. Pixel numbers count up from left to right and then top to bottom, starting with pixel 1 in the top left corner of the array and ending with pixel 25 in the bottom right corner. Pixels 7 and 22 were non-operational during South Pole observations.

other hand, is based on the average of 92 highly resolved TREND laser scans and was found to be robust and consistent over time.

As previously mentioned, the laser lines trace the HOFPI transmission profile (during a HOFPI scan). The transmission profiles are expected to be sharpest when the FPI plates are parallel. If they are not parallel, then different sections of the cavity will be in tune to the laser frequency at different cavity spacings, broadening the observed spectral line. This provided a means of parallelizing the HOFPI: tweak the parallelization PZTs between scans until the transmission profiles are peaked. This method was found to be quicker, easier, and more reliable than the previous parallelization method, in which one observed the interference fringes of a HeNe laser reflected from the FPI meshes.

The LOFPI, on the other hand, is in an image plane of the spectrometer, so that every pixel of the detector array sees a different portion of the LOFPI etalon. Therefore, if the LOFPI is out of parallel, different pixels will see a peak signal at different spacings of the LOFPI (*i.e.* during a LOFPI scan). To correct for this effect, we counter-tilted the LOFPI with its PZTs to make all pixels resonant at the same LOFPI position. However, we found that when the outer pixels were in resonance at a given etalon spacing, the inner pixels were out of resonance, and vice-versa – indicating that the LOFPI mesh was warped.

1.2.2 Filtration

Bolometer detectors are sensitive to radiation at all wavelengths, so we need excellent filtration to ensure spectrally pure observations. For the South Pole campaign, three new filters were employed in SPIFI: First, a 200 μm "band-

pass" filter was placed on the SPIFI filter wheel, blocking wavelengths outside of $194 \lesssim \lambda \lesssim 210$. This filter was found to have a resonant leak at $\lambda \sim 400\,\mu$m and had to be sandwiched with a "leak filter." Finally, a specialty "dualpass" filter ($182 \lesssim \lambda \lesssim 403$), designed to transmit radiation from both the 200 and 350 μm windows, was mounted directly on the SPIFI detector house (the filter wheel held a 350 μm bandpass at a different position than the sandwiched 200 μm bandpass and leak filters, so that SPIFI observations at both 200 μm and 350 μm were possible during the South Pole campaign). The dualpass filter was critical to ensure that the detectors were protected from 1.5 K radiation from within the ADR helium shields. Unfiltered, this radiation (peaking at $\lambda \sim 2$ mm) is much more intense than the background radiation from the sky and telescope.

Table 1.8 provides a complete outline of the elements in SPIFI's optical train, and Figures 1.11 and 1.12 show detailed transmission profiles for the filters and FPIs. The maximum system transmission at 205 μm was ~ 27 %. All of SPIFI's filters were manufactured by Peter A. R. Ade, Carole E. Tucker, and their group at Cardiff University (*e.g.* Ade *et al*. 2006).

The FWHM of the bandpass filter must be greater than the LOFPI's FWHM, which in turn must be greater than the HOFPI's FWHM (at the selected n_{LOFPI} and n_{HOFPI}). However, if these FWHMs are *too* large the system may transmit, or "leak," additional flux from undesired orders of the LOFPI or HOFPI. In particular, for good spectral purity (*i.e.* minimum flux "leakage" from undesired orders), we desire $\Delta\lambda_{\mathrm{FWHM,\ LOFPI}} < (2/3)\Delta\lambda_{\mathrm{FSR,\ HOFPI}}$ (or equivalently $R_{\mathrm{LOFPI}} > (3/2)\, n_{\mathrm{HOFPI}}$) and $\Delta\lambda_{\mathrm{FWHM,\ Bandpass}} < (2/3)\Delta\lambda_{\mathrm{FSR,\ LOFPI}}$ (or equivalently $R_{\mathrm{Bandpass}} > (3/2)\, n_{\mathrm{LOFPI}}$; Lugten 1987). Leakage can also occur when the bandpass, LOFPI, and HOFPI transmission peaks are misaligned (*i.e.* out of resonance).

Table 1.8: Elements in the SPIFI Optical Train During 205 μm Observations

Optical element	**Material or P. Ade ID#**	**Location**	**T (K)**	**Spectral property**	$\mathbf{t_{205\mu m}}$
Entrance window	PE	Dewar shell	275	–	0.95
Mirrors ($\times$ 6)	Cr/Au	6 locations	1.5 – 56	–	$(0.98)^6$
HOFPI	Ni Mesh	N_2 surface	56	$\frac{\lambda}{\Delta\lambda} \sim 500 - 10^4$	0.78
Scatter filter	R5 (S1256)	Lyot stop	3.8	$\lambda > 100\ \mu$m	0.90
LOFPI	Ni Mesh	^{4}He surface	3.8	$\frac{\lambda}{\Delta\lambda} \sim 100 - 10^3$	0.78
Bandpass filter	B625	Filter wheel	3.8	$194 < \lambda < 210$	0.76
Leak filter	R105 (S0239)	Filter wheel	3.8	$164 < \lambda < 278$	0.90
Longpass filter	B688	ADR snout	1.5	$\lambda > 175\ \mu$m	0.97
Dualpass filter	W944 + W949	Detector	0.4	$182 < \lambda < 403$	0.87
Total				$\frac{\lambda}{\Delta\lambda} \sim 500 - 10^4$	0.27

This leakage greatly complicates the flux calibration of lines (since we calibrate with respect to continuum sources, large amounts of leakage make a line source appear weaker than it is), can lead to troublesome baseline wiggles, and will certainly lead to excess background radiation leaking into the system which will hurt the sensitivity of a background-limited system such as SPIFI (§1.2.2).

SPIFI's leakage can be seen in Figures 1.11 and 1.12, and includes all of the "windows" in the convolved transmission profile outside of the 205.1782 μm peak. We estimate that, when configured for 205 μm observations, leakage accounts for $\sim$ 50 % of SPIFI's total flux throughput.

Figure 1.11 *(following page)*: SPIFI Transmission Profile, 150 – 450 μm

Transmission profiles are displayed for elements of the SPIFI optical train during 205 μm observations, with $n_{HOFPI} = 242$ and $n_{LOFPI} = 17$. The transmission profiles of the polyethylene entrance window, six Au/Cr-plated mirrors, and the P. Ade 100 cm edge (scatter) filter are not shown, but have roughly flat transmissions of 0.95, 0.98 (per mirror), and 0.90, respectively, at 205 μm. The HOFPI transmission profile is not shown for clarity. The lowest profile on the plot is the final SPIFI throughput, which is computed by convolving all the displayed profiles with the entrance window, mirrors, scatter filter and HOFPI.

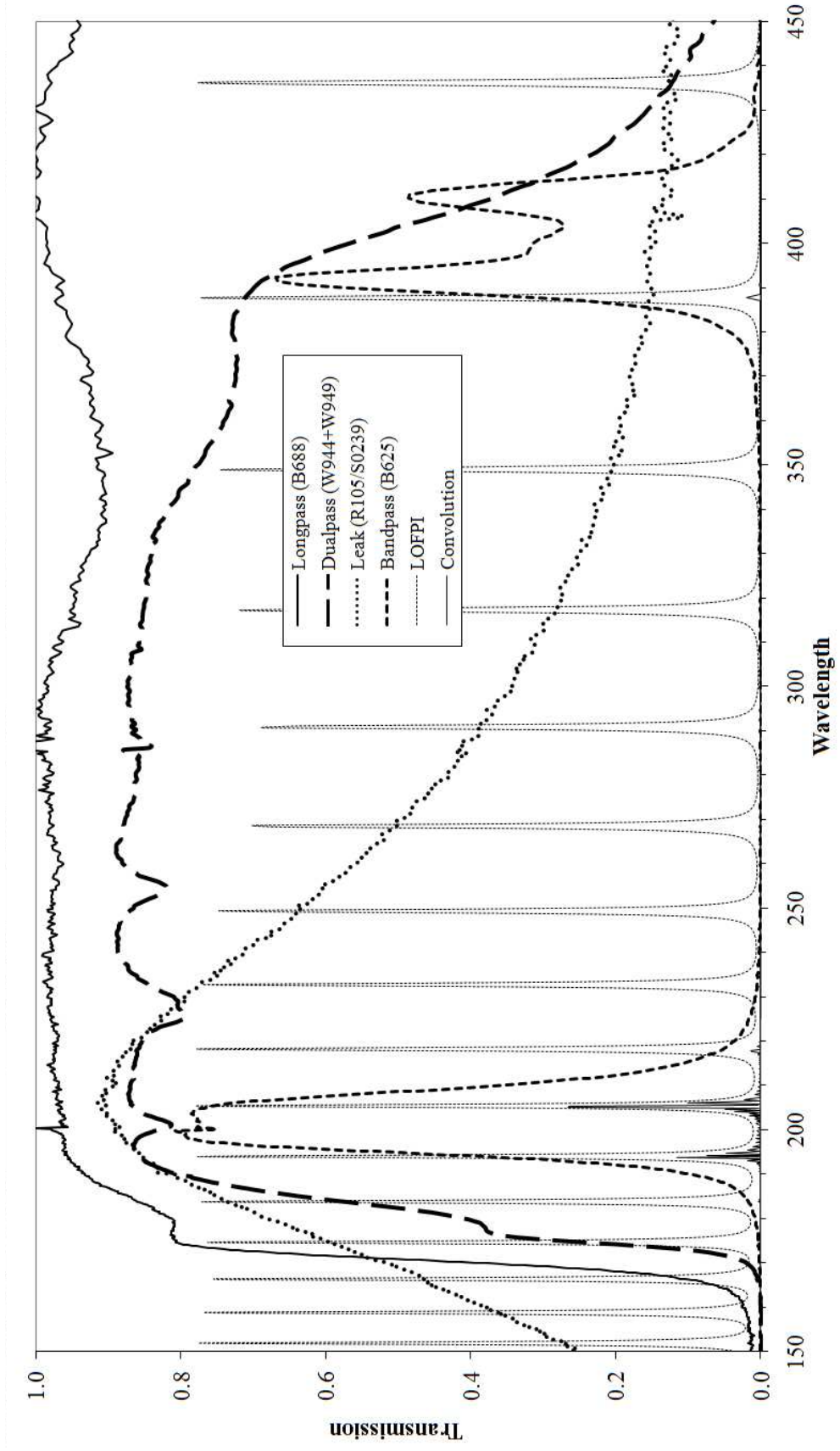
Longpass (B688)
Dualpass (W944+W949)
Leak (R105/S0239)
Bandpass (B625)
LOFPI
Convolution
Transmission
Wavelength
1.0
0.8
0.6
0.4
0.2
0.0
150
200
250
300
350
400
450

Figure 1.12 *(following page)*: SPIFI Transmission Profile, 190 – 220 μm (*Zoomed-in view of Figure 1.11*)

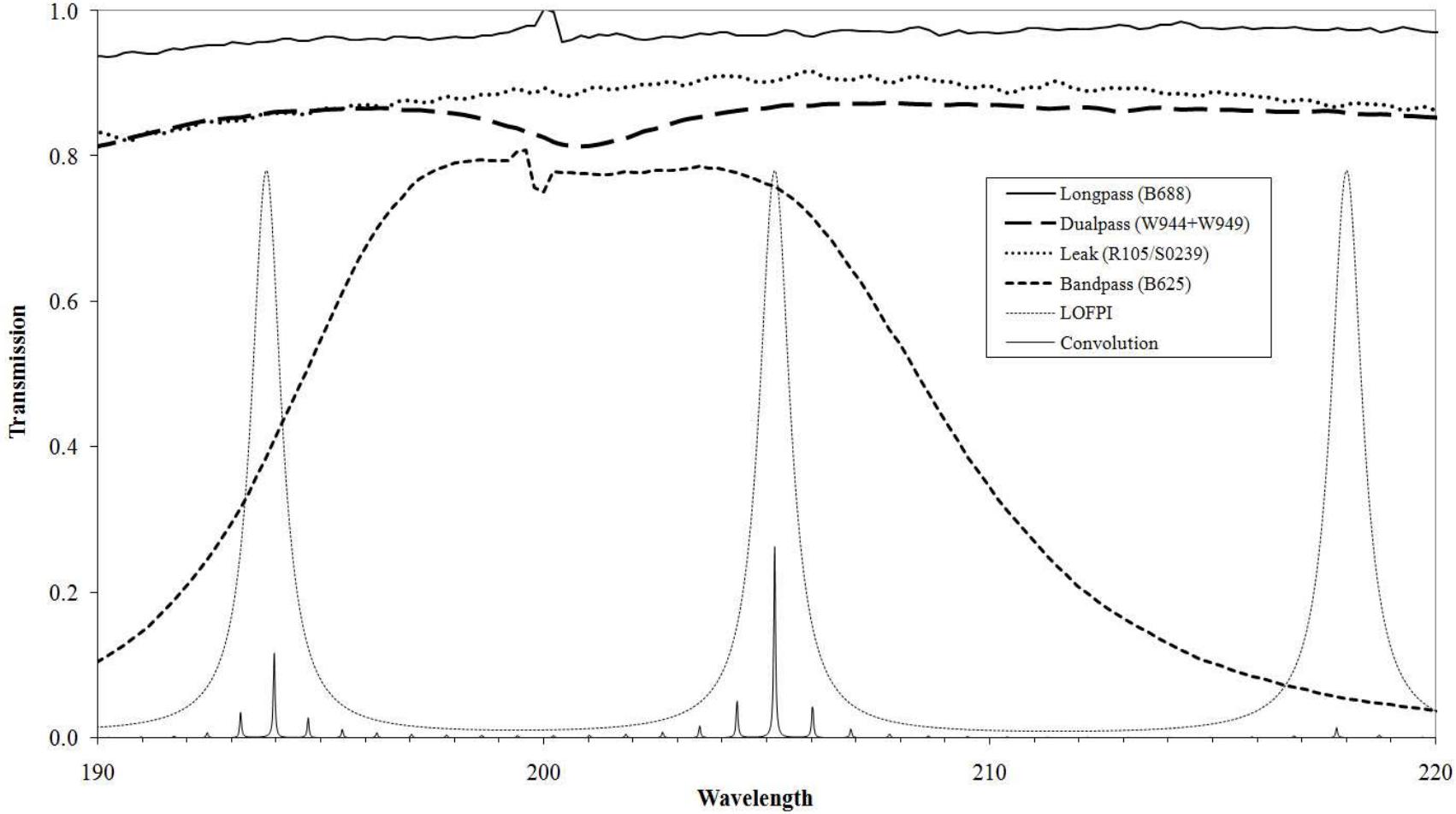
1.0
0.8
0.6
0.4
0.2
0.0
Transmission
190
200
210
220
Wavelength
Longpass (B688)
Dualpass (W944+W949)
Leak (R105/S0239)
Bandpass (B625)
LOFPI
Convolution

Sensitivity

SPIFI's bolometers are sufficiently sensitive such that the fundamental source of noise in our system should be the photon shot noise of the thermal background from the (highly emissive) atmosphere and warm optics – in which case we refer to the system as "background-limited." Cooling the filters and optics within SPIFI ensures that they contribute little to this thermal background.

Referred to the main beam at the front-end of the spectrometer, the noise equivalent power (NEP) of a background-limited spectrometer is given by (Bradford *et al.* 2002):

$$\mathrm{NEP} = \frac{h\nu}{\eta\tau t_{\mathrm{w}}} \left[8\,\Delta\nu\, N\epsilon\eta\tau\tilde{n}\,(1 + N\epsilon\eta\tau\tilde{n}\,) \right]^{1/2} \tag{1.14}$$

where the variables are defined as follows: h is Planck's constant; ν is the radiation frequency; η is the detector quantum efficiency; τ is the total transmission of the cold optical elements (for which emissivity is assumed to be zero); t_{w} is the total transmission of the warm optical elements; $\Delta\nu$ is the detection bandwidth; $N = 2A_{\mathrm{tel}}\Omega_{\mathrm{MB}}/\lambda^2$ is the number of spatial and polarization modes accepted by the detector (where A_{tel} is the area of the telescope primary, Ω_{MB} is the solid angle of the main beam on the sky, and λ is the wavelength); ϵ is the emissivity of the warm optical elements; and $\tilde{n} = (e^{h\nu/k_{\mathrm{B}}T} - 1)^{-1}$ is the photon mode occupation number (where k_{B} is Boltzmann's constant and T is the temperature of the warm optical elements). The factor of 8 arises from: (1) a factor of 2 for expressing the NEP in $\mathrm{Hz}^{-1/2}$ and (2) a factor of 2×2 for chopping losses.

For SPIFI-AST/RO 205 μm observations, these variables took on the following values: The detector quantum efficiency was $\eta \approx 50$ %. Excluding the con-

tribution of the (warm) PE window, the total transmission of the cold optical elements was $\tau \sim 28$ % (*cf.* Table 1.8). Referred to the main beam at the front-end of the Dewar (just outside SPIFI's PE window), the total transmission of the warm optical elements included only that of the PE window, $t_w = \eta_{window} \approx 95$ % (Table 1.8). Since the FPI has a Lorentzian profile, the detection bandwidth is a factor of $\pi/2$ larger than the resolution bandwidth: $\Delta\nu = (\pi/2) \cdot (\nu/R)$, where $R = \lambda/\Delta\lambda \sim 4250$ is the resolving power (Table 1.7). But since the leakage was $\sim$ 50 %, the effective detection bandwidth was twice this value, or $\Delta\nu \sim 1.1 \times 10^9$ Hz. The diameter of the AST/RO primary was 1.7 m and the diameter of the SPIFI-AST/RO main beam was $\theta \approx 54''$ (Table 1.10), resulting in a collection area of $A_{tel} \approx 2.3$ m^2 and a main beam solid angle of $\Omega_{MB} = \pi(\theta/2)^2 \approx 5.4 \times 10^{-8}$ sr, respectively, so that $N \approx 5.8$. The emissivity of the warm optical elements was $\epsilon = 1 - t_{sky}t_{tel}t_{window} \sim 98$ %, where the line-of-sight transmission for SPIFI observations of the Carina Nebula (Chapter 2) averaged $t_{sky} \sim 4.5$ %, the telescope transmission was $t_{tel} \approx 51$ %, and, as mentioned above, the transmission of the PE window was $t_{window} \approx 95$ %. Finally, assuming an ambient temperature of 229 K (which was the atmospheric temperature at the time of the SPIFI skydips; Page 18), the photon occupation mode was $\tilde{n} \approx 2.8$.

Substituting these values into Equation 1.14 results in a background-limited sensitivity of NEP $\sim 1.8 \times 10^{-15}$ W Hz$^{-1/2}$, referred to the main beam at the front-end of the SPIFI Dewar. As calibrated by our chopper wheel, over the course of an hour integration, the best pixels in SPIFI achieved an instrument NEP (referred to the main beam at the front-end of the Dewar) of $\sim 2.5 \times 10^{-15}$ W Hz$^{-1/2}$, so that our noise figure is ~ 1.4 times the background limit.

This NEP is about a factor of 10 better than the best NEPs obtained with

stressed Ge:Ga photoconductors at these wavelengths under similar backgrounds (Colgan *et al*. 1993). This sensitivity advantage is consistent with the much better detective quantum efficiency of bolometers ($\eta_{\rm bol} \sim 50$ %) compared with stressed Ge:Ga photoconductors at these wavelengths ($\eta_{\rm Ge:Ga} \sim 3$ %; Stacey *et al*. 1992) and the presence of generation-recombination noise in the photoconductors (see Rieke 2003).

It is also instructive to compare SPIFI's sensitivity to that of heterodyne receivers. A simple method is to compare the noise temperatures measured at the front-end of the receiver. The noise temperature we obtain with SPIFI is related to the double sideband receiver temperature, $T_{\rm rec}$(DSB), by the radiometer equation:

$$\Delta T = \frac{4\kappa\,(T_{\rm rec} + T_{\rm bac})}{(\Delta\nu t)^{1/2}} \tag{1.15}$$

where κ is the back-end degradation factor (= 1.15 for a 2-bit correlator), $T_{\rm bac}$ is the background temperature, and t is the integration time. The factor of 4 is the product of two independent factors of 2 resulting from (1) chopping losses and (2) double sideband detection in the heterodyne receiver. Over the course of an hour, the best pixels in SPIFI averaged a chopped noise figure of $\Delta T = 0.052$ K at 205 μm, referred to a 1 s integration time. With a sky temperature of 229 K, the background temperature is $T_{\rm bac} = \epsilon\, T = 224$ K, so that we obtain $T_{\rm rec}$(DSB) $\sim$ 150 K, a factor of ~ 7 better than the best reported values at 1.4 THz (Yngvesson *et al.* 2004).

The NEP translates into the noise equivalent flux (NEF, referred to the main beam above the atmosphere) by:

$$\mathrm{NEF} = \frac{\mathrm{NEP}}{\eta_{\mathrm{tel}}\eta_{\mathrm{sky}}A_{\mathrm{tel}}} \tag{1.16}$$

Since SPIFI is multi-moded at 205 μm, essentially all the flux from a point source is coupled into the main beam. For the best quartile of weather at South Pole ($\eta_{\mathrm{sky}} \sim 9$ % at 205 μm; Figure 1.4), we would obtain a zenith NEF of $\sim 2.4 \times 10^{-14}$ W m^{-2} Hz$^{-1/2}$. Under the poorer conditions we had for the Carina observations ($\eta_{\mathrm{sky}} \sim 4.5$ %), the NEF was $\sim 4.8 \times 10^{-14}$ W m^{-2} Hz$^{-1/2}$.

1.2.3 Calibration Box

SPIFI employs a gas cell calibration system. This system consists of three main components – a gas cell, blackbody, and chopper – which are collectively housed in a calibration box, or "cal box." This device is simple, readily inserted into the beam, and enables three very important things: (1) spectral line calibration, (2) flux (or brightness) calibration, and (3) simple alignment of the SPIFI beam to the optical axis of the telescope. (These calibrations and alignment are discussed in full detail in §2.3.)

Such a cal box was used successfully on previous SPIFI runs at the JCMT, but it was mounted out of the telescope beam path and accessed via a flip mirror. At AST/RO, on the other hand, this was not an option, for two main reasons. First, the compact rooftop design of the AST/RO had a closed elevation-axis beam tube accessible only through a small hatch near the quaternary mirror. Second, SPIFI's size and weight required that it be mounted at the Nasmyth focus flush against the beam tube (§1.3.1). As a result, the cal box needed to be permanently mounted inside the AST/RO elevation-axis beam tube, in the SPIFI-

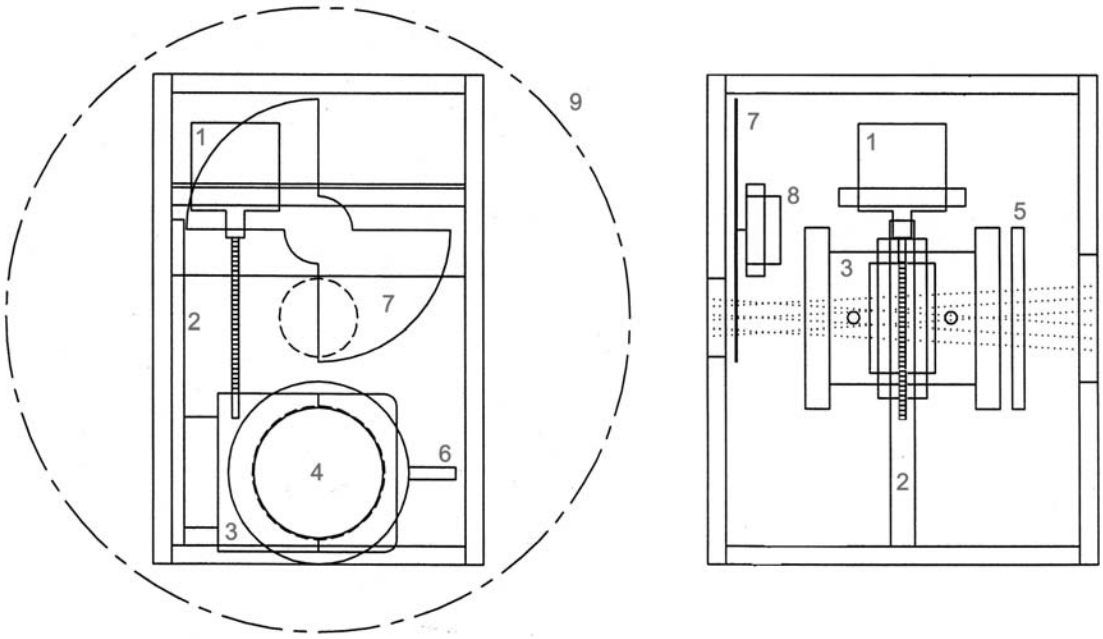

Figure 1.13: SPIFI Calibration Box

***Numbered Components*:** (1) Stepper motor; (2) Gas cell track; (3) Gas cell cylinder; (4) Gas cell Teflon window; (5) Blackbody; (6) Gas cell nipple for gas injection and evacuation; (7) Chopping blade; (8) Variable-speed chopper motor; (9) AST/RO elevation beam tube inner diameter, $(12\frac{5}{8})''$.
***Left Panel*:** The cal box along the beam path. The outside dimensions of the box are 10″ tall × 6.75″ wide. The large dashed circle marks the inner diameter of the AST/RO beam tube. The inner dashed circle is the beam opening in the back side of the box. In this view the gas cell is in the out-of-beam position, and the chopper blade is occulting about half of the beam path.
***Right Panel*:** The cal box perpendicular to the beam path. The outside dimensions are 10″ tall × 8″ deep. The dotted lines trace the beam, which focuses between the gas cell and chopper. The gas cell is shown in the in-beam position.

telescope beam path. Thus, a new, compact, remotely operable cal box was needed. The most challenging design aspect was that the components would need to be moved into the beam during calibration and out of the beam during observations, all via remote control.

The resulting design (originally by Alberto D. Bolatto, with modifications by the author) is shown in Figure 1.13, and the components are discussed below.

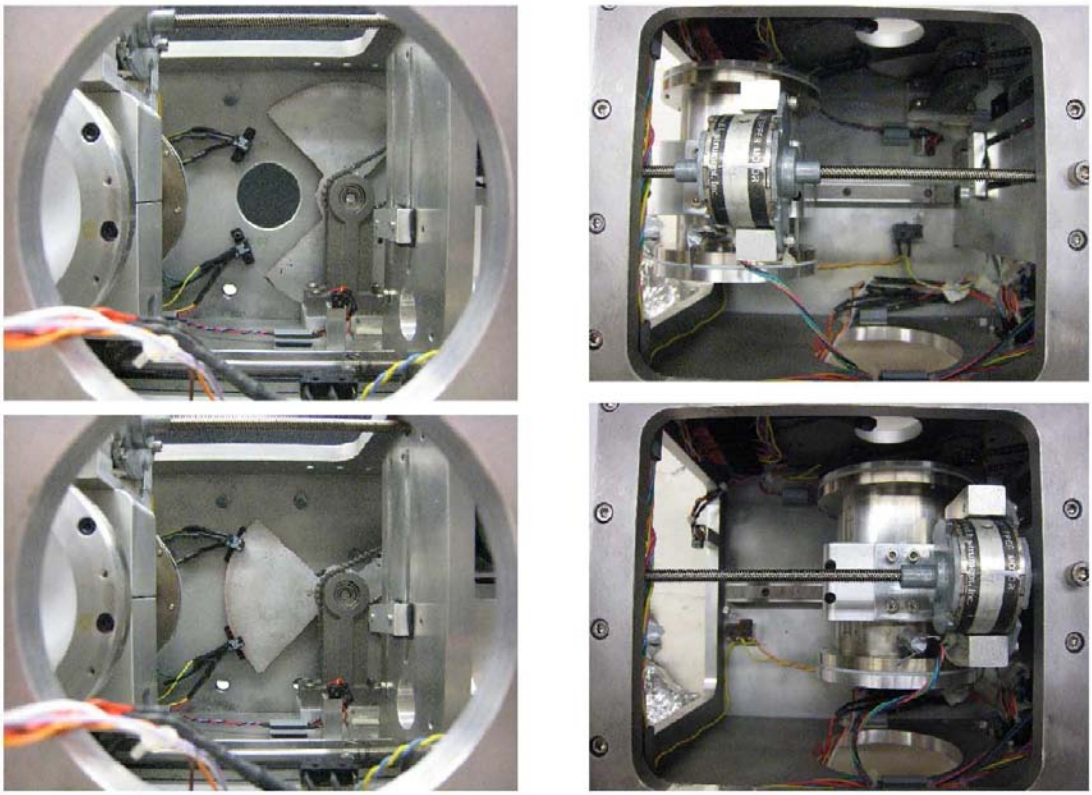

Figure 1.14: Chopper and Gas Cell Modes

***Left Side*:** Picture of the new SPIFI cal box along the beam path. The chopper blade is shown in the out-of-beam position (top) and the in-the beam path (bottom). The gas cell is in the out-of-beam position in both pictures, and part of the gas cell cylinder and white Teflon window can be seen to the left. (The view is rotated 90° clockwise from the left panel of Figure 1.13).
***Right Panel*:** Picture of the new SPIFI cal box perpendicular to the beam path. The gas cell is shown in the out-of-beam position (top) and the in-beam position (bottom). The chopper blade is in the out-of-beam position in both pictures. (The view is rotated 90° clockwise from the right panel of Figure 1.13).

Gas Cell To obtain line widths and strengths well-matched to SPIFI's resolution and sensitivity (which are tuned for astrophysical lines), the calibration gas must be held at a low fixed pressure ($P \sim 50 - 150$ Torr). To accomplish this, the gas is placed in small cylindrical container, or "gas cell," which can be evacuated or filled through a flexible PVC tube connected to an external pump and gas storage bottle. The cell's ends are fitted with $\frac{1}{16}$" thick Teflon windows –

strong enough to withstand a gauge pressure of ~ 1 atm but still transparent to submm light ($t_{205\mu\mathrm{m}} \sim 65\%$ per window, Benford *et al.* (2003)). The entire assembly is mounted on a track perpendicular to the beam path and can be moved in and out of the beam by a remotely controlled stepper motor (Figure 1.14).

Blackbody To provide a continuum calibration source, a heated blackbody is placed on the far side of the gas cell with respect to SPIFI's entrance window. The blackbody consists of a glass surface warmed to $T \sim 80$ °C by a resistive circuit (glass is very opaque – and hence, emissive – in the FIR). It is mounted directly on the gas cell on the opposite side from the entrance window, and is held just a short distance from the cell's Teflon window by standoffs. Because the HOFPI must scan to produce a single spectrum, data at different wavelengths are collected at different times. This is fine so long as the blackbody temperature remains constant, however fluctuations or drift in the blackbody temperature can confuse the spectra. Therefore, to help stabilize the blackbody temperature, a resistance temperature detector (RTD) on the blackbody was fedback to a proportional-integral-derivative (PID) controller.

Chopper SPIFI's detectors and J-FET readouts have strong $1/f$ noise, so that their signals are best detected using lock-in amplifier techniques. The modulation frequency is provided by "chopping" the beam on and off the source at rates of ~ few Hz or more (see §1.3.3). For astronomical observations, chopping is essential since the astrophysical lines are very weak in comparison to the foreground emission from the sky and telescope (which slowly varies). Therefore, the cal box includes a variable-speed two-bladed fan which can be used to chop the beam entering SPIFI, creating a square wave signal. The chop frequency –

which was usually selected at ~ 8 Hz at the AST/RO – is precisely measured by two photodiodes and fed to the lock-in program. The chopper was mechanically decoupled from the gas cell and blackbody so that it could be used for other calibration measurements when the gas cell was out of the beam path (*e.g.* skydips, gain, focusing). During observations, the SPIFI chopper blade is stopped out of the beam path (Figure 1.14), and the chopping function is served by the AST/RO tertiary mirror (§1.3.2).

Many aspects of this design performed well, but some did not. Here are the lessons learned:

1. The absorption lines were weak and difficult to see due to the short path length within the gas cell. We realized during construction that this may be a problem, but the cell size was limited by the physical dimensions of the AST/RO elevation-axis beam tube.
2. The blackbody temperature was found to be highly sensitive to outside weather conditions – particularly wind – and calibration spectra were confused by temperature gradient wiggles on ~ 10 s timescales. At the beam tube entrance, the cal box was situated on a strong temperature gradient between the heated "Spifihaus" (§1.3.1) and the outside air. Although the PID was highly stable in tests at Cornell, the hardware was simply inadequate for Antarctic conditions.
3. The gas cell plumbing leaked, with pressure climbing from ~ 50 Torr to 760 Torr in a few minutes, roughly the length of one integration. The leaking occurred partially at the hose-clamped connection between the gas cell nipple and flexible PVC tube, which is exposed to the same temperature gradient as the blackbody, and is subjected to frequent motion as the gas

cell is moved in and out of the beam path. Despite good performance at 293 K, a more robust connection is needed for the Antarctic.

1.3 SPIFI on AST/RO

The US Amundsen-Scott South Pole station is run by the NSF Office of Polar Programs (OPP) with contracted support from Raytheon Polar Services Co. (RPSC). Station operations are tied to the annual cycle of access to the Pole: The station is "open" during the austral summer, from late October through mid-February. During this time there are ~ 6 cargo flights and 1 passenger flight daily on ski-equipped LC-130 aircraft, operated by the New York Air National Guard out of Christchurch, New Zealand, via US McMurdo Station on Ross Island near the Antarctic coast. Outside of this period, during winter, aircraft oils can freeze, and there are no flights. A ~ 50 person "winter-over" crew operates the station and scientific instruments in isolation for more than eight months. Communication is limited to ~12 hours per day of satellite Internet access (with voice-over-IP phones) and "emergency" Iridium satellite phones.

SPIFI was first deployed to the Pole during the 2003 – 2004 summer, with observations scheduled for August (2004), when the best submm weather was expected (§1.1.2). Due to summertime population restrictions, only two SPIFI team members could be at the Pole at a time. During the winter, two AST/RO "winterovers" would operate the AST/RO and its receivers (Table 1.2). Therefore, SPIFI had to be fully installed, calibrated, and the winterovers trained before station closing. Standard OPP logistics required that SPIFI personnel travel dates be set by March, 2003, and SPIFI ship from Cornell by September 2003.

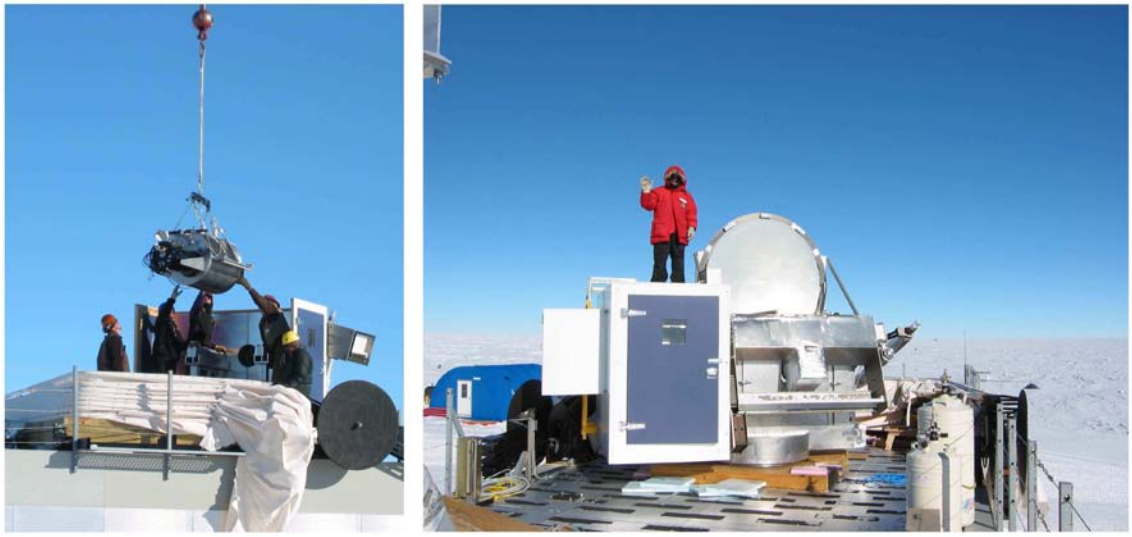

Figure 1.15: SPIFI Installation on the AST/RO (*Credit: Thomas Nikola*)
***Left Panel*:** SPIFI is craned onto the AST/RO rooftop, December 21, 2003.
***Right Panel*:** SPIFI engineer Stephen Parshley on top of *Spifihaus*, December 29, 2003.

SPIFI began testing in a "Jamesway" tent next to the AST/RO on December 4, 2003, was installed on AST/RO on December 21 (Figure 1.15), and had "first light" on January 3, 2004. SPIFI remained at the Pole for its entire campaign (2 years), meaning that all troubleshooting and equipment repairs had to take place on-site. If additional parts or supplies were needed, they could only be obtained during summer and could take weeks or months to arrive. In the winter, no outside supplies could be had. SPIFI felt the direct consequences of this when the station ran out of ℓ–^{4}He in early August, 2004, so that no useful astrophysical observations were obtained during this season. The SPIFI team returned in the 2004 – 2005 summer to prepare for August, 2005. This time, the helium supply was ample, and observations were successful (Chapter 2). The success was due to many factors, not the least of which was SPIFI team member Stephen Parshley, who served as one of the 2005 AST/RO winterovers.

The following sections outline key aspects of the integration of SPIFI with the AST/RO telescope and SPIFI operations at South Pole.

1.3.1 The Nasmyth Platform: *Spifihaus*

The AST/RO had receiver mounts at both the Coudé focus (along its azimuth axis) and Nasmyth focus (along its elevation axis). The optical train consisted of two powered mirrors, an off-axis parabolic primary and ellipsoidal secondary, and two redirecting mirrors, a flat tertiary which directed the beam along the elevation axis and a flat quaternary which directed the beam along the azimuthal axis (Figure 1.16). The tertiary, which was located at the exit pupil, also served as the chopper (§1.3.3), with a motorized mount that could be tilted up to 3° between the source and background sky at low frequencies (~ a few Hz). AST/RO optics are discussed in greater detail in Stark *et al*. (1997b, 2001).

SPIFI is a large instrument, spanning nearly 2 m with the ADR and cal box attached and weighing ~ 250 kg with full cryogen tanks. AST/RO's Coudé focus was positioned above an optical bench in a heated "receiver room" beneath the primary. Unfortunately, because several other receivers used the bench, SPIFI was simply too large for this space. It was mounted instead on the Nasmyth platform, on the AST/RO rooftop. Because AST/RO had only one Nasmyth platform, counterweights were added on the opposite side of the azimuth bearing to balance the telescope.

The AST/RO rooftop had a retractable canvas ("baby-buggy") cover for shielding winds, but the Nasmyth mount was otherwise exposed to the elements. SPIFI could not run in this environment without a warm enclosure:

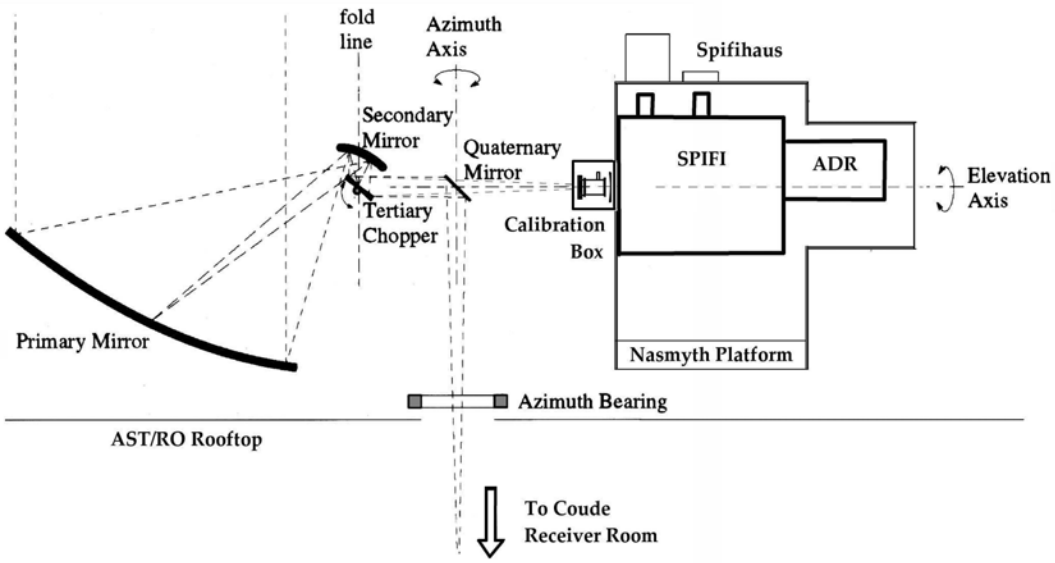

Figure 1.16: SPIFI on the AST/RO (*Not to scale*)

SPIFI is shown mounted in the *Spifihaus* on the AST/RO's Nasmyth platform. For clarity, the primary has been rotated 90° about the "fold line" into the plane of the page. The dotted lines trace beams for both the AST/RO and SPIFI secondaries (*i.e.*, the Coudé and Nasmyth foci). This figure has been modified from one in Stark *et al*. (1997b).

- At South Pole's temperatures, the O-rings of both SPIFI and the ADR would freeze, causing a loss of vacuum and internal damage
- SPIFI relies on significant supporting electronic and mechanical equipment: the control computer, motor indexers and drivers, ADR magnet controllers, the cal box, pumps, *etc*. In this extreme cold, mechanical devices will seize and passive components behave differently. The Nasmyth rotates in azimuth, so relocating these devices would require dozens of ~ 100 ft cables to be routed through the AST/RO cable wrap, straining the azimuth bearing. And for some analog signals, 100 feet is too far.
- The lead-acid batteries which bias the detectors would lose power

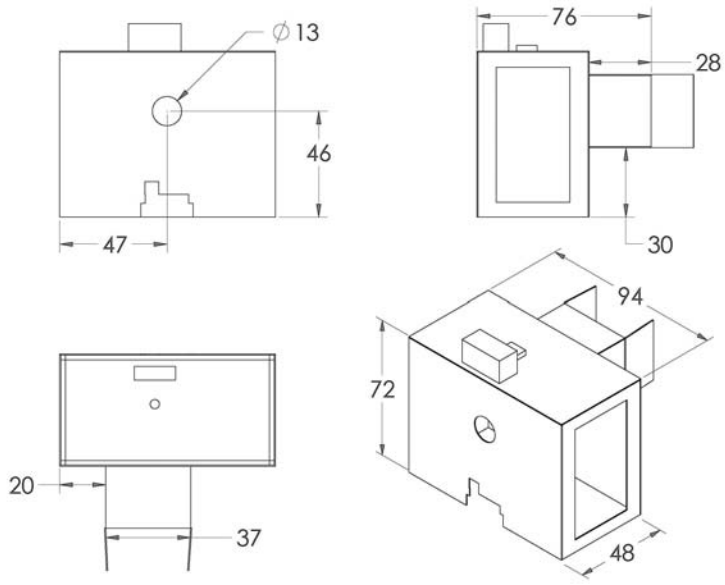

Figure 1.17: *Spifihaus* (*All measurements in inches*)
Top Left: Front elevation; the circular opening mates with the AST/RO elevation tube. ***Top Right***: Side elevation; the cantilevered box, or "pillbox," houses the ADR. ***Bottom Left***: Overhead; the pillbox doors are for ADR cycling and cryogen filling. ***Bottom Right***: Angled view; the two roof hatches are for filling SPIFI cryogens; side doors of the main *haus* give access to SPIFI.

- SPIFI team members would be exposed to the elements while working on the instrument and during cryo-maintenance. Because cryo-maintenance is a daily task, this was a serious concern for the winterovers (§1.3.6).

The partial solution was the construction of an insulated, heated shed directly on the Nasmyth platform, which became affectionately known as *Spifihaus* (Figure 1.17). *Spifihaus* had an Al base, wood-frame sides and top, Al siding, and was insulated with a double layer of 1" R5 polystyrene insulation board. Roughly 3 kW of electrical power were supplied through the cable wrap, and electric heaters maintained $T \sim 10\,^{\circ}\mathrm{C}$. *Spifihaus* weighed ~ 350 kg; to keep the *haus* as compact and lightweight as possible (so as to minimize torque on the azimuth bearing), a cantilevered "pillbox" was constructed around the ADR.

Doors in the pillbox allowed access for ADR cycling and cryo-maintenance, a ladder and roof hatches enabled SPIFI cryo-maintenance, and side doors gave access to the equipment. Just inside each side door was enough space for one person to stand – providing a temporary haven for personnel during troubleshooting or cryo-maintenance.

1.3.2 Foreoptics

Because the AST/RO Coudé and Nasmyth mounts sat along different axes of the telescope and had different focal lengths, changeable "foreoptics" – optical components between the telescope primary and receiver entrance window – were required to allow observers to switch between SPIFI and other receivers at the AST/RO. Two changes were needed to make the switch:

1. the quaternary, which redirects the beam 90° out of the elevation axis and into the azimuthal axis, must moved out of the beam path.
2. the focal length along the elevation axis must be readjusted to bring the beam to an $f/8.4$ focus at the entrance window to the SPIFI optical Dewar.

The simplest solution was to use manually swappable mirrors. For item 1 above, this meant removing the quaternary. However, with AST/RO's compact design and only two focusing mirrors, options for refocusing the beam (item 2 above) were limited. The best solution was to manufacture two different secondary mirrors: an "AST/RO" secondary for the Coudé focus, and a "SPIFI" secondary for the Nasmyth focus. For both the quaternary and secondary mirrors, this presented the challenge of re-achieving alignment after each swap. This was solved by the use of kinematic mounts (Stark *et al*. 1997b; Hsieh 1998).

Table 1.9: SPIFI and AST/RO Secondary Mirror Specifications

	AST/RO (*Original*)	**AST/RO** (*Best-Fit*)		**SPIFI** (*Original*)	**SPIFI** (*Best-Fit*)
x_0	-79.3750 mm	-78.8636 mm	x_0	-81.3300 mm	-82.7762 mm
y_0	1820.9390 mm	1820.9413 mm	y_0	494.8500 mm	495.4400 mm
z_0	0.0000 mm	0.0041 mm	z_0	0.0000 mm	0.0047 mm
θ_x	0.0000 ˚	-0.0074 ˚	θ_x	0.0000 ˚	-0.0021 ˚
θ_z	27.2208 ˚	27.2663 ˚	θ_z	31.3950 ˚	31.6245 ˚
a	1891.0990 mm	1891.0191 mm	a	570.0170 mm	570.4816 mm
b	606.8110 mm	604.4725 mm	b	321.2500 mm	322.0508 mm

(Hsieh 1998)

Beam refocusing at the Coudé and Nasmyth foci were found to be satisfied by sections of oblate spheroids described by the equation:

$$\left(\frac{x''}{b}\right)^2 + \left(\frac{y''}{a}\right)^2 + \left(\frac{z''}{b}\right)^2 = 1 \tag{1.17}$$

The mirror coordinates (x'', y'', z'') are related to the telescope coordinates (x', y', z') by the transformation:

$$\begin{pmatrix} x'' \\ y'' \\ z'' \end{pmatrix} = \begin{pmatrix} \cos\theta_z & \sin\theta_x \sin\theta_z & -\cos\theta_x \sin\theta_z \\ \sin\theta_z & -\sin\theta_x \cos\theta_z & \cos\theta_x \cos\theta_z \\ 0 & -\cos\theta_x & -\sin\theta_x \end{pmatrix} \begin{pmatrix} x' \\ y' \\ z' \end{pmatrix} + \begin{pmatrix} x_0 \\ y_0 \\ z_0 \end{pmatrix} \tag{1.18}$$

where (x_0, y_0, z_0) are translational offsets and θ_x and θ_z are rotations about the x'' and z'' axes, respectively (Hsieh 1998).

The mirrors were machined from aluminum on a five-axis computer numerical control (CNC) mill. The specified ("original") and measured ("best-fit") mirror parameters are shown in Table 1.9. The AST/RO secondary was pol-

ished to a measured RMS surface accuracy of 4.3 μm. However, the figure of the delivered SPIFI mirror was worse than expected (RMS $\sim$ 32.6 μm) and additional hand polishing was performed by the SPIFI team to improve the surface smoothness.

1.3.3 Chopping

Astrophysical signals in the FIR and submm bands are quite small compared to the thermal background from the atmosphere. For example, at 205 μm, our observed line strength from the Carina Nebula at the Dewar entrance window was only $\sim$ 0.01 K. Observing this small signal against the bright ($\sim$ 230 K) sky requires rapid switching, or "chopping," between the source and adjacent (source free) sky. For many calibration procedures, chopping is achieved using the chopping blade of SPIFI's calibration box (§1.2.3). For astronomical observations, on the other hand, chopping was achieved by nutating the AST/RO tertiary mirror.

Chopping the tertiary mirror throws the beam across the sky up to three degrees, but keeps the system pupil on the primary mirror, so that the only source of background that is strongly modulated is the sky. There is, however, some small movement of the pupil on the primary mirror which can introduce a modest modulation of the background. This component is removed by "nodding" the telescope in azimuth by an angle precisely equal to the beam throw on the sky. In this way, the source is alternately placed in the "plus" beam and then in the "minus" beam, where the plus beam is in phase with the source signal, and the minus beam is 180° out of phase with the source signal. Chopping is con-

tinuous, while nodding is switched only before the start of each new spectral scan.

In addition to subtracting out the very large thermal background on short timescales (few Hz), chopping enables us to AC-couple the bolometer signals (*i.e.* to use lock-in amplification techniques), which is necessary due to the large $1/f$ component of the J-FETs in our signal amplification chain. At frequencies $\gtrsim$ 2 Hz, the J-FETS are significantly quiet, with a voltage noise of ~ 8 nV Hz$^{-1/2}$.

1.3.4 Field of View

The rotation of the field of view (FOV) of SPIFI on AST/RO is influenced by three factors:

1. *Reflections*: The beam encounters three reflections (at the primary, secondary, and tertiary mirrors) and passes through two focal points before entering SPIFI. The net effect is a 180° inversion of the azimuthal axis (Az.).
2. *Hardware Mounting Offset*: The vertical axis of SPIFI's 5×5 detector array (which intersects pixels 3 and 23, with pixel 3 being in the positive direction) is installed at a fixed angle of 19.4° to the vertical axis of the mounted Dewar (*i.e.* to the plumb line). This rotation is independent of the telescope and is clockwise as viewed from the SPIFI entrance window.
3. *Elevation Angle*: Because of its location at the Nasmyth focus, SPIFI's field of view (FOV) of the sky rotates with elevation (El.). Because AST/RO's (single) Nasmyth platform lies to the side of the primary of smaller azimuth, SPIFI's FOV of will rotate counterclockwise as the primary increases in elevation.

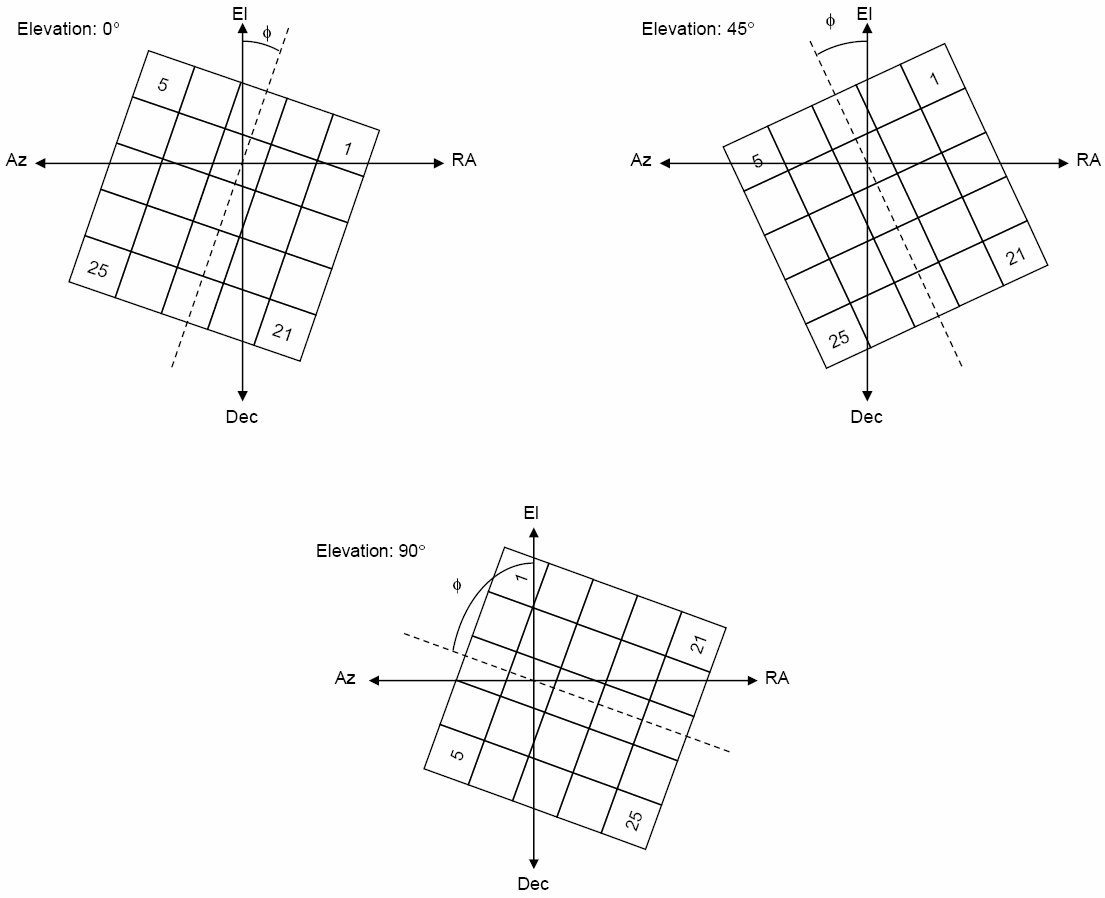

Figure 1.18: Rotation of the SPIFI Field of View on the AST/RO
The SPIFI FOV on AST/RO is shown for three different elevation angles: 0° (top left), 45° (top right), and 90° (bottom). Each pixel subtends ~ 65″× 65″on the sky, and the entire array subtends ~ 5.′4 × 5.′4.

When considering the FOV on the sky at the Geographic South Pole, + Dec. increases downwards (towards the horizon) and + R.A. increases to the right (clockwise around the horizon), and + El. increases upward (towards zenith) and + Az. increases to the left (counterclockwise around the horizon). Since pixel 8 was the most sensitive pixel in the array, we chose it as the "boresite" pixel – *i.e.* the one to which we align astronomical point sources. Pixel 8 therefore becomes the origin of the coordinate system for the array. The "position

angle," ϕ, is defined as the angle between the positive vertical axis of the array and + El., where $\phi > 0$ implies a counterclockwise rotation on the sky.

Item 1 inverts the footprint about the array's vertical axis, so that pixels 1, 6, 11, 17, and 21 appear in the rightmost column of the footprint and pixels 5, 10, 15, 20, and 25 appear in the leftmost column. Item 2 adds a zero-point offset of + 19.4° (clockwise as viewed on the sky). Finally, as the elevation angle of the telescope increases from 0° to 90°, the position angle of the footprint will rotate counterclockwise by an equal amount from its zero-point, as described in item 3 above. The resulting relation is:

$$\phi = 19.4^\circ - \text{Dec.} \tag{1.19}$$

SPIFI's FOV is plotted for three declination angles in Figure 1.18. Note that, for a given source (*i.e.* a fixed declination), the array position angle stays constant. This unique attribute of the South Pole site enables one to integrate for indefinite lengths of time on a source without needing to worry about elevation-dependent field rotation.

The angle subtended by the FOV (also "beam size") can be determined from the physical detector pixel size, d, detector $f/\#$, and the diameter of the AST/RO primary, D:

$$\text{FOV} = \frac{180^\circ}{\pi} \frac{d}{(f/\#)\, D} \tag{1.20}$$

In SPIFI, mirror 4 re-images the f/8.4 beam at the entrance window to an f/12.6 beam at the detector. Also, the 6.5 mm × 6.5 mm pixels are fed by compound parabolic "Winston" cones with circular apertures of diameter 5.6 mm (Harper *et al.* 1976). These values should be used in Equation 1.20. Table 1.10 lists

Table 1.10: SPIFI's Field of View on AST/RO

Instrument Properties	
Detector size	6.5 mm × 6.5 mm
Detector center spacing	6.8 mm
Winston cone diameter	5.6 mm
SPIFI-AST/RO $f/\#$	8.4
Detector $f/\#$	12.6
AST/RO primary diameter	1.7×10^3 mm
Field of View (FOV) Properties	
Beam diameter for a single cone-fed detector	54″
Beam center spacing	65″
5 × 5 array FOV	5′.4 × 5′.4
Filling factor	53 %

SPIFI detector and FOV parameters and the angular size of the SPIFI FOV on AST/RO. The beam size is plotted over the Carina Nebula in Figure 2.3.

1.3.5 Remote Controls

The *Spifihaus* enabled much of SPIFI's support equipment to be installed on the Nasmyth platform, greatly simplifying cabling, minimizing strain on the azimuth bearing, and keeping analog cable runs short. However, this did nothing to minimize the amount of rooftop work required by SPIFI team members and winterovers. Due to the frigid temperatures and high altitude, outdoor work at the Pole is physically and mentally trying. Under these conditions, human work efficiency is cut roughly in half. Thus, previous AST/RO winterovers recommended maximum remote control of rooftop equipment.

As a result, designing remotely controlled components was a high priority for the SPIFI South Pole campaign. The resulting systems are outlined here:

- ***FPI Scanning***: Scanning of the FPI plates was upgraded with cryogenic stepper motors (§1.2.1). The motors were controlled by SINCOS linear power stages in the *Spifihaus* which were linked to the Fabry computer. Through standard File Transfer Protocol (FTP), the motors could be operated entirely from the warm AST/RO telescope control room, or "ballroom."

- ***FPI Parallelization***: In the traditional method of parallelizing SPIFI's FPIs, a (roughly collimated) 633 nm He-Ne laser beam was directed into the Dewar by a flat "flip" mirror. The beam illuminated the FPI etalon, and the reflected beam formed an interference pattern which could be monitored as three PZT actuators were adjusted to parallelize the FPI plates (§1.2.1). For South Pole, special remote control boxes were constructed to control the PZT voltage via the cable wrap, the flip-mirror motor was operated via FTP to Fabry, and the fringes monitored by a webcam. Thus, parallelization could be done entirely from the ballroom.

- ***Chopping***: A similar remote was designed to control the chopper blade (§1.2.3) via the cable wrap. This included a variable speed adjustment, a connector for oscilloscope monitoring of the square wave lock-in reference signal (from the calbox's photodiode detectors), and a special circuit for stopping the blade out of the beam path.

- ***Calibration***: To produce calibration spectra, the cal box gas cell (§1.2.3) is moved into the SPIFI beam path by a stepper motor and filled with a low pressure gas through a single flexible PVC hose connected to a small pump and storage bottle in the *Spifihaus*. In previous applications, three hand valves were used to alternate between the pump (to evacuate the cell) and storage bottle (to fill the cell). For the Pole, these were replaced

with solenoid valves which could be opened and closed by relay switches from the ballroom (via the cable wrap). The pump was operated by a separate relay, and a pressure monitor was also routed though the cable wrap. The stepper motor was controlled via FTP to Fabry.

- ***Pumping***: Large "roughing" pumps are used to create vacuums in the SPIFI Dewar and cryogen tanks. The size, power requirements, and noise of the pumps were too great for the *Spifihaus*, and they were instead placed in the receiver room and their hoses routed through the cable wrap. An additional "turbo" pump for low vacuum was kept in the *Spifihaus* and its pressure could be monitored by webcam.
- ***Other***: Several additional relay switches were made for remotely turning on and off miscellaneous *Spifihaus* equipment, such as motor controllers.

1.3.6 Cryo-maintenance

Cryo-maintenance was the single greatest challenge in operating SPIFI at South Pole. SPIFI's refrigeration system is complex, with four cryogen reservoirs, a ^{3}He fridge, and an ADR. Keeping the detectors at 60 mK required filling the ADR tanks daily and and cycling the ADR/^{3}He fridge system every 2 days – a $\sim$ 4 hr process bookended by cryo-filling. The cryo needs of the SPIFI (optical) Dewar were more modest, with ℓ–N_2 filling every other day and ℓ–^{4}He filling every other week. The maintenance schedule is summarized in Table 1.11.

In a laboratory setting such as Cornell, or even in an enclosed observatory such as the JCMT, SPIFI cryo-maintenance is routine and easily managed by two skilled SPIFI team members. At South Pole, things were not so simple.

Table 1.11: SPIFI Cryo-maintenance

Component	**Task**	**Cryogens** [a]	**Frequency**
SPIFI ℓ–N_2 tank	fill	20 l	2 days
SPIFI ℓ–^{4}He tank	fill	100 l	14 days
ADR ℓ–N_2 tank	fill	6 – 7 l	daily
ADR ℓ–^{4}He tank	fill	8 – 10 l	daily ($\times$ 2 on cycling days)
ADR/^{3}He fridge	cycle [b]	–	2 days

[a] Cryogens per fill at the specified frequency. The tank capacities, in the order listed, are: 25, 65, 5 & 5 liters. [b] Cycling of the ^{3}He fridge is nested within ADR cycling, a ~ 4 hr. combined process.

First, all cryo-maintenance had to occur at the Nasmyth platform, outdoors on the AST/RO rooftop. Although the baby-buggy cover helped shield the wind, it did not protect against the cold. Another non-trivial obstacle was that storage Dewars had to be transported to the rooftop. Once filling was complete, they had to be removed from the roof, since their O-rings could freeze in a few hours. Finally, AST/RO winterovers – who are not normally familiar with SPIFI cryo-filling and cycling – had to be trained for these tasks.

At South Pole, ℓ–N_2 was obtained by AST/RO winterovers from the condenser in the Martin A. Pomerantz Observatory (MAPO) building roughly 50 m from the AST/RO. In the winter, due to high snow drifts, it was found that two persons were needed to transport the empty 50 l storage Dewar by sled. The return trip was best accomplished with three or four persons: two to pull and one or two to steady the Dewar. After the initial cool-down, when smaller amounts of ℓ–N_2 were required, the 50 l Dewar was abandoned for a 10 l hand Dewar which could be carried by one person. Liquid helium was delivered to the AST/RO by science support personnel in lightweight (aluminum) 100 l De-

wars. These 100 l Dewars were refilled from large $\ell-^4$He storage Dewars which were transported to the Pole during the summer.

During the first SPIFI winter, in 2004, Dewars were initially hauled to the AST/RO rooftop by brute force using the outdoor staircase. A full 100 l lightweight (aluminum) $\ell-^4$He Dewar weighs $\sim$ 65 kg, making this somewhat difficult and dangerous in Antarctic conditions. The AST/RO had a crane, but the hand-crank winch was slow, requiring winterovers to be exposed to the elements for too long. This was partially solved by powering the winch with a cordless drill. However, two fully charged drill batteries were required, since a single lift (one-way up or down) drained one entire battery. Thus, the winterovers found it easiest to continue to carry the 50 l $\ell-N_2$ Dewars up the stairs. In many cases, they also continued to carry the 100 l $\ell-^4$He Dewars.

For the second SPIFI winter, in 2005, winterover Stephen Parshley, who was also a SPIFI team member, designed a "cryogen elevator" to lift the storage Dewars through a rooftop hatch from the heated receiver room below. The elevator consisted of a platform to hold the Dewars and a motorized winch to pull the platform up a vertical track. Parshley also ordered a custom transfer tube with the proper span and stinger lengths and angles to reach from the cryo-elevator to the ADR fill necks without moving the Dewar. This eliminated many of the difficulties and dangers encountered during the previous winter, and made Nasmyth cryo-filling manageable during the winter.

CHAPTER 2

205 MICRON [NII] OBSERVATIONS OF THE CARINA NEBULA

2.1 Introduction

2.1.1 The Carina Nebula

The Carina Nebula (NGC 3372) is a giant diffuse emission nebula in the southern Galactic plane. It lies at a nominal position of R.A. = 10^h44^m and Dec. = -59°53′ (J2000) and has a visible span of $\sim 2^\circ \times 2^\circ$. The Carina Nebula was first described by French astronomer Nicolas Louis de Lacaille during his two year journey to the Cape of Good Hope in 1751 – 1752, and is listed as object Lac III.6 in his *Coelum Australe Stelliferum* ("Catalog of Nebulae of the Southern Sky"; Lacaille 1763). Carina belongs to the ancient Greek constellation of Argo Navis, the ship Jason and the Argonauts sailed in search of the golden fleece in the Greek mythology legend. Lacaille subdivided it into three separate constellations: Carina (the keel of the ship), Puppis (the poop deck), and Vela (the sails).

The Carina Nebula contains the peculiar star η Carinae (η Car). From the 1600s until the 1830s, it was usually reported as a second-magnitude (m_V = 2) star but sometimes as a m_V = 4 star. This variability went essentially unnoticed until, beginning in 1837, η Car brightened to m_V = 1 and fluctuated between m_V = 1 and m_V = 0 for nearly 20 years. In 1843 it briefly became the second brightest extra-solar-system object in the sky, at m_V = -1. This event, called the "Great Eruption," was made known partly through John Herschel's visit to the Cape of Good Hope in 1847, and his sketch of the "Keyhole Nebula." After 1856, η

Car faded, stabilizing to m_V = 7 or 8 around 1870. Except for the Lesser Eruption between 1887 and 1895, η Car has since been more or less stable, gradually brightening to a current magnitude of m_V = 6.21 (Davidson & Humphreys 1997).

η Car is now known to be an extreme case of a Luminous Blue Variable (LBV) star of luminosity $L = 10^{6.67} L_\odot$ and mass $M \sim 100 M_\odot$ (Smith 2006a). It is possibly the brightest star in the Milky Way. The great eruption resulted the ejection of a dense bipolar nebula ($\sim 15''$ across), or "Homunculus," which now obscures the central star. Damineli (1996) identified a companion in a close 5.5 yr orbit to η Car – possibly an O5V star (Smith 2006a). Measurements of the expansion parallax of the Homunculus nebula give a distance to η Car of 2.3 kpc ± 2 % (Allen & Hillier 1993; Smith 2006b). (In the remainder of this work, we assume this value as the common distance for the Carina Nebula.) Both η Car and the surrounding Carina Nebula are located in the Carina spiral arm of the galaxy.

Multiwavelength studies over the past $\sim$ 50 years have yielded a wealth of information about the Carina Nebula. Among the prominent structures in Carina are dust lanes, two HII regions known as Car I and Car II (*e.g.* Gardner & Morimoto 1968; McGee & Gardner 1968; Huchtmeier & Day 1975; Retallack 1983; Ghosh *et al*. 1988; Whiteoak 1994; Brooks *et al*. 2001; and Mizutani *et al*. 2002), photodissociation regions (PDRs; *e.g.* Zhang *et al*. 2001; Rathborne *et al*. 2002; Brooks *et al*. 2003; Mizutani *et al*. 2004; Tapia *et al*. 2006; and Kramer *et al*. 2008), giant molecular clouds (*e.g.* Gardner *et al*. 1973; Dickel & Wall 1974; Dickel 1974; de Graauw *et al*. 1981; Brooks *et al*. 1998; Zhang *et al*. 2001; Brooks *et al*. 2003; and Kramer *et al*. 2008), and several open clusters (*e.g.* Feinstein 1995; Walborn 1995; Tapia *et al*. 2003; and Smith 2006a). Recent studies have revealed many of the exciting features associated with active star formation in

the nebula, including "elephant trunk" pillars of neutral gas extending into the HII regions, visible disks of dust around embedded stars (proplyds), and jets associated with the birth of massive stars (*e.g.* Megeath *et al*. 1996; Brooks *et al*. 2001; Rathborne *et al*. 2002; Tapia *et al*. 2003; Tapia *et al*. 2006; Sanchawala 2007a and 2007b; and the recent Hubble legacy image by Nathan Smith, in prep.).

Carina has a more impressive concentration of very luminous stars than any other known place in the galaxy, containing 6 of the 16 known O2 and O3 spectral-type stars in the galaxy (Maíz-Apellániz *et al*. 2004; Smith 2006a). It rivals the 30 Doradus region of the Large Magellanic Cloud (see §2.6.7). Carina is currently powered by UV radiation from 65 O-type stars and 3 WNH stars, but for most of its lifetime, when η Car was on the main-sequence, the Carina Nebula was powered by 70 O-type stars that produced a hydrogen ionizing luminosity 150 times stronger than that in the Orion Nebula (Smith 2006a).

At visible wavelengths, the northern part of the nebula forms an arrowhead-shaped nebulosity whose edges are defined by the two prominent ("east" and "west") dust lanes (Figure 2.1). This region contains two open clusters, Trumpler (Tr) 14 and 16 (Figure 2.1), where the most massive stars of Carina reside (η Car is a member of Tr 16). The strong UV radiation from Tr 14 and 16 is powering the two HII regions, Car I and II, respectively. Car I and II are outlined by contours of 843 MHz (thermal) radio continuum emission (Whiteoak 1994) in Figure 2.1.

Figure 2.1 *(following page)*: The Carina Nebula

Major components of the Carina Nebula are overlaid on an optical Digital Sky Survey (DSS) negative photograph (http://skyview.gsfc.nasa.gov/; Lasker *et al*. 1990). Solid contours outline the Car I and II HII regions at ~ 50 % of peak intensity in 843 MHz (thermal) radio continuum emission (Whiteoak 1994). Dotted contours outline the Giant Molecular Cloud (GMC) at ~ 15 and 30 % of peak intensity in 115 GHz ^{12}CO(1→0) emission (Brooks *et al*. 1998). OB stars (through B2V) are shown by cluster: Tr 14 in (blue) diamonds, Tr 16 in (red) squares, and Tr 15 in (yellow) circles (Smith 2006a). The centers of the major sources are marked with crosses, as determined by Röser & Bastian (1988) for η Car, Whiteoak (1994) for Car I and II, and Kharchenko *et al*. (2005) for Tr 14 and 16.

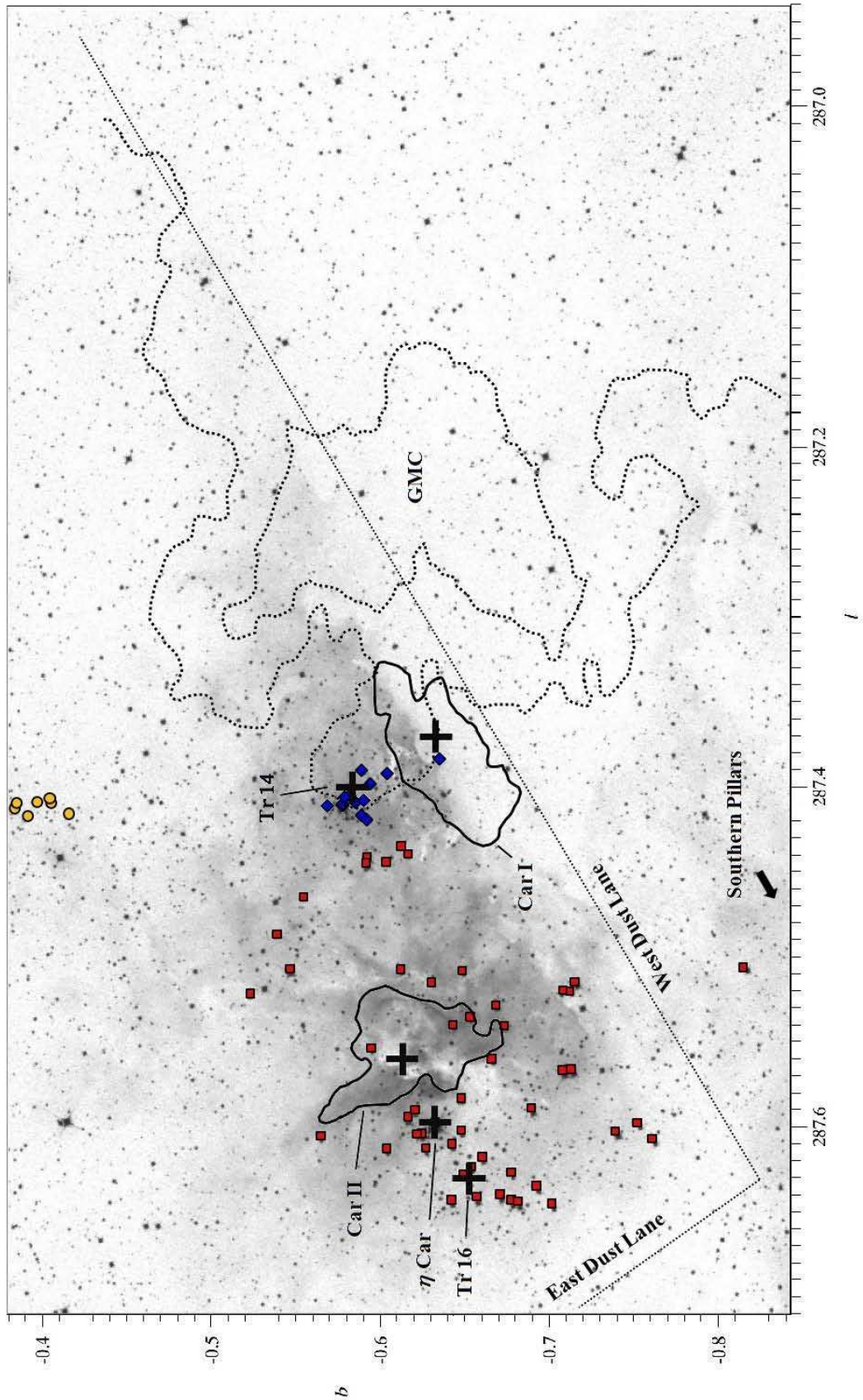
GMC
Tr 14
Car I
Car II
η Car
Tr 16
West Dust Lane
East Dust Lane
Southern Pillars
-0.4
-0.5
-0.6
-0.7
-0.8
b
287.6
287.4
287.2
287.0
l

The age of Tr 16 is probably $\sim 2 - 3$ Myr – near the end of the lifetime of η Car and Tr 16's other most massive members (Smith 2006a). We are witnessing this region in a relatively quiescent state before a series of several supernovae which are likely to occur in the next 1 – 2 Myr, to which the Great Eruption of η Car was a precursor. In its life, Tr 16 has swept away most of the gas and dust in its vicinity. Car II is likely all that remains of the densest core of a once giant molecular cloud (GMC) which spawned these stars. Car II is primarily heated from the outside by members of Tr 16, although ultracompact cores and outflows have recently been discovered inside Car II (*e.g.* Yonekura *et al*. 2005). Feedback from Tr 16 is also triggering star formation in the peripheral areas of the nebula, particularly in the Southern Pillars (*e.g.* Rathborne *et al*. 2004; Smith *et al*. 2005), and is possibly contributing flux to Car I as well.

Tr 14 is smaller, more compact, and somewhat younger than Tr 16, with an age of about $\sim 1 - 2$ Myr (Smith 2006a). Because of this, Tr 14 has not cleared away its parent cloud to the extent that Tr 16 has, and Tr 14 sits inside a cavity (open along our line of sight) within a GMC extending $\sim 0.^{\circ}5$ to the west. In Figure 2.1, dotted contours outline the GMC in 115 GHz ^{12}CO(1→0) emission (Brooks *et al*. 1998). UV flux from Tr 14 is powering the intense Car I HII region and PDR, which lie ~ 2 pc to the southwest of the cluster's center – although at least one O9/B0 star is believed to be embedded within Car I (Tapia *et al*. 2003).

The Carina Nebula is our richest nearby laboratory in which to study feedback through UV radiation and stellar winds from very massive stars before supernova explosions have disrupted the environment. This feedback is triggering new generations of star formation while simultaneously evaporating the gas and dust reservoirs out of which young stars are trying to accrete. At a dis-

tance of 2.3 kpc, Carina has the most extreme stellar population within a few kpc of the Sun, and suffers little interstellar extinction. It is our best bridge between the detailed star-formation processes that can be studied in nearby regions like Orion, and much more extreme but also more distant regions like 30 Doradus (Smith & Brooks 2008).

Our current observations probe the most abundant species of gas which have been ionized and dissociated by the intense UV flux of the nebula. Arguably, the best way to observe the properties of these gases is through their emission in the far-infrared (FIR) fine-structure lines. These lines provide important coolants for the ionized gas, and are the dominate coolants for the warm neutral medium (WNM).

2.1.2 FIR and Submm fine-structure Lines

Stars form from the gravitational collapse of dense cores within giant clouds of molecular gas and dust in the interstellar medium (ISM) of galaxies. The largest and brightest of these stars, spectral class O and B stars (T > 10,000 K), in turn influence the structure and evolution of the "parent" molecular cloud: extreme-ultraviolet (EUV) photons ($h\nu$ > 13.6 eV) from the stars ionize the surrounding gas, forming HII (ionized hydrogen) regions; far-ultraviolet (FUV) photons (6 eV < $h\nu$ < 13.6 eV) penetrate beyond the HII region and into the molecular cloud, where they heat the dust and dissociate the primary (non-hydrogen) molecules (*e.g.* CO, O_2, OH, H_2O) into neutral atomic gas species; and stellar winds and the expansion of the HII region(s) around main sequence stars can compress the molecular cloud, triggering the next generation of starformation (the supernova

explosion of a massive star at the end of its life can do this as well). On the other hand, the added turbulent energy from these processes can also sometimes halt the formation of the next generation of stars, or even disrupt the cloud entirely.

The neutral regions formed on the surfaces of molecular clouds by impinging FUV flux are known as "photodissociation regions" (PDRs). PDRs typically have hydrogen densities of $10 \lesssim n_{\rm H} \lesssim 10^5$ cm^{-3} and temperatures of $T \sim 50 - 500$ K. For PDRs on the surfaces of giant molecular clouds, there will be a layer of atomic hydrogen which extends from the cloud surface to a visual magnitude extinction depth of $A_V \sim 1$ - 2 (deeper into the cloud the hydrogen is molecular in form), a layer of ionized carbon which extends to $A_V \sim 2$ - 4, and a layer of atomic oxygen which extends to $A_V \sim 5$ - 10. Thus, PDRs include material in which the hydrogen is molecular and the carbon mostly in CO, but where FUV flux still strongly affects the gas phase chemistry and trace species ionization. Since most molecular clouds have column densities less than $\sim 2 \times 10^{22}$ cm^{-2} ($A_{\rm V} \sim 10$), most (~ 90 %) of the molecular gas in the Galaxy is in PDRs as defined here (Hollenbach & Tielens 1999). Only the dense, FUV-shielded cloud cores (with $n_{\rm H} \sim 10^3 - 10^7$ cm^{-3} and $T \sim 3 - 30$ K) are not PDRs.

In PDRs, FUV photons are absorbed by dust grains (ranging from ~ 0.001 μm up to $\sim 0.3\,\mu$m) and large carbonacious chain molecules, often termed "polycyclic aromatic hydrocarbons," or PAHs. The dust is heated to temperatures of $\sim$ few 10 K and cools primarily through continuum blackbody emission peaking in the FIR. The PAHs cool through several near- and mid-IR emission lines. The gas in PDRs is thermally decoupled from the dust, but undergoes photoelectric heating, whereby a minor fraction (~ 10 %) of the incident FUV photons eject electrons from grains. After overcoming the work function of the grains and the

(positive) grain charge, only ~ 10 % of the energy of the FUV photons causing the ejections actually goes into the kinetic energy of the photoelectrons. This excess kinetic energy is distributed to the gas via inelastic collisions. The overall photoelectric heating efficiency is thus ~ 1 % or less (typically 0.1 – 1 %).

The primary coolants of the gas in PDRs between ~ 50 K and ~ few 100 K are the FIR and submm emission lines from the [CII], [OI] and [CI] fine-structure transitions and the mid-J CO rotational transitions. These FIR and submm lines are effective coolants because they are easily excited at the temperatures prevalent in PDRs, they do not suffer from extinction (as do optical lines) and, with the exception of the 63 μm [OI] line, they are typically optically thin. Thus, these lines can escape the gas and dust which enshrouds star-forming regions. For low density ($n_{\rm H}$ < few 1000 cm^{-3}) PDRs, the 158 μm [CII] line dominates the cooling, accounting for ~ 0.3 % of the total FIR luminosity of the Milky Way and other starforming galaxies, rivaling the luminosity of the brightest optical lines (see page 81).

Our observations of the Carina Nebula include some of the most prominent fine-structure emission lines arising from PDRs and the warm ionized medium (WIM): the 63 and 146 μm [OI] lines, the 158 μm [CII] line, and the 122 and 205 μm [NII] lines.

The 122 and 205 μm [NII] Lines

Since the ionization potential (I.P.) of nitrogen is ~ 14.53 eV, [NII] is only found in HII regions.[1] The ground-state of the N^+ ion's $2p^2$ electron configuration is

[1]The values for ionization potentials cited in this work were taken from the NIST Atomic Spectra Database at http://physics.nist.gov/PhysRefData/IonEnergy/ionEnergy.html, and

split by the spin-orbit interaction into the three levels, $^3P_{2,1,0}$, from which the 121.897572 μm ($^3P_2 \rightarrow {}^3P_1$) and 205.178231 μm ($^3P_1 \rightarrow {}^3P_0$) lines arise (Figure 2.2).[2] Nitrogen is the fifth most abundant element in the ISM (N/H $\sim 7.8 \times 10^{-5}$; Savage & Sembach 1996), and the ground-state levels are energetically accessible (T < 200 K), making the FIR [NII] lines important coolants of the WIM. At electron temperatures of T_e = 8000 K, the critical densities (for collisional de-excitation by electrons) are $n_{\rm crit} \approx 293$ cm^{-3} and 44 cm^{-3} for the 122 and 205 μm lines, respectively, so that the 122/205 line intensity ratio is an excellent density probe for low-density ionized gas (§2.6.2).

Of the most abundant gas phase elements in the WIM (H, He, O, C, N, Ne and S), only C, N, and Ne will be found in ionization states (C^+, N^+, Ne^+) that have fine-structure splitting of their ground state terms. The 158 μm fine-structure line of C^+ traces the WIM very well, but also traces neutral gas regions such as atomic clouds and PDRs on the surfaces of molecular clouds. The 12.8 μm fine-structure line of Ne^+ has $n_{\rm crit} \approx 5 \times 10^5$ cm^{-3} and I.P. $\approx$ 21.56 eV, so it traces higher ionization, higher density HII regions than the WIM. Thus, the [NII] 122 and 205 μm lines are arguably the best tracers of the diffuse extended WIM.

Observations of the 122 and 205 μm [NII] lines by the Cosmic Microwave Background Experiment (COBE) Far Infrared Absolute Spectrophotometer (FIRAS; Wright *et al*. 1991) found that, after the 158 μm [CII] line, the [NII] lines are by far the brightest lines in the 100 μm – 1 mm FIRAS bandpass, with line luminosities of approximately 0.045% and 0.03% of the total Milky Way FIR luminosity for the 122 μm and 205 μm lines, respectively (Wright *et al*. 1991; references therein.

[2]The values for wavelengths of observed ISO and SPIFI species are referenced in Table 2.1.

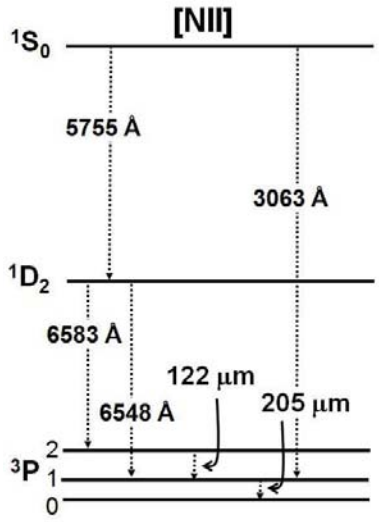

Figure 2.2: [NII] Energy Level Diagram

Bennett *et al*. 1994; Fixsen *et al*. 1999). Observations by ESA's Infrared Space Observatory (ISO) Long-Wavelength Spectrometer (LWS) show that the [NII] 122 μm line is very bright in external galaxies as well, especially in the disks of normal galaxies (*e.g.* M83 and M51; Kramer *et al*. 2005).

Despite the strength and importance of the [NII] lines, measurements are scarce. For the 122 μm line, this is because the line lies very close to a strong telluric water vapor absorption feature (§1.1.2), so that telluric transmission is poor ($\sim$ 30%) – even at the high altitudes reached by airborne observatories. The 205 μm line also suffers from poor telluric transmission, and, until recently, the 205 μm transition frequency was poorly known. In addition, spectrometers have had difficulty acheiving the sensitivity at 205 μm needed to detect this line. Until the advent of SPIFI, all astronomical direct-detection spectrometers operating in the FIR bands used Ge:Ga photoconductors as detectors. These detectors are significantly easier to implement than low temperature bolometers, but have relatively modest detective quantum efficiencies (*e.g.* Stacey *et al.* 1992). Furthermore, the 205 μm line lies near the long-wavelength cutoff of stressed

Ga:Ge photoconductors, strongly limiting the sensitivity of these spectrometers at this wavelength.

The 122 μm line was first observed by NASA's Kuiper Airborne Observatory (KAO; Colgan *et al*. 1993), and the 205 μm line by COBE FIRAS (Wright *et al*. 1991). The first lab detection of the 205 μm line was obtained even later by Brown *et al*. (1994). The 122 μm line has since been observed extensively in both the Milky Way and extragalactic sources by the ISO LWS (*e.g.* Negishi *et al*. 2001; Liu *et al*. 2001; Young Owl *et al.* 2002). However, since the LWS had a long-wavelength cutoff of 197 μm, the 205 μm line remains relatively unexplored. COBE could detect the 205 μm line, but COBE's all-sky maps used 7° beams, and are thus only useful for studying the WIM on galactic scales. After COBE, 205 μm spectra were collected by KAO in only four Galactic sources (G333.6-0.2, Colgan *et al*. 1993; DR 21, Petuchowski *et al.* 1996; G0.18-0.04, Simpson *et al*. 1997; and W43, Simpson *et al*. 2004) and one extragalactic source (M82, Petuchowski *et al*. 1994), the last of these observations coming in 1992. The 205 μm [NII] line was not observed again until the observations of the Carina Nebula by SPIFI in 2005 (Oberst *et al*. 2006 and the present work).

The 158 μm [CII] Line

The [CII] 157.74093 μm $^2P_{3/2} \rightarrow {}^2P_{1/2}$ fine-structure line arises from the ground state of the $2p^1$ configuration of the C^+ ion. It is the brightest FIR line, and has been abundantly detected in the local Universe by spectrometers on KAO, COBE, ISO and other facilities. It typically amounts to 0.3% of the observed FIR luminosity for star-forming galaxies such as the Milky Way (*cf*. Crawford *et al*. 1985; Stacey *et al*. 1985, 1991; Wright *et al*. 1991). Carbon is the fourth

most abundant element in the ISM (C/H $\sim 1.4 \times 10^{-4}$; Kaufman *et al*. 1999) and has an ionization potential of just 11.26 eV, making the 158 μm [CII] line the most important coolant for much of the neutral ISM in galaxies. Since the $^2P_{3/2}$ [CII] line-emitting level has a low critical density ($n_{\rm crit} \sim 46$ cm^{-3}, $T_e = 8000$ K) for thermalization by electron impact excitation, the [CII] line is an important coolant for low-density ionized gas regions as well.

Since it is bright, and the most important coolant for much of the ISM, studies of the C^+ line are critical to understanding star formation in galaxies. However, modeling the cooling of the ISM phases is complicated because the relative fraction of [CII] arising from each phase is not clear. Even for the Milky Way, the fractions arising from the ionized and neutral phases are unknown. Estimates of the contribution from the ionized phase range from 10 to 30% (*e.g*. Stacey *et al*. 1985) to near 50% (*e.g*. Petuchowski & Bennett 1993; Heiles 1994), depending on the assumed gas-phase (*i.e*. non-dust bound) abundance of C and the ionized gas density.

Fortunately, the FIR fine-structure 122 and 205 μm [NII] lines offer a method for sorting the contributions of C^+. The [NII] 205 μm line and the [CII] 158 μm line have nearly identical critical densities for excitation in ionized gas regions. Therefore, the line ratio in ionized media is essentially only a function of the N^+/C^+ abundance ratio, and is insensitive to the hardness of the stellar radiation fields, since the photon energies required to doubly ionize each species are similar: 29.6 eV and 24.4 eV to form N^{++} and C^{++}, respectively. The present 205 μm [NII] SPIFI observations, combined with 158 μm [CII] observations by ISO, therefore constrain the cooling of two major components of the ISM.

The 63 and 146 μm [OI] Lines

For most starforming galaxies, the next brightest FIR line after the [CII] line is the [OI] 63.18372 μm $^3P_2 \rightarrow {}^3P_1$ line. The [OI] 63 μm line and its companion [OI] 145.5255 μm $^3P_1 \rightarrow {}^3P_0$ line arise from the ground state of the $2p^4$ electron configuration of the O atom. These two lines have been abundantly observed by spectrometers on the KAO, COBE, ISO and other facilities, although the 146 μm line has been harder to detect due to its much weaker intensity. Since the ionization potential of oxygen is 13.62 eV, The 63 and 146 μm [OI] lines arise only from the neutral ISM. Oxygen is the third most abundant element in the ISM – trailing only H and He – with O/H $\sim 3.0 \times 10^{-4}$ (Kaufman *et al*. 1999).

Together, the [CII] 158 μm and [OI] 63 μm lines are the primary coolants of PDRs. Tielens and Hollenbach (1985) found that the 158 μm [CII] dominates for hydrogen nuclei densities $n_{\rm H} < 10^3$ cm^{-3} and $T < 10^4$ K, while [OI] dominates for $n_{\rm H} > 10^4$ cm^{-3} and $T > 10^2$ K. Because they are the primary PDR coolants, the ratio of the combined intensities of the 63 and 158 μm lines to that of the total FIR continuum intensity, $[I(63\,\mu{\rm m}) + I(158\,\mu{\rm m})]/I({\rm FIR})$, is often used as a measure of the efficiency of the photoelectric heating of PDR gas. The $I(63\,\mu{\rm m})/I(158\,\mu{\rm m})$ ratio itself can be used to constrain the gas temperature and density, as can the $I(146\,\mu{\rm m})/I(63\,\mu{\rm m})$ ratio of the [OI] lines (which has the complication that the [OI] line is often optically thick; *cf.* Stacey *et al*. 1983). These ratios and other spectral probes of PDRs are predicted by the PDR models of Tielens & Hollenbach (1985), which were improved upon by Kaufman *et al*. (1999). We use these models in §2.6.2 and §2.6.3 to interpret the observed ratios of the fine-structure lines in the Carina Nebula.

In addition to PDRs, shock-heated media may contribute significantly to the 63 μm [OI] line. Shocks are created when molecular or neutral gas is supersonically swept-up by winds from protostars, supernova remnants, or cloud-cloud collisions. Shocks are considered to be ubiquitous throughout the ISM, particularly in areas of high star formation with many protostars. Theoretical modeling of shocks (*e.g.*, Draine *et al*. 1983; Hollenbach & McKee 1989; Draine & McKee 1993) suggests that 63 μm [OI] line emission is strong in "J-type" dissociative shocks. J-type shocks occur primarily in ionized and neutral media, or at high velocities ($v \gtrsim 50$ km s^{-1}) in molecular gas. (Nondissociative "C-type" shocks occur primarily at moderate speeds ($v \lesssim 40 - 50$ km s^{-1}) in molecular gas, and emit weakly in [OI] 63 μm). The 63 μm to 158 μm line intensity ratio has been suggested as a J-type shock diagnostic (*e.g.* Hollenbach & McKee 1989), but a recent statistical study of ISO LWS spectra by Liseau *et al*. (2005) finds these lines, as well as the 146 μm line, to be of only limited use as shock diagnostics. Greater study is needed to establish the relation between shocks and observed FIR fine-structure emission.

2.2 Observations

2.2.1 SPIFI Observations

Using SPIFI on the AST/RO telescope at South Pole, we made the first ground-based detection of the [NII] 205 μm line. The observations were made of the Carina Nebula over the course of 15 days during the Polar winter, from August 15 to August 30, 2005. During this time, the 205 μm line-of-sight (l.o.s.) trans-

mission ranged from ~ 3 – 6 %, with an average value of 4.54 % and standard deviation fluctuation of 0.73 % between SPIFI pointings (*i.e.* on ~ 1 day timescales). SPIFI mapped two separate areas in the nebula: a ~ 14′ × 14′ area containing the Car I HII region (*e.g.* Retallack 1983; Whiteoak 1994) and a portion of the Giant Molecular Cloud (GMC) to the west (*e.g.* Brooks *et al*. 1998), and a ~ 12′ × 10′ area containing the Car II HII region (*e.g.* Retallack 1983; Whiteoak 1994). In both maps, the full 25 pixel array (~ 5.′4 × 5.′4 FOV; §1.3.4) was moved through a raster with a 130″ grid spacing (three pixel overlap) to minimize flatfielding errors (§2.3.2). Each pixel had a circular beam of 54″ diameter, resulting in a ~ 53 % map filling factor (Table 1.10), with more extended spatial coverage being favored over denser spatial sampling. Figure 2.3 shows the raster boudaries and beams overlaid on an optical Digital Sky Survey (DSS) photograph (*cf*. Lasker *et al*. 1990).

Roughly 100 HOFPI scans were performed at each raster position. Each scan covered ~ 7 resolution elements (where the resolution element has width ~ 28 counts or ~ 71 km s^{-1}; $R = 4250$; see §1.2.1 and §2.3.3), slightly over-sampled in 16 spectral bins (each of width 12 counts or ~ 31 km s^{-1}). In each spectral bin, SPIFI measured the lockin voltage difference between the source and background sky using a 3-position, 30″ azimuth throw, 2 Hz chop of the AST/RO telescope tertiary mirror (§1.3.3). SPIFI integrated for ~ 9.2 s per bin, corresponding to ~ 147 s per scan and ~ 4.09 hr per raster position (with 100 scans per raster position, on average). There were 35 raster positions, resulting in ~ 143 hr of total integration for the Carina campaign.

SPIFI calibration and data reduction are discussed in §2.3 and §2.4.

Figure 2.3 *(following page)*: SPIFI and ISO Beams

SPIFI and ISO rasters are shown overlaid on an optical DSS (inverted-grayscale) image of the Carina Nebula (http://skyview.gsfc.nasa.gov/; Lasker *et al*. 1990). The area mapped by ISO is outlined with solid lines, and larger (79.″3 diameter) circles indicate the observed raster positions and average beam diameter of the ISO LWS. The area mapped by SPIFI is outlined with dashed lines, and smaller (54″ diameter) circles indicate the observed positions and beam diameter of SPIFI on the AST/RO.

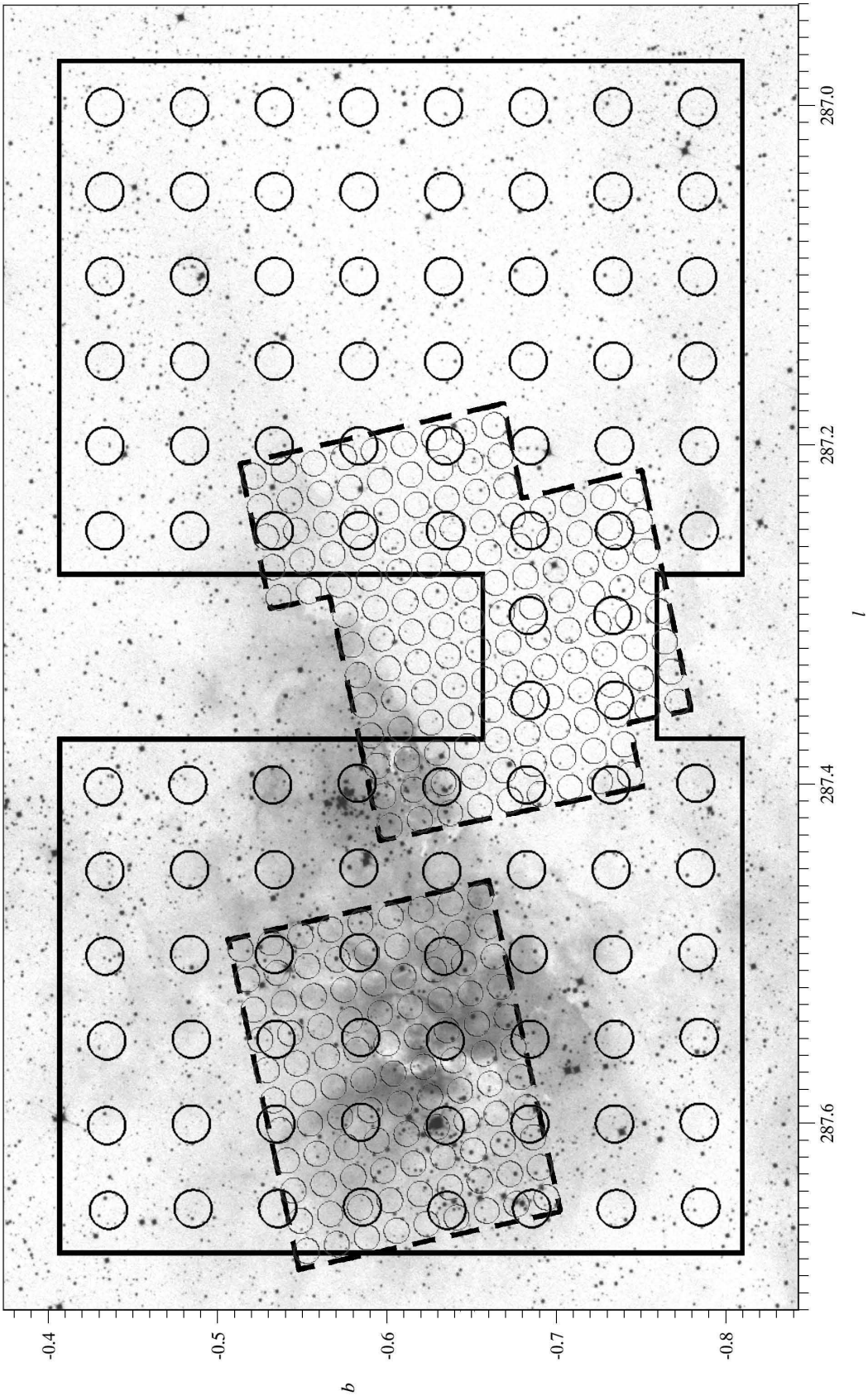
-0.4
-0.5
-0.6
-0.7
-0.8
q
287.0
287.2
287.4
287.6
l

2.2.2 ISO Observations

The European Space Agency's (ESA's) Infrared Space Observatory (ISO; Kessler *et al*. 1996) offered unprecedented sensitivity (NEP ~ few $\times 10^{-16}$ W Hz$^{-1/2}$) in the FIR. Its vantage point above the atmosphere avoided telluric absorption and the large photon background from the sky (§1.1.2), and its cooled optics avoided the photon background encountered by warm airborne telescopes, such as the KAO. Observations lasted from November 1995 through April 1998, when the $\ell-^4$He used to cool the 60 cm primary dish and instrumentation was depleted. ISO was equipped with two spectrometers – the Short Wavelength Spectrometer (SWS; de Graauw *et al*. 1996) and Long Wavelength Spectrometer (LWS; Clegg *et al*. 1996) – a camera (ISOCAM; Cesarsky *et al*. 1996) and an imaging photo-polarimeter (ISOPHOT; Lemke *et al*. 1996). The SWS and LWS each had both a grating spectrometer and a FPI. The grating spectrometers had resolving powers of ~ 150 – 350 for the LWS and ~ 1000 – 2000 for the SWS. The FPIs had resolving powers of ~ 5000 – 12,000 for the LWS and ~ 20,000 - 35,000 for the SWS. These instruments jointly covered $\lambda \approx 2.5 - 240$ μm with spatial resolutions ranging from ~ 1.5″ (at short wavelengths) to ~ 90″ (at long wavelengths).

In a guaranteed time observation (GTO) by T. Onaka, full bandwidth (43 – 197 μm) LWS spectra were taken of the Carina Nebula during four days: July 23 and 24 and August 1 and 4, 1996. The fine-structure lines of [OI] 63 μm, [NII] 122 μm, [OI] 146 μm, and [CII] 158 μm (among others) were detected, as previously reported by Mizutani *et al*. (2004). The map covered a ~ 40′ × 20′ area centered at (l, b) = (287.°4, -0.°6) and containing the Car I and Car II regions. Five separate rasters were performed within this area: Car 1 - Car 4, each containing 24 beam pointings, and Car 6, containing eight pointings, four of which overlapped po-

Table 2.1: Observed Spectral Lines

Species	λ [μm]	**Beam** [$''$][a]	**R** $(\lambda/\Delta\lambda)$[b]	**Reference for** λ
ISO:				
[OI]	63.18372	87.2	223	Watson *et al*. (1984)
[NII]	121.897572	78.2	209	Brown *et al*. (1994)
[OI]	145.5255	70.0	249	Davies *et al*.. (1978)
[CII]	157.74093	70.1	270	Cooksy *et al*. (1986)
SPIFI:				
[NII]	205.178231	54	4250	Brown *et al*. (1994)

[a] The ISO beam diameters have been taken from Gry *et al*. (2003); the SPIFI beam diameter comes from §1.3.4. [b] The ISO resolving powers assume a spectral resolution element of $\Gamma \sim 0.283$ at 63 μm (detector SW3), and $\Gamma \sim 0.584$ μm for the three higher wavelengths (detectors LW2, LW3, and LW4; Gry *et al*. 2003); the SPIFI resolving power comes from §1.2.1.

sitions in Car 3 and Car 4. Thus, the data contain 100 distinct pointings in total. The ISO beam had an average diameter of $\sim 80''$ over the LWS band and the beam pointings within each raster were spaced by $180''$, resulting in a ~ 16 % map filling factor (with more extended spatial coverage favored over denser spatial sampling).

The grating was scanned in the AOT LWS01 mode (or "fast" mode), sampling every 1/4 of a spectral resolution element, where the spectral resolution element was 0.283 μm in the second grating order (detectors SW1 – SW5, covering 43 – 93 μm) and 0.584 μm in the first grating order (detectors LW 1 – LW 5, covering 84 – 197 μm; Gry *et al*. 2003). The effective integration time in each spectral bin was 0.45 s, and the total integration time for the entire map was $\sim$ 22 hr.

2.3 Calibration

In the following discussion, SPIFI's calibration is divided into three categories:

1. Pointing and focus (*Spatial*)
2. Brightness calibration (*Spectral y-axis*)
3. Wavelength calibration (*Spectral x-axis*)

2.3.1 Pointing and Focus

SPIFI alignment was initially achieved by directing a heat lamp towards the secondary mirror from various locations on the 1.7 m AST/RO primary. The flux from the lamp – a standard 250 W R40 infrared bulb – was chopped by the SPIFI chopper and the lockin signal integrated for ~ 10 seconds with the FPIs at fixed positions peaked for 370 μm. An "aperture map" was created by measuring the lamp at 13 locations on the primary: one at the center, three each along the positive and negative elevation axes, and three each along the positive and negative azimuth axes – thus forming a "+" pattern on the dish. The radii of the Az and El positions from the dish center were ~ 0.4 m, 0.75 m, and 1.0 m; for the latter, the lamp was held just beyond the primary edge to measure "spill-over" – the fraction of the beam sent out by the instrument that spills-over the primary mirror and does not end up on the sky.

Several iterations were performed and the SPIFI mount was adjusted each time to improve symmetry. Figure 2.4 shows the aperture map for the final mount corrections. The map values are the brightness temperature difference between the signal and the SPIFI chopper. Absolute lamp temperature is not

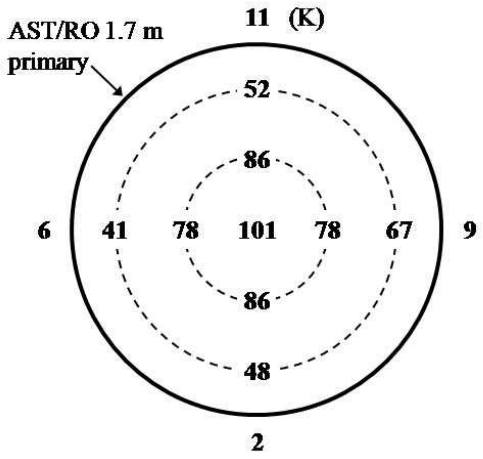

Figure 2.4: SPIFI-AST/RO Aperture Map

SPIFI measurements of the 370 μm signal from a heat lamp of constant wattage held at different positions over the AST/RO 1.7 m primary. Values represent the brightness temperature difference between the signal and SPIFI chopper (in Kelvins) recorded by pixel 8. The location of each value on the figure is the location of the heat lamp for which that measurement was taken. They lie along lines of constant El (vertical axis) and Az (horizontal axis) at radii of ~ 0.4 m, 0.75 m, and 1.0 m. The symmetry of the central measurements reflects good alignment of SPIFI to the AST/RO.

easily recovered (since the bulb does not fill the beam and the chopper temperature was not recorded) but is not important, since gain calibration was performed separately (§2.3.2). The symmetry of the central measurements show that excellent alignment was achieved and that spill-over was less than 8 %.

Initial pointing estimates for the SPIFI-AST/RO system were made during the polar summer by taking scans across the (very low elevation) Sun. With line of sight transmissions < 0.5 %, the Sun's ~ 5900 K brightness temperature in the submm bands is received as < 30 K, well within the dynamic range of the system. (Most of the power of the Sun, which falls in the optical and near-IR bands, is scattered by the machined aluminum surfaces of the AST/RO mirrors, and is therefore not a danger to the polyethylene window of the SPIFI dewar.)

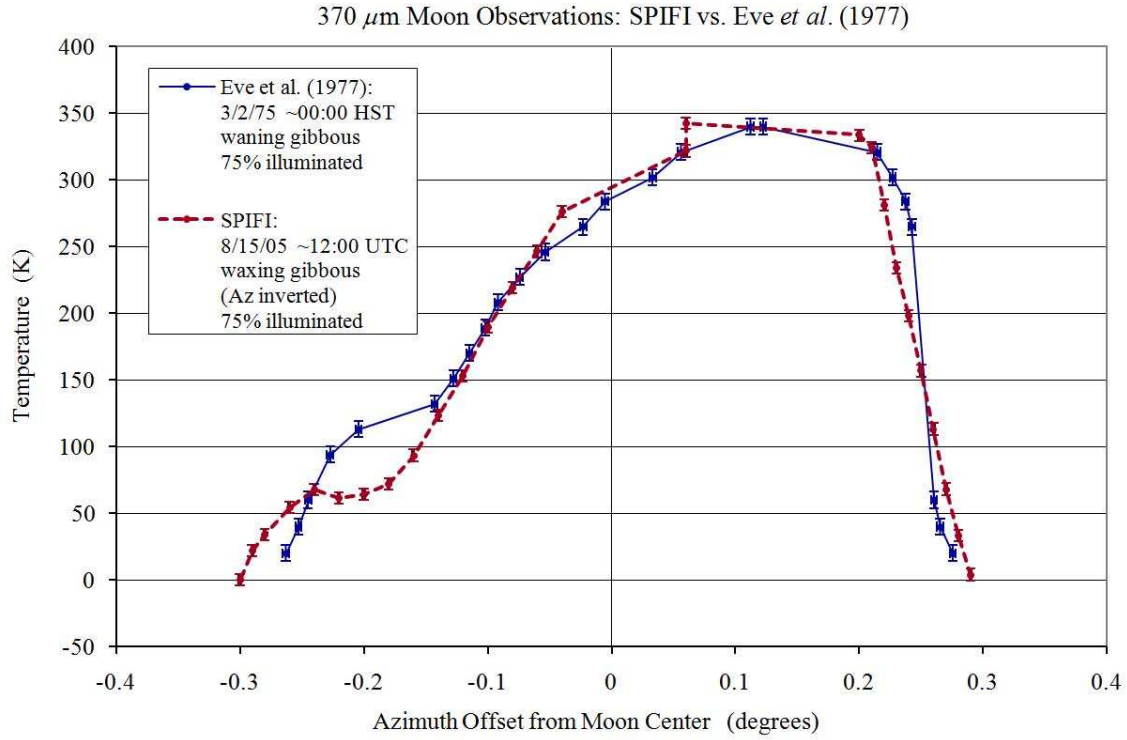

Figure 2.5: 370 μm Moon Observations: SPIFI vs. Eve *et al.* (1977)
SPIFI observations of the Moon at 370 μm are shown against those of Eve *et al.* (1977). In both cases the Moon was 75 ± 1 % illuminated, but in opposite orbital phase; the SPIFI azimuth axis has been inverted for comparison. The SPIFI temperature has been scaled and the SPIFI azimuth has been offset based on a χ^2 fit between the two data sets. 1σ $x-$ and $y-$error bars for noise fluctuations are shown for both data sets, but do not include the absolute instrument calibration uncertainties (26 % and 1′ for SPIFI temperature and pointing, respectively).

Pointing calibration was refined by observing Az and El "cuts" across the Moon at 370 μm in August 2005. Similar 370 μm measurements have been conducted by Eve *et al.* (1977). In both data sets, the Moon was 75 ± 1 % illuminated, albeit in opposite phase.[3] For comparison, both data sets are plotted in Figure 2.5 with the SPIFI azimuth axis inverted. A χ^2 fit was performed between the two data sets and used to derive a scaling factor for the SPIFI brightness temperature (vertical axis) and an offset for the SPIFI azimuth (horizontal axis).

[3]Moon almanac data service, US Naval Observatory website: http://www.usno.navy.mil/.

The scaling factor was used to improve the estimates of telluric transmission as measured by the the 860 GHz CMU/NRAO tipper on the AST/RO (§2.3.2). The azimuth offset was used to correct pointing. The higher "knee" in the waning gibbous data is due to the thermal inertia of the Moon.

The pointing model of the AST/RO as a function of Az and El is well understood and compensated for by the AST/RO control computer (Stark *et al*. 2001), and so additional pointing corrections between the location of the Moon and the Carina Nebula were assumed to be negligible. Final SPIFI pointing accuracy – given by the azimuth error of the χ^2 fit to the Moon data – was $\approx 1'$ (which is roughly the array pixel spacing).

Focusing was achieved by moving the SPIFI Dewar by small ($\sim$ 1/4 inch) increments towards the AST/RO tertiary (shortening the optical path through the elevation beam tube) while measuring the sharpness of 370 μm cuts across the limb of the Sun during the polar summer. In this method, the sharpest edge corresponds to a well-focused instrument. The SPIFI data in Figure 2.5 between $+0.2 \lesssim \mathrm{Az} \lesssim +0.3$ show the maximum sharpness of the (illuminated) limb of the Moon as measured by SPIFI, corresponding to SPIFI's best focus. (This sharpness is limited (*i.e.* smoothed) by the instrument beam size, which for SPIFI was 54″.)

2.3.2 Brightness Calibration

The *y*-axis of a raw SPIFI spectrum is measured in units of the detector lockin voltage. This voltage can be converted to the source brightness (in units of [W

m^2 sr^{-1} Hz^{-1}] or [Jy sr^{-1}]) by doing both (a) gain calibration and (b) transmission correction.

Gain

The "gain" – or volts-to-Kelvins conversion – can be determined by filling the beam at the SPIFI entrance window with submm blackbodies of known temperatures and measuring their lockin voltage signals. If a linear bolometer response is assumed, only two temperatures are needed to derive the gain:

$$g = \frac{V_2 - V_1}{T_2 - T_1} \tag{2.1}$$

where V is the voltage response of the detector and T is the temperature of the calibration blackbody that fills the SPIFI beam.

In theory, if the bolometers and amplification circuits are identical, all of the pixels in the array should have identical gains. In practice, the gains are not the same. Because the bolometers' thermistors and load resistors are nominally identical, and because the amplification circuits are similar, the different gains are most likely due to different thermal characteristics (conductances or heat capacities) of the different bolometers in the array. We suspect that the variations are due largely to broken silicon legs of some of the pixels (the breaking may have occurred during transport). Furthermore, transmission variations of the LOFPI and other filters in the image planes can cause gain variations which are unrelated to variations in detector response. To compensate for the net variations, the array is "flat-fielded," or normalized to the gain of one particular pixel.

Table 2.2: SPIFI Flat-field Matrix and Gain for 205 μm

2.287	1.106	0.967	1.811	1.832
2.411	–	1.000*	2.124	1.290
2.405	2.168	2.333	2.386	1.098
1.177	2.184	1.525	1.246	1.875
0.883	–	1.038	2.265	2.627
* ***Pixel 8 Gain***: g **= 0.171 ± 0.004 K mV**$^{-1}$				

Pixel numbers count up from left to right and top to bottom starting with pixel 1 in the top left and ending with pixel 25 in the bottom right. Raw data must be multiplied by the flat-field matrix and then (every pixel) by the pixel 8 gain to achieve flux calibration.

SPIFI brightness was calibrated against reference blackbodies of: (a) Echosorb submerged in ℓ–N_2 held in a submm-transparent container (polystyrene or polyethylene) and (b) boiling water held in a glass container. These sources were chosen for their constant liquid-gas phase transition temperatures of 77 K and 373 K, respectively, and high submm emissivities. Both signals were chopped by the SPIFI chopper and the lockin signal integrated over ~ 10 seconds at a fixed FPI plate separation. This was done twice during the 2005 winter – on August 6 and September 5 – bookending the Carina observations. At 205 μm the two data sets show good agreement: of the 23 live pixels, eight had < 5% drift, 16 had < 20 % drift, and 20 had < 25 % drift. The largest drift was 34 %. The response of pixel 8 (our best pixel) was chosen as the flatfield reference, and the scaling factors were obtained by dividing pixel 8's response by that of each pixel. The two data sets were averaged to obtain a single flatfield matrix, shown in Table 2.2, with a gain of 0.171 K mV^{-1}. Raw SPIFI data must be multiplied by both the flatfield matrix and (every pixel) by the pixel 8 gain to achieve flux calibration (see Equation 2.3).

Transmission

Because gain calibration was done with a blackbody held just outside the SPIFI entrance window, the instrument transmission (27 %; Table 1.8) is accounted for in the gain factor, g (Table 2.2). However, telescope and atmospheric transmission must be considered separately. The AST/RO aperture efficiency is known to be $\sim$ 51 % at 205 μm (A. A. Stark 2004, private communication). 860 GHz zenith opacity was measured every $\sim$ 13 min by the AST/RO's CMU/NRAO tipper (§1.1.2). The tipper output was compared to SPIFI measurements of the atmospheric temperature (skydips, Page 18) at 205 μm and the Moon temperature (Figure 2.5) at 370 μm. Although the skydips showed good agreement, matching the 370 μm Moon measurements of Eve *et al*. (1977) required a -0.202 offset to the tipper $\tau_{860\,\mathrm{GHz}}$. Incorporating this with Equations 1.1, 1.3, 1.5 and 1.6, and assuming a constant zenith angle of $z = 31^\circ$ for the Carina observations, the final l.o.s. atmospheric transmission for the 205 μm Carina Nebula observations is given by:

$$\begin{aligned} \eta_{\mathrm{tel},\,205\mu m}\,(31^\circ) &= \exp\left\{-\left(1.714\left(\tau_{860\,\mathrm{GHz}} - 0.202\right) + 0.530\right)\,A(31^\circ)\right\} + 0.0069 \\ &= \exp\left\{-\left(1.999\,\tau_{860\,\mathrm{GHz}} + 0.214\right)\right\} + 0.0069 \end{aligned} \qquad (2.2)$$

Over the entire Carina Nebula campaign (August 15 – 30, 2005), 205 μm l.o.s. transmission ranged from $\sim$ 3 – 6 %, with an average value of 4.54 ± 0.73 %.

The Kelvin units in the gain factor derived above represent the temperature of an opaque blackbody that fills the SPIFI beam. SPIFI's 54″ beam is not diffraction limited at 205 μm ($1.22\lambda/D \sim 30''$), and is therefore expected to have nearly

a top-hat profile. Thus, a blackbody that fills this beam fills the main beam of the telescope, and its measure calibrates the system in terms of "main beam (MB) brightness temperature," or $T_{\rm MB}$. The "brightness temperature" is defined as the temperature of a blackbody that would produce the same brightness as the source at the observed wavelength.

The complete main beam brightness temperature calibration equation for SPIFI, including the telescope and atmospheric transmission corrections, is given by:

$$\left(T_{\rm MB}\right)_{nm} = \left(V\right)_{nm} \left(f_\nu\right)_{nm} g_\nu \, \eta_{{\rm tel},\nu}^{-1} \left(\eta_{{\rm atm},\nu}(z)\right)^{-1} \tag{2.3}$$

where the subscripts *nm* refer to the $nm^{\rm th}$ pixel of the SPIFI array, $T_{\rm MB}$ is the main beam brightness temperature of the source in units of K, V is the lockin signal measured by the detector in units of mV, f_ν is the flat-field factor, g_ν is the gain in units of K $\rm mV^{-1}$, $\eta_{{\rm tel},\nu}$ is the telescope efficiency, and $\eta_{{\rm atm},\nu}(z)$ is the l.o.s. atmospheric transmission. For $\lambda = 205\ \mu$m, g and f are given in Table 2.2, $\eta_{\rm tel} = 0.51 \pm 0.10$, and $\eta_{\rm atm}$ can be derived from the tipper $\tau_{860\,\rm GHz}$ by Equation 2.2. Combining the errors of these factors during the Carina observations yields a total SPIFI calibration uncertainty of ± 26 %.

In the FIR and submm bands, the "brightness" (also "specific intensity"), I_ν, of the source can be related to the main beam brightness temperature through the Rayleigh-Jeans limit ($h\nu \ll k_B T$) of the Planck radiation function (*e.g.* Rybicki & Lightman 2004):

$$I_\nu = 2\left(\frac{\nu}{c}\right)^2 k_{\rm B} T_{\rm MB} = \frac{2k_{\rm B}}{\lambda^2}\, T_{\rm MB} \tag{2.4}$$

where c is the speed of light and $k_{\rm B}$ is Boltzmann's constant; I_ν is often expressed

in units of either W m^{-2} Hz^{-1} sr^{-1} or Jy sr^{-1}. Multiplying by the solid angle of the 54″ diameter SPIFI main beam (Table 1.10), Ω_{MB}, yields the specific flux, F_ν, usually expressed in units of either W m^{-2} Hz^{-1} or Jy:

$$F_\nu = I_\nu \, \Omega_{MB} \approx (5.4 \times 10^{-8} \, \mathrm{sr}) \, I_\nu \tag{2.5}$$

The (non-specific) intensity (in units of W m^{-2} sr^{-1}) and flux (in units of W m^{-2}) can be obtained by multiplying by the bandwidth, $\Delta\nu \approx c\,\Delta\lambda/\lambda^2$ (in units of Hz):

$$I = I_\nu \Delta\nu \approx I_\nu \left(\frac{c\Delta\lambda}{\lambda^2}\right) \qquad \text{and} \qquad F = F_\nu \Delta\nu \approx F_\nu \left(\frac{c\Delta\lambda}{\lambda^2}\right) \tag{2.6}$$

By combining Equations 2.4 and 2.6, and noting that the bandwidth is given in velocity units by $\Delta v \approx c\,\Delta\lambda/\lambda$ (*cf.* Equation 2.10), we find that the intensity can be expressed as:

$$I = \frac{2k_B}{\lambda^3} \left(T_{MB} \, \Delta v\right) \tag{2.7}$$

If T_{MB} is the main beam brightness temperature measured in a given spectral bin (*i.e.* at a given etalon spacing), and the bandwidth used in Equations 2.6 and 2.7 represents the width of the spectral bin in which T_{MB} was measured, then Equation 2.7 gives the intensity per spectral bin, and must be integrated over all the bins in the spectrum to obtain the total (integrated) intensity.

If T_{MB} is instead taken as the height of a spectral line, and Δv is taken as the FWHM of the line, then Equation 2.7 must be altered to include an extra factor of $\pi/2$:

$$I = \frac{2k_B}{\lambda^3} \left(\frac{\pi}{2} \, T_{MB} \, \Delta v\right) \tag{2.8}$$

This factor arises from the integrated intensity of the FPI's Lorentzian profile, $\frac{\pi}{2} L_0 \Gamma$, with $L_0 = T_{\rm MB}$ and $\Gamma = \Delta v$ (*cf.* Equation 2.12). In this case Equation 2.8 gives the total line intensity, and does not need to be integrated. Equation 2.8 is the conversion used in the present work to calculate the intensity values reported in Tables 2.4 and 2.5 (and in the contour map of Figure 2.7) from the Lorentzian fits to SPIFI spectra (§2.4.1 and Figure 2.6).

2.3.3 Wavelength Calibration

The *x*-axis of a raw SPIFI spectrum is measured in units of HOFPI stepper motor counts. Counts can be converted to optical wavelengths (λ), by measuring the centroids of calibration lines of well-known wavelengths. At the AST/RO, the strong stable laser lines of TREND and PoleSTAR – which were used to characterize the HOFPI and LOFPI finesses and orders (see Page 34 above) – were ideal wavelength calibration sources. Because the cryogenic motor steps are linear, only two calibration lines were needed to derive the wavelength scaling factor, s (*cf.* Equation 2.1):

$$s = \frac{\lambda_2 - \lambda_1}{Count_2 - Count_1} \tag{2.9}$$

Because all of SPIFI's pixels share the same FPIs, the (multiplicative) wavelength scaling factor, s, is uniform over the array. However, array pixels can have varying (additive) wavelength offsets. It is a fundamental property of FPIs in the pupil plane of an optical system that there be a wavelength shift across the array for pixels that are not on the optical axis. This is because, for a given plate spacing, rays passing through the etalon off-axis see shorter resonant wavelengths than those passing through the etalon along the optical

axis. This blueshift is proportional to the square of the angle off the optical axis ($\Delta\lambda = -\lambda_0\,\theta^2/2$). For SPIFI, off-axis rays enter the HOFPI at a maximum angle of $\sim$ 0.7°, corresponding to $\Delta\lambda \sim -0.0153$ μm, or $\sim$ -9 stepper motor counts. Therefore, the wavelength scale of the outermost pixels will tend to be labeled +9 counts too *red*. The correction offset would then be -9 counts (to the *blue*). (This is roughly in agreement with the average measured correction offset for the array's outer pixels as shown in Table 2.3). Additional (noise) wavelength shifts may be present if the plates are not perfectly flat or parallel.

To correct for these varying wavelength shifts, the array is "flat-wavelengthed," or zeroed to the offset of one particular pixel. To derive the "flat-wavelength" matrix, the 205.4229 μm CD_3OH line of the TREND laser was measured and fit to Lorentzian functions using χ^2 methods (see Figures 1.9 and 1.10). The offset of pixel 8 was chosen as the "flat-wavelength" reference, and the line centroids from the χ^2 fit were used to construct the matrix, shown in Table 2.3 (*cf*. Table 2.2, noting that Table 2.2 is multiplicative while Table 2.3 is additive). Raw data must be added to both the "flat-wavelength" matrix and (every pixel) to the pixel 8 offset to achieve wavelength calibration (see Equation 2.11).

For a given line, converting the spectral wavelength into the Doppler velocity shift gives a direct measurement of the source velocity:

$$\Delta v \approx c\Delta\lambda/\lambda_0 \tag{2.10}$$

where Δv is the Doppler velocity of the source, c is the speed of light, λ_0 is the rest wavelength of the line, and $\Delta\lambda$ is the difference between the measured and rest wavelengths. In terms of the Doppler velocity, the HOFPI spectral resolution

Table 2.3: SPIFI "Flat-wavelength" Matrix and Offset for 205 μm

-13	-7	-17	-20	-23
-4	–	0*	5	-18
-3	2	0	1	-12
-12	-4	-2	0	-12
-13	–	0	-6	-20
* ***Pixel 8 Offset*:** **Λ = -26975 ± 1 counts**				

This table shows SPIFI wavelength calibration offsets as derived from TREND laser observations (see Figures 1.9 and 1.10). The offset units are in HOFPI counts. SPIFI's resolution element was 28 counts, or 71.6 km s^{-1}. Pixel numbers increase from left to right and top to bottom starting with pixel 1 in the top left and ending with pixel 25 in the bottom right. Raw data must be added to both the flat-wavelength matrix and (every pixel) to the pixel 8 offset to achieve wavelength calibration.

element (which spans 28 stepper motor counts) is ~ 71.6 km s^{-1}, as derived from Equations 1.10 and 2.10 and Table 1.7.

In the current calibration discussion, $\Delta\lambda = s$ is the wavelength change corresponding to a plate separation change of 1 count, so the scaling factor (Equation 2.9) for Doppler velocities becomes $s' = cs/\lambda_0$. If the antenna velocity[4] is then removed, one can obtain the source velocity:

$$\left(v_{LSR}\right)_{mn} = \frac{cs}{\lambda_0}\left[\left(C_0\right)_{mn} + \left(F\right)_{mn} + \Lambda\right] + v_{antenna} \tag{2.11}$$

where the subscripts nm refer to the nm^{th} pixel of the SPIFI array, v_{LSR} is the Doppler velocity of the source relative to the LSR in units of km s^{-1}, c is the speed of light in km s^{-1}, λ_0 is the transition (rest) wavelength of the target line in μm, s is the wavelength scaling factor in μm counts^{-1}, C_0 is the observed line cen-

[4]The antenna velocity is the velocity of the AST/RO relative to the Local Standard of Rest (LSR).

troid in counts, F is the "flat-wavelength" offset in counts, Λ is the wavelength offset in counts, and $v_{antenna}$ is the LSR antenna velocity in km s^{-1}.

For SPIFI 205 μm Carina Nebula observations, cs/λ_0 = 2.5560 ± 0.0211 km s^{-1} $counts^{-1}$, F and Λ are given by Table 2.3, and $v_{antenna}$ averaged 23.47 ± 0.01 km s^{-1}. Combining the errors of these quantities gives a total velocity error of ± ~ 2.7 km s^{-1}. However, there is likely also a systematic blueshift error due to imperfect wavelength calibration: because the laser lines used for calibration were poorly collimated, they would have tended to be labeled too *red* (see discussion on Page 100 above); a (collimated) astrophysical line would thus appear too *blue*. Comparison of the centroids of SPIFI's 205 μm lines in the Carina Nebula with previous radio recombination line observations there indicates that this blueshift error may be ~ -7.5 km s^{-1} (see §2.6.6).

2.3.4 ISO Calibration

LWS data were run through the standard ISO Off-Line Processing version 11.1 (OLP v11.1) pipeline. The reduction steps in the OLP include first-level deglitching, responsivity drift and absolute response correction, dark current subtraction, and wavelength and flux calibration. Full details of the ISO LWS performance and calibration can be found in Swinyard *et al*. (1998) and Gry *et al*. (2003). The data were further processed with the LWS L01 pipeline to produce "highly-processed data products" (HPDP; Lloyd *et al*. 2003). The purpose of the L01 pipeline was to provide a uniform post-OLP pipeline for de-glitching, de-fringing, correction for NIR-leak and SW1 double-peaked features, and scan averaging. Finally, the author performed his own data reduction to remove

(rare) remaining glitches, and to fit baselines and Gaussian profiles to detected spectral lines (§2.4.1).

The OLP pipeline automatically corrects for diffraction losses from on-axis point sources. These losses do not occur for extended sources, resulting in a flux overestimation. Conversion factors have been derived with the assumption of an infinitely extended and homogeneously distributed source at the key wavelength of each LWS detector (Salama 2000), and we apply these extended source correction factors (found in Gry *et al*. 2003) to the Carina data presented here.

For cross-calibration purposes, the LWS observed several positions in Tr 14 and 16 and the Galactic Center and compared them with IRAS 100 μm fluxes at the same positions. The absolute flux calibration uncertainty in the IRAS 100 μm band has been reported as 10 % (Beichman *et al*. 2002). Both sources contain large areas of extended emission, which, although relatively smooth within the ISO and IRAS beams, varies by a factor of $\sim$ 40 over the fields. A mean ratio of the fluxes from the two instruments was found to be a very satisfying (LWS/IRAS) $\sim 1.0 \pm 0.1$. It is likely that some of the uncertainty is due to unresolved structure within the beams.

Estimates of the final LWS absolute flux calibration uncertainty (including the pipelines, extended source correction, and Gaussian profile fitting) range from 10 % (Peeters *et al*. 2002) to 30 % (Mizutani *et al*. 2002 and 2004). Thus, in the present work, we adopt a value of $\sim$ 20 %. Wavelength calibration was measured to have an accuracy better than 1/4 resolution element (0.07 μm for SW detectors and 0.15 μm for LW detectors; Gry *et al*. 2003). The pointing accuracy of the ISO at the time of the Carina observations was $< 2''$ (Kessler 2003).

2.4 Data Reduction

2.4.1 Markov Chain Monte Carlo Fitting

SPIFI spectra were deglitched (at a 3σ level relative to adjacent spectral bins) and averaged (weighted by noise) to obtain a final spectrum in each of SPIFI's 236 raster positions. Spectra showing the 205 μm [NII] line were fit to the Lorentzian FPI profile and a linear baseline:

$$L(\lambda) = L_0 \left[1 + \frac{(\lambda - \lambda_0)}{\Gamma/2}\right]^{-1} + y\,\lambda + b \tag{2.12}$$

where L_0 is the line peak (in units of the main beam brightness temperature, K; §2.3.2), λ_0 is the line centroid (in μm, later converted to LSR Doppler velocities in km s^{-1}; §2.3.3), Γ is the line FWHM (μm or km s^{-1}), and y and b are the linear baseline slope and offset, respectively.

The best fit was found using a χ^2 Markov Chain Monte Carlo (MCMC) routine developed by the author following the Metropolis-Hastings algorithm (*e.g.* Gregory 2005). The MCMC is surprisingly simple but extremely powerful. It starts with a random walk through the five-dimensional parameter space $(L_0, \lambda_0, \Gamma, y, b)$, at each step calculating the χ^2 fit between the data and Equation 2.12. The step direction is completely random, but the choice of the step size in each direction is weighted by the error distribution of the parameter corresponding to that dimension – so that the step size in, say, the Γ-dimension, will have length $\leq \sigma_\Gamma$ approximately 68 % of the time (assuming a normal error distribution).[5]

[5] Note that this requires the user to provide estimates for the errors of each parameter as inputs. However, the accuracy of the fit is not affected by these values, only the efficiency,

After each step, the MCMC has the option to accept or reject the new position. The criterion for acceptance is $\chi^2_n/\chi^2_{(n+1)'} \geq r$, where left-hand-side is the ratio of reduced χ^2's of Markov Chain steps n and n+1 (the prime indicates that the n+1 position has not yet been accepted into the chain), and on the right-hand-side r is a random number between 0 and 1. As a result, positions with better fits are always accepted, but positions with worse fits are not necessarily rejected (the probability of rejection is proportional to the ratio of χ^2 values). Thus, the program never converges, yet spends the majority of its time sampling the areas of parameter space most likely to provide good fits. The best fit is taken as the step in the (accepted) Markov Chain with the lowest χ^2.

In an MCMC, every real number in the parameter space has a non-zero chance of being sampled at any time while the program is running. This offers two distinct advantages over other fitting methods: (1) the solution will not be quantized, as in grid-search methods which have fixed resolutions in the parameter space; and (2) it is impossible for the fit to ever get stuck in a local χ^2 minima, as nested one-dimensional searches often do. These attributes were found to be especially advantageous for fitting high-noise spectra, which often have numerous closely-spaced local minima and cannot easily be fit with traditional routines without severely restricting the parameter space or fixing some of the parameters outright.

ISO LWS spectra were fit in a similar manner to the SPIFI data, except that, because it was a grating, a Gaussian profile was used:

---

so approximations are okay. Because the MCMC assembles the real error distributions as a by-product, if one finds the fit converging too slowly, the program can be stopped after a reasonable number of iterations and restarted using updated error estimates from the aborted fit.

$$G(\lambda) = G_0 \exp\left\{\frac{-(\lambda - \lambda_0)^2}{\left(\Gamma/\sqrt{4\ln 2}\right)^2}\right\} + y\,\lambda + b \tag{2.13}$$

Here the parameters are the same as above, with G_0 replacing L_0 as the peak temperature of the line.

2.4.2 Contour Maps

To study the morphology of the region, the detected line intensities were plotted as contour maps over the nebula. Because both the SPIFI and ISO rasters were spatially under-sampled, intensities between raster beams were interpolated by averaging the intensities from surrounding observed positions weighted by both their noise and beam profiles. The final map for each species was convolved with a two-dimensional Gaussian filter matching the instrument beam size to smooth ersatz features with size scales smaller than the beam size (see Table 2.1 for a list of beam sizes used in these observations). The interpolation and smoothing have attenuated the maxima of the maps. The peak attenuation varies by map but is expected to be $\sim$ 20 % based on the theoretical convolution of two 2D Gaussians. Overall, the maps offer a good representation of the morphology of the region and are used to study the structure of the nebula. For quantitative comparisons and calculations, the original intensity values should be used (Tables 2.4, 2.5 and 2.6).

2.5 Results

2.5.1 SPIFI 205 μm [NII] Map

Fine-structure 205 μm [NII] emission was detected over > 40 % of the regions of the Carina Nebula mapped by SPIFI (Figure 2.3). Line intensities derived from Lorentzian fits (§2.4.1) to the data are listed in Tables 2.4 and 2.5. Statistical noise values (1σ) are also listed, but do not include the absolute instrument calibration uncertainty of ~ 26 % (§2.3.2). The cutoff for detection was set at SNR ~ 3. Of the 236 spectra, three exceptions to this cutoff were permitted: Car I position 38 (Car I-38) and Car II-32, both with SNR = 2.9, and Car II-5, with SNR = 2.3. The average SNR for the detected positions is ~ 5. At positions falling below the SNR cutoff, upper limits to intensity are estimated from the product of the noise and the HOFPI spectral width (71 km s^{-1}; §2.3.3). Sample spectra are shown in Figure 2.6, and a contour map (§2.4.2) of the complete data is plotted in Figure 2.7.

These data, along with our discovery paper (Oberst *et al*. 2006), constitute the first published detection of the 205 μm [NII] line from a ground-based instrument, and only the third detection overall after those of COBE and KAO collected between 1989 and 1992 (§2.1.2). COBE's all-sky map in 205 μm [NII] used a very broad (7°) beam, and hence only probes the WIM on galactic scales (Wright *et al*. 1991; Bennet *et al*. 1994; Fixen *et al*. 1999). Pioneering efforts by the KAO team resulted in the first detection of 205 μm [NII] in discrete HII regions – however, these spectra are few and do not map the detailed spatial structure of [NII] emission within these sources (Colgan *et al*. 1993; Petuchowski *et al*. 1994; Petuchowski *et al*. 1996; Simpson *et al*. 1997; Simpson *et al*. 2004). The present

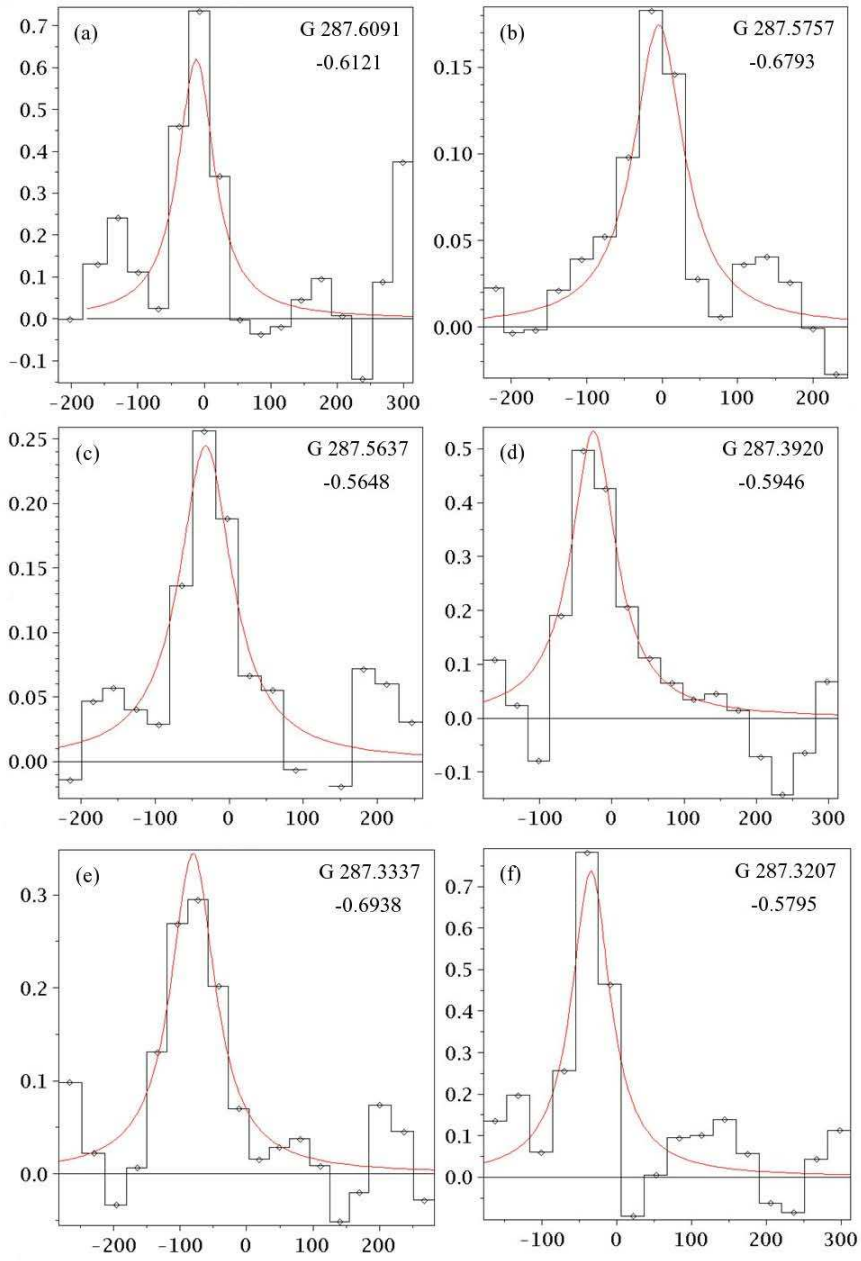

Figure 2.6: Select Detections of the 205 μm [NII] Spectral Line

Spectra in the vicinity of Car II are shown in panels (a), (b), and (c) (SPIFI Car II raster positions 32, 37, and 61, respectively), and spectra in the vicinity of Car I are shown in panels (d), (e), and (f) (SPIFI Car I raster positions 29, 45, and 73, respectively). The *x*-axes give the source velocity relative to the Local Standard of Rest (LRS) in units of [km s^{-1}], and the *y*-axes give the main beam brightness temperature in units of [K]. (The conversion between these units and those of Tables 2.4 and 2.5 is given by Equation 2.8). The (black) data points and bars mark the processed data, and the (red) smooth lines are the least χ^2 Lorentzian fits. The data have been smoothed with a Hann window.

data comprise the first extended, medium resolution (~ 1′) map of 205 μm [NII] over an HII region, offering a unique opportunity to compare the 205 μm emission to the 122 μm [NII] line and other tracers of the WIM in Carina and other similar regions (see Discussion in §2.6).

Table 2.4: SPIFI 205 μm [NII] Observations of Car I

Raster Point [a]	Galactic Coordinates [a] [deg]		Line Intensity [b] [10^{-8} W m^{-2} sr^{-1}]	
I.D.	l	b	I	(σ_I)
1	287.3973	-0.7445	18.0	(5.8)
2	287.4010	-0.7267	< 4.4	
3	287.4048	-0.7089	< 9.4	
4	287.4086	-0.6911	< 3.8	
5	287.4123	-0.6734	< 2.5	
6	287.4161	-0.6556	< 12.8	
7	287.4199	-0.6378	< 8.5	
8	287.4237	-0.6200	25.5	(4.3)
9	287.4276	-0.6022	< 5.9	
10	287.3795	-0.7407	< 4.5	
11	287.3832	-0.7229	–	
12	287.3870	-0.7051	< 2.9	
13	287.3908	-0.6873	16.4	(5.4)
14	287.3946	-0.6696	< 4.5	
15	287.3983	-0.6518	–	
16	287.4021	-0.6340	< 6.3	
17	287.4060	-0.6162	< 14.3	
18	287.4098	-0.5984	–	
19	287.3543	-0.7725	< 8.3	
20	287.3580	-0.7547	< 1.5	
21	287.3617	-0.7369	8.6	(1.7)
22	287.3655	-0.7191	12.8	(4.1)
23	287.3692	-0.7014	< 8.8	
24	287.3730	-0.6836	29.3	(4.1)
25	287.3768	-0.6658	16.7	(3.1)
26	287.3806	-0.6480	33.1	(6.9)
27	287.3844	-0.6302	51.7	(11.0)
28	287.3882	-0.6124	42.8	(9.1)
29	287.3920	-0.5946	23.1	(3.2)
30	287.3365	-0.7687	< 7.2	
31	287.3402	-0.7509	< 10.3	
32	287.3440	-0.7332	< 3.5	
33	287.3477	-0.7154	< 7.6	
34	287.3514	-0.6976	32.9	(3.9)
35	287.3552	-0.6798	10.8	(1.9)

Table 2.4 Continued

I.D.	l	b	I	(σ_I)
36	287.3590	-0.6620	31.8	(5.8)
37	287.3628	-0.6442	30.5	(7.5)
38	287.3665	-0.6264	25.3	(8.6)
39	287.3704	-0.6086	13.9	(4.3)
40	287.3742	-0.5908	$<$ 7.7	
41	287.3187	-0.7650	17.2	(4.0)
42	287.3224	-0.7472	25.7	(7.2)
43	287.3262	-0.7294	$<$ 2.9	
44	287.3299	-0.7116	26.0	(3.0)
45	287.3337	-0.6938	14.2	(1.9)
46	287.3374	-0.6760	21.4	(2.2)
47	287.3412	-0.6582	26.8	(5.2)
48	287.3450	-0.6404	$<$ 1.8	
49	287.3487	-0.6226	20.2	(6.7)
50	287.3525	-0.6048	23.7	(5.4)
51	287.3564	-0.5870	$<$ 5.5	
52	287.3009	-0.7612	13.0	(2.4)
53	287.3047	-0.7434	12.8	(3.6)
54	287.3084	-0.7257	23.2	(6.0)
55	287.3121	-0.7079	$<$ 1.5	
56	287.3159	-0.6901	34.7	(6.0)
57	287.3196	-0.6723	6.7	(1.5)
58	287.3234	-0.6545	$<$ 2.1	
59	287.3271	-0.6367	$<$ 2.3	
60	287.3309	-0.6189	31.7	(4.4)
61	287.3347	-0.6011	$<$ 3.4	
62	287.3385	-0.5833	–	
63	287.2832	-0.7575	3.5	(1.0)
64	287.2869	-0.7397	23.4	(5.6)
65	287.2906	-0.7219	$<$ 8.5	
66	287.2943	-0.7041	$<$ 1.5	
67	287.2981	-0.6863	$<$ 1.9	
68	287.3018	-0.6685	6.6	(1.1)
69	287.3056	-0.6507	19.7	(4.2)
70	287.3093	-0.6329	7.1	(2.0)
71	287.3131	-0.6151	11.0	(3.2)
72	287.3169	-0.5973	$<$ 2.5	
73	287.3207	-0.5795	24.6	(7.3)
74	287.2654	-0.7538	14.2	(3.5)
75	287.2691	-0.7360	15.4	(4.1)
76	287.2728	-0.7182	$<$ 2.7	
77	287.2765	-0.7004	$<$ 3.2	
78	287.2802	-0.6826	$<$ 2.1	
79	287.2840	-0.6648	11.4	(2.6)
80	287.2878	-0.6470	$<$ 3.8	
81	287.2915	-0.6292	$<$ 2.6	
82	287.2953	-0.6113	15.1	(2.8)
83	287.2991	-0.5935	$<$ 13.1	

Table 2.4 Continued

I.D.	l	b	I	(σ_I)
84	287.3029	-0.5757	< 14.0	
85	287.2476	-0.7501	< 8.9	
86	287.2513	-0.7323	< 13.1	
87	287.2550	-0.7145	10.0	(1.7)
88	287.2587	-0.6967	< 3.3	
89	287.2624	-0.6788	40.9	(8.0)
90	287.2662	-0.6610	< 2.9	
91	287.2699	-0.6432	25.2	(7.4)
92	287.2737	-0.6254	26.2	(5.9)
93	287.2775	-0.6076	8.8	(1.8)
94	287.2813	-0.5898	< 4.8	
95	287.2851	-0.5720	< 4.9	
96	287.2889	-0.5542	< 2.6	
97	287.2927	-0.5363	< 12.2	
98	287.2298	-0.7464	< 5.6	
99	287.2335	-0.7286	< 14.0	
100	287.2372	-0.7108	< 9.5	
101	287.2409	-0.6929	< 6.1	
102	287.2446	-0.6751	< 13.2	
103	287.2484	-0.6573	< 19.1	
104	287.2521	-0.6395	< 9.2	
105	287.2559	-0.6217	< 13.8	
106	287.2596	-0.6039	38.1	(11.0)
107	287.2634	-0.5861	< 15.2	
108	287.2672	-0.5682	< 5.2	
109	287.2710	-0.5504	< 13.5	
110	287.2748	-0.5326	–	
111	287.2268	-0.6714	18.4	(4.1)
112	287.2305	-0.6536	< 2.8	
113	287.2343	-0.6358	< 6.7	
114	287.2380	-0.6180	< 8.3	
115	287.2418	-0.6002	< 3.1	
116	287.2456	-0.5823	13.6	(3.8)
117	287.2494	-0.5645	< 13.9	
118	287.2532	-0.5467	< 4.1	
119	287.2570	-0.5289	18.1	(3.7)
120	287.2090	-0.6677	14.6	(3.4)
121	287.2127	-0.6499	< 8.7	
122	287.2164	-0.6321	< 7.6	
123	287.2202	-0.6143	< 12.1	
124	287.2240	-0.5964	< 7.2	
125	287.2277	-0.5786	< 10.4	
126	287.2315	-0.5608	45.5	(10.8)
127	287.2353	-0.5430	< 4.5	
128	287.2391	-0.5252	< 14.1	
129	287.1911	-0.6640	13.3	(3.1)
130	287.1949	-0.6462	< 5.6	
131	287.1986	-0.6284	< 4.7	

Table 2.4 Continued

I.D.	l	b	I	(σ_I)
132	287.2023	-0.6106	< 10.7	
133	287.2061	-0.5927	< 9.8	
134	287.2099	-0.5749	< 5.9	
135	287.2136	-0.5571	< 6.6	
136	287.2174	-0.5393	< 8.1	
137	287.2212	-0.5214	< 9.3	

[a] Coordinates refer to the center positions of the SPIFI 54″ beam, as shown in the raster map in Figure 2.3. [b] For spectra with χ^2 fits of SNR $\lesssim$ 3, theoretical upper limits to intensity are given, as indicated by the "<" signs (see text for more details). Intensity errors (σ_I) do not include the SPIFI absolute calibration error of 26 %. In a few rare cases, no intensity (or upper limit) is reported, indicating that only the non-functional SPIFI array pixels (7 or 22) were pointed at that raster position.

Table 2.5: SPIFI 205 μm [NII] Observations of Car II

Raster Point [a]	Galactic Coordinates [a] [deg]		Line Intensity [b] [10^{-8} W m^{-2} sr^{-1}]	
I.D.	l	b	I	(σ_I)
1	287.6467	-0.6950	< 12.9	
2	287.6506	-0.6772	< 9.4	
3	287.6545	-0.6595	< 5.9	
4	287.6584	-0.6417	< 6.5	
5	287.6623	-0.6240	12.9	(5.6)
6	287.6663	-0.6062	14.9	(3.4)
7	287.6702	-0.5885	12.4	(3.3)
8	287.6742	-0.5707	< 9.1	
9	287.6782	-0.5530	< 5.5	
10	287.6289	-0.6910	11.3	(3.7)
11	287.6328	-0.6733	–	
12	287.6367	-0.6555	13.5	(2.8)
13	287.6407	-0.6378	< 7.8	
14	287.6446	-0.6200	14.0	(4.1)
15	287.6485	-0.6023	< 10.9	
16	287.6525	-0.5845	20.7	(5.9)
17	287.6564	-0.5668	< 6.4	
18	287.6604	-0.5490	–	
19	287.6112	-0.6871	< 6.4	
20	287.6151	-0.6693	7.8	(2.6)
21	287.6190	-0.6516	< 4.1	
22	287.6229	-0.6338	14.5	(3.4)

Table 2.5 Continued

I.D.	l	b	I	(σ_I)
23	287.6268	-0.6161	6.7	(1.7)
24	287.6308	-0.5983	20.1	(6.0)
25	287.6347	-0.5806	< 3.8	
26	287.6386	-0.5629	< 3.9	
27	287.6426	-0.5450	< 4.0	
28	287.5935	-0.6832	17.1	(3.6)
29	287.5973	-0.6654	< 12.3	
30	287.6012	-0.6477	11.4	(2.8)
31	287.6052	-0.6299	< 2.6	
32	287.6091	-0.6121	22.2	(7.7)
33	287.6130	-0.5944	< 2.5	
34	287.6170	-0.5766	10.1	(3.1)
35	287.6208	-0.5590	< 6.4	
36	287.6248	-0.5411	< 11.2	
37	287.5757	-0.6793	7.3	(1.1)
38	287.5796	-0.6615	10.9	(2.1)
39	287.5835	-0.6438	8.9	(1.5)
40	287.5874	-0.6260	6.8	(0.8)
41	287.5913	-0.6082	15.3	(2.2)
42	287.5953	-0.5904	13.8	(1.9)
43	287.5992	-0.5727	< 3.5	
44	287.6030	-0.5551	< 3.1	
45	287.6070	-0.5372	10.0	(2.7)
46	287.5580	-0.6754	7.0	(1.5)
47	287.5618	-0.6576	< 6.1	
48	287.5657	-0.6398	16.5	(2.1)
49	287.5696	-0.6221	10.4	(2.1)
50	287.5736	-0.6042	24.4	(4.2)
51	287.5775	-0.5865	13.4	(3.3)
52	287.5814	-0.5688	12.3	(2.4)
53	287.5852	-0.5512	14.2	(3.5)
54	287.5892	-0.5332	< 8.6	
55	287.5402	-0.6715	17.0	(2.6)
56	287.5441	-0.6537	11.9	(3.1)
57	287.5480	-0.6360	27.3	(4.0)
58	287.5519	-0.6182	27.4	(3.3)
59	287.5558	-0.6003	25.0	(4.6)
60	287.5598	-0.5825	12.1	(1.9)
61	287.5637	-0.5648	26.7	(4.7)
62	287.5674	-0.5473	< 4.1	
63	287.5714	-0.5293	< 3.0	
64	287.5224	-0.6676	< 4.2	
65	287.5263	-0.6498	< 5.4	
66	287.5302	-0.6321	16.9	(3.3)
67	287.5341	-0.6143	< 2.5	
68	287.5381	-0.5963	< 2.7	
69	287.5420	-0.5786	16.2	(1.8)
70	287.5459	-0.5609	< 6.0	

Table 2.5 Continued

I.D.	l	b	I	(σ_I)
71	287.5496	-0.5434	< 5.2	
72	287.5536	-0.5254	< 7.2	
73	287.5046	-0.6637	8.4	(2.8)
74	287.5085	-0.6460	17.6	(2.3)
75	287.5124	-0.6282	8.5	(1.9)
76	287.5164	-0.6104	< 1.5	
77	287.5203	-0.5924	7.4	(1.8)
78	287.5243	-0.5746	6.9	(1.4)
79	287.5282	-0.5569	< 4.0	
80	287.5318	-0.5395	< 3.9	
81	287.5358	-0.5215	< 3.2	
82	287.4869	-0.6599	< 3.2	
83	287.4907	-0.6421	< 17.0	
84	287.4946	-0.6243	< 4.5	
85	287.4986	-0.6065	< 5.0	
86	287.5026	-0.5884	19.3	(3.7)
87	287.5065	-0.5707	< 6.1	
88	287.5104	-0.5530	< 5.5	
89	287.5140	-0.5356	< 2.3	
90	287.5180	-0.5176	< 14.7	
91	287.4691	-0.6560	< 7.4	
92	287.4729	-0.6382	< 5.1	
93	287.4768	-0.6205	15.0	(3.8)
94	287.4809	-0.6026	< 2.5	
95	287.4848	-0.5845	< 4.0	
96	287.4888	-0.5667	< 3.7	
97	287.4926	-0.5491	< 4.4	
98	287.4962	-0.5317	< 5.5	
99	287.5002	-0.5138	< 10.6	

[a] Coordinates refer to the center positions of the SPIFI 54″ beam, as shown in the raster map in Figure 2.3. [b] For spectra with χ^2 fits of SNR $\lesssim$ 3, theoretical upper limits to intensity are given, as indicated by the "<" signs (see text for more details). Intensity errors (σ_I) do not include the SPIFI absolute calibration error of 26 %. In a few rare cases, no intensity (or upper limit) is reported, indicating that only the non-functional SPIFI array pixels (7 or 22) were pointed at that raster position.

Figure 2.7 *(following page)*: SPIFI 205 μm [NII] Map of the Carina Nebula

205 μm [NII] line emission in the Carina Nebula, observed by SPIFI from the AST/RO in August 2005. The inverted grayscale bar measures intensity in units of $[10^{-8}\,\mathrm{W\,m^{-2}\,sr^{-1}}]$. Contours are shown every 1σ starting at the 2σ level, where $\sigma = 3.8{\times}10^{-8}\,\mathrm{W\,m^{-2}\,sr^{-1}}$ is the average intensity error over the map. The map has been re-sampled and smoothed with a Gaussian filter of FWHM = 54″, matching the SPIFI beam. Smoothing has attenuated the maxima; the original data are listed in Tables 2.4 and 2.5.

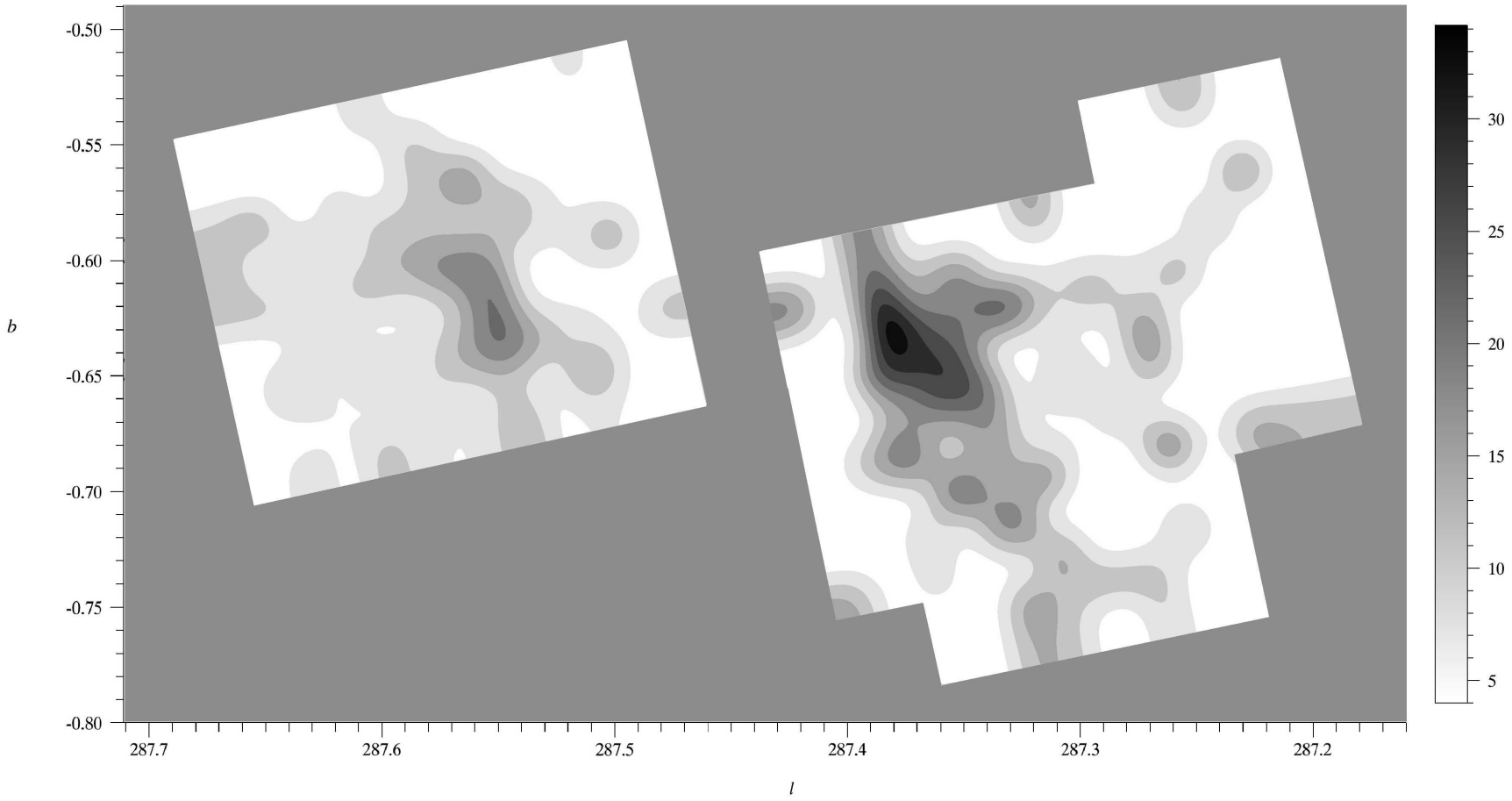
-0.50
-0.55
-0.60
-0.65
-0.70
-0.75
-0.80
b
287.7
287.6
287.5
287.4
287.3
287.2
l
30
25
20
15
10
5

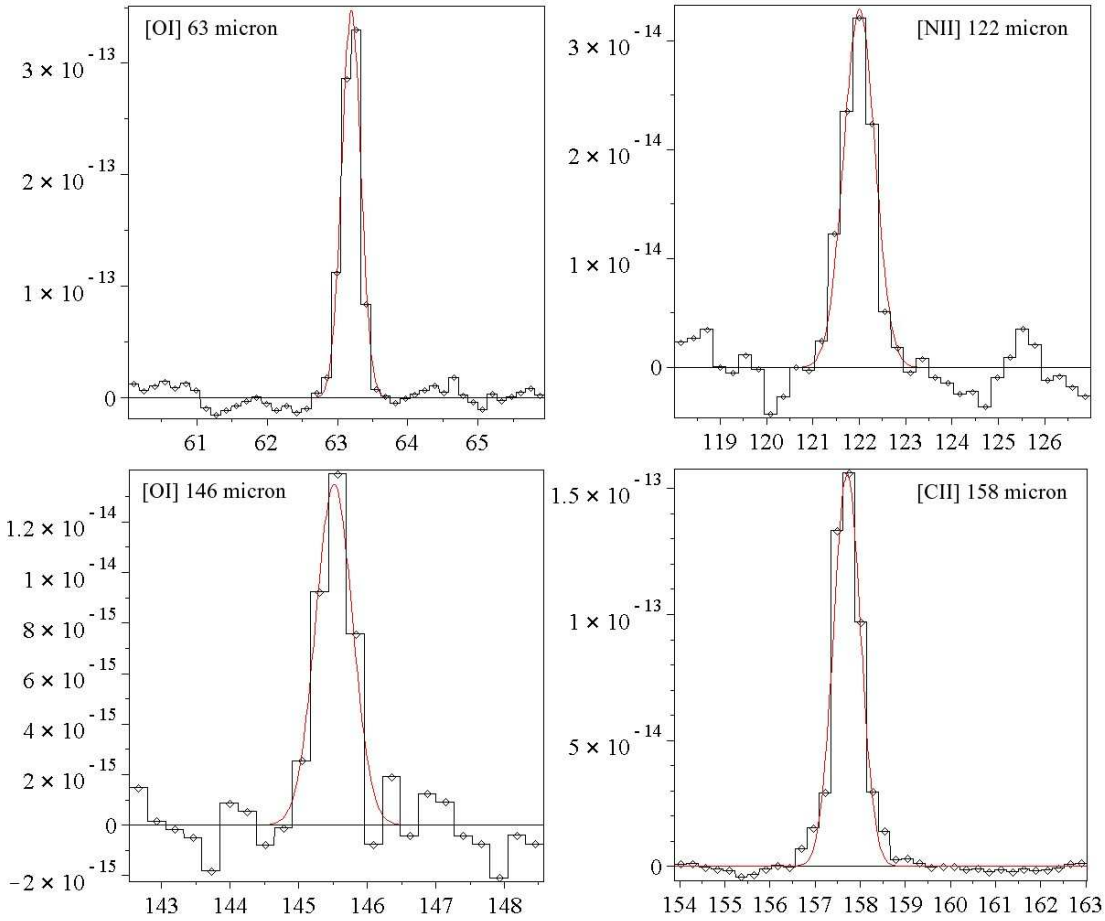

Figure 2.8: Select Detections of ISO Spectral Lines in the Carina Nebula

Detections of the [OI] 63 μm (top left), [NII] 122 μm (top right), [OI] 146 μm (bottom left), and [CII] 158 μm (bottom right) spectral lines in the Carina Nebula by the ISO LWS. All four spectra were taken at the Car 4-19 raster position (G287.405-0.637), which lies between the Car I peak and Tr 14. The *x*-axes give the wavelength in units of μm, and the *y*-axes give the specific flux in units of W m^{-2} μm^{-1}. The (black) data points and bars mark the processed data, the (red) smooth lines are the least χ^2 Gaussian fits.

2.5.2 ISO Maps

Fine-structure emission lines of 63 μm [OI], 122 μm [NII], 146 μm [OI], and 158 μm [CII] were detected by the LWS at every position in the ISO Carina raster (Figure 2.3). Intensities derived from Gaussian fits to the spectra (§2.4.1) are

reported in Table 2.6. The table includes statistical (1σ) errors for each measurement – these errors represent fluctuations from the fit, and do not include the absolute instrument calibration uncertainty of ~ 20 % (§2.3.4). Sample spectra of each species are shown in Figure 2.8.

We found the 158 μm [CII] intensities to be consistently ~ 35 % higher and the 122 μm [NII] intensities to be consistently ~ 25 % lower than those found by Mizutani *et al*. (2002, 2004) for the same raw data sets, while the 63 μm [OI] intensities were more or less the same. More significantly, we found good detections of 146 μm [OI] at all of the 100 raster positions observed by ISO, with an average SNR ratio of ~ 8.4 over the entire map. Previously, detections were reported at only 10 of the positions, with marginal SNRs ~ 2.5 – 3. We believe these differences can be attributed to improvements in the OLP pipeline and the improvement and formalization of post-OLP processing (the L01 HPDP; §2.3.4), as well as advantages of the author's Markov Chain Monte Carlo algorithm for fitting low-signal spectra (§2.4.1). The average SNRs of our fits to the other lines were: SNR ~ 40 for the 63 μm [OI] line, SNR ~ 21 for the 122 μm [NII] line, and SNR ~ 71 for the 158 μm [CII] line.

From these data we have created contour maps (§2.4.2) over the Carina region for the emission intensity of each of the four spectral species (Figures 2.9 – 2.12). The dimensions of the axes match those of Figure 2.1, with areas outside of the ISO raster (indicated by the solid line) grayed-out.

Table 2.6: ISO Observations of the Carina Nebula

Raster Point [a]		Galactic Coordinates [a]		Line Intensities [10^{-8} W m^{-2} sr^{-1}] [b]							
		[deg]		[OI] 63 μm		[NII] 122 μm		[OI] 146 μm		[CII] 158 μm	
I.D.		l	b	I	(σ_I)	I	(σ_I)	I	(σ_I)	I	(σ_I)
Car 1	1	287.006	-0.587	10.1	(0.2)	1.4	(0.2)	1.0	(0.1)	26.0	(0.3)
Car 1	2	287.056	-0.587	11.3	(0.2)	1.7	(0.2)	0.7	(0.1)	25.7	(0.3)
Car 1	3	287.106	-0.586	12.7	(0.3)	2.5	(0.3)	0.8	(0.1)	37.7	(0.3)
Car 1	4	287.156	-0.586	24.5	(0.6)	1.8	(0.4)	0.8	(0.1)	49.9	(1.0)
Car 1	5	287.206	-0.585	39.3	(0.6)	6.6	(0.4)	2.0	(0.2)	77.7	(1.9)
Car 1	6	287.256	-0.585	53.3	(0.6)	6.3	(0.4)	3.1	(0.3)	91.7	(2.3)
Car 1	7	287.006	-0.537	6.4	(0.2)	1.4	(0.1)	0.5	(0.1)	18.8	(0.5)
Car 1	8	287.056	-0.537	11.9	(0.4)	1.1	(0.2)	0.5	(0.1)	24.1	(0.3)
Car 1	9	287.106	-0.536	19.0	(0.3)	2.3	(0.3)	1.4	(0.1)	53.2	(1.3)
Car 1	10	287.156	-0.536	15.1	(0.3)	3.7	(0.2)	0.7	(0.1)	39.6	(0.4)
Car 1	11	287.206	-0.535	26.9	(0.7)	3.8	(0.2)	1.4	(0.1)	49.1	(0.8)
Car 1	12	287.256	-0.535	14.8	(0.4)	3.0	(0.2)	0.9	(0.1)	40.7	(0.5)
Car 1	13	287.005	-0.487	5.4	(0.3)	1.5	(0.1)	0.4	(0.1)	16.3	(0.5)
Car 1	14	287.055	-0.487	10.8	(0.4)	2.0	(0.1)	0.5	(0.1)	17.3	(0.2)
Car 1	15	287.105	-0.486	13.4	(0.4)	3.5	(0.2)	0.6	(0.1)	29.3	(0.3)
Car 1	16	287.155	-0.486	7.6	(0.3)	1.3	(0.1)	0.3	(0.1)	18.8	(0.4)
Car 1	17	287.205	-0.485	8.9	(0.3)	1.7	(0.1)	0.7	(0.1)	26.8	(0.3)
Car 1	18	287.255	-0.485	8.3	(0.3)	3.1	(0.3)	0.4	(0.1)	26.4	(0.4)
Car 1	19	287.005	-0.437	5.2	(0.3)	1.3	(0.1)	0.3	(0.1)	18.0	(0.4)
Car 1	20	287.055	-0.437	10.3	(0.3)	2.8	(0.2)	0.4	(0.1)	20.9	(0.3)
Car 1	21	287.105	-0.436	15.8	(0.4)	1.1	(0.2)	0.5	(0.1)	25.9	(0.3)
Car 1	22	287.155	-0.436	7.4	(0.2)	1.1	(0.1)	0.4	(0.1)	22.5	(0.2)
Car 1	23	287.205	-0.435	8.6	(0.3)	1.4	(0.1)	0.5	(0.1)	17.5	(0.4)
Car 1	24	287.255	-0.435	8.8	(0.3)	1.6	(0.1)	0.5	(0.1)	21.0	(0.3)
Car 2	1	287.405	-0.586	40.3	(1.0)	7.7	(0.5)	1.6	(0.2)	73.7	(1.5)
Car 2	2	287.455	-0.586	40.3	(0.6)	9.2	(0.3)	2.1	(0.2)	67.5	(1.6)
Car 2	3	287.505	-0.586	17.7	(0.9)	12.8	(0.8)	1.4	(0.2)	36.6	(0.4)
Car 2	4	287.555	-0.586	130.7	(2.2)	11.9	(0.6)	4.4	(0.3)	56.3	(0.6)
Car 2	5	287.605	-0.586	10.8	(0.6)	7.4	(0.3)	1.1	(0.1)	27.7	(0.4)
Car 2	6	287.655	-0.586	7.6	(0.4)	6.0	(0.3)	0.7	(0.1)	28.0	(0.3)
Car 2	7	287.405	-0.536	148.9	(1.7)	6.2	(0.4)	6.9	(0.4)	92.2	(2.3)
Car 2	8	287.455	-0.536	116.3	(1.2)	5.9	(0.5)	4.6	(0.4)	95.5	(2.1)
Car 2	9	287.505	-0.536	18.8	(0.4)	5.7	(0.3)	2.0	(0.2)	37.1	(0.4)
Car 2	10	287.555	-0.536	13.0	(0.5)	3.3	(0.2)	0.8	(0.1)	33.0	(0.4)
Car 2	11	287.605	-0.536	15.2	(0.3)	5.8	(0.4)	0.8	(0.1)	33.6	(0.4)
Car 2	12	287.655	-0.536	16.7	(0.5)	5.8	(0.3)	1.4	(0.1)	32.2	(0.4)

Table 2.6 Continued

I.D.		l	b	[OI] 63 μm I	(σ_I)	[NII] 122 μm I	(σ_I)	[OI] 146 μm I	(σ_I)	[CII] 158 μm I	(σ_I)
Car 2	13	287.405	-0.486	20.7	(0.5)	2.9	(0.2)	1.1	(0.1)	38.4	(0.5)
Car 2	14	287.455	-0.486	12.9	(0.4)	3.3	(0.3)	0.8	(0.1)	32.9	(0.5)
Car 2	15	287.505	-0.486	27.6	(0.6)	5.8	(0.3)	1.5	(0.1)	42.1	(0.4)
Car 2	16	287.555	-0.486	17.7	(0.3)	3.7	(0.2)	1.0	(0.1)	31.4	(0.4)
Car 2	17	287.605	-0.486	14.7	(0.4)	4.2	(0.2)	1.0	(0.1)	28.9	(0.5)
Car 2	18	287.655	-0.486	10.7	(0.4)	3.3	(0.2)	0.8	(0.1)	22.6	(0.3)
Car 2	19	287.405	-0.436	11.1	(0.4)	2.2	(0.2)	0.3	(0.1)	31.8	(0.3)
Car 2	20	287.455	-0.436	14.7	(0.3)	3.5	(0.3)	0.8	(0.1)	30.7	(0.3)
Car 2	21	287.505	-0.436	17.0	(0.5)	3.3	(0.2)	0.6	(0.1)	27.2	(0.3)
Car 2	22	287.555	-0.436	12.4	(0.4)	5.1	(0.3)	0.6	(0.1)	25.2	(0.4)
Car 2	23	287.605	-0.436	11.6	(0.3)	2.2	(0.2)	0.6	(0.1)	23.2	(0.6)
Car 2	24	287.655	-0.436	8.7	(0.4)	3.6	(0.2)	0.7	(0.1)	23.6	(0.3)
Car 3	1	287.006	-0.788	7.2	(0.3)	3.9	(0.1)	0.1	(0.1)	18.3	(0.2)
Car 3	2	287.056	-0.787	12.1	(0.4)	3.3	(0.1)	0.8	(0.1)	21.7	(0.3)
Car 3	3	287.107	-0.786	11.2	(0.3)	4.0	(0.2)	0.8	(0.2)	35.8	(0.4)
Car 3	4	287.156	-0.786	22.6	(0.4)	5.0	(0.2)	1.1	(0.1)	52.9	(0.6)
Car 3	5	287.207	-0.785	25.8	(0.6)	5.1	(0.2)	1.2	(0.2)	41.1	(0.7)
Car 3	6	287.257	-0.784	15.7	(0.3)	9.2	(0.3)	1.1	(0.1)	47.0	(1.5)
Car 3	7	287.006	-0.738	5.4	(0.2)	5.3	(0.2)	0.3	(0.1)	17.3	(0.3)
Car 3	8	287.056	-0.737	6.2	(0.2)	3.4	(0.1)	0.4	(0.1)	22.5	(0.3)
Car 3	9	287.106	-0.736	16.7	(0.3)	4.6	(0.3)	1.3	(0.1)	36.7	(0.4)
Car 3	10	287.156	-0.736	24.3	(0.5)	7.0	(0.3)	1.5	(0.2)	49.4	(0.9)
Car 3	11	287.206	-0.735	25.7	(0.5)	8.2	(0.3)	0.9	(0.1)	56.3	(0.6)
Car 3	12	287.256	-0.737	27.7	(0.5)	11.6	(0.2)	2.0	(0.2)	62.9	(0.7)
Car 3	13	287.005	-0.688	8.1	(0.3)	4.3	(0.1)	0.4	(0.1)	24.2	(0.2)
Car 3	14	287.055	-0.687	7.0	(0.3)	5.5	(0.3)	0.4	(0.1)	26.7	(0.3)
Car 3	15	287.105	-0.686	10.8	(0.4)	5.7	(0.2)	0.9	(0.2)	33.9	(0.3)
Car 3	16	287.155	-0.686	15.7	(0.4)	8.1	(0.4)	1.2	(0.1)	49.2	(1.0)
Car 3	17	287.205	-0.685	42.3	(0.6)	8.7	(0.3)	3.3	(0.2)	70.4	(0.6)
Car 3	18	287.255	-0.687	27.0	(0.7)	10.0	(0.5)	2.5	(0.3)	81.6	(1.2)
Car 3	19	287.004	-0.638	10.2	(0.3)	2.3	(0.1)	0.7	(0.1)	24.1	(0.4)
Car 3	20	287.054	-0.637	12.9	(0.3)	2.3	(0.2)	0.9	(0.1)	31.3	(0.5)
Car 3	21	287.104	-0.636	11.1	(0.2)	2.8	(0.2)	0.7	(0.1)	32.1	(0.4)
Car 3	22	287.154	-0.636	18.9	(0.3)	2.0	(0.3)	2.0	(0.2)	41.9	(0.6)
Car 3	23	287.204	-0.635	23.5	(0.4)	2.1	(0.3)	1.5	(0.2)	51.5	(1.0)
Car 3	24	287.254	-0.634	34.3	(0.5)	4.8	(0.3)	1.8	(0.2)	77.0	(1.9)
Car 4	1	287.406	-0.787	6.2	(0.3)	3.7	(0.2)	0.2	(0.1)	18.7	(0.3)
Car 4	2	287.456	-0.786	7.7	(0.3)	3.7	(0.2)	0.2	(0.1)	25.4	(0.3)
Car 4	3	287.506	-0.786	21.9	(0.9)	3.6	(0.3)	0.6	(0.1)	26.9	(0.5)

Table 2.6 Continued

I.D.		l	b	[OI] 63 μm I	(σ_I)	[NII] 122 μm I	(σ_I)	[OI] 146 μm I	(σ_I)	[CII] 158 μm I	(σ_I)
Car 4	4	287.556	-0.786	9.8	(0.4)	3.7	(0.2)	0.7	(0.1)	31.1	(0.4)
Car 4	5	287.606	-0.786	8.3	(0.3)	5.8	(0.3)	0.8	(0.2)	34.8	(0.6)
Car 4	6	287.656	-0.786	12.3	(0.3)	5.2	(0.2)	1.1	(0.1)	39.6	(0.5)
Car 4	7	287.406	-0.736	7.7	(0.4)	6.0	(0.3)	0.6	(0.1)	31.9	(0.5)
Car 4	8	287.456	-0.736	21.1	(0.5)	4.0	(0.3)	1.7	(0.2)	39.4	(0.5)
Car 4	9	287.506	-0.736	9.7	(0.6)	3.5	(0.3)	0.8	(0.1)	24.8	(0.5)
Car 4	10	287.556	-0.736	12.8	(0.5)	5.4	(0.2)	0.7	(0.2)	36.2	(0.5)
Car 4	11	287.606	-0.736	7.5	(0.3)	6.0	(0.2)	0.5	(0.1)	22.4	(0.4)
Car 4	12	287.656	-0.736	25.2	(0.5)	6.8	(0.3)	3.9	(0.3)	55.2	(1.3)
Car 4	13	287.405	-0.686	72.0	(0.8)	13.5	(0.5)	6.6	(0.3)	73.4	(1.8)
Car 4	14	287.455	-0.686	33.7	(1.0)	6.7	(0.4)	3.1	(0.3)	55.9	(0.5)
Car 4	15	287.505	-0.686	15.3	(0.5)	5.1	(0.3)	1.1	(0.1)	34.4	(0.3)
Car 4	16	287.555	-0.686	12.0	(0.6)	9.9	(0.3)	0.9	(0.1)	20.2	(0.3)
Car 4	17	287.605	-0.686	4.7	(0.4)	5.4	(0.2)	0.4	(0.1)	24.1	(0.3)
Car 4	18	287.655	-0.686	24.2	(0.4)	6.8	(0.2)	1.1	(0.1)	41.6	(0.8)
Car 4	19	287.405	-0.637	69.9	(1.4)	16.6	(0.6)	5.8	(0.3)	72.9	(1.3)
Car 4	20	287.455	-0.636	42.2	(0.6)	15.1	(1.3)	2.3	(0.3)	60.2	(1.1)
Car 4	21	287.505	-0.636	8.9	(1.0)	5.3	(0.3)	0.9	(0.1)	31.9	(0.4)
Car 4	22	287.555	-0.636	21.9	(1.5)	14.4	(0.4)	1.4	(0.2)	41.6	(0.4)
Car 4	23	287.605	-0.636	30.8	(9.7)	17.3	(1.9)	1.2	(0.5)	32.1	(0.4)
Car 4	24	287.655	-0.636	10.6	(0.6)	9.2	(0.2)	0.7	(0.2)	38.9	(0.7)
Car 6	1	287.256	-0.737	26.4	(0.4)	12.3	(0.3)	1.5	(0.2)	61.8	(0.7)
Car 6	2	287.306	-0.736	22.8	(0.5)	12.5	(0.3)	1.5	(0.2)	60.5	(0.5)
Car 6	3	287.356	-0.736	12.8	(0.5)	13.4	(0.3)	1.3	(0.2)	58.9	(1.4)
Car 6	4	287.406	-0.736	7.7	(0.6)	5.7	(0.4)	1.1	(0.1)	19.0	(0.3)
Car 6	5	287.255	-0.687	35.1	(0.5)	7.5	(0.4)	2.5	(0.3)	86.4	(1.4)
Car 6	6	287.305	-0.686	53.1	(0.8)	10.7	(0.5)	3.4	(0.4)	115.3	(1.6)
Car 6	7	287.355	-0.686	89.2	(1.4)	22.4	(0.5)	7.3	(0.4)	163.4	(4.2)
Car 6	8	287.405	-0.686	73.5	(1.0)	12.4	(0.5)	6.3	(0.3)	96.2	(1.9)

[a] Coordinates refer to the center positions of the ISO beam, as shown in the raster map in Figure 2.3. [b] Intensity errors (σ_I) do not include the ISO absolute calibration error of ~ 20 %.

Figure 2.9 *(following page)*: ISO 63 μm [OI] Map of the Carina Nebula

63 μm [OI] line emission in the Carina Nebula, observed by the ISO LWS in July/August 1996. The inverted grayscale bar measures intensity in units of $[10^{-8}\,\mathrm{W\,m^{-2}\,sr^{-1}}]$. Contours are shown every 10σ, where $\sigma = 0.6\times10^{-8}\,\mathrm{W\,m^{-2}\,sr^{-1}}$ is the average intensity error over the map. The map has been re-sampled and smoothed with a Gaussian filter of FWHM = 87.″2, matching the LWS beam. Smoothing has attenuated the maxima; the original data are listed in Table 2.6.

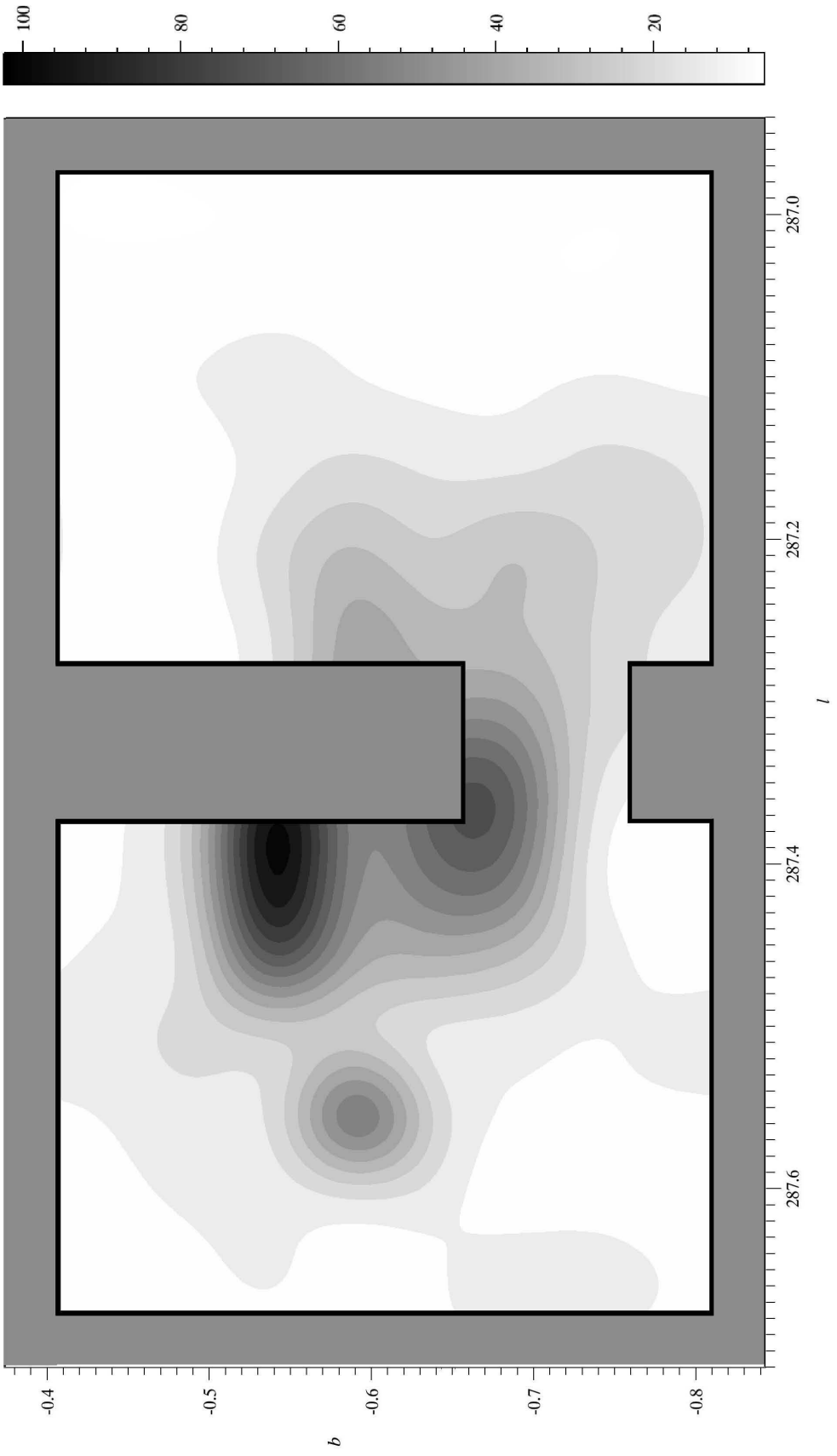
100
80
60
40
20
287.0
287.2
287.4
287.6
l
-0.4
-0.5
-0.6
-0.7
-0.8
b

Figure 2.10 *(following page)*: ISO 122 μm [NII] Map of the Carina Nebula

122 μm [NII] line emission in the Carina Nebula, observed by the ISO LWS in July/August 1996. The inverted grayscale bar measures intensity in units of $[10^{-8}\,\mathrm{W\,m^{-2}\,sr^{-1}}]$. Contours are shown every 3σ, where $\sigma = 0.3 \times 10^{-8}\,\mathrm{W\,m^{-2}\,sr^{-1}}$ is the average intensity error over the map. The map has been re-sampled and smoothed with a Gaussian filter of FWHM = 78.″2, matching the LWS beam. Smoothing has attenuated the maxima; the original data are listed in Table 2.6.

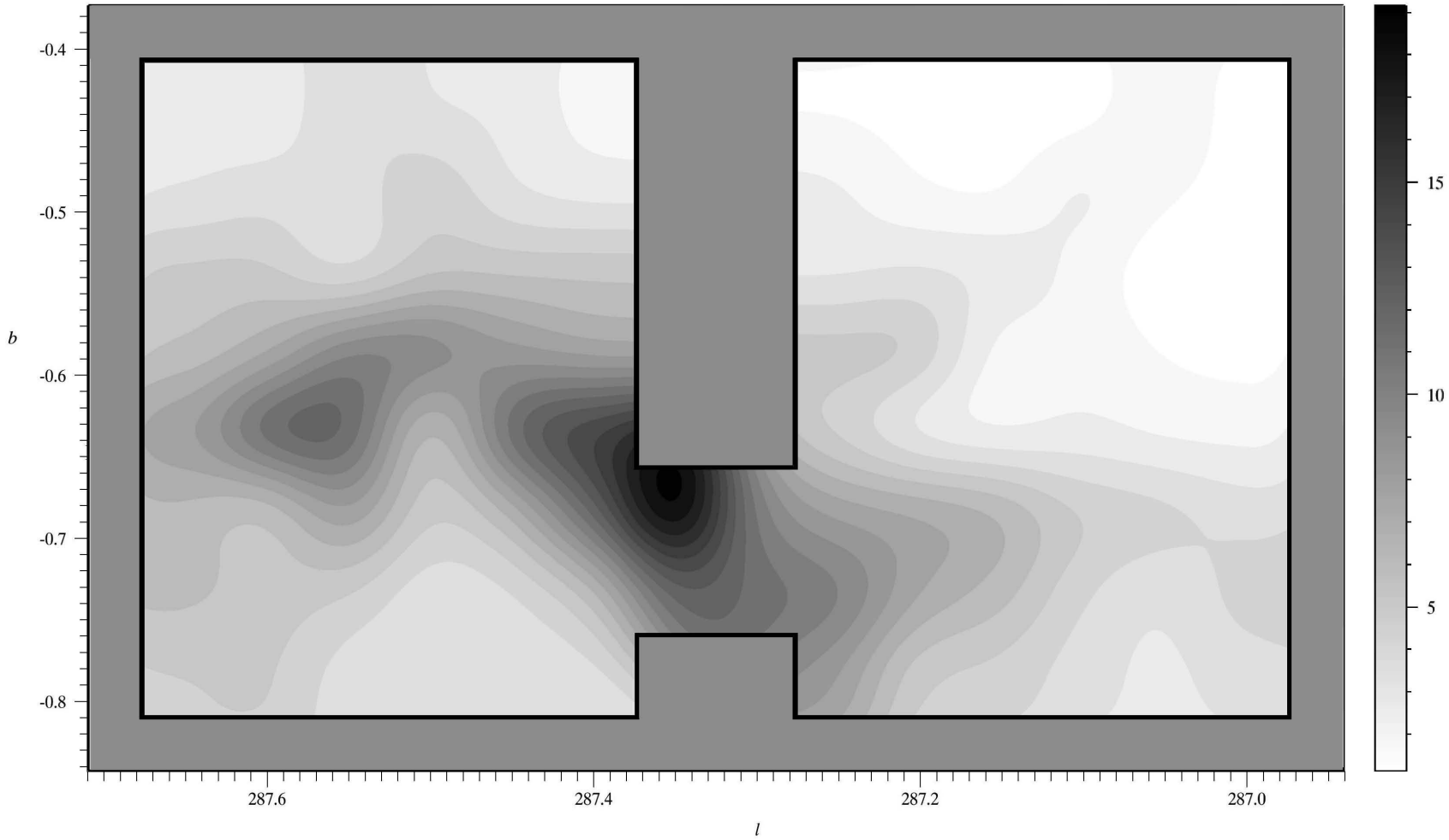
-0.4
-0.5
-0.6
-0.7
-0.8
b
287.6
287.4
287.2
287.0
l
15
10
5

Figure 2.11 *(following page)*: ISO 146 μm [OI] Map of the Carina Nebula

146 μm [OI] line emission in the Carina Nebula, observed by the ISO LWS in July/August 1996. The inverted grayscale bar measures intensity in units of $[10^{-8}\,\mathrm{W\,m^{-2}\,sr^{-1}}]$. Contours are shown every 3σ, where $\sigma = 0.1 \times 10^{-8}\,\mathrm{W\,m^{-2}\,sr^{-1}}$ is the average intensity error over the map. The map has been re-sampled and smoothed with a Gaussian filter of FWHM = 70.″0, matching the LWS beam. Smoothing has attenuated the maxima; the original data are listed in Table 2.6.

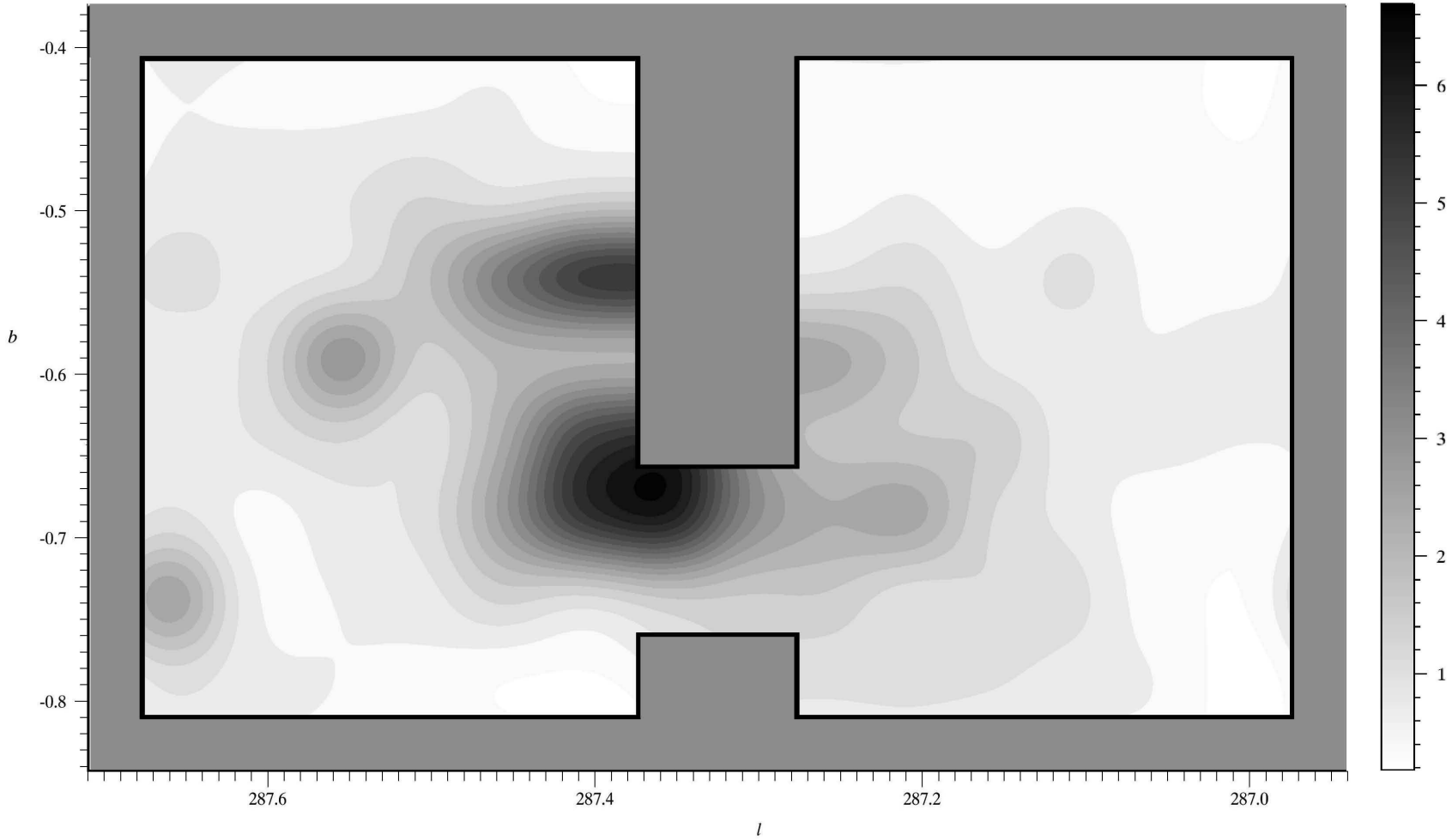
-0.4
-0.5
-0.6
-0.7
-0.8
b
287.6
287.4
287.2
287.0
l
6
5
4
3
2
1

Figure 2.12 *(following page)*: ISO 158 μm [CII] Map of the Carina Nebula

158 μm [CII] line emission in the Carina Nebula, observed by the ISO LWS in July/August 1996. The inverted grayscale bar measures intensity in units of $[10^{-8}\,\mathrm{W\,m^{-2}\,sr^{-1}}]$. Contours are shown every 10σ, where $\sigma = 0.7\times10^{-8}\,\mathrm{W\,m^{-2}\,sr^{-1}}$ is the average intensity error over the map. The map has been re-sampled and smoothed with a Gaussian filter of FWHM = 70.″1, matching the LWS beam. Smoothing has attenuated the maxima; the original data are listed in Table 2.6.

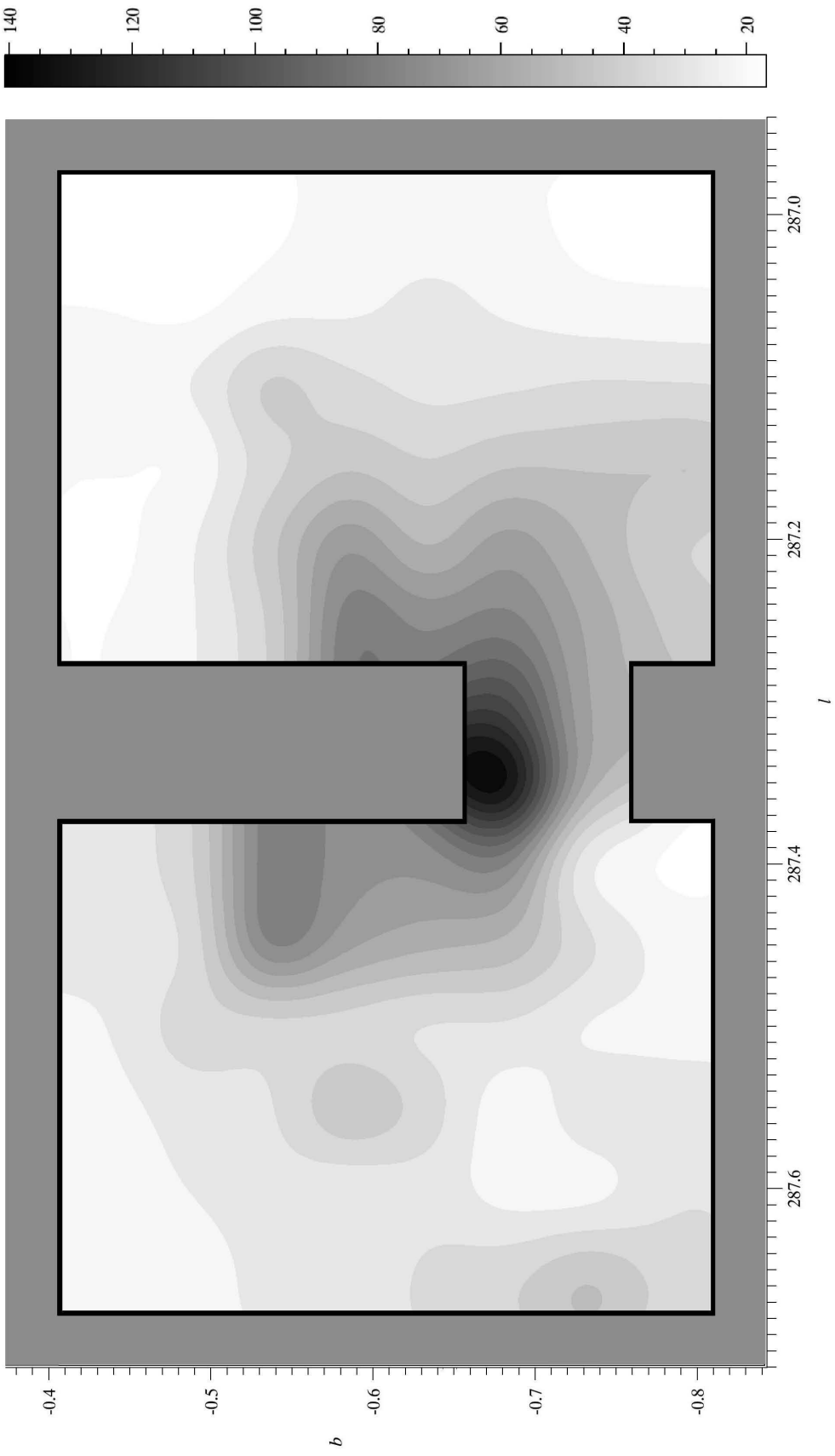
140
120
100
80
60
40
20
287.0
287.2
287.4
287.6
l
-0.4
-0.5
-0.6
-0.7
-0.8
b

2.6 Discussion

2.6.1 Morphology

In this section, we present a number of overlays of our 205 μm [NII] SPIFI map with our ISO maps and also with multiwavelength maps from previous studies by other authors. By comparing the morphology of the maps, we aim to understand the structure of the nebula in its various ionic, atomic, and molecular components. These comparisons will help in our efforts to understand the dynamics and evolution of the nebula.

In Figure 2.13, our 205 μm [NII] contours are placed on the composite image previously shown in Figure 2.1. In the region mapped, the 205 μm [NII] map shows two main peaks: G287.3843-0.6301 and G287.5519-0.6182 (raster positions Car I-27 and Car II-58 in Tables 2.4 and 2.5, respectively). These peaks both lie within the 50 % of peak contours of the Car I and II HII regions as outlined in the 843 MHz radio continuum emission by Whiteoak (1994), and are relatively close to the respective radio peaks: offset just 51″ (0.57 pc) eastward of Car I and 41″ (0.46 pc) southwest of Car II. The 205 μm peaks themselves are separated by 10′.08 (6.74 pc).

Figure 2.13 *(following page)*: Morphological Comparison of Carina Sources and 205 μm [NII] Emission

Major components of the Carina Nebula (Figure 2.1) are drawn over SPIFI 205 μm [NII] contours (Figure 2.7).

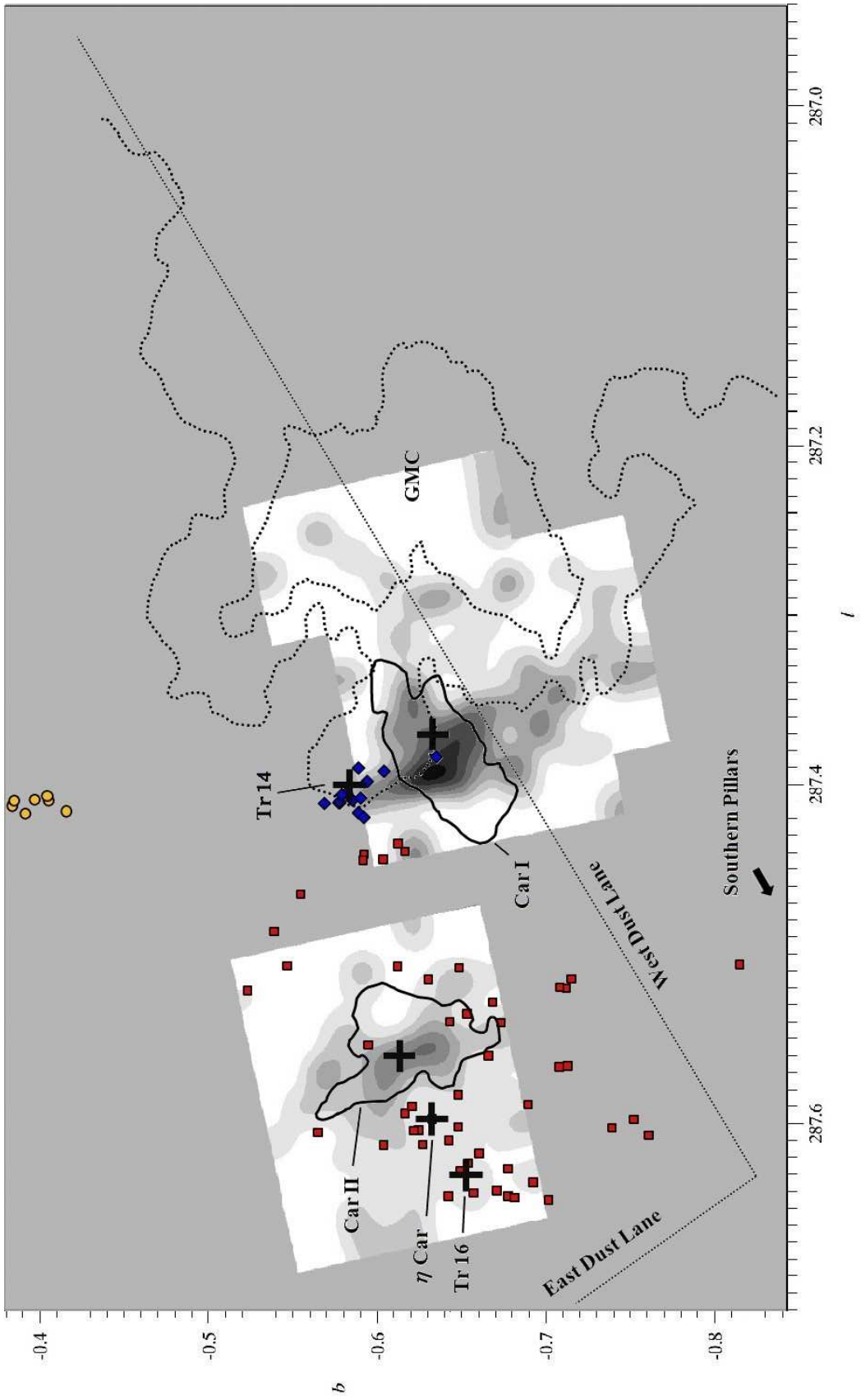
GMC
Tr 14
Car I
Car II
η Car
Tr 16
West Dust Lane
East Dust Lane
Southern Pillars
287.6
287.4
287.2
287.0
-0.4
-0.5
-0.6
-0.7
-0.8
l
b

Figure 2.14 *(following page)*: 205 μm [NII] and 843 MHz Radio Continuum Overlay

SPIFI [NII] 205 μm contours (corresponding to Figure 2.7) are overlaid on an inverted-grayscale image of 843 MHz radio continuum from the Sydney University Molonglo Sky Survey (Whiteoak 1994). The 843 MHz grayscale bar ranges linearly from 0 – 2 Jy beam^{-1}; the beam size was 43″.

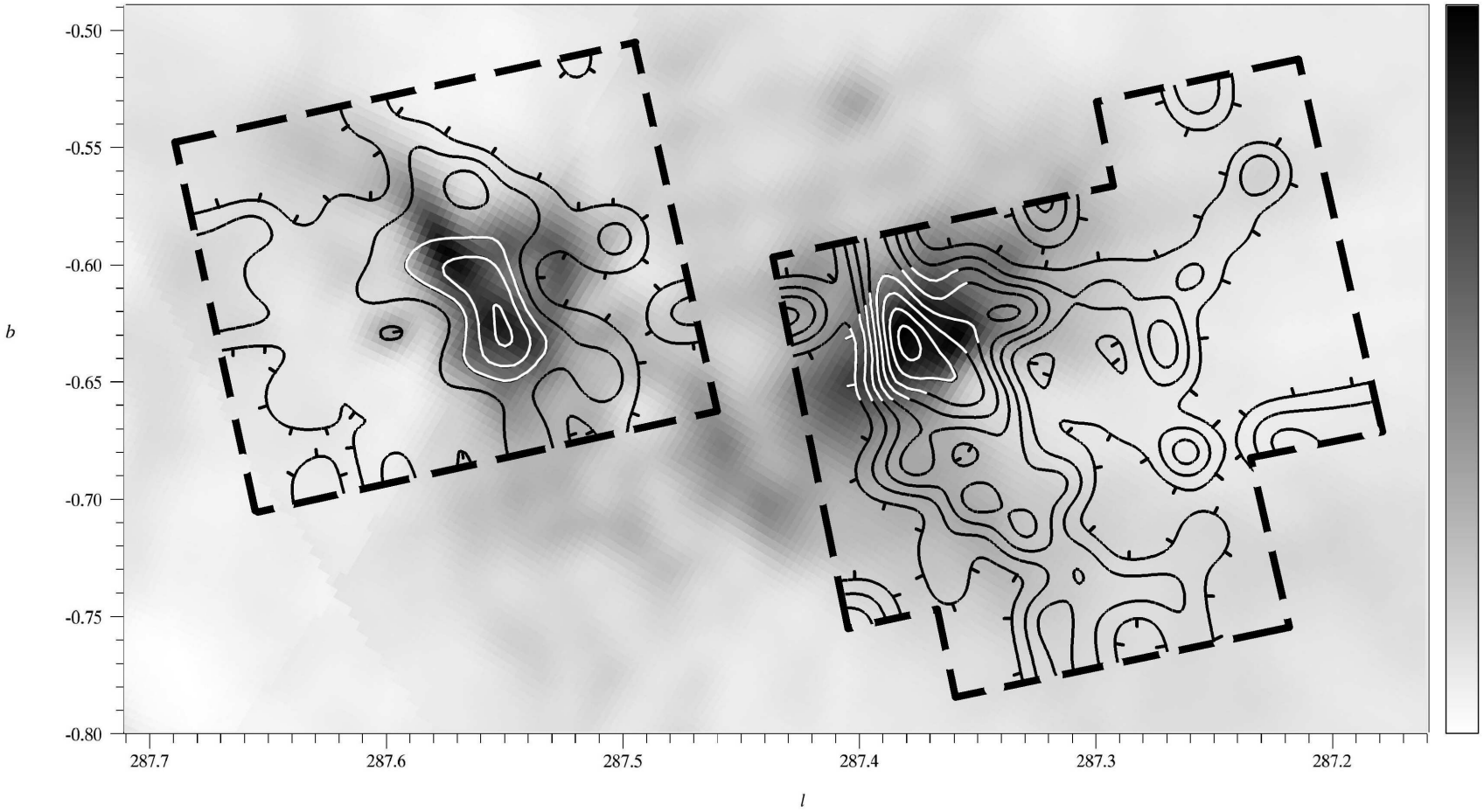
-0.50
-0.55
-0.60
-0.65
-0.70
-0.75
-0.80
b
287.7
287.6
287.5
287.4
287.3
287.2
l

For a more detailed comparison with the radio emission, in Figure 2.14, we plot the 205 μm [NII] contours directly over the grayscale 843 MHz radio continuum of Whiteoak (1994). From a super-resolution image of this radio map, Whiteoak (1994) has discerned a number sub-structures within the Car I and II peaks. This super-resolution image and a cartoon schematic (Whiteoak 1994, Figures 3d and 5), in which these substructures have been labeled, are reproduced in Figure 2.15. In Car II, the 205 μm [NII] emission traces the ridge formed by the substructures Car II-E and Car II-W but does not resolve between them. There is also a concavity in the 205 μm [NII] map that roughly corresponds to the partial ring structure of Car II-N, although it is somewhat more extended and westward than on the radio map. It also appears that SPIFI has resolved a lack of ionized emission from η Car (SPIFI raster position Car II-31 was centered directly on the star).

In Car I, although the 205 μm and radio peaks roughly match, the Car I-E and Car I-W ridges are not resolved by SPIFI. The western side of the plateau is roughly traced by the 205 μm contours, but the eastern side of the plateau is conspicuously absent. Another difference is the thin ridge of 205 μm emission which stretches north towards Tr 14. We note, however, that the faint "arms" of radio emission stretching to the south and west of Car I are roughly traced by 205 μm emission.

Figure 2.15 *(following page)*: 843 MHz Super-resolution Map of the Carina Nebula

Left Panel: A reproduction of Whiteoak (1994) Figure 3d, a super-resolution 843 MHz radio continuum contour map of the Carina Nebula. Right Panel: Whiteoak (1994) Figure 5, a cartoon schematic of the nebula's radio and optical features.

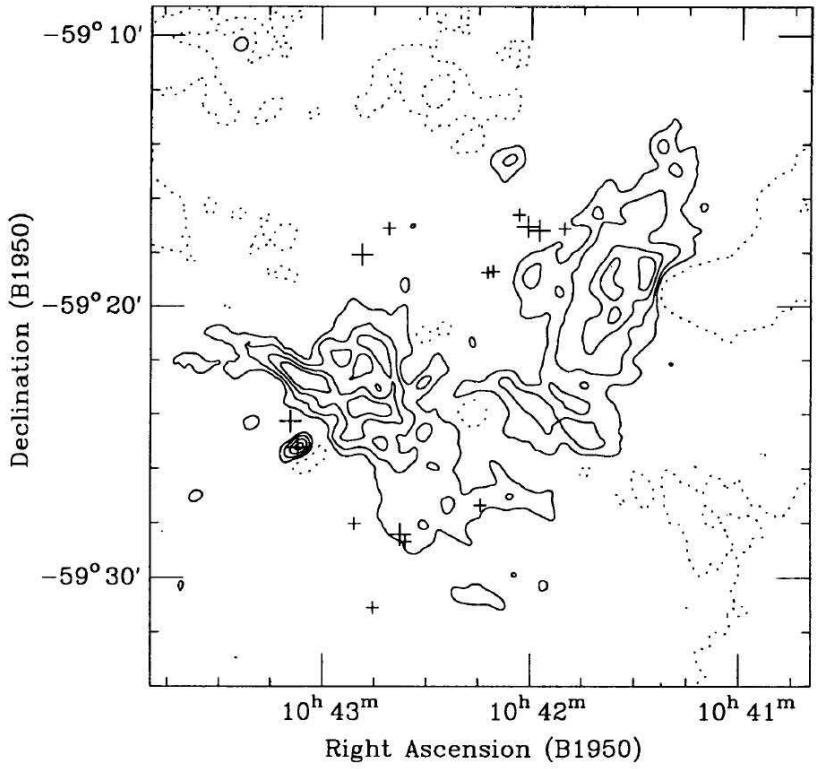
−59° 10′
−59° 20′
−59° 30′
Declination (B1950)
10h 43m
10h 42m
10h 41m
Right Ascension (B1950)

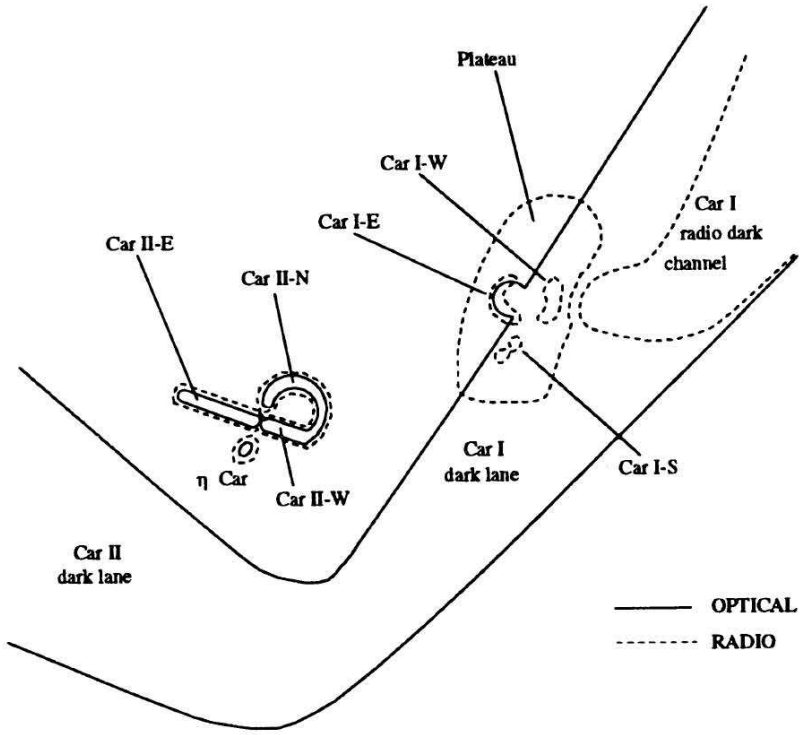
Plateau
Car I-W
Car I-E
Car I
radio dark
channel
Car II-E
Car II-N
η Car
Car II-W
Car I
dark lane
Car I-S
Car II
dark lane
OPTICAL
RADIO

The FWHM SPIFI beam size was 54″ (0.60 pc), which is very close to the Molonglo Observatory Synthesis Telescope beam of 43″ × 50″ (R.A. × Dec.), used for the radio map. The super-resolution map, however, has an effective resolution of 27″ × 32″ (R.A. × Dec.). At this point, we remind the reader that the SPIFI map was spatially under-sampled, with a filling factor of ∼ 50 %. In making the 205 μm contour map, intensity levels at unobserved locations have been interpolated from nearby observed beams (§2.4.2). Therefore, some structures of the nebula falling between raster beams will be absent in the SPIFI map, and some observed structures will be appear more extended than they should. We also emphasize the low SNR (cutoff of 3 and average ∼ 5) of the SPIFI data, due to the inherent difficulty of detecting the 205 μm [NII] line. We conceed to the possibility of artifacts (noise) in the map on the order of the SPIFI beam size due to this low SNR. These effects, if present, would would be more prominent within three beam positions (∼ 3′) of the raster boundaries (see Figure 2.3), where fewer overlaps of the array footprint occured, and hence where integration times and SNRs are generally lower than at the center of the maps. This could explain the absence of the eastern side of the Car I plateau in 205 μm emission and the presence of a 205 μm ridge extending to Tr 14. In general, however, the fine-structure N^+ emission shows good correspondence to the radio emission: it is clear that both originate in the ionized medium of the nebula (with the radio continuum arising from thermal free-free transitions).

Figure 2.16 *(following page)*: 205 and 122 μm [NII] Overlay

SPIFI [NII] 205 μm contours (corresponding to Figure 2.7) are overlaid on 122 μm [NII] grayscale contours (Figure 2.10).

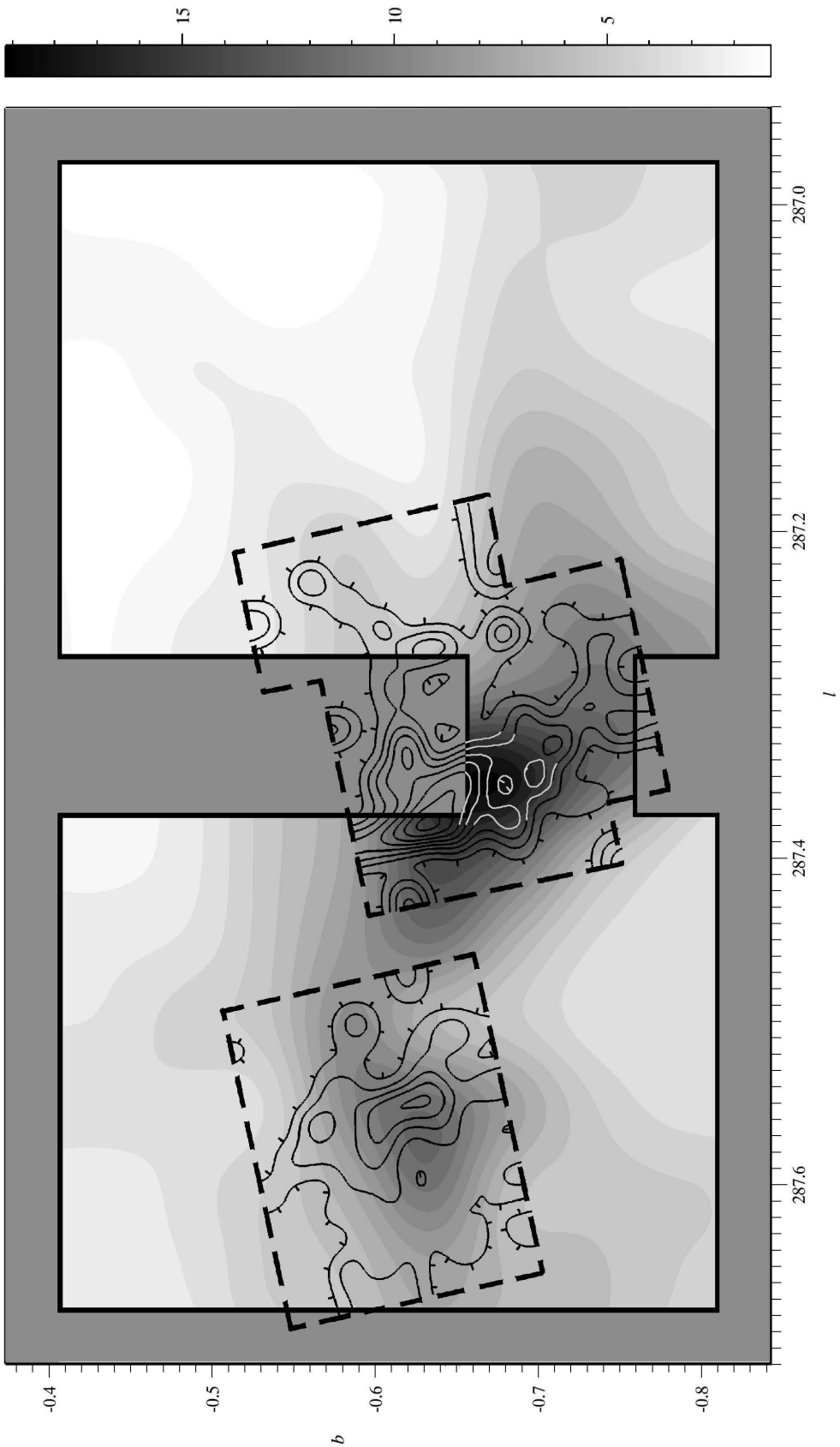
15
10
5
287.0
287.2
287.4
287.6
l
-0.4
-0.5
-0.6
-0.7
-0.8
q

Figure 2.17 *(following page)*: 205 μm [NII] and 57 μm [NIII] Overlay

SPIFI [NII] 205 μm contours (from Figure 2.7) are overlaid on 57 μm [NIII] grayscale contours created by the author from the intensity data of Mizutani *et al*. (2002). The [NIII] contours are shown every 5σ, where $\sigma = 3.1 \times 10^{-8}\,\mathrm{W\,m^{-2}\,sr^{-1}}$ is the average intensity error over the map. The map has been re-sampled and smoothed with a Gaussian filter of FWHM = 84.″5, matching the LWS beam.

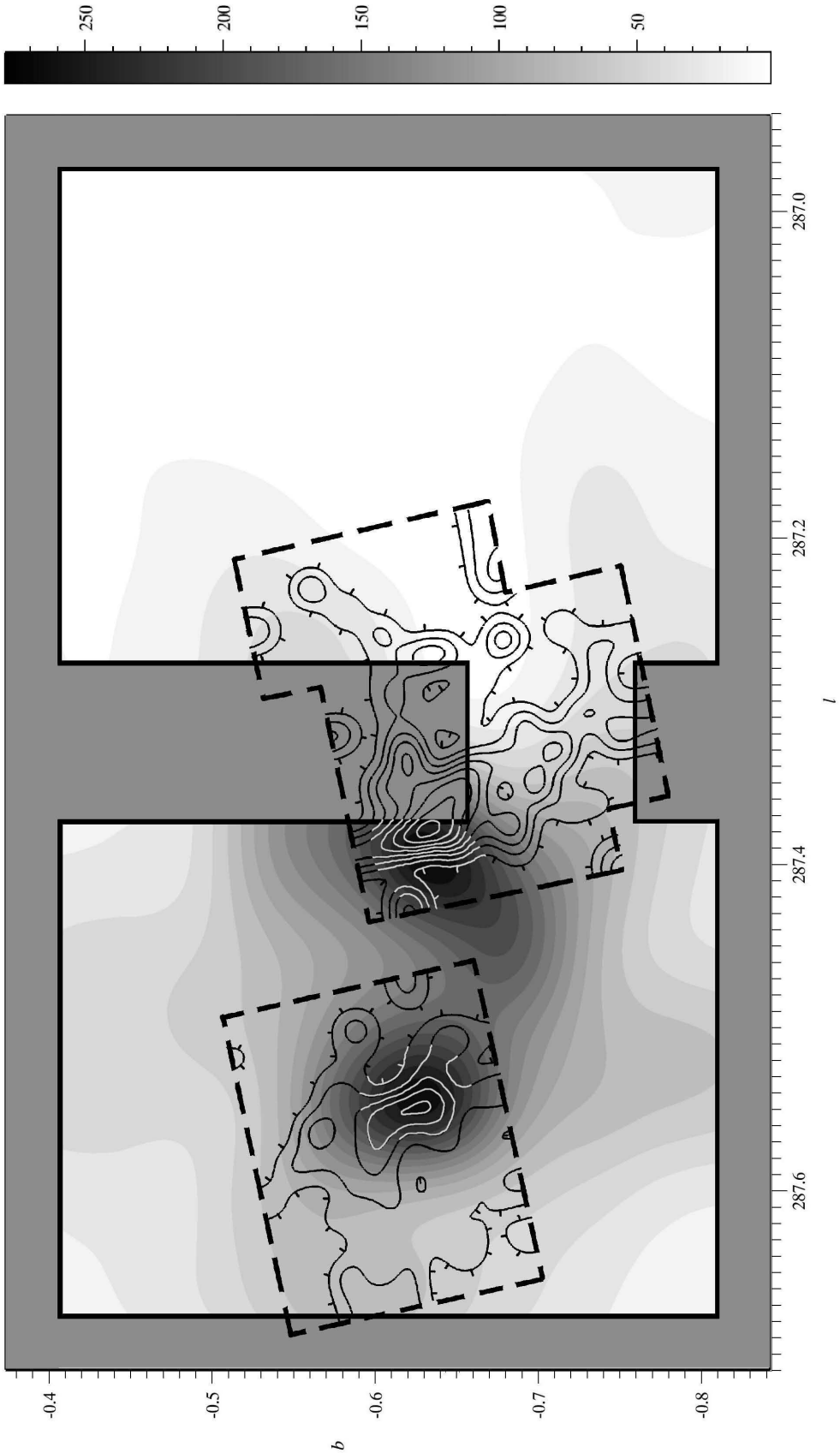
250
200
150
100
50
287.0
287.2
287.4
287.6
l
-0.4
-0.5
-0.6
-0.7
-0.8
q

To complete our morphological study of the ionized component, in Figure 2.16 we overlay the SPIFI 205 μm [NII] contours on the grayscale map of the 122 μm [NII] (*cf.* Figure 2.10 above), and in Figure 2.17 we overlay 205 μm [NII] contours on the more highly ionized 57 μm [NIII] emission as observed by the ISO LWS. The [NIII] map was created by the author using the methods of §2.4.2 and the data presented in Miztuani *et al*. (2002).[6] Compared with SPIFI, the ISO beam is larger (84.″5 at 57 μm and 78.″2 at 122 μm) and the spatial sampling coarser (3′). Nevertheless, it is immediately evident that the lower ionization 122 μm [NII] peaks farther to the southwest than the [NIII], with the peaks occuring at raster positions G287.355-0.686 and G287.405-0.638, respectively. The [NII] is also clearly extended over a greater area to the west than the [NIII]. As was also seen in the 843 MHz radio map, the 205 μm [NII] roughly follows the southern and western arms seen extending from Car I in the 122 μm [NII] map. Comparison with Figure 2.13 reveals that the [NII] emission appears to extend into the GMC, while the [NIII] does not. In Carina, the ionized gas is apparently extended over a very large region, and the lower ionization state gas is either projected along the same line of sight as the molecular phase or appears intermixed at the angular resolution of our beam. In §2.6.2 we derive a density of $n_e \sim 29$ cm^{-3} from the [NII] emission, supporting the suggestion by Mizutani *et al*. (2002) of an extended low-density (ELD) HII region spanning 30 pc or more across the nebula.

[6]Unlike the other ISO LWS fine-structure lines presented here (namely 63 and 146 μm [OI], 122 μm [NII], and 158 μm [CII]), the [NIII] intensities were not re-reduced and re-fit by the author, and thus have a different flux calibration (possibly up to a 35 % difference, *cf.* §2.5.2). Hence, the [NIII] map is considered here only for purposes of morphological comparison.

Figure 2.18 *(following page)*: 205 μm [NII], 609 μm [CI], and 650 μm ^{12}CO(4→3) Overlay

SPIFI [NII] 205 μm contours (white; from Figure 2.7) are overlaid on 609 μm [CI] color-scale and 650 μm ^{12}CO(4→3) contours (black; Zhang *et al*. 2001). The [CI] color-scale bar spans 0 – 12 K km s^{-1}, and the ^{12}CO(4→3) contours span 10 – 90 % of the peak of 80 K km s^{-1}. The beam sizes for [CI] and ^{12}CO(4→3) were 3.5′ and 3′ respectively. The graininess of the [CI] color-scale is a result of copying and reproducing the image, and does not reflect any real effect. All three lines were observed from the AST/RO at South Pole.

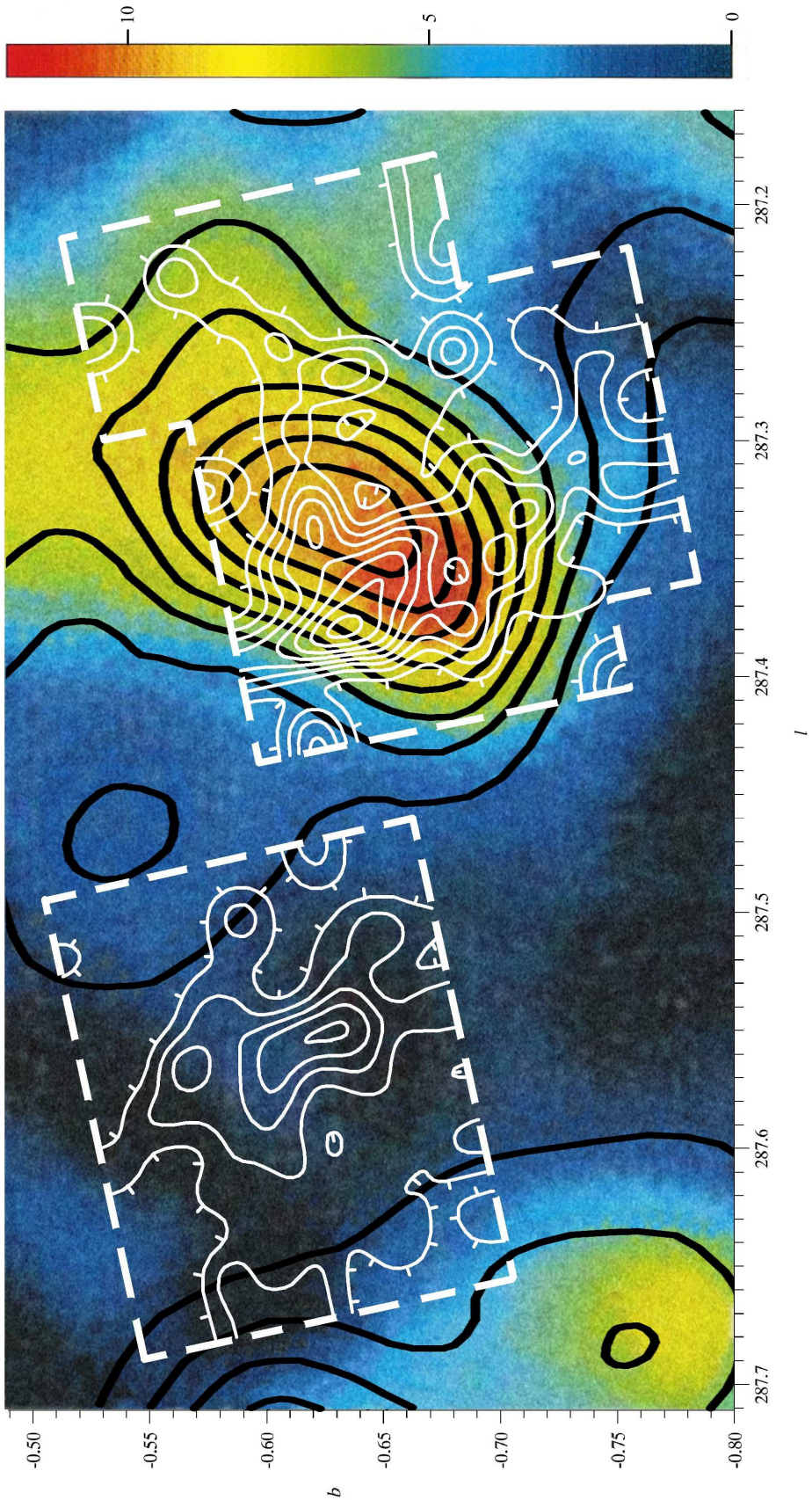
10
5
0
287.2
287.3
287.4
287.5
287.6
287.7
l
-0.50
-0.55
-0.60
-0.65
-0.70
-0.75
-0.80
b

We continue our morphological study by overlaying the 205 μm [NII] emission (white contours) on both neutral carbon [CI] 609 μm $^3P_1 \rightarrow {}^3P_0$ emission (color-scale) and molecular ^{12}CO(J=4→3) 650 μm emission (black contours) in Figure 2.18 (Zhang *et al*. 2001). The [CI] and ^{12}CO(4→3) were both observed by the SIS heterodyne receiver on the AST/RO (§1.1.1), with a beam size of ∼ 3′ and spatial sampling of 1′. This map is fully sampled, and gives a good representation of the location and extent of the GMC (the GMC is also seen in higher resolution (43″) in the 15 and 30 % contours of ^{12}CO(1→0) of Brooks *et al*. (1998) in Figure 2.13). We note the lack of molecular and neutral material in the vicinity of Tr 16 and Car II, consistent with Tr 16 being an older (age of ∼ 3 Myr), more evolved, cluster which has swept away most of its parental cloud. On the contrary, the younger (age of ∼ 1.5 Myr) Tr 14 cluster lies ∼ 2 pc from the eastern edge of the GMC, which also wraps behind Tr 14 along the line of site.

The [CI] and ^{12}CO(4→3) peaks straddle the Car I radio peak, with the molecular peak lying slightly farther west (1 pc, very roughly). The 205 μm [NII] peak lies directly between Tr 14 and the [CI] and ^{12}CO(4→3) peaks. This supports the prevailing view that Car I is predominantly powered by external radiation from the most massive members of Tr 14 (*e.g.* Retallack 1983; Whiteoak 1994; Mizutani *et al*. 2002; Brooks *et al*. 2003; Tapia *et al*. 2006). Based on the total luminosity of the OB stars of Tr 14 (Smith 2006a), the FUV field impinging on the position of Car I is $G_0 \sim 7500$ (in units of the local interstellar FUV field, 1.6×10^{-6} W m^{-2}, Habing 1968), consistent with the observed neutral line fluxes (see §2.6.7). Although Tr 14 is thought to be the dominant heating source for Car I, embedded sources cannot be ruled out, as Tapia *et al*. (2003) have detected an embedded stellar population in Car I which includes at least one O9/B0 star.

Figure 2.19 *(following page)*: 205 μm [NII] and 63 μm [OI] Overlay

SPIFI [NII] 205 μm contours (corresponding to Figure 2.7) are overlaid on 63 μm [OI] grayscale contours (Figure 2.9).

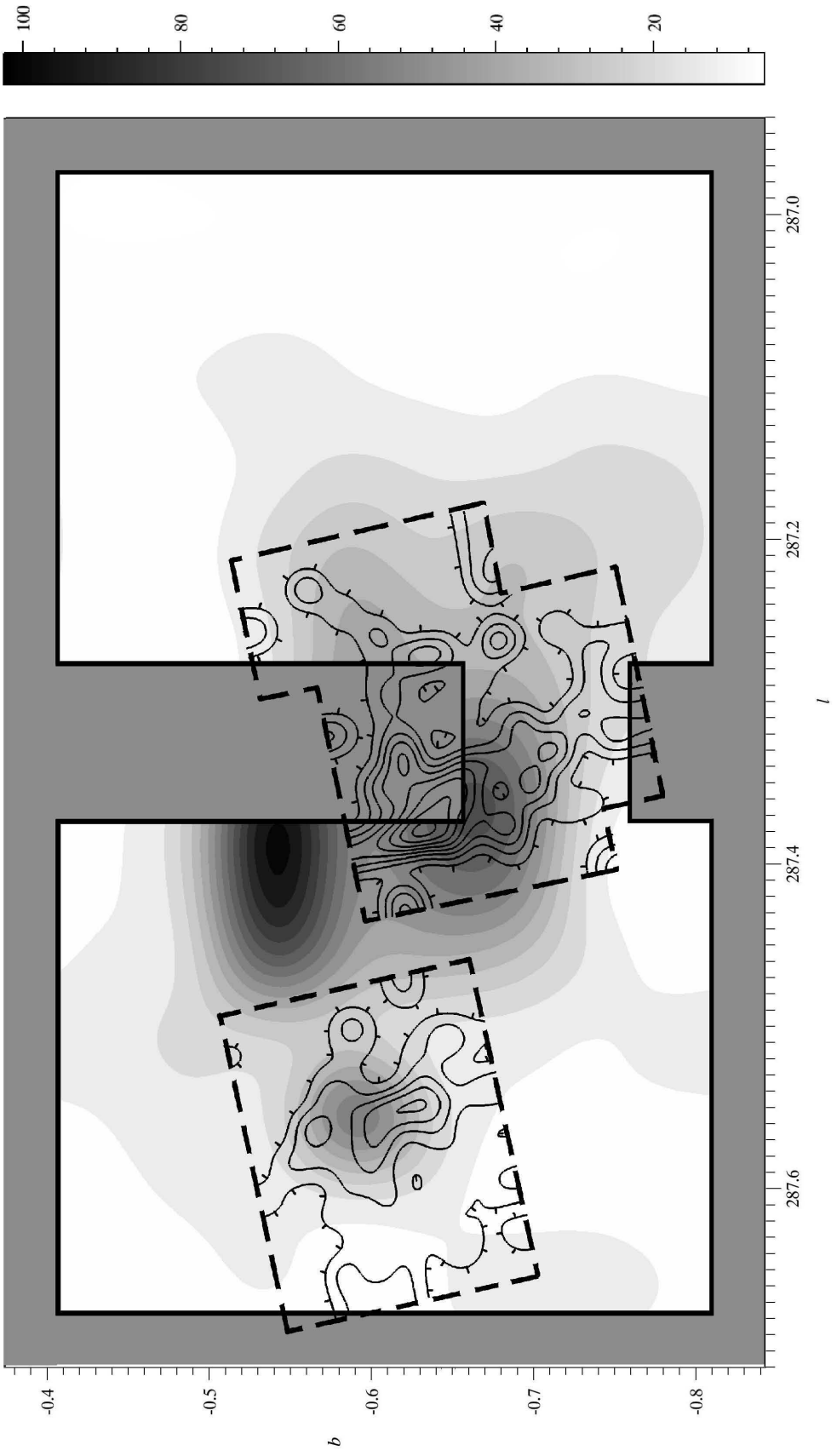
100
80
60
40
20
287.0
287.2
287.4
287.6
l
-0.4
-0.5
-0.6
-0.7
-0.8
q

Figure 2.20 *(following page)*: 205 μm [NII] and 146 μm [OI] Overlay

SPIFI [NII] 205 μm contours (corresponding to Figure 2.7) are overlaid on 146 μm [OI] grayscale contours (Figure 2.11).

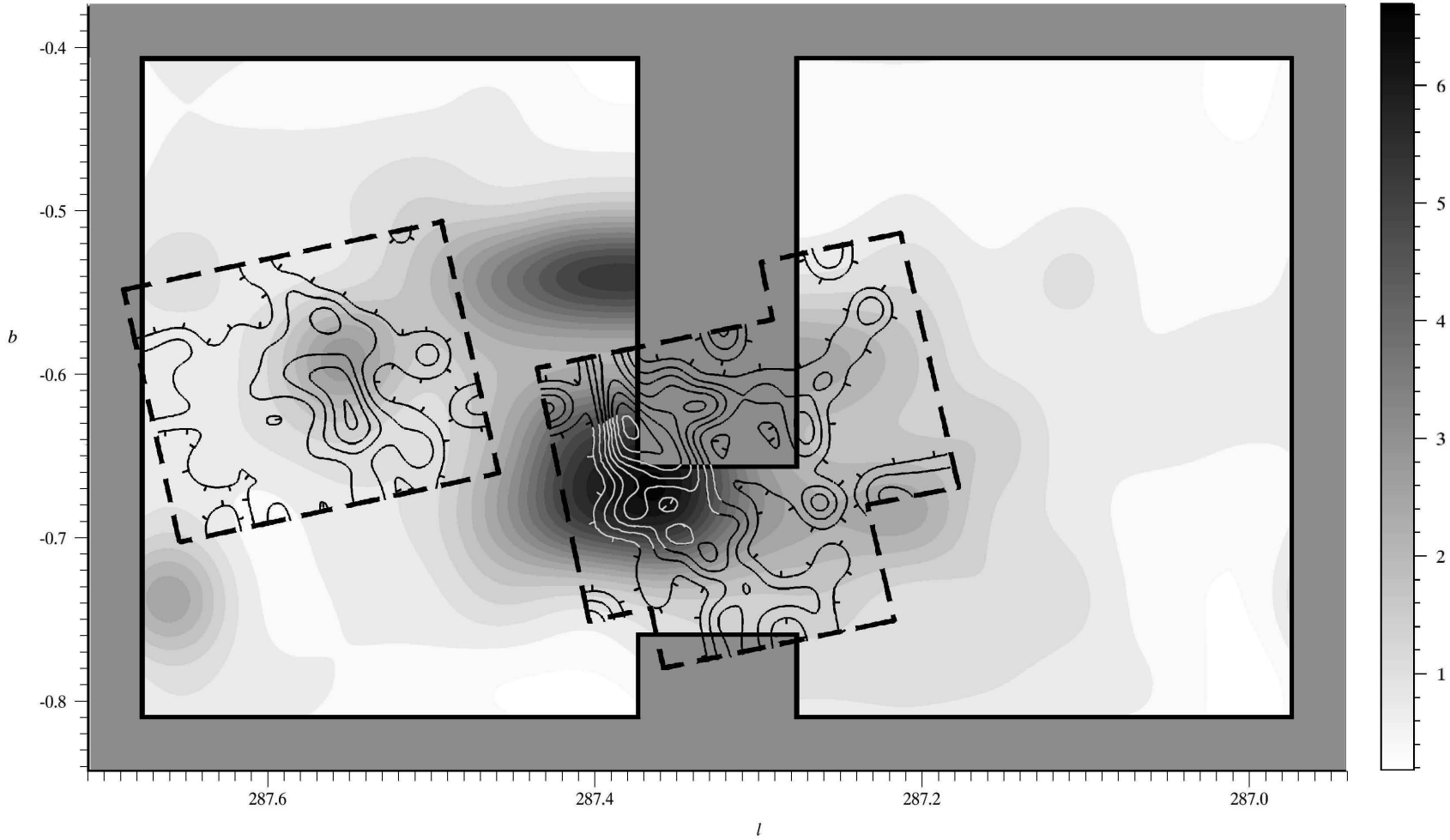
-0.4
-0.5
-0.6
-0.7
-0.8
b
287.6
287.4
287.2
287.0
l
6
5
4
3
2
1

Figure 2.21 *(following page)*: 205 μm [NII] and 158 μm [CII] Overlay

SPIFI [NII] 205 μm contours (corresponding to Figure 2.7) are overlaid on 158 μm [CII] grayscale contours (Figure 2.12).

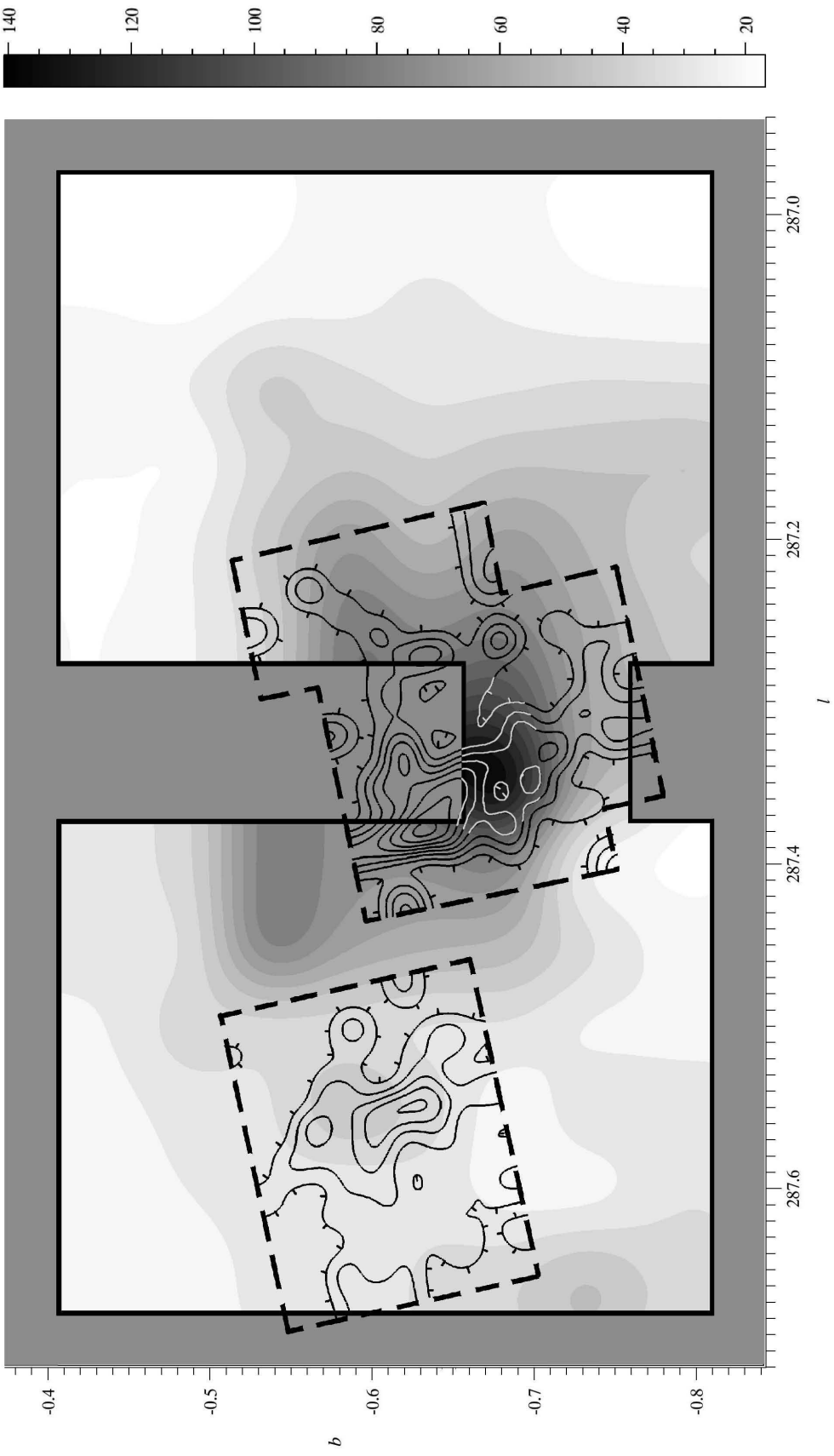
140
120
100
80
60
40
20
287.0
287.2
287.4
287.6
l
-0.4
-0.5
-0.6
-0.7
-0.8
q

Figures 2.19, 2.20, and 2.21 show SPIFI 205 μm [NII] contours overlayed on the 63 μm [OI], 146 μm [OI], and 158 μm [CII] ISO LWS maps produced in §2.5.2. Oxygen has an ionization potential of 13.62 eV, so [OI] arises entirely in the neutral ISM. Carbon, on the other hand, has an ionization potential of 11.26 eV, and can arise from both the neutral and ionized phases of the ISM. In the analysis of §2.6.3 below, we find that, on average, ~ 63 % of the C^+ arises from the neutral medium over the observed region of the Carina Nebula. In the overlays shown here, we see that the C^+ is morphologically much more akin to the plots of 63 and 146 μm [OI] than the [NII] contours. Of particular interest is the strong neutral peak seen in all three maps near the position of Tr 14 (G287.40-0.58), which is entirely absent from the ISO plots of the ionized gases 57 μm [NIII] and 122 μm [NII] (Tr 14 was not covered by the 205 μm [NII] SPIFI raster) and the thermal radio maps. This peak occurs in ISO raster position Car 2-7 (G287.405-0.536). The ratio of the 63 μm [OI] intensity to the 122 μm [NII] intensity at this location is 24.0, as compared to an average ratio of 4.5 over the map.

The KAO maps of 63 μm [OI] and 158 μm [CII] (Brooks *et al*. 2003) do not cover Tr 14. As an alternative tracer of PDRs, we look at infrared (IR) observations of the 3.29 PAH feature by the South Pole Infrared Explorer (SPIREX) telescope (Rathborne *et al*. 2002) and an 8 μm band (half-power width extending from 6.8 - 10.8 μm) image from the Midcourse Space Experiment (MSX), which captures flux from both the 7.7 – 7.9 μm and 8.6 μm PAH features (Figures 2.22 and 2.23). Slightly enhanced emission is seen in both observations near the ISO raster position Car 2-7, consistent with PDR activity at this location. However, the relative intensity of the PAH emission at this location to the PAH emission peak at Car I appears to be roughly 0.2, at best, whereas in 63 μm [OI] the emission there exceeds the 63 μm peaks at both Car I and Car II by factors of 1.67 and

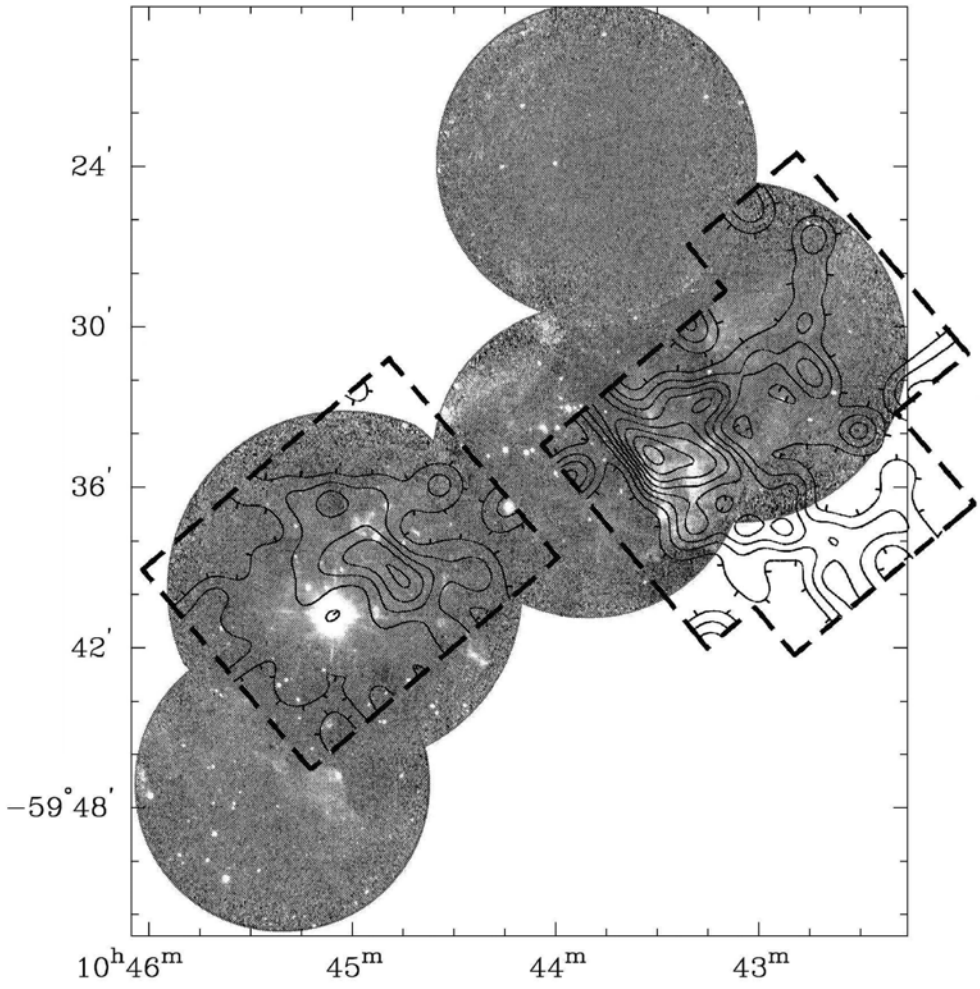

Figure 2.22: 205 μm [NII] and 3.29 μm PAH Emission Overlay
SPIFI [NII] 205 μm contours (corresponding to Figure 2.7) are overlaid on 3.29 μm PAH emission observed by the South Pole Infra-Red Explorer (SPIREX) telescope (Rathborne *et al*. 2002). The coordinate epoch is J2000. The beam size of the PAH image is 1.″4.

1.14, respectively (0.95 and 1.57 in 146 μm [OI]). The 63 μm [OI] line is enhanced in shocks, so one might consider invoking shock excitation for this line at the Tr 14 position. However, the [OI]/[CII] line ratio there is similar to other positions in the map, and the [CII] line is not enhanced by shocks. In terms of PDR parameters, this region is a peak not unlike other peaks in the neutral gas line maps. At low densities, the [NII] line intensities should scale as the emission

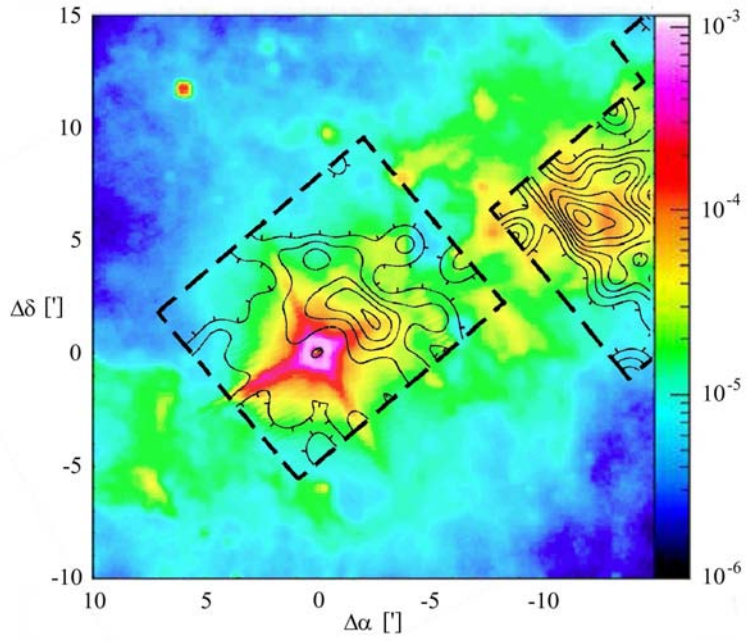

Figure 2.23: 205 μm [NII] and 8 μm Broadband Overlay
SPIFI [NII] 205 μm contours (corresponding to Figure 2.7) are overlaid on 8 μm broadband (half-power width extending from 6.8 – 10.8 μm) color-scale image from the Midcourse Space Experiment satellite observatory (MSX; Kramer *et al*. 2008). The image is centered at $10^h\,45^m\,3\overset{s}{.}59$ -59°41′04″.3 (J2000). The MSX beam size was 18″.3. The colorbar units are W m^{-2} sr^{-1}.

measure ($n_e^2\,d$), as does the radio free-free emission flux. At Tr 14, there is no peak in the free-free emission so that the large [OI]/[NII] ratio there likely just reflects less ionized gas in this region.

Of more general interest regarding the [OI], [CII] and PAH maps is that the Car I peak again lies slightly to the southwest of the 205 μm [NII] Car I peak – as it did in the [CI] map of Figure 2.18. This is consistent with a geometry in which we are viewing the Car I PDR edge-on, with the exciting FUV flux coming from Tr 14 (which lies ~ 2 pc to the northeast) and the PDR existing on the surface of the molecular cloud that extends to the south and west. As was the case for the ionized gas (*cf*. the 122 μm line, Figure 2.16), the tracers of photodissociated neutral gas extend well (several pc) to the south and west

of Car I, indicating either that the FUV flux of Tr 14 penetrates deep into the GMC, or that a large fraction of the GMC surface (perpendicular to our line of sight) has undergone some photodissociation. At Car II, the neutral gas peak is relatively much weaker compared to Car I than was the case for the ionized gas. This is consistent with the suggestions above (page 146) that the neutral gas associated with the Tr 16 cluster has been photoionized and/or dispersed to a larger extent than that associated with the Tr 14 cluster, since the former cluster is ~ 1 Myr older.

2.6.2 The Density of the Ionized Medium

The ratio of the 122 μm to 205 μm [NII] line intensities is an excellent density probe of diffuse weakly-ionized gas in the ISM. The [NII] fine-structure lines have critical densities for thermalization (via electron collision de-excitation) of $n_e \sim 44\ \mathrm{cm}^{-3}$ and $293\ \mathrm{cm}^{-3}$ at $T = 8000$ K for the 205 and 122 μm lines, respectively, so that the 122 to 205 μm line intensity ratio is sensitive to gas densities of $n_e \lesssim 300\ \mathrm{cm}^{-3}$. In terms of ionization potentials, it takes relatively low energy photons (14.53 eV) to form N^+, so that these lines arise in the lower ionization "outskirts" of HII regions.

We have used the ratio of the 122 μm [NII] line intensity from ISO to the 205 μm [NII] line intensity from SPIFI to derive the electron density of the diffuse low-ionization gas component in the Carina Nebula. The SPIFI and ISO rasters do not spatially match (Figure 2.3), so a direct division of the 122 μm and 205 μm [NII] intensity maps was not possible. However, because the SPIFI map is more densely sampled than the ISO map, every observed ISO beam falling within the

SPIFI raster boundaries is overlapped by one or more observed SPIFI beams. We interpolated the 205 μm [NII] intensities from these overlapping beams to the center of each ISO beam, averaged and weighted by the SPIFI beam profiles and noises (similar to the method used to create the contour plots; §2.4.2). We emphasize that we only include measurements for which there was a direct overlap of SPIFI and ISO beams, which amounts to 27 ISO raster positions across the nebula. Finally, we divide the 122 μm ISO intensities at these positions by the interpolated 205 μm intensities to determine the line ratios.

To derive electron densities, we have calculated the theoretical [NII] 122 μm to 205 μm line intensity ratio as a function of gas density assuming electron impact excitation and using the collision strengths from Hudson & Bell (2004), scaled to an assumed electron temperature of 8000 K. We plot both the theoretical curve and our data points along this curve in Figure 2.24 (solid line and circles). The average electron density in the low-ionization gas is found to be a modest $n_e \sim 29$ cm^{-3}, with little spatial variation over the nebula. This average value is close to the value previously determined at the Car II peak ($n_e \sim 32$ cm^{-3}, Oberst *et al*. 2006).

Using the intensity ratio of the higher ionization 52 and 88 μm [OIII] lines, Mizutani *et al*. (2002) found two distinct components to the electron density in the Carina Nebula: a high-density ($n_e \sim 100 - 350$ cm^{-3}) component at Car I and II, and an extended low-density (ELD; $n_e < 100$ cm^{-3}) component detectable over the entire ~ 30 pc mapped region. From our measurement of the 122/205 [NII] ratio, it is clear the ELD "halo" also contains gas of lower ionization states.

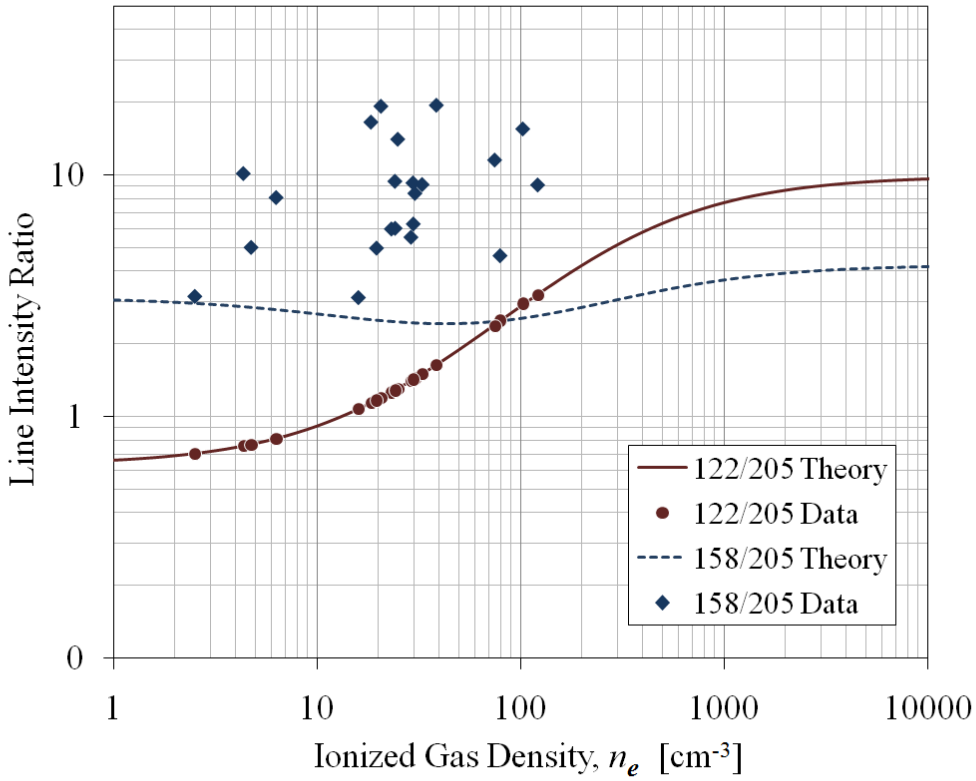

Figure 2.24: [CII] and [NII] Line Intensity Ratios in the Carina Nebula

Theoretical and measured values of observed line intensity ratios are plotted versus the electron density of the ionized medium. The 122/205 μm [NII] line ratio theoretical curve and data are shown as the (red) solid line and circles, respectively, and the 158 μm [CII] to 205 μm [NII] ratio theoretical curve and data are shown as the (blue) dashed line and diamonds, respectively. The 122/205 μm data and theory coincide because the theoretical curve was used to derive the electron densities from the measured line ratios (see text). Error bars are omitted for clarity, but follow directly from the errors provided in Tables 2.4, 2.5, and 2.6.

2.6.3 The fraction of C^+ from PDRs

C^+ has an ionization potential of 11.26 eV, and hence can arise from both PDRs and HII regions. Because the 158 μm [CII] line is often the brightest FIR line, and is a dominant coolant for much of the ISM, determining the fraction of the observed [CII] line radiation that arises from the neutral and ionized gas components is critical to the study of star-forming regions. Our observations of

205 μm [NII] provide a direct means to measure this abundance ratio: since the critical densities for electron impact excitation of the 158 μm [CII] and 205 μm [NII] lines are very similar (40 and 44 cm^{-3} respectively), to a good approximation the $I([\mathrm{NII}]\,205\,\mu\mathrm{m})/I([\mathrm{CII}]\,158\,\mu\mathrm{m})$ line intensity ratio is dependent only on the relative abundance of C^+ and N^+ in the ionized medium.

Using the collision rates for exciting the ground-state levels of C^+ from Blum & Pradhan (1992), we plot the expected ratio of the two lines as a function of electron density in Figure 2.24 (dashed line). The temperature dependence is quite small, as the levels are only 91 and 70 K above ground, respectively – small compared with the temperature (8000 K) of an HII region. For the calculation, we take the gas-phase abundances of $\mathrm{C/H} = 1.4 \times 10^{-4}$ (Kaufman *et al*. 1999) and $\mathrm{N/H} = 7.8 \times 10^{-5}$ (Savage & Sembach 1996) and correct for the fraction of the two elements expected in the first ionization state using the HII region models of Rubin (1985). The line ratio from ionized gas is 3.1 at low densities and 4.3 at high densities, and dips to below 3 between densities of $n_e \sim 20$ and 100 cm^{-3} since the upper $J = 2$ level of the N^+ begins to be significantly populated at densities above $n_e \sim 20$ cm^{-3}.

As in our determination of the $I([\mathrm{NII}]\,122\,\mu\mathrm{m})/I([\mathrm{NII}]\,205\,\mu\mathrm{m})$ line intensity ratio in §2.6.2 above, we interpolate the SPIFI 205 μm [NII] observations to the centers of the 27 ISO beams that overlap the SPIFI raster, and then divide the 158 μm [CII] intensities at these positions by the interpolated 205 μm [NII] to determine the line ratios. With the electron density taken as that derived from the $I([\mathrm{NII}]\,122\,\mu\mathrm{m})/I([\mathrm{NII}]\,205\,\mu\mathrm{m})$ ratio, the $I([\mathrm{CII}]\,158\,\mu\mathrm{m})/I([\mathrm{NII}]\,205\,\mu\mathrm{m})$ ratio data points are plotted in Figure 2.24 (diamonds). All of the data lie above the theoretical curve, indicating that some fraction of the C^+ arises from the neutral

medium at every position. For each point, the ratio of the expected to measured value represents the fraction of C^+ which arises from the ionized gas. The remaining fraction must arise from the PDRs. Over the regions in which the SPIFI and ISO rasters overlap, we find that, on average, 63 % of the C^+ comes from PDRs and 37 % from the ionized gas. This result agrees with previous studies which contend that the majority of the observed [CII] line emission from Galactic star-forming regions, the Galaxy as a whole, and from external galaxies arises in warm dense PDRs on the surfaces of molecular gas clouds (*e.g.* Crawford *et al.* 1985; Stacey *et al.* 1985, 1991; Shibai *et al.* 1991; Wright *et al.* 1991)

The percentage of C^+ arising from PDRs has been plotted as a contour map in Figure 2.25, and these contours are compared with the location of major sources in the Carina Nebula in Figure 2.26. The contours show interesting spatial variation. In particular, we note that the contour minima – which correspond to a larger fraction of the 158 μm [CII] arising from ionized gas – generally occur in regions that have relatively little background molecular ISM, so no PDR is formed. This is most obvious for the minima centered at roughly $(l, b) \sim (287.6, -0.65)$, near the center of the Tr 16 star cluster, where winds from stellar members have ionized or swept away nearly all of the gas and dust. The contour maxima, on the other hand – which correspond to a larger fraction of the 158 μm [CII] arising from PDRs – generally occur in regions where the ionizing flux impinges on molecular clouds, so that PDRs are formed. The highest contour, for instance, occurs for $l < 287.25$, coinciding with the regions of stronger 115 GHz ^{12}CO(1→0) emission from Carina's westerly GMC (Brooks *et al.* 1998).

Figure 2.25 *(following page)*: The Fraction of 158 μm [CII] in PDRs

This map shows inverse-grayscale contours of the percentage of 158 μm [CII] emission arising from PDRs, as derived from the 158 μm [CII] to 205 μm [NII] line intensity ratio data (see Figure 2.24). Contours are drawn every 10 %. The map has been re-sampled and smoothed with a Gaussian filter matching the 70.″1 ISO beam at 158 μm, and the maxima are thus slightly attenuated. Data are only available where the SPIFI and ISO rasters overlap (the intersection of the regions outlined in solid and dotted lines).

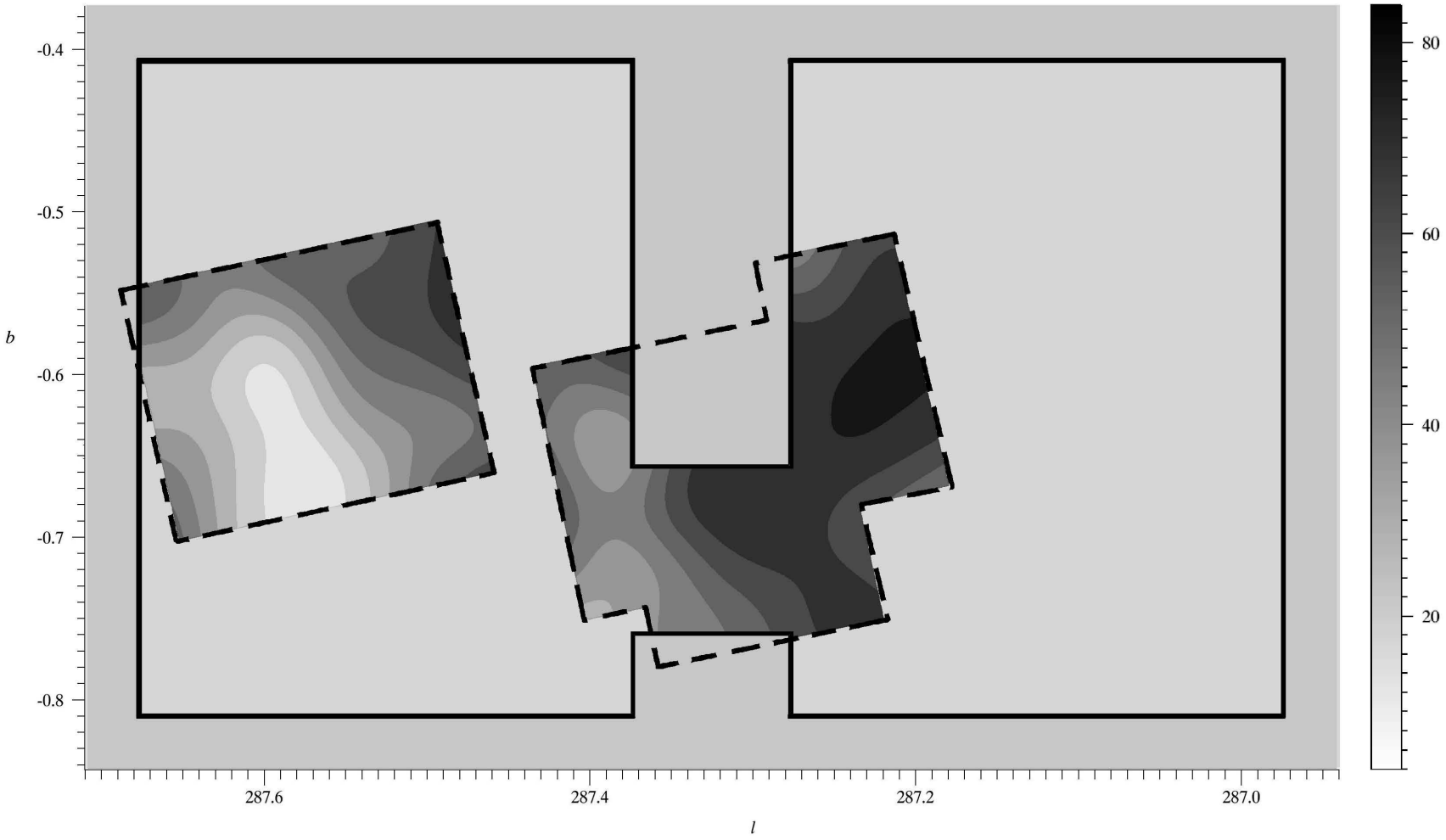
-0.4
-0.5
-0.6
-0.7
-0.8
b
287.6
287.4
287.2
287.0
l
80
60
40
20

Figure 2.26 *(following page)*: Morphological Comparison of Carina Sources with the Fraction of 158 μm [CII] in PDRs

Here we see Figure 2.1, showing major sources in the Carina Nebula, overlaid on Figure 2.25, showing grayscale contours of the percentage of 158 μm [CII] emission arising from PDRs.

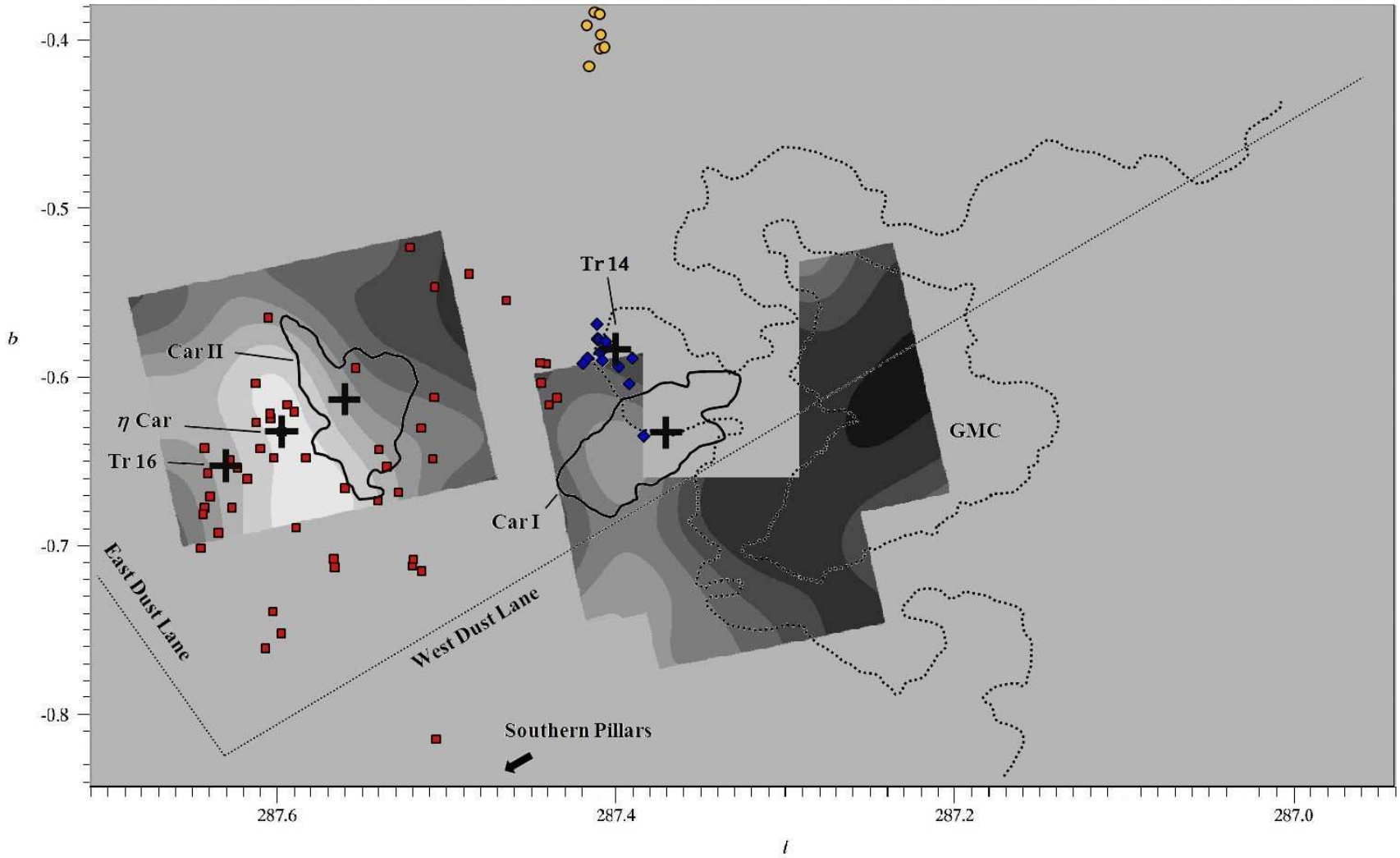
-0.4
-0.5
-0.6
-0.7
-0.8
b
Car II
η Car
Tr 16
Tr 14
Car I
GMC
East Dust Lane
West Dust Lane
Southern Pillars
287.6
287.4
287.2
287.0
l

2.6.4 PDR Model

The PDR model put forth by Tielens & Hollenbach (1985) and refined by Kaufman *et al*. (1999) has shown good agreement with observations for a wide variety of astrophysical environments (*e.g.* Hollenbach & Tielens 1997, 1999, and references therein). In their model, the PDR is taken as a homogeneous infinite plane slab of hydrogen nuclei density n_H, with an incident FUV (6 eV $< h\nu <$ 13.6 eV) parameterized in units of the local interstellar radiation field, G_0 (1.6×10^{-6} W m^{-2}; Habing 1968). The model assumes a number of fixed parameters, including the elemental,[7] PAH, and dust abundances (relative to hydrogen), absorption properties, and a Gaussian turbulent velocity field. The defining aspect of the model is the gas heating mechanism: about 10 % of the incident FUV photons eject hot photoelectrons from the dust grains and PAH molecules, and these electrons collisionally heat the gas. The gas subsequently cools via FIR fine-structure line emission. Finally, the model is solved simultaneously for chemical and energy equilibrium in the slab, and the fine-structure emission of the various chemical species is predicted. The model can also be inverted, such that observed intensities of fine-structure lines can be used to determine $n_{\rm H}$ and G_0.

We have modeled $n_{\rm H}$ and G_0 over the 100 ISO raster positions in the Carina Nebula using the LWS observations of the fine-structure lines of 63 μm [OI], 146 μm [OI], and 158 μm [CII] (§2.5.2), as well as the FIR intensity derived from a graybody fit to the entire LWS spectrum by Mizutani *et al*. (2004). The 158 μm [CII] intensities have been corrected for the fraction arising from the ionized medium (*i.e.* the 158 μm [CII] line intensities used in the PDR model have had

[7] C/H = 1.4×10^{-4} and O/H = 3.0×10^{-4} (see Kaufman *et al*. 1999, Table 1).

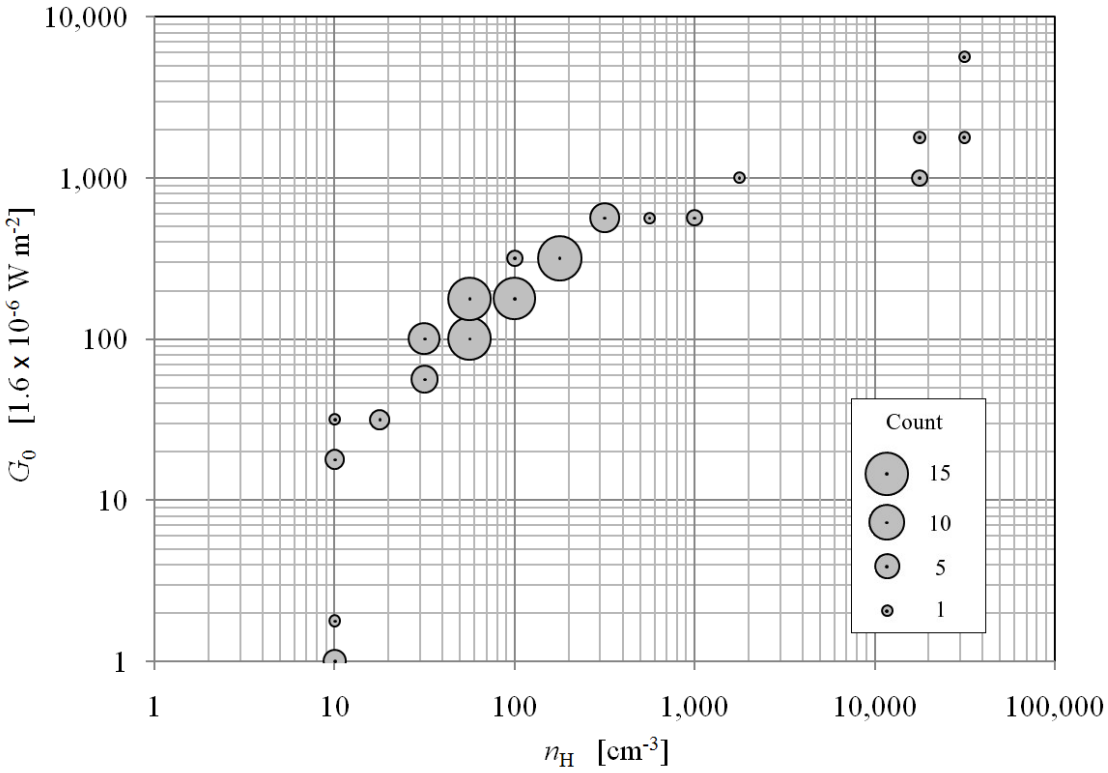

Figure 2.27: PDR model for Carina: G_0 vs. n_H

The FUV (6 eV < E < 13.6 eV) flux in units of the local interstellar radiation field, G_0 (1.6 $\times 10^{-6}$ W m^{-2}; Habing 1968), is plotted versus the hydrogen nucleus density, n_H (cm^{-3}), for the region of the Carina Nebula mapped by ISO (Figure 2.3). The data points were calculated using the PDR model of Kaufman *et al*. (1999) with the ratios of the ISO line intensities of 63 and 146 μm [OI] and 158 μm [CII] (from the present work), and the ISO FIR continuum intensity (from Mizutani *et al*. 2004). The calculations were performed with the online *PDR Toolbox* (PDRT; Pound & Wolfire 2008). Because the PDRT solution space is quantized (in four equal divisions per decade on a logarithmic scale), the relative areas of circles placed around each data point are used to indicate the number of raster positions (out of the 100 total observed by ISO) yielding each (n_H, G_0) solution.

the fraction arising from the ionized medium subtracted; see §2.6.3). The calculations were performed with the online *PDR Toolbox* (PDRT; Pound & Wolfire 2008).[8] The standard set of model parameters was assumed (see Kaufman *et al.* 1999), and the calculator searched for the best fit of $n_{\rm H}$ and G_0 to the combined intensity ratios of 63/146 μm [OI], 63/158 μm [OI]/[CII], 146/158 μm [OI]/[CII], and (63+158)/FIR.

Our PDR model results are shown in Figure 2.27. The solution space of the PDRT is quantized in four equal divisions per decade on a logarithmic scale, resulting in recurrences of the same $n_{\rm H}$ and G_0 values for several of the beam positions. To show this effect, circles are plotted around each data point, where the areas of the circles are proportional to the number of ISO raster positions yielding each solution. From the plot, we see that over most of the nebula $10 < n_H < 1000$ cm^{-3} and $10 < G_0 < 1000$. The maximum is $(n_H, G_0) = (31600, 5620)$, but the average is (1250, 303). The data follow a clear trend, which can be fit by the power law $G_0 = 4.84\, n_H^{0.74}$. The values found for Carina lie near the low end of observed galactic star-forming regions, in which $n_{\rm H}$ and G_0 are both typically $\sim$ 10,000 or more. Rather, we find that Carina is more akin to the giant star-forming region of 30 Doradus in the Large Magellanic Cloud (see §2.6.7).

[8] http://dustem.astro.umd.edu/pdrt/index.html

Figure 2.28 *(following page)*: FUV Radiation Field (G_0) Map of the Carina Nebula

The FUV (6 eV < E < 13.6 eV) flux in the units of the local interstellar radiation field, G_0 (1.6×10^{-6} W m^{-2}; Habing 1968) is mapped over the Carina Nebula. Contour levels are shown every 5 % of the peak flux (1514). The map has been re-sampled and smoothed with a Gaussian filter of FWHM = 79.′3, the average LWS beam.

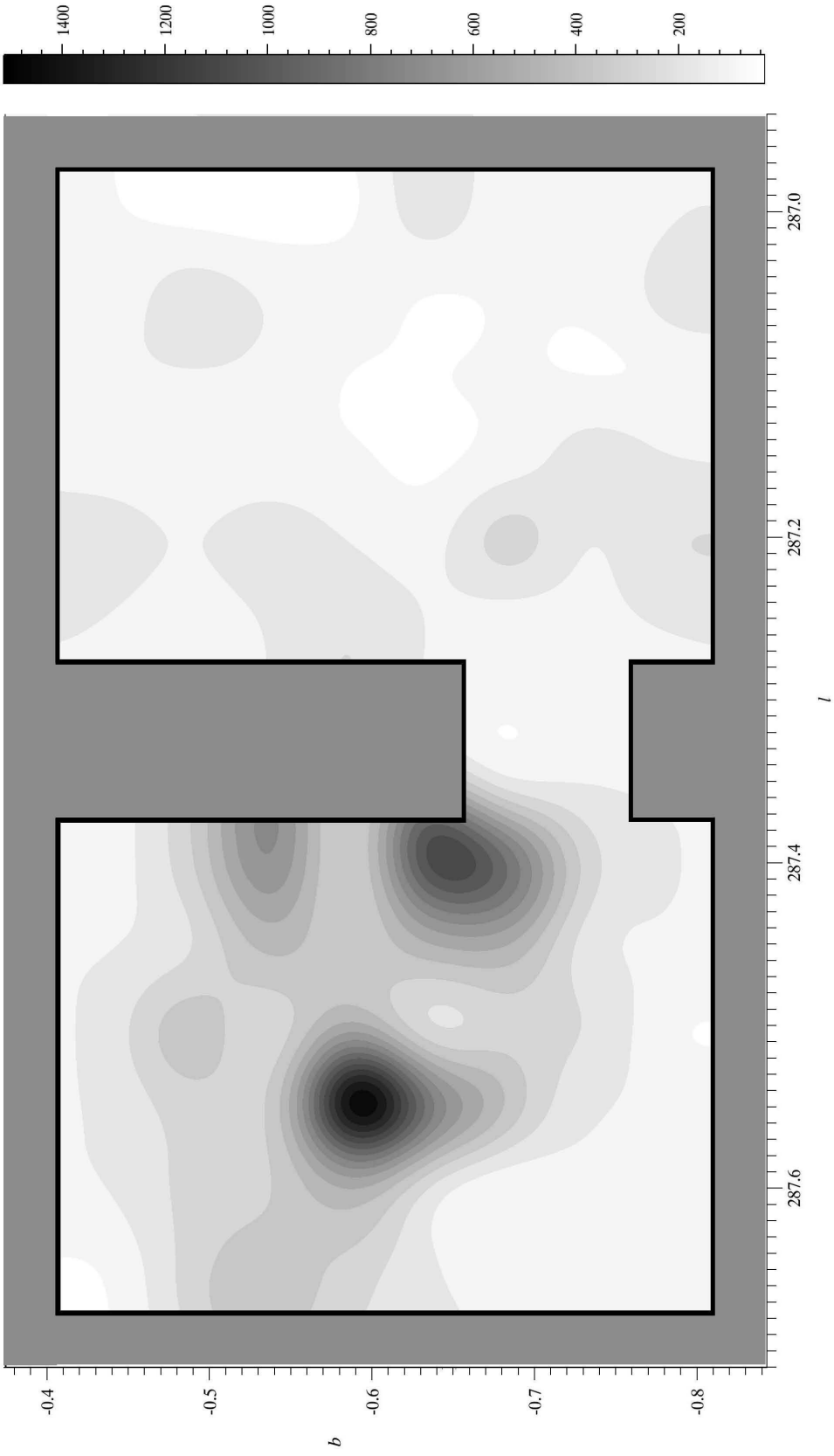
1400
1200
1000
800
600
400
200
287.0
287.2
287.4
287.6
l
-0.4
-0.5
-0.6
-0.7
-0.8
b

Figure 2.29 *(following page)*: n_H Map of the Carina Nebula

The hydrogen nuclei density, $n_{\rm H}$, in units of $\rm cm^{-3}$, is mapped over the Carina Nebula. Contour levels are shown every 2.5 % of the peak density (5905 $\rm cm^{-3}$). The map has been re-sampled and smoothed with a Gaussian filter of FWHM = 79.″3, the average LWS beam.

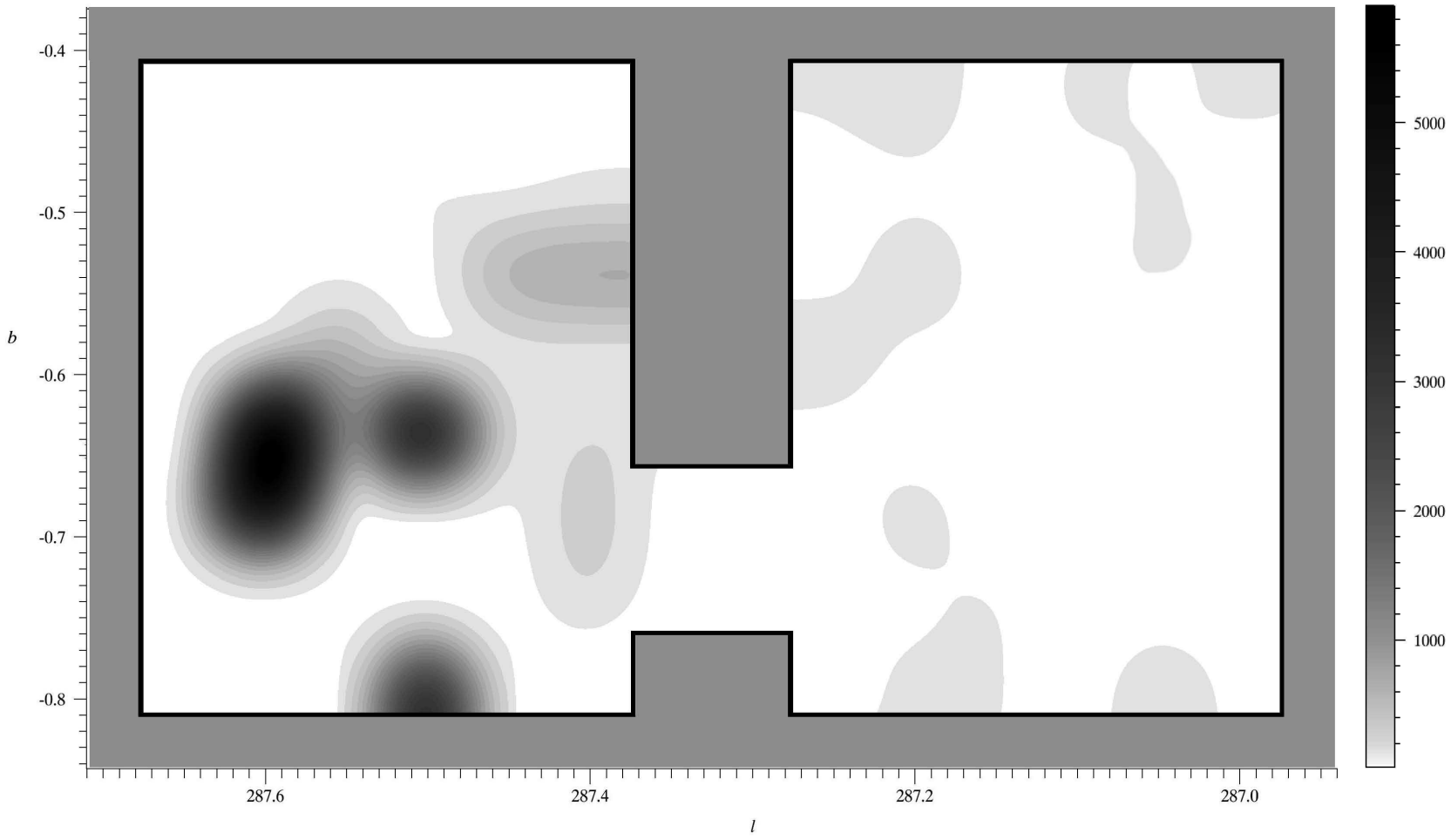
-0.4
-0.5
-0.6
-0.7
-0.8
b
287.6
287.4
287.2
287.0
l
5000
4000
3000
2000
1000

The modeled G_0 and $n_{\rm H}$ values over Carina have been plotted as contours in Figures 2.28 and 2.29. The morphology of the G_0 distribution roughly follows the PDR emission (*cf.* Figures 2.19 – 2.23), with the G_0 fields peaking near the positions of Car I, Car II/η Car, and just north of Tr 14. The strongest G_0 is found in the vicinity of Car II, as would be expected from the collection of massive early-type stars there (η Car and Tr 16). Little G_0 flux is seen westward of $l \sim 287.3$, in the GMC. In its lower level contours, $n_{\rm H}$ shows a similar morphology to G_0. However, the eastern peaks (in the vicinity of η Car and Car II) are significantly larger relative to those at Car I and Tr 14. One explanation is the proximity of the dense Homunculus and Car II molecular cloud remnant to the strong G_0 flux in these locations, so relatively higher density PDRs might be expected near these sources.

The values of $n_{\rm H}$ and G_0 for sources within Carina and for other galactic and extragalactic sources are compared in §2.6.7. PDR surface temperatures, which are an additional output of the Kaufman *et al*. (1999) model, are also presented there.

2.6.5 Photoelectric Heating Efficiency

In PDR models of Tielens & Hollenbach (1985) and Kaufman *et al*. (1999), FUV (6 eV $< E <$ 13.6 eV) photons from early-type stars are absorbed by dust. Most of the photon energy heats the dust, but a small fraction ($\sim$ 10 %) of the photons eject energetic electrons from the dust grains. These photoelectrons carry away roughly 10 % of the "ionizing" photon energy, and subsequently collisionally

exite the gas species in the PDR. Thus, the net gas heating efficiency in PDRs is on the order of 1 % or less.

After being heated, the dust cools primarily through (graybody) FIR continuum radiation and the gas cools primarily through FIR fine-structure line emission. The most important of these cooling lines are the 158 μm [CII] and 63 μm [OI] lines. Tielens & Hollenbach (1985) found that the 158 μm [CII] emission dominates for hydrogen nuclei densities of $n_{\rm H} < 10^3$ cm^{-3} and temperatures of $T < 10^4$ K, while [OI] dominates for $n_{\rm H} > 10^4$ cm^{-3} and $T > 10^2$ K. Because they are the primary PDR coolants, the ratio of the combined intensities of the 63 and 158 μm lines to that of the total FIR continuum intensity, $[I(63\,\mu{\rm m}) + I(158\,\mu{\rm m})]/I({\rm FIR})$, is often used as a measure of the efficiency of the photoelectric heating of the gas (*i.e.* the ratio of the gas to dust heating) in PDRs, ϵ.

Using the observed intensities of 158 μm [CII] and 63 μm [OI] from the ISO LWS (from the present work, with the 158 μm [CII] intensity again corrected for the fraction of C^+ arising in the ionized medium; §2.6.3), and the FIR intensity derived from a graybody fit to the entire LWS spectrum (from Mizutani *et al*. 2004), we have calculated the photoelectric heating efficiency, ϵ, in the Carina Nebula. The values are plotted against G_0 in Figure 2.30 (left panel). (In this plot, note that G_0 is not a truly independent variable, since the 63 μm [OI] and 158 μm [CII] line intensities were used to derive G_0.) Values range from $\epsilon \sim 6 \times 10^{-4}$ to 6×10^{-3} with an average of 3.42×10^{-3}. These values are typical for Galactic star formation regions exposed to moderate ($G_0 \sim 100 - 1000$) FUV fields (*cf.* Stacey *et al*. 1991), and agree well with previous Carina studies: for example Mizutani *et al*. (2004) find $0.0006 < \epsilon < 0.012$, and Brooks *et al*. (2003) find $\epsilon \sim 5 \times 10^{-3}$.

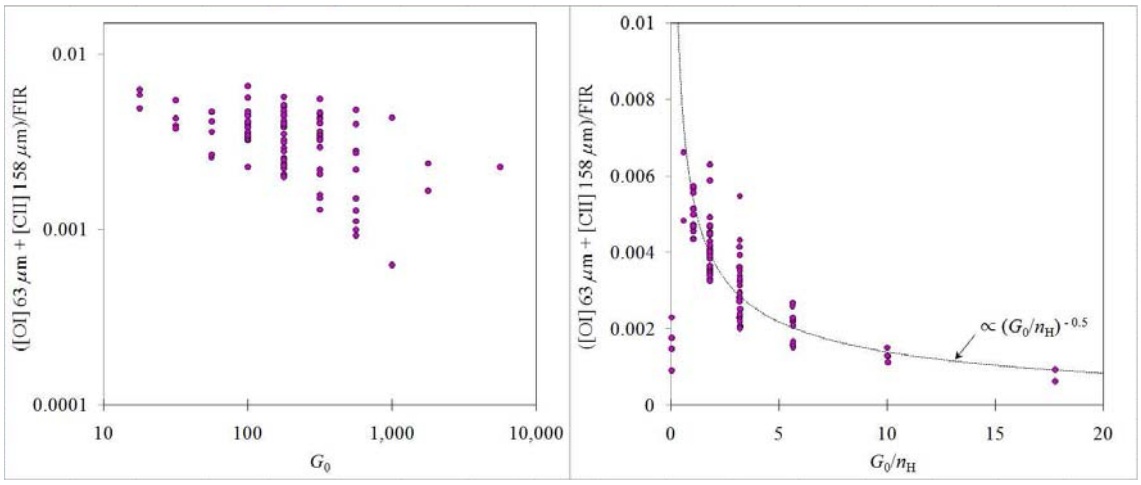

Figure 2.30: Photoelectric Heating Efficiency

The photoelectric heating efficiency, $[I(63\,\mu\text{m}) + I(158\,\mu\text{m})]/I(\text{FIR})$, is plotted as a function of G_0 (left panel) and G_0/n_H (right panel) for the Carina Nebula. The fine-structure line intensities of 63 μm [OI] and 158 μm [CII] were observed by the ISO LWS (§2.2.2 and §2.5.2), and the FIR intensity was derived by Mizutani *et al*. (2004) using a graybody fit to the entire LWS spectrum. The quantization of the data in G_0 is due to the quantization of the solution space of the PDRT calculator (see §2.6.4). A reasonable (but not unique) fit to the data is given by a function $\propto (G_0/n_\text{H})^{-0.5}$. (Note that the x-axis variables in both plots are not truly independent variables, since the 63 μm [OI] and 158 μm [CII] line intensities were used to derive G_0.)

According to PDR models, the photoelectric heating efficiency varies roughly as $(G_0/n_\text{H})^{-\alpha}$ for the range $10^2 < G_0 < 10^4$ and $10^2 < n_\text{H} < 10^4$ cm^{-3}, where $0.5 < \alpha < 1$ (*e.g.* Wolfire *et al*. 1990). In Figure 2.30 (right panel) we plot the photoelectric heating efficiency as a function of G_0/n_H. (Again, in this plot, note that G_0/n_H is not a truly independent variable, since the 63 μm [OI] and 158 μm [CII] line intensities were used to derive G_0.) Although the data did not provide a unique fit, they could be reasonably fit by a function $\propto (G_0/n_\text{H})^{-\alpha}$ with α near the lower end of the range suggested by PDR models. One such fit is shown for $\alpha = 0.5$. We note that several of our n_H and G_0 values are at the lower end of the limits for which this fitting function has been suggested.

2.6.6 Kinematics

Previous kinematic studies of the Carina Nebula have consistently found two large-scale effects:

(1) Spectral lines near Car II show strong line splitting, while spectral lines near Car I are single-profiled. The double-peak profiles near Car II have been interpreted as arising from an expanding bubble of hot ionized gas, likely centered on Tr 16 or η Car. Thus, along our line of sight we see spectral lines split into the approaching (blueshifted) near side of the bubble and the receeding (redshifted) far side of the bubble. Car I, on the other hand, which shows only single spectral profiles, has been interpreted as an HII region which is expanding only into the GMC which wraps beneath and behind it (mostly receeding along our line of sight), while the foreground is largely devoid of gas and dust. Using the highly spectrally-resolved observations of the radio recombination lines of 6 cm H 109α and 3.4 cm H 90α reported in Huchtmeier & Day (1975), we estimate the average centroids of the two peaks of the nebula's double-peaked profiles to be -32.5 km s^{-1} and -5.4 km s^{-1} (with an average peak separation of 27.1 km s^{-1}). Line splitting near Car II has also been observed by Zhang *et al*. (2001) (in the submm lines of ^{12}CO(4→3) and [CI]), Deharveng & Maucherat (1975) (in several optical lines), and Gardner *et al*. (1970) (in several radio recombination lines).

(2) Radial velocities measured in Car II are more negative than those in Car I (for the split profiles, the radial velocity referred to here is the average centroid of the two peaks). Thus, it appears that Car II is approaching slightly faster than Car I along our line of sight. Huchtmeier & Day (1975) report a radial velocity of $\sim$ -24 km s^{-1} at Car II and $\sim$ -16 km s^{-1} at Car I, with a monotonic gradient between the two positions. Velocity channel maps of the H 110α radio

recombination line observed by Brooks *et al.* (2001) show peak emission in Car II in the velocity channel centered at -28 km s^{-1}, and peak emission in Car I in the velocity channel centered at -16 km s^{-1} (the velocity resolution of these channel maps is 4 km s^{-1}).

Given the SNR at an individual position in our 205 μm [NII] map, the resolving power of SPIFI is insufficient to provide useful constraints on line widths and velocity centroids in the 205 μm [NII] spectra at any one spatial position. However, when averaged over several beams, sufficient SNR is obtained, and we find that our 205 μm [NII] data shows good agreement with the two kinematic effects discussed above. In §2.6.7, the intrinsic line widths and velocities of our 205 μm [NII] spectra are averaged over key sources within the Carina Nebula, including Car I and Car II. The results – which can also be found in Table 2.7 – are discussed here:

Line Widths Although SPIFI cannot spectrally resolve the line splitting discussed above, we might expect to see unresolved (single-profile) peaks at Car II which are wider than single-profile peaks elsewhere in the nebula. In particular, we might expect to see unresolved line widths near Car II of 27.9 km s^{-1} (the average width per peak in the split radio profiles) + 27.1 km s^{-1} (the average peak separation in the split radio profiles) = 55.0 km s^{-1}. Near Car I, on the other hand, we might expect to see line widths similar to the average radio recombination line width at Car I of 45.0 km s^{-1}.

Before making this comparison, the intrinsic line width must be recovered by de-convolving the FWHMs of SPIFI's spectra with the spectral profile of the instrument. SPIFI's instrument profile is dominated by the Lorentzian profile

of the HOFPI, which has a FWHM of $\Gamma \sim 71.6$ km s^{-1}. We assume the intrinsic profiles of the astrophysical lines to be Gaussian. Thus, to recover the intrinsic line widths, we must deconvolve a Lorentzian and Gaussian. For this, we use the approximation of Lee (1977), which gives the relation between a Lorentzian FWHM, Γ_L, and Gaussian FWHM, Γ_G, which would result in a convolved line width of unity:

$$\Gamma_L \approx 1 - 1.12\,\Gamma_G^2 + 0.12\,\Gamma_G^3 \tag{2.14}$$

Thus, if Γ_L and Γ_G are both normalized to the convolved line width, this equation provides a quick and easy means of deriving one from the other. For example, the average measured width of the 205 μm [NII] line over the entire Carina Nebula is 88.2 km s^{-1}. Therefore, the normalized width of the instrument's Lorentzian profile is $\Gamma_L = 71.6/88.2$. Plugging this value into Equation 2.14, the intrinsic line width is found to be $\Gamma_G = 0.427$, which is also normalized to the convolved line width. Finally, taking the product 0.427×88.2 km s^{-1} = 37.7 km s^{-1}, we recover the average intrinsic line width over the Carina Nebula.

Using this method, the SPIFI 205 μm [NII] spectra give an average intrinsic line width of 55.3 km s^{-1} at Car II and 40.9 km s^{-1} at Car I, in very good agreement with the values of 55.0 km s^{-1} and 45.0 km s^{-1} expected from the preexisting radio data. Full results for the Carina Nebula are provided in Table 2.7.

Radial Velocities We find the average radial velocities of the 205 μm [NII] lines near Car I and Car II to be -24.8 km s^{-1} and -30.4 km s^{-1}, respectively (Table 2.7). These values are somewhat more negative than the average radial

velocities found in the radio data of Huchtmeier and Day (1975) (-16 km s^{-1} and -24 km s^{-1} for Car I and II, respectively). However, both data sets are in agreement that Car II is approaching slightly faster than Car I along our line of sight. It is likely that this ~ -7.5 km s^{-1} (~ 10 % of a SPIFI resolution element) blueshift of the SPIFI data relative to the radio data is the result of imperfect velocity calibration in our system. Our method of calibration against poorly collimated laser lines will always result in a small blueshift of the (collimated) lines from astronomical sources (see §2.3.3). Taking into account such effects, the radial velocities we observed are in very good agreement with those of the radio recombination lines.

2.6.7 Comparison of Sources

To compare the contributions from various sources within Carina to one another and to other galactic and extragalactic sources, we have averaged our data over six spatial "bins" corresponding to Car I and II, Tr 14 and 16, η Car, and the westerly GMC. The results are shown in Table 2.7, where the sources are listed in order of decreasing galactic longitude, *l*. We have also included averages over the whole nebula. With the exception of η Car, all of these sources are extended realtive our beam size (54″ for SPIFI and ~ 80″ for ISO), and thus had to be averaged over several raster positions. The raster positions assigned to each source were chosen by proximity to the nominal central position of the source (see Figure 2.1) and multi-wavelength morphological considerations (see §2.6.1). Our assignments are as follows (*cf.* Tables 2.4, 2.5, and 2.6):

- *Tr 16*: ISO Car 4 (17, 18, 24); SPIFI Car II (1-5, 10-14, 19-22, 23-30)
- *η Car*: ISO Car 4 (23); SPIFI Car II (31)

- *Car II*: ISO Car 2 (4) and Car 4 (22); SPIFI Car II (48-51, 57-60, 66-69)
- *Tr 14*: ISO Car 2 (1, 7, 8); SPIFI Car I (9, 18, 29, 40)
- *Car I*: ISO Car 4 (19) and Car 6 (7); SPIFI Car I (16, 24-28, 34-39, 44-49)
- *GMC*: ISO Car 1 (1-24), Car 3 (1-24), and Car 6 (1, 2, 4, 5); SPIFI Car I (52-137)

For each of these sources, Table 2.7 includes the average measured line intensities (from §2.5.1 and §2.5.2) as well as the average measured radial velocities (R.V.) and intrinsic line widths (Γ) of the 205 μm [NII] lines (see §2.6.6). In addition to these measured parameters, Table 2.7 also includes averages for all of the derived parameters in the present work: the electron density (n_e; §2.6.2); the percentage of 158 μm [CII] emission arising from PDRs (§2.6.3); the FUV flux (G_0), hydrogen nuclei density ($n_{\rm H}$), and PDR surface temperature (§2.6.4); and the photoelectric heating efficiency, ϵ (§2.6.5).

In Table 2.7 we have also calculated the hydrogen and electron column densities, $N_{\rm H}$ and N_e, for PDRs and HII regions, respectively, using the measured intensities of 146 μm [OI] for PDRs (since this line is typically optically thin), and 122 μm [NII] for HII regions. We assumed a PDR temperature equal to the PDR surface temperature (which will be higher than in the bulk of the PDR), so that our column densities for PDRs are likely to be underestimates. From these column densities we find a relative mass fraction for PDRs/(PDRs + HII Regions) of $\sim$ 91 to 98 % for all sources except Car II, where it is 72 %. Thus, despite the fact that the [CII] emission from PDRs is only $\sim$ 2 times greater than from HII regions, the mass of PDR gas greatly exceeds that of ionized gas. This is not surprising, as it takes very little ionized gas to produce nearly as much [CII] emission as arises from the neutral gas. This is because the collision strengths

Table 2.7: Parameters Averaged Over Major Components of the Carina Nebula

	Tr 16	**η Car**	**Car II**	**Tr 14**	**Car I**	**GMC**	**Entire Nebula**[‡]	*Units*
l [†]	287.63	287.5969	287.56	287.40	287.37	< 287.33	–	[deg]
b	-0.65	-0.6295	-0.61	-0.58	-0.63	–	–	·
Measured Parameters:								
I ([OI] 63 μm)	15.0	30.8	57.5	81.2	79.2	12.6	13.4	[10^{-8} W m^{-2} sr^{-1}]
I ([NII] 122 μm)	6.9	17.3	13.7	6.6	19.8	2.9	3.7	·
I ([OI] 146 μm)	0.6	1.2	2.4	3.2	6.4	0.6	0.7	·
I ([CII] 158 μm)	28.3	32.1	46.7	83.5	80.8	27.8	29.2	·
I ([NII] 205 μm)	12.3	< 2.6	16.2	12.2	18.7	9.5	11.3	·
R.V. ([NII] 205 μm)	-34.7	–	-30.4	-32.2	-24.8	-27.9	-31.6	[km s^{-1}]
Γ ([NII] 205 μm)	52.8	–	55.3	47.1	40.9	35.6	37.7	·
Derived Parameters:								
% [CII] from PDRs	41	45	39	75	43	73	63	%
G_0	119	< 10	3310	580	1390	152	303	[1.6 μW m^{-2}]
$n_{\rm H}$ (PDRs)	78	17800	918	685	316	104	1250	[cm^{-3}]
n_e (HII Regions)	7	79	18	17	24	18	29	·
$N_{\rm H}$ (PDRs)	417	70	46	184	356	180	31	10^{20} cm^{-2}
N_e (HII Regions)	22	6	18	9	19	4	3	·
$T_{\rm surface}$ (PDRs)	263	71	432	295	486	332	234	[K]
ϵ (([OI] 63 + [CII] 158)/FIR)	2.8	–	1.5	3.7	2.7	4.3	3.4	[10^{-3}]

[†] Coordinates refer to the centers of the sources, listed in order of decreasing l (Röser and Bastian (1988) for η Car; Whiteoak (1994) for Car I and II; Kharchenko *et al*. (2005) for Tr 14 and 16). The areas of the sources (over which the parameters were averaged) were determined by a multi-wavelength comparison with previous observations, and are limited by the observed raster positions (*see text for details*). [‡] The "entire nebula" consists of all the observed raster positions, which differ between the ISO and SPIFI data (Figure 2.3).

for the electron/ion impact excitation of [CII] in HII regions are much greater than those in the neutral gas regions. These large PDR/HII region mass ratios are reminiscent of the high ratios observed in the Galaxy as a whole and in external galaxies (*cf.* Crawford *et al*. 1985; Stacey *et al*. 1985, 1991).

In Figure 2.31 we plot the fine-structure line intensities from Table 2.7 as a function of galactic longitude, *l*. In this plot we see that the dominant coolants of Carina are the 158 μm [CII] and 63 μm [OI] lines, with the two [NII] lines being several factors weaker in all the sources. We also see a clear dichotomy in the two pairs of lines: with the [CII] and [OI] tracing each other and the two [NII] lines tracing each other. The correlation between [CII] and [OI] suggests that much of the C^+ arises in PDRs. This is in agreement with the results of §2.6.3 and the averages reported in Table 2.7, by which an average of 63 % of the C^+ arises in PDRs over the entire nebula.

To investigate line intensity correlations further, in Figure 2.32 we plot the [OI] line pair intensities and the [NII] line pair intensities against the 158 μm [CII] intensity for the entire Carina data set. We see similar correlations as in Figure 2.31 and as in our previous morphology study (§2.6.1): namely that the [CII] is more strongly correlated with the [OI] lines (sample correlation coefficients of r = 0.75 and 0.83 for 63 μm and 146 μm, respectively) than the [NII] lines (correlation coefficients of r = 0.64 and 0.30 for 122 μm and 205 μm respectively). Again, these data imply that, on average over the entire nebula, the majority of the [CII] arises in PDRs. This argument is especially strong for the 205 μm [NII] to 158 μm [CII] correlation (Figure 2.32, lower right panel): for ionized media, these lines have essentially the same critical density, so that the lack of correlation is especially significant. The other three correlations have the caveat that

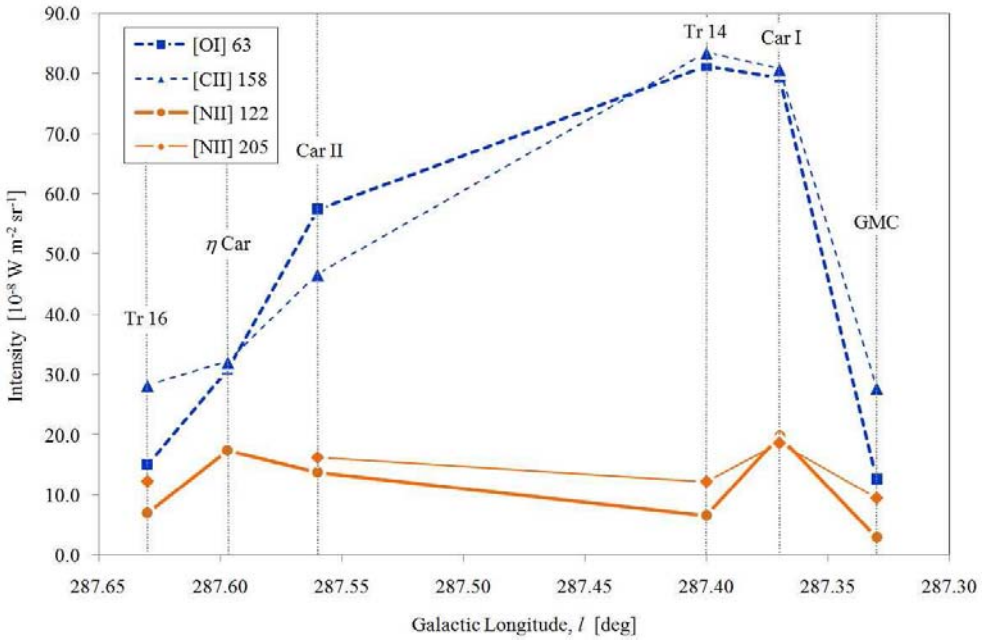

Figure 2.31: Comparison of Intensities Across the Carina Nebula
The intensities of 63 μm [OI], 158 μm [CII], and 122 and 205 μm [NII] fine-structure emission are compared for major sources across the Carina Nebula. The data points are taken from Table 2.7. The 205 μm [NII] line was not detected at the position of η Car, so no data point is given there. The connecting lines are meant only to guide the eye, and do not represent data between sources.

the line ratios of 63/158, 122/158, and 146/158 are density dependent – *i.e.* only a uniform density source could yield a very high correlation.

For completeness, we also compare the [OI] lines to each other and the [NII] lines to each other (Figure 2.33). As expected, we find reasonably good correlations in both sets: sample correlation coefficients of $r = 0.88$ and 0.54 for [OI] and [NII], respectively. Again, these correlations have the caveat that the 63/146 and 122/205 ratios are both density dependent – *i.e.* only a uniform density source could yield a very high correlation. The good correlation for the [OI] 63/146 um line is because both transitions are in the low-density limit for most positions (Table 2.7), so that the line ratio is nearly constant. The correlation is less good for the [NII] lines since the densities are in the regime where the line ratio

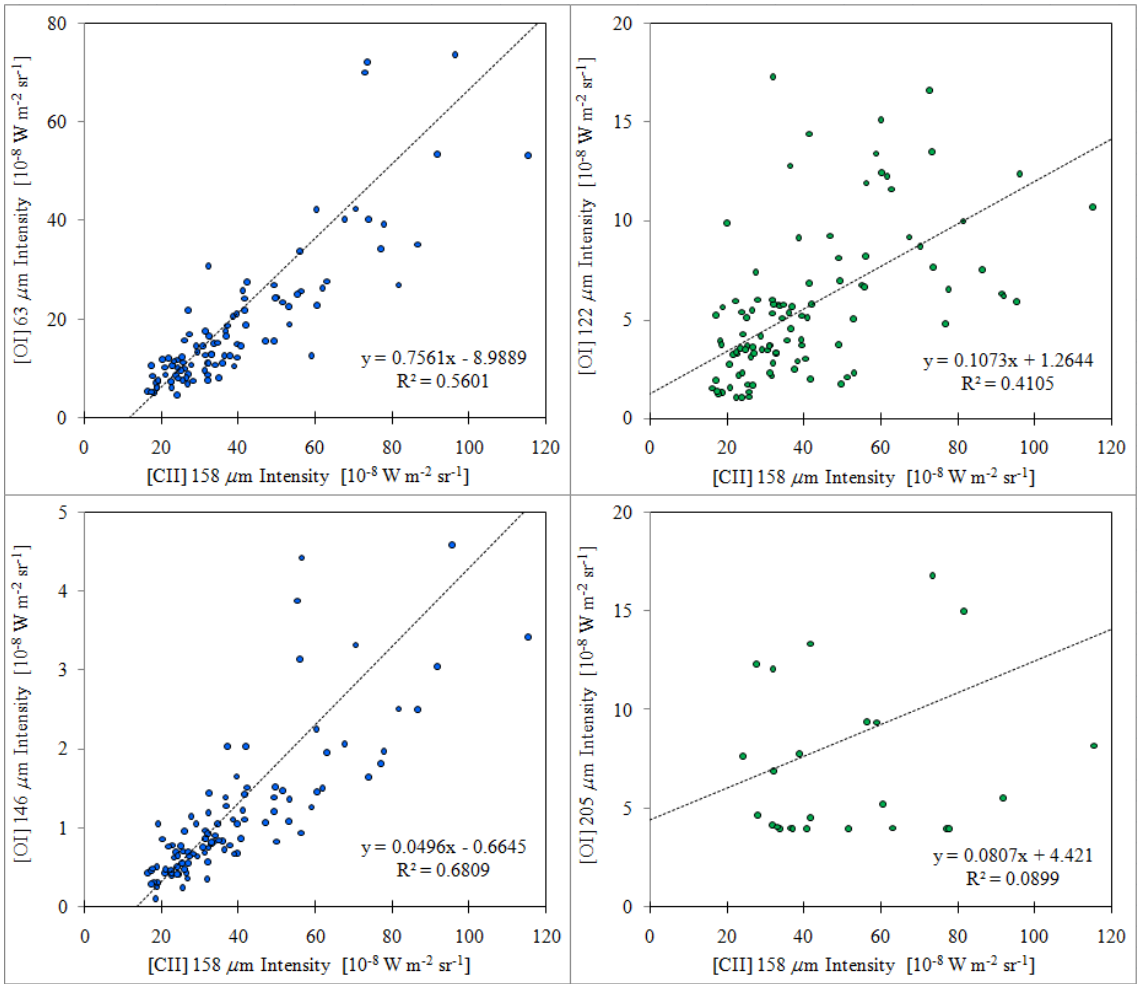

Figure 2.32: [CII] 158 μm Correlations

Line intensities of 63 and 146 μm [OI] (top left and bottom left panels, respectively) and 122 and 205 μm [NII] (top right and bottom right panels, respectively) are plotted against the line intensity of 158 μm [CII]. The 63, 146, and 122 μm plots include all 100 observed ISO raster positions. The 205 μm plot includes only the 27 raster positions at which SPIFI and ISO beams overlap (*cf.* §2.6.2), and the SPIFI 205 μm data are cut-off at a lower detection limit of 3.8 $\times 10^{-8}$ W m^{-2} sr^{-1}. Linear best-fit lines are plotted for each data set. The equation of the best fit line and the sample correlation coefficient, r, are listed in the lower right-hand corner of each panel.

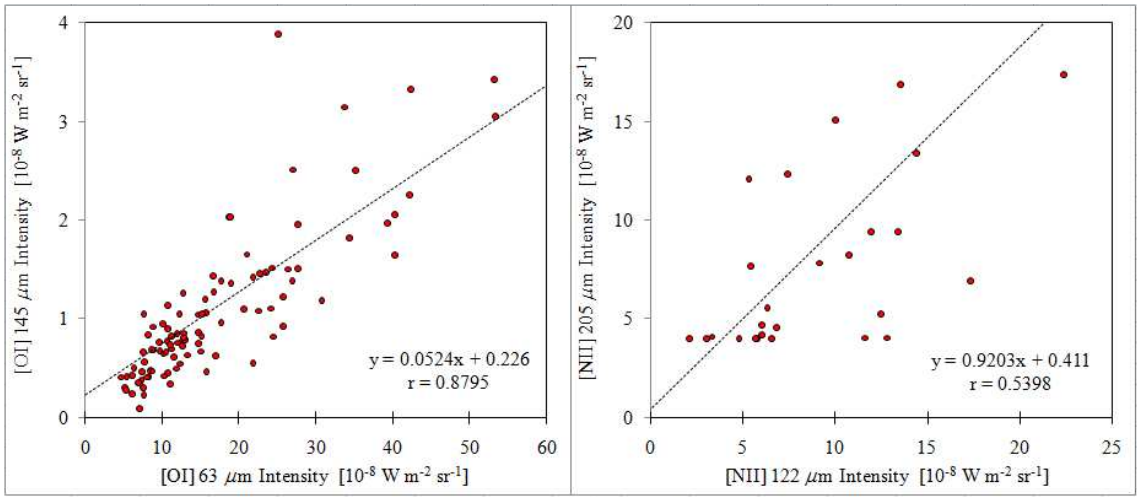

Figure 2.33: [OI] and [NII] Correlations

The intensities of the 63 and 146 μm [OI] lines (left panel) and 122 and 205 μm [NII] lines (right panel) are compared. The [OI] plot includes all 100 observed ISO raster positions. The [NII] plot includes only the 27 raster positions at which SPIFI and ISO beams overlap (*cf.* §2.6.2), and the SPIFI 205 μm data are cut-off at a lower detection limit of 3.8 $\times 10^{-8}$ W m^{-2} sr^{-1}. Linear best-fit lines are plotted for each data set. The equation of the best fit line and the sample correlation coefficient, r, are listed in the lower right-hand corner of each panel.

is very density-sensitive for most positions (Table 2.7). The lower correlation between the [NII] data may also be due to the limited number of overlapping beams (27) between the ISO and SPIFI data sets and the lower SNR of the 205 μm data. However, for comparison, note that the 205 μm [NII] line has much stronger correlation to the 122 μm [NII] line (r = 0.54) than to the 158 μm [CII] line (r = 0.30).

In Figures 2.34 and 2.35 we compare the densities and and FUV radiation field, G_0, across galactic longitude. For all the sources within Carina, we see good correlation between the hydrogen nuclei density, $n_{\rm H}$ (as measured in the PDRs), and the electron density, n_e (as measured in the HII regions), with $n_{\rm H}/n_e$ averaging ~ 43 over the nebula. Since typical HII region gas temperatures are ~

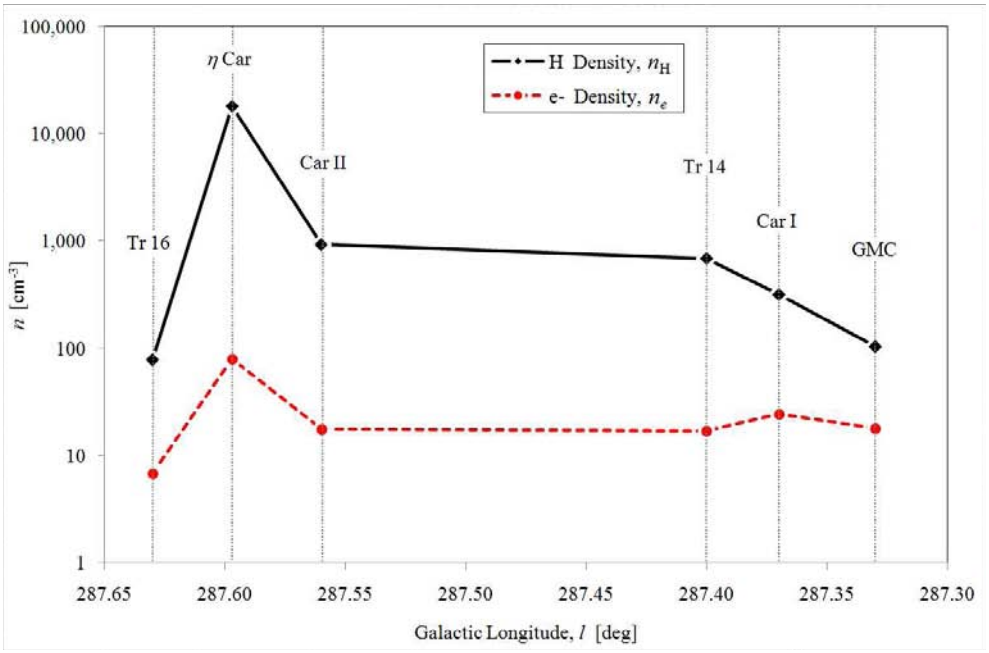

Figure 2.34: Density Across the Carina Nebula

The hydrogen nuclei density, $n_{\rm H}$ (representing the density of neutral gas), and the electron density, n_e (representing the density of ionized gas), are plotted for the major sources across the Carina Nebula. The data points are taken from Table 2.7. The connecting lines are meant only to guide the eye, and do not represent data between sources.

8000 K, the ratio of gas temperatures $T_{\rm H}/T_e$ is also ~ 40, so that there is rough pressure equilibrium between the neutral and ionized gas phases.

In Figure 2.35, we note the density spike and corresponding G_0 minimum at the position of η Car. The Homunculus is contained in an area of roughly 15″ × 15″ (*e.g.* Davidson 1999), filling approximately 10 % of the SPIFI beam or 5 % of the ISO beam. The density of the outer ejecta of η Car has been reported as $n_{\rm H}$ $\sim 0.5 - 1 \times 10^7$ cm^{-3} (Smith 2006b). It is thus possible that the gas densities we infer there are an average of a higher density component associated with η Car's outer ejecta and a lower density component associated with the surrounding ISM. The gas densities should be naturally enhanced here, and the FUV fields

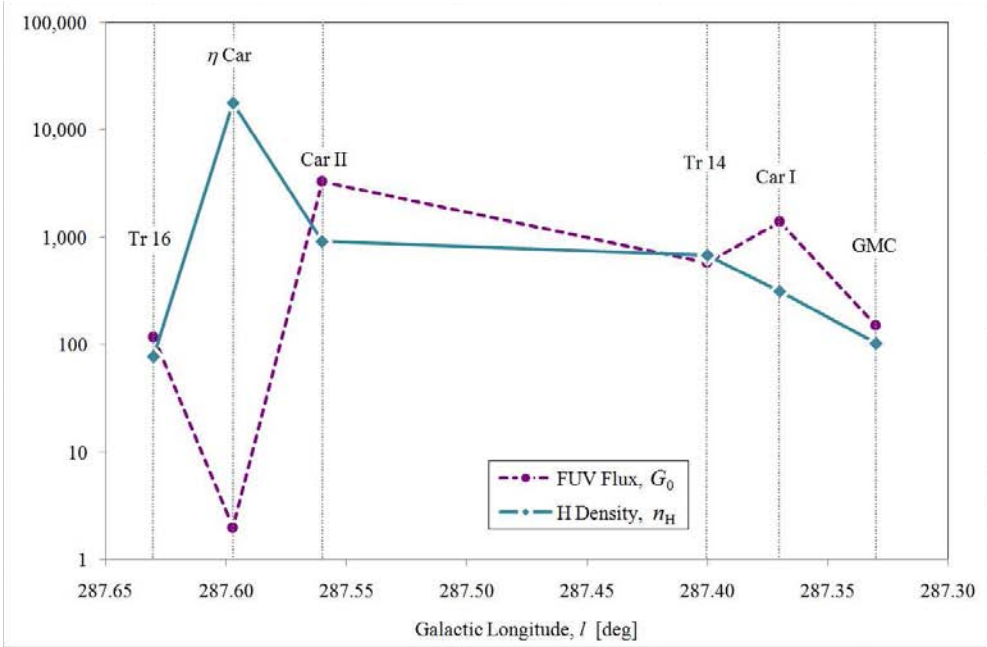

Figure 2.35: G_0 and n_H Across the Carina Nebula

The FUV flux, G_0 (in units of the local interstellar radiation field, 1.6 $\times 10^{-6}$ W m^{-2}, Habing 1968), and hydrogen nuclei density, n_H (in units of cm^{-3}), are plotted for the major sources across the Carina Nebula. The data points are taken from Table 2.7, and represent the PDR conditions in the Carina Nebula as modeled in §2.6.4. The connecting lines are meant only to guide the eye, and do not represent data between sources.

in the Homumculus may be diminished due to the substantial shielding by dust from prior ejections.

As a check on our PDR model for Carina (§2.6.4), it is instructive to compare the FUV flux predicted by the model with the the FUV flux expected from the total luminosity of the nebula's known O and B spectral-type stars. It is now generally accepted – and further supported by the present work – that Car I is excited externally by the Tr 14 cluster to the northeast, and that Car II is excited externally by the Tr 16 cluster to the southeast. The O and B members of Tr 14 have a total FUV luminosity of $L_{\rm FUV} = 10^{6.31} L_\odot = 7.84 \times 10^{32}$ W (Smith 2006a), and the distance from Tr 14 to Car I is $d \sim 2.34$ pc $= 7.22 \times 10^{16}$ m (using the nominal

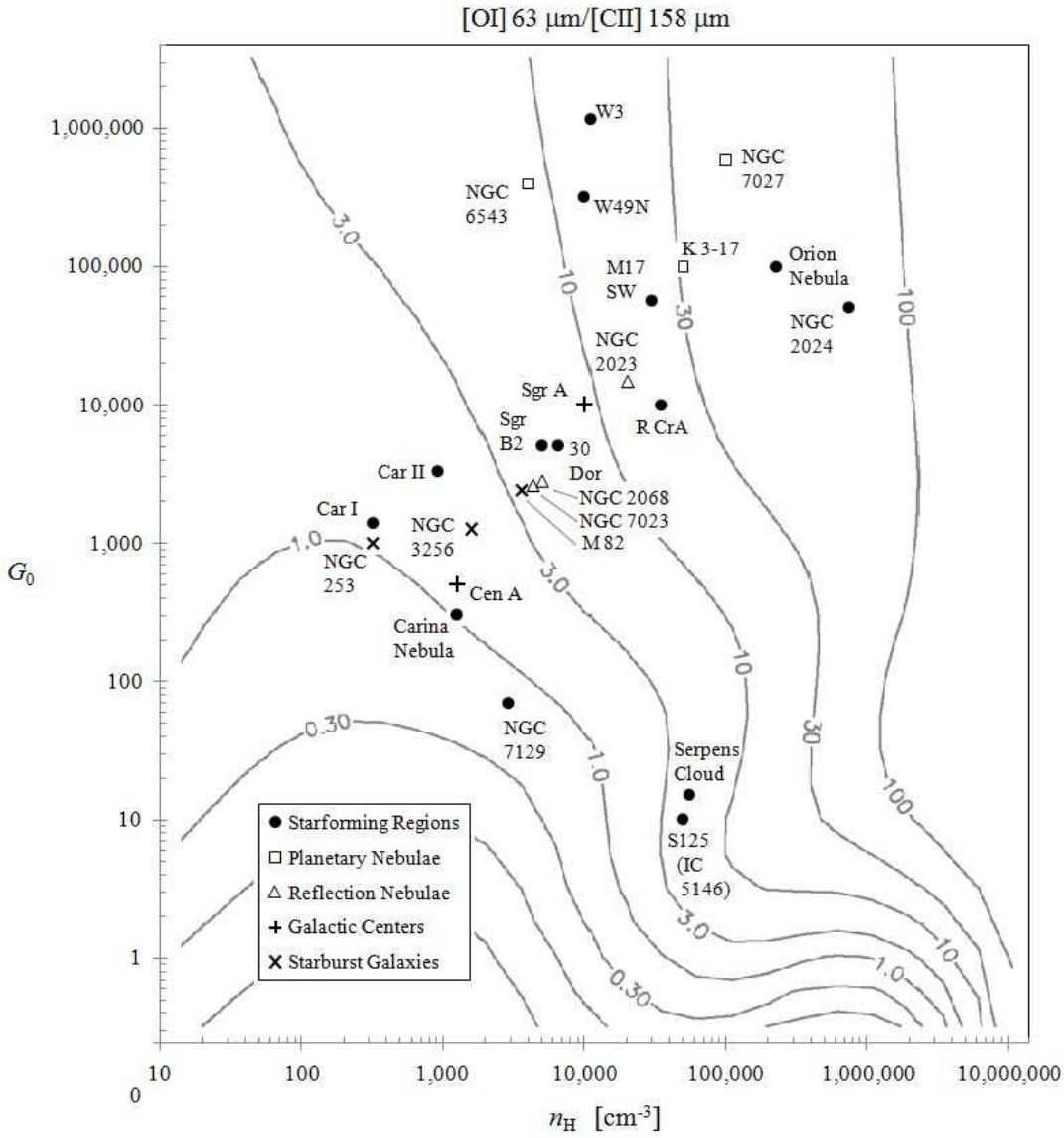

Figure 2.36: Comparison of PDRs in Astrophysical Sources

The PDR properties (n_H and G_0) of Car I, Car II, and the entire Carina Nebula (Table 2.7) are compared to other Galactic and extragalactic sources. The contours show the line intensity ratio of 63 μm [OI] to 158 μm [CII] (taken from Kaufman *et al*. 1999). ***References***: Orion Nebula, Tielens & Hollenbach (1985b); M17 SW, Meixner *et al*. (1992); R CrA, Giannini *et al*. (1998); NGC 7129, Tommasi *et al*. (1998); Sgr A and NGC 7027, Hollenbach & Tielens (1999); NGC 2024, Giannini *et al*. (2000); Cen A, Negishi *et al*. (2001) and Unger *et al*. (2000); M 82, NGC 253 and NGC 3256, Negishi *et al*. (2001); 30 Dor, Vastel *et al*. (2001) and Poglitsch *et al*. (1995); W49N, Vastel *et al*. (2001); Serpens Cloud, Larsson *et al*. (2002); NGC 2023, NGC 2068, and NGC 7023, Young Owl *et al*. (2002); S125 (IC 5146), Aannestad *et al*. (2003); Sgr B2, Goicoechea *et al*. (2004); W3, Kramer *et al*. (2004); K 3-17 and NGC 6543, Barnard-Salas *et al*. (2005).

source center positions from Table 2.7). Therefore, the expected FUV flux at Car I is $G_0 = L_{\rm FUV}/(4\pi d^2) \sim 7480$ (in units of the local interstellar FUV field, $1.6{\times}10^{-6}$ W m^{-2}, Habing 1968). The O and B stars of Tr 16 have a combined FUV luminosity of $L_{\rm FUV} = 10^{6.79} L_\odot = 2.37 \times 10^{33}$ W, and a distance to Car II of $d \sim 3.24$ pc $= 10.0 \times 10^{16}$ m. Therefore, the expected FUV flux at Car II is $G_0 = L_{\rm FUV}/(4\pi d^2) \sim 11800$ (in Habing 1968 units). For both Car I and II, the expected FUV flux from O and B stars (7480 and 11800, respectively) is a few times larger than the FUV flux predicted by our PDR model (1390 and 3310, respectively; Table 2.7). Thus, our findings agree with the established hypothesis that there is more than enough radiation from the O and B members of Tr 14 and 16 to externally excite Car I and II, respectively, without the need invoke unbeknownst embedded sources.

In Figure 2.36 we have plotted the data for Car I, Car II, and the entire Carina Nebula on $n_{\rm H}$ and G_0 axis with several other Galactic and extragalactic sources. The data points are overlayed on contours of the line intensity ratio of 63 μm [OI] to 158 μm [CII] from the PDR model of Kaufman *et al.* (1999). The Carina sources have lower densities and FUV fields ($n_{\rm H} < 10^4$ and $G_0 < 10^4$) than most other Galactic star-forming regions – such as the Orion Nebula, M17, and W49. Instead, we find Carina to be more akin to 30 Doradus (as previously suggested by Brooks *et al.* 2003) and the reflection nebulae NGC 7023 and NGC 2068. The separation between Tr 14 and the Car I PDR is similar to the distance between the [CII] peak and star cluster R136 in 30 Dor (Israel *et al.* 1996). In both of these regions, the bulk of the molecular matter in the vicinity of the early-type stars has been destroyed or swept away, and the PDRs we see are forming on the peripheral edges of the remaining GMCs. On the other hand, in the case of Orion, the parent molecular cloud (OMC-1) appears to still be relatively intact, resulting in PDRs which have formed much closer to the exciting stars. We also

notice that the conditions in Carina are similar to those in large (~ 500 pc scale) beam studies of the nearby starburst galaxies NGC 253, NGC 3256 and M82. The very high rates of starformation over large scales in Carina have resulted in FUV fields and gas excitation conditions that mimic those in starburst galaxies as a whole.

CHAPTER 3

SUMMARY

After six observing runs at the JCMT, the SPIFI spectrometer was upgraded and outfitted for observations at the AST/RO telescope at South Pole, where the dry conditions, high altitude, and low temperatures combine to create some of the best submm skies on the planet. The upgrades included a new High Order Fabry Perot Interferometer (HOFPI) which improved the efficiency and quality of spectral scans, new filtration which optimized the instrument for work in the 200 μm telluric window, and a new calibration unit customized for the AST/RO Nasmyth mount. To integrate SPIFI with the AST/RO and optimize its performance at South Pole, a heated weather enclosure (*Spifihaus*) was constructed on the AST/RO Nasmyth mount, a custom secondary mirror was machined for the AST/RO, and several functions of the instrument were automated or outfitted with remote controls.

SPIFI was installed on the AST/RO on December 21, 2003, and had first light on January 3, 2004. Several tests and calibrations were carried out to verify and optimize the performance of the SPIFI-AST/RO system, including instrument pointing, focus, brightness calibration, and wavelength calibration. SPIFI conducted 205 μm skydips to check the calibration of the AST/RO tipper. At the time of scientific observations, SPIFI had a resolving power of $R = \lambda/\Delta\lambda \sim 4250$, a spatial resolution (FWHM beam size) of $\Gamma \sim 54''$, and a sensitivity of NEP $\sim 2.5 \times 10^{-15}$ W Hz$^{-1/2}$ (referred to the front-end of the Dewar). This NEP is within a factor of ~ 1.4 of the of the fundamental limits imposed by the photon shot noise associated with the large thermal background from the (nearly opaque) sky at 205 μm. SPIFI's NEP is also a factor of ~ 10 better than the best NEPs achieved

by direct detection spectrometers using photoconductor detectors, and SPIFI's equivalent receiver temperature ($T_{\rm rec}$(DSB) ~ 150 K) is a factor of ~ 7 better than the best temperatures achieved by heterodyne receivers.

SPIFI's primary scientific observations were carried out between August 15 and August 30, 2005. The target was the Carina Nebula, a nearby (~ 2.3 kpc) active star-forming region which has a more impressive collection of O and B spectral type stars than any other location in the galaxy. SPIFI obtained 236 spectra of the 205 μm [NII] fine-structure line over ~ 250 arcmin^2 of the northern Carina Nebula, including the Car I and II HII regions. These data constitute the first ground-based detection of the 205 μm [NII] line, and only the third detection overall since those of the Cosmic Background Explorer (COBE) Far Infrared Absolute Spectrophotometer (FIRAS) and the Kuiper Airborne Observatory (KAO) in the early 1990s.

SPIFI 205 μm [NII] data are supplemented with new reductions of FIR fine-structure spectra from the Infrared Space Observatory (ISO) in 63 μm [OI], 122 μm [NII], 146 μm [OI], and 158 μm [CII]. We believe the new reductions are more robust than previously published values for these species due to improvements in the ISO OLP pipeline and the improvement and formalization of post-OLP processing (*i.e.* the L01 HPDP). Furthermore, our 146 μm [OI] data include 90 raster positions which have not been previously published.

Contour maps have been plotted for all of the SPIFI and ISO species, and morphological comparisons are made with optical, radio continuum and CO maps. We find good spatial correlation between the [NII] maps and other ionized species and thermal radio emission. The [OI] and [CII] show good spatial correlation with other neutral species. Our morphological results support the

predominant view that the Car I and II regions are powered externally by the Tr 14 and 16 clusters, respectively. We also find that the region surrounding Tr 16 is largely devoid of neutral gas, consistent with the view that the gas near Tr 16 cluster has been photoionized and dispersed to a larger extent than that associated with the Tr 14 cluster, since the former cluster is ~ 1 Myr older.

The average widths and velocities of our 205 μm [NII] data agree very well with previous kinematic studies of the Carina Nebula. In particular, we find that line widths in the vicinity of Car II are substantially fatter (~ 55 km s^{-1}) than those near Car I (~ 41 km s^{-1}). We believe that these lines appear wider because they consist of a double-peaked profile which cannot be resolved by SPIFI. This line splitting is due to a hot "bubble" of ionized gas expanding outward from Tr 16. In addition, we find that the average radial velocity of lines near Car II (~ -30 km s^{-1}) are more negative than those near Car I (~ -25 km s^{-1}), consistent with previous observations which show Car II approaching at a faster rate than Car I along our line of sight.

The 122 [NII] / 205 [NII] line ratio is used to probe the density of the low-ionization gas, from which we find an average electron density over the Carina Nebula of $n_e \sim 29$ cm^{-3}. Except for a density spike at the position of η Car, the electron density shows little spatial variation over the nebula. This result suggests that the extended low-density ($n_e < 100$ cm^{-3}) ionized gas component in Carina (Mizutani *et al*. 2002) must also contain gas in lower-ionization states.

The 158 [C II] / 205 [NII] line ratio is used to probe the fraction of C^+ arising from PDRs, and we find that an average of 63 % of the C^+ arises from PDRs. This result agrees with previous studies which contend that the majority of the observed [CII] line emission from Galactic star-forming regions, the Galaxy as a

whole, and from external galaxies arises in warm dense PDRs on the surfaces of molecular gas clouds. We find that a lower percentage of C^+ arises from PDRs in regions which are largely devoid of molecular material, such as Tr 16.

The (63 [OI] + 158 [CII]) / FIR continuum ratio is used to derive the photoelectric heating efficiency, which we find to average $\epsilon \sim 3.42 \times 10^{-3}$ over the nebula. These values are typical for Galactic star formation regions exposed to moderate ($G_0 \sim 100 - 1000$) FUV fields, and agree well with previous Carina studies.

Finally, the [OI] and [CII] lines are used to construct a PDR model of Carina following Kaufman *et al*. (1999). Carina is found to have lower values for the FUV flux G_0 ($\lesssim 10^4$) and hydrogen nuclei density $n_{\rm H}$ ($\lesssim 10^3$) than are typical for other galactic star-forming regions (such as the Orion Bar, M17, or W49). Instead, Carina is found to be more akin to 30 Doradus in the Large Magellanic Cloud, consistent with the view of Carina as a more evolved region, where much of the parent molecular cloud has been ionized or swept away.

BIBLIOGRAPHY

Aannestad, P. A., & Emery, R. J. 2003, A&A, 406, 155

Ade, P. A. R., Pisano, G., Tucker, C., & Weaver, S. 2006, in Proc. SPIE 6275, Millimeter and Submillimeter Detectors and Instrumentation for Astronomy III, ed. J. Zmuidzinas, W. S. Holland, S. Withington, & W. D. Duncan (Bellingham, WA: SPIE), 62750U

Allen, D. A., & Hillier, D. J. 1993, PASA, 10, 338

Beichman, C. A., Neugebauer, G., Habing, H. J., Clegg, P. E., & Chester, T. J. 2002, Infrared Astronomical Satellite (IRAS) Catalogs and Atlases, Volume 1: Explanatory Supplement, http://irsa.ipac.caltech.edu/IRASdocs/exp.sup/

Benford, D. J., Gaidis, M. C., & Kooi, J. W. 2003, Appl. Opt., 42, 5118

Bennett, C. L., *et al.* 1994, ApJ, 434, 587

Bernard-Salas, J., & Tielens A. G. G. M. 2005, A&A, 431, 523

Blum, R. D., & Pradhan, A. K. 1992, ApJS, 80, 425

Bradford, C. M. 2001, Ph.D. thesis, Cornell Univ.

Bradford, C. M., Nikola, T., Stacey, G. J., Bolatto, A. D., Jackson, J. M., Savage, M. L., Davidson, J. A., & Higdon, S. J. 2003, ApJ, 586, 891

Bradford, C. M., Stacey, G. J., Nikola, T., Bolatto, A. D., Jackson, J. M., Savage, M. L., & Davidson, J. A 2005, ApJ, 623, 866

Bradford, C. M., *et al.* 2002, Appl. Opt., 41, 2561

Brooks, K. J., Cox, P., Schneider, N., Storey, J. W. V., Poglitsch, A., Geis, N., & Bronfman, L. 2003, A&A, 412, 751

Brooks, K. J., Storey, J. W. V., & Whiteoak, J. B. 2001, MNRAS, 327, 46

Brooks, K. J., Whiteoak, J. B., & Storey, J. W. V. 1998, PASA, 15, 202

Brown, J. M., Varberg, T. D., Evenson, K. M., & Cooksy, A. L. 1994, ApJL, 428, L37

Calisse, P. G., Ashley, M. C. B., Burton, M. G., Phillips, M. A., Storey, J. W. V., Radford, S. J. E., & Peterson, J. B. 2004, PASA, 21, 256

Cesarsky, C. J., *et al.* 1996, A&A, 315, L32

Chamberlin, R. A. 2001, J. Geophys. Res., 106, 20101

Chamberlin, R. A., & Bally, J. 1994, Appl. Opt., 33, 1095

Chamberlin, R. A., & Bally, J. 1995, Int. J. Infrared Millimeter Waves, 16, 907

Chamberlin, R. A., Lane, A. P., & Stark, A. A. 1997, ApJ, 476, 428

Chamberlin, R. A., Martin, R. N., Martin, C. L., & Stark, A. A. 2003, in Proc. SPIE 4855, Millimeter and Submillimeter Detectors for Astronomy, ed. T. G. Phillips & J. Zmuidzinas (Bellingham, WA: SPIE), 609

Clegg, P. E., *et al.* 1996, A&A, 315, L38

Colgan, S. W. J., Haas, M. R., Erickson, E. F., Rubin, R. H., Simpson, J. P., & Russell, R. W. 1993, ApJ, 413, 237

Cooksy, A. L., Blake, G. A., & Saykally, R. J. 1986, ApJ, 305, L89

Crawford, M. K., Genzel, R., Townes, C. H., & Watson, D. M. 1985, ApJ, 291, 755

Damineli, A. 1996, ApJL, 460, L49

Davidson, K., & Humphreys, R. M. 1997, ARA&A, 35, 1

Davies, P. B., Handy, B. J., Lloyd E. K. M., & Smith, D. R. 1978, J. Chem Phys., 68, 1135

Dickel, H. R. 1974, A&A, 31, 11

Dickel, H. R., & Wall, J. V. 1974, A&A, 31, 5

de Graauw, T., Lidholm, S., Fitton, B., Beckman, J., Israel, F. P., Nieuwenhuijzen, H., & Vermue, J. 1981, A&A, 102, 257

de Graauw, T., *et al.* 1996, A&A, 315, L49

Deharveng, L., & Maucherat, M. 1975, A&A, 41, 27

de Lacaille, N. L. 1763, Coelum Australe Stelliferum, ed. J. D. Maraldi (Paris), http://seds.lpl.arizona.edu/Messier/xtra/history/lacaille.html

Dragovan, M., Platt, S. R., Pernic, R. J., & Stark, A. A. 1989, in AIP Conf. Proc. 198, Astrophysics in Antarctica, ed. D. J. Mullan, M. A. Pomerantz, & T. Stanev (New York, NY: AIP), 97

Dragovan, M., Stark, A. A., Pernic, R., & Pomerantz, M. A. 1990, Appl. Opt., 29, 463

Draine, B. T., & McKee, C. F. 1993, ARA&A, 31, 373

Draine, B. T., Roberge, W. G., & Dalgarno, A. 1983, ApJ, 264, 485

Dufek, G. J. 1957, Operation Deepfreeze (New York, NY: Harcourt, Brace and Co.)

Engargiola, G., Zmuidzinas, J., & Lo, K.-Y. 1994, Rev. Sci. Instrum., 65, 1833

Eve, W. D., Sollner, T. C. L. G., & Robson, E. I. 1977, A&A, 59, 209

Feinstein, A. 1995, in RevMexAA Serie de Conferencias 2, The η Carinae Region: A Laboratory of Stellar Evolution, ed. V. Niemela, N. Morrell, & A. Feinstein (México, D.F.: Inst. Astron. UNAM), 57

Fixsen, D. J., Bennett, C. L., & Mather, J. C. 1999, ApJ, 526, 207

Gardner, F. F., Dickel, H. R., & Whiteoak, J. B. 1973, A&A, 23, 51

Gardner, F. F., Milne, D. K., Mezger, P. G., & Wilson, T. L. 1970, A&A, 7, 349

Gardner, F. F., & Morimoto, M. 1968, AuJPh, 21, 881

Gerecht, E., *et al.* 2003, in Proc. SPIE 4855, Millimeter and Submillimeter Detectors for Astronomy, ed. T. G. Phillips and J. Zmuidzinas (Bellingham, WA: SPIE), 574

Ghosh, S. K., Iyengar, K. V. K., Rengarajan, T. N., Tandon, S. N., Verma, R. P., & Daniel, R. R. 1988, ApJ, 330, 928

Giannini, T., Lorenzetti, D., Benedettini, M., Nisini, B., Saraceno, P., Tommasi, E., Smith, H. A., & White, G. J. 1998, in ASP Conf. Ser. 132, Star Formation with the Infrared Space Observatory, ed. J. L. Yun & R. Liseau (San Francisco: ASP), 350

Giannini, T., *et al.* 2000, A&A, 358, 310

Goff, J. A., & Gratch, S. 1946, Trans. Am. Soc. Heat. Vent. Eng., 52, 95

Goicoechea, J. R, Rodríguez-Fernández, N. J., & Cernicharo, J. 2004, ApJ, 600, 214

Grec, G., Fossat, E., & Pomerantz, M. 1980, Nature, 288, 541

Gregory, P. C. 2005, Bayesian Logical Data Analysis for the Physical Sciences (Cambridge, UK: Cambridge Univ. Press)

Groppi, C., Walker, C., Hungerford, A., Kulesa, C., Jacobs, K., & Kooi, J. 2000, in ASP Conf. Ser. 217, Imaging at Radio through Submillimeter Wavelengths, ed. J. G. Mangum & S. J. E. Radford (San Francisco: ASP), 48

Gry, C. *et al.* 2003, in ESA SP-1262, The ISO Handbook, Vol. III: LWS - The Long Wavelength Spectrometer, ed. T. G. Müller, J. A. D. L. Blommaert, & P. García-Lario (SAI-99-077/Dc, Version 2.1; Noordwijk, Netherlands: ESA Pub.), http://iso.esac.esa.int/manuals/HANDBOOK/lws_hb/

Habing, H. J. 1968, Bull. Ast. Inst. Netherlands, 19, 421

Harper, A., Hildebrand, R. H., Stiening, R., & Winston, R. 1976, Appl. Opt., 15, 53

Heiles, C. 1994, ApJ, 436, 720

Hollenbach, D. J., & McKee, C. F. 1989, ApJ, 342, 306

Hollenbach, D. J., & Tielens, A. G. G. M. 1997, ARA&A, 35, 179

Hollenbach, D. J., & Tielens, A. G. G. M. 1999, Rev. Mod. Phys., 71, 173

Honingh, C. E., Hass, S., Hottgenroth, K., Jacobs, J., & Stutzki, J. 1997, IEEE Trans. Appl. Superconductivity, 7, 2582

Hsieh, H. H. 1998, AST/RO Technical Memorandum #33 (Cambridge, MA: Harvard-Smithsonian CFA), http://www.cfa.harvard.edu/ adair/AST_RO/pub.html

Huchtmeier, W. K., & Day, G. A. 1975, A&A, 41, 153

Hudson, C. E., & Bell. K. L. 2004, MNRAS, 348, 1275

Indermuehle, B. T., Burton, M. G., & Maddison, S. T. 2005, PASA, 22, 73

Israel, F. P., Maloney, P. R., Geis, N., Herrmann, F., Madden, S. C., Poglitsch, A., & Stacey, G. J. 1996, ApJ, 465, 738

Kaufman, M. J., Wolfire, M. G., Hollenbach, D. J., & Luhman, M. L. 1999, ApJ, 527, 795

Kessler, M. F., *et al.* 1996, A&A, 315, L27

Kessler, M. F., *et al.* 2003, in ESA SP-1262, The ISO Handbook, Vol. I: ISO - Mission & Satellite Overview, ed. T. G. Müller, J. A. D. L. Blommaert, & P. García-Lario (SAI-2000-035/Dc, Version 2.0; Noordwijk, Netherlands: ESA Pub.), http://iso.esac.esa.int/manuals/HANDBOOK/gen_hb/

Kharchenko, N. V., Piskunov, A. E., Röser, S., Schilbach, E., & Scholz, R. -D. 2005, A&A, 438, 1163

Kramer, C., Jakob, H., Mookerjea, B., Schneider, N., Brüll, M., & Stutzki, J. 2004, A&A, 424, 887

Kramer, C., Mookerjea, B., Bayer, E., Garcia-Burillo, S. Gerin, M., Israel, F. P., Stutzki, J., & Wouterloot, J. G. A. 2005, A&A, 441, 961

Kramer, C., *et al.* 2008, A&A, 477, 547

Kulesa, C. A., *et al.* 2008, in Proc. SPIE 7012, Ground-based and Airborne Telescopes II, ed. L. M. Stepp & R. Gilmozzi (Bellingham, WA: SPIE), 701249

Lane, A. P. 1998, in ASP Conf. Ser. 141, Astrophysics from Antarctica, ed. G. Novak & R. H. Landsberg (San Francisco: ASP), 289

Larsson, B., Liseau, R., & Men'shchikov, A. B. 2002, A&A, 386, 1055

Lasker, B. M., Sturch, C. R., McLean, B. J., Russell, J. L., Jenkner, H., Shara, M. M. 1990, AJ, 99, 2019

Lawrence, J. S., Ashley, M. C. B., Tokovinin, A. & Travouillon, T. 2004, Nature, 431, 278

Lay, O. P., & Halverson, N. 2000, ApJ, 543, 787

Lee, P. L. 1977, Nucl. Instrum. Methods, 144, 363

Lemke, D., *et al.* 1996, A&A, 315, L64

Liseau, R., Justtanont, K., & Tielens, A. G. G. M. 2006, A&A, 446, 561

Liu, X. -W., *et al.* 2001, MNRAS, 323, 343

Lloyd, C., Lerate, M. R., & Grundy T. W. 2003, The LWS L01 Pipeline, Version 1, http://ida.esac.esa.int:8080/hpdp/technical_reports/technote34.html

Loewenstein, R. F., Bero, C., Lloyd, J. P., Mrozek, F., Bally, J., & Theil, D. 1998, in ASP Conf. Ser. 141, Astrophysics From Antarctica, ed. G. Novak & R. H. Landsberg (San Francisco, CA: ASP), 296

Lugten, J. B. 1987, Ph.D. thesis, University of California, Berkeley

Maíz-Apellániz, J., Walborn, N. R., Galué, H. Á., Wei, L. H. 2004, ApJS, 151, 103

Marks, R. D., Vernin, J., Azouit, M., Briggs, J. W., Burton, M. G., Ashley, M. C. B., & Manigault, J. F. 1996, A&AS, 118, 385

Marks, R. D., Vernin, J., Azouit, M., Manigault, J. F., & Clevelin, C. 1999, A&AS, 134, 161

Martin, C. L., Walsh, W. M., Xiao, K., Lane, A. P., Walker, C. K., & Stark, A. A. 2004, ApJS, 150, 239

McGee, R. X., & Gardner, F. F. 1967, AuJPh, 21, 149

Megeath, S. T., Cox, P., Bronfman, L., & Roelfsema, P. R. 1996, A&A, 305, 296

Meixner, M., Haas, M. R., Tielens, A. G. G. M., Erickson, E. F., & Werner, M. 1992, ApJ, 390, 499

Mizutani, M., Onaka, T., & Shibai, H. 2002, A&A, 382, 610

Mizutani, M., Onaka, T., & Shibai, H. 2004, A&A, 423, 579

Murcay, D. G., Murcay, F. J., Murcay, F. H., & Barker, D. B. 1981, Antarctic Journal of the U.S., 15, 199

Negishi, T., Onaka, T., Chan, K. -W., & Roellig, T. L. 2001, A&A, 375, 566

Oberst, T. E., *et al.* 2006, ApJL, 652, L125

Padin, S., *et al.* 2008, Appl. Opt., 47, 4418

Pajot, F., Gispert, R., Lamarre, J. M., Boisse, P., Puget, J. L. 1986b, A&A, 157, 393

Pajot, F., Gispert, R., Lamarre, J. M., Peyturaux, R., Puget, J. L. 1986a, A&A, 154, 55

Pajot, F., *et al.* 1989, A&A, 223, 107

Pardo, J. R., Cernicharo, J., & Serabyn, E. 2001, IEEE Trans. Antennas Propagation, 49, 1683

Parsons, N. R. 1957a, AuJPh, 10, 387

Parsons, N. R. 1957b, AuJPh, 10, 462

Peeters, E., *et al.* 2002, A&A, 381, 571

Peterson, J. B., Radford, S. J. E., Ade, P. A. R., Chamberlin, R. A., O'Kelly, M. J., Peterson, K. M., & Schartman, E. 2003, PASP, 115, 383

Petuchowski, S. J., & Bennett, C. L. 1993, ApJ, 405, 591

Petuchowski, S. J., Bennett, C. L., Haas, M. R., Colgan, S. W. J., Erickson, E. F. 1996, ApJ, 459, 181

Petuchowski, S. J., Bennett, C. L., Haas, M. R., Erickson, E. F., Lord, S. D., Rubin, R. H., Colgan, S. W. J., & Hollenbach, D. J. 1994, ApJL, 427, L17

Poglitsch, A., Krabbe, A., Madden, S. C., Nikola, T., Geis, N., Johansson, L. E. B., Stacey, G. J., & Sternberg, A. 1995, ApJ, 454, 293

Pound, M. W., & Wolfire, M. G. 2008, in ASP Conf. Ser. 394, Astronomical Data Analysis Software and Systems (ADASS) XVII, ed. R. W. Argyle, P. S. Bunclark, & J. R. Lewis. (San Francisco, CA: ASP), 654

Rathborne, J. M., Brooks, K. J., Burton, M. G., Cohen, M., & Bontemps, S. 2004, A&A, 418, 563

Rathborne, J. M., Burton, M. G., Brooks, K. J., Cohen, M., Ashley, M. C. B., & Storey, J. W. V. 2002, MNRAS, 331, 85

Retallack, D. S. 1983, MNRAS, 204, 669

Rieke, G. 2003, Detection of Light (2nd ed.; Cambridge, UK: Cambridge Univ. Press)

Röser, S., & Bastian, U. 1988, A&AS, 74, 449

Rubin, R. H. 1985, ApJS, 57, 349

Ruhl, J., *et al.* 2004, in Proc. SPIE 5498, Millimeter and Submillimeter Detectors for Astronomy II, ed. J. Zmuidzinas, W. S. Holland & S. Withington (Bellingham, WA: SPIE), 11

Rybicki, G. B., & Lightman, A. P. 2004, Radiative Processes in Astrophysics (Weinheim, Germany: Wiley-VCH Verlag GmbH & Co. KGaA)

Sanchawala, K., Chen, W. -P., Lee, H. -T., Chu, Y. -H., Nakajima, Y., Tamura, M., Baba, D., & Sato, S. 2007a, ApJ, 656, 462

Sanchawala, K., *et al.* 2007b, ApJ, 667, 963

Sakai, K., & Genzel, L. 1983, in Rev. Infrared and Millimeter Waves 1, ed. K.J. Buttons (New York, NY: Plenum Press), 155

Salama, A. 2000, in ESA SP-455, ISO Beyond Point Sources: Studies of Extended Infrared Emission, ed. R. J. Laurejis, K. Leech, & M. F. Kessler (Noordwijk, Netherlands: ESA Pub.), 7

Savage, B. D., & Sembach, K. R. 1996, ARA&A, 34, 279

Shibai, H., *et al.* 1991, ApJ, 374, 522

Simpson, J. P., Colgan, S. W. J., Cotera, A. S., Erickson, E. F., Haas, M. R., Morris, M., & Rubin, R. H. 1997, ApJ, 487, 689

Simpson, J. P., Rubin, R. H., Colgan, S. W. J., Erickson, E. F., & Haas, M. R. 2004, ApJ, 611, 338

Smith, N. 2006a, MNRAS, 367, 763

Smith, N. 2006b, ApJ, 644, 1151

Smith, N., & Brooks, K. J. 2008, in ASP Monograph Pub. 5, Handbook of Star Forming Regions: Volume II, The Southern Sky, ed. B. Reipurth (San Francisco, CA: ASP), 138

Smith, N., Stassun, K. G., & Bally, J. 2005, ApJ, 129, 888

Smythe, W. D., & Jackson, B. V. 1977 ApOpt, 16, 2041

Stacey, G. J., Beeman, J. W., Haller, E. E., Geis, N., Poglitsch, A., & Rumitz, M. 1992, Int. J. Infrared Millimeter Waves, 13, 1689

Stacey, G. J., Geis, N., Genzel, R., Lugten, J. B., Poglitsch, A., Sternberg, A., & Townes, C. H. 1991, ApJ, 373, 423

Stacey, G. J., Smyers, S. D., Kurtz, N. T., & Harwit, M. 1983, ApJL, 265, L7

Stacey, G. J., Viscuso, P. J., Fuller, C. E., & Kurtz, N. T. 1985, ApJ, 289, 803

Staniszewski, Z., *et al.* 2008, arXiv:0810.1578

Stark, A. A. 1989, in AIP Conf. Proc. 198, Astrophysics in Antarctica, ed. D. J. Mullan, M. A. Pomerantz, & T. Stanev, (New York, NY: AIP), 106

Stark, A. A., Bolatto, A. D., Chamberlin, R. A., Lane, A. P., Bania, T. M., Jackson, J. M., & Lo, K.-Y. 1997a, ApJL, 480, L59

Stark, A. A., Carlstrom, J. E., Israel, F. P., Menten, K. M., Peterson, J. B., Phillips, T. G., Sironi, G., & Walker, C. K. 1998, in Proc. SPIE 3357, Advanced Technology MMW, Radio, and Terahertz Telescopes, ed. Thomas G. Phillips (Bellingham, WA: SPIE), 495

Stark, A. A., Chamberlin, R. A., Ingalls, J., Cheng, J., & Wright, G. 1997b, Rev. Sci. Instr., 68, 2200

Stark, A. A., *et al.* 2001, PASP, 113, 567

Storey, J. W. V. 1998, in ASP Conf. Ser. 141, Astrophysics From Antarctica, ed. G. Novak & R. H. Landsberg (San Francisco, CA: ASP), 313

Swain, M. R., Bradford, C. M., Stacey, G. J., Bolatto, A. D., Jackson, J. M., Savage, M., & Davidson, J. A. 1998, in Proc. SPIE 3354, Infrared Astronomical Instrumentation, ed. A. M. Fowler (Bellingham, WA: SPIE), 480

Swinyard, B. M., *et al.* 1998, in Proc. SPIE 3354, Infrared Astronomical Instrumentation, ed. A. M. Fowler (Bellingham, WA: SPIE), 888

Tapia, M., Persi, P., Bohigas, J., Roth, M., & Gómez, M. 2006, MNRAS, 367, 513

Tapia, M., Roth, M., Vázquez, R. A., Feinstein, A. 2003, MNRAS, 339, 44

Tielens, A. G. G. M., & Hollenbach, D. 1985a, ApJ, 291, 722

Tielens, A. G. G. M., & Hollenbach, D. 1985b, ApJ, 291, 747

Tommasi, E., Lorenzetti, D., Giannini, T., Nisini, B., Palla, F. 1998, Ap&SS, 261, 187

Travouillon, T., Ashley, M. C. B., Burton, M. G., Storey, J. W. V., & Loewenstein, R. F., 2003a, A&A, 400, 1163

Travouillon, T., *et al.* 2003b, A&A, 409, 1169

Unger, S. J., *et al.* 2000, A&A, 355, 885

Vastel, C., Spaans, M., Ceccarelli, C., Tielens, A. G. G. M., & Caux, E. 2001, A&A, 376, 1064

Walborn, N. R. 1995, in RevMexAA Serie de Conferencias 2, The η Carinae Region: A Laboratory of Stellar Evolution, ed. V. Niemela, N. Morrell, & A. Feinstein (México, D.F.: Inst. Astron. UNAM), 51

Walker, C. K., Kooi, J. W., Chan, W., LeDuc, H. G., Schaffer, P. L., Carlstrom, J. E., & Phillips, T. G. 1992, Int. J. Infrared Millimeter Waves, 13, 785

Walker, C. K., *et al.* 2004, in Proc. SPIE 5489, Ground-based Telescopes, ed. J. M. Oschmann, Jr. (Bellingham, WA: SPIE), 470

Watson, D. M., Genzel, R., Townes, C. H., Werner, M. W., & Storey, J. W. V. 1984, ApJ, 279, L1

Whiteoak, J. B. Z. 1994, ApJ, 429, 225

Wolfire, M. G., Tielens, A. G. G. M., & Hollenbach, D. 1990, ApJ, 358, 116

Wright, G. 2004, Optics and Photonics News, January, 34

Wright, E. L., *et al.* 1991, ApJ, 381, 200

Yngvesson, S., *et al.* 2004, in 15th Int. Symp. Space THz Technology, ed. G. Narayanan (Amherst: Univ. Massachusetts), 365

Yonekura, Y., Asayama, S., Kimura, K., Ogawa, H., Kanai, Y., Yamaguchi, N., Barnes, P. J., & Fukui, Y. 2005, ApJ, 634, 476

Young Owl, R. C., Meixner, M. M., Fong, D., Haas, M. R., Rudolph, A. L., & Tielens, A. G. G. M. 2002, ApJ, 578, 885

Zhang, X., Lee, Y., Bolatto, A., Stark, A. A. 2001, ApJ, 553, 274

Zmuidzinas, J., & LeDuc, H. G. 1992, IEEE Trans. Microwave Theory Tech., 40, 1797